AGH UNIVERSITY OF SCIENCE AND TECHNOLOGY

FIELD OF SCIENCE: ENGINEERING AND TECHNOLOGY

SCIENTIFIC DISCIPLINE: AUTOMATION, ELECTRONIC, ELECTRICAL ENGINEERING AND SPACE TECHNOLOGIES

DOCTORAL THESIS

Powering Medical Internet of Things Systems in a Steam Sterilisation Environment

Author: mgr inż. Mateusz Danioł

Supervisor: dr hab. inż. Ryszard Sroka, prof. AGH
Assisting supervisor: dr hab. inż. Piotr Burnos, prof. AGH

Completed in: AGH University of Krakow,
Faculty of Electrical Engineering, Automatics, Computer Science and Biomedical Engineering
Department of Metrology and Electronics

Kraków, 2023

AKADEMIA GÓRNICZO-HUTNICZA IM. STANISŁAWA STASZICA W KRAKOWIE

DZIEDZINA: NAUKI INŻYNIERYJNO-TECHNICZNE

DYSCYPLINA: Automatyka, Elektronika, Elektrotechnika i Technologie Kosmiczne

ROZPRAWA DOKTORSKA

Zasilanie Medycznych Systemów Internetu Rzeczy w Środowisku Sterylizacji Parą Wodną

Autor: mgr inż. Mateusz Danioł

Promotor rozprawy: dr hab. inż. Ryszard Sroka, prof. AGH
Promotor pomocniczy: dr hab. inż. Piotr Burnos, prof. AGH

Praca wykonana: Akademia Górniczo-Hutnicza im. Stanisława Staszica w Krakowie
Wydział Elektrotechniki, Automatyki, Informatyki
i Inżynierii Biomedycznej
Katedra Metrologii i Eelektroniki

Kraków, 2023

Chciałbym podziękować mojemu promotorowi dr. hab. inż. Ryszardowi Sroce za nieocenione wsparcie naukowe i merytoryczne, cierpliwość oraz wyrozumiałość w trakcie powstawania pracy. Dziękuję także dr. hab. inż. Piotrowi Burnosowi za pomoc oraz wsparcie merytoryczne.

Chciałbym podziękować także dr. hab. Józefowi Kozakowi za bycie mentorem oraz opiekunem podczas mojego pobytu w firmie B.Braun Aesculap AG, gdzie miałem okazję uczyć się od wspaniałych specjalistów, konstruktorów i inżynierów medycznych. W szczególności dziękuję Lukasowi Böhlerowi za spędzone wspólnie godziny nad pracami badawczo-rozwojowymi, prototypami oraz wnioskami patentowymi.

Dziękuję także Julii, rodzinie oraz przyjaciołom za wsparcie oraz wyjątkową cierpliwość.

Dziękuję również serdecznie wszystkim koleżankom i kolegom z Katedry oraz Wydziału za okazaną mi pomoc.

Abstract

This thesis deals with powering sensors embedded in surgical equipment and containers that regularly undergo steam sterilisation. The aim of this thesis was to develop a method of power supply to the sensors that would allow their operation during the steam sterilisation process. This would enable collection of steam sterilisation procedure data that would be useful in an Internet of Medical Things environment. First chapters present the research aims, internet of medical things ecosystem and an analysis of hospital logistics and the processes that surgical instruments go through. The impact on electronics and electrochemical energy storage devices of the different sterilisation methods used in medical facilities was analysed. Steam sterilisation was selected for further analysis as it is the most popular sterilisation method. The possibility of using electrochemical energy sources in a steam sterilisation environment is analysed next. The analysis has shown that the use of electrochemical power sources is not feasible from the point of view of both safety (possible self-ignition) and usability (self degradation and capacity loss) and, in the author's opinion, the prospect of market adoption of high-temperature power sources in the near future should be treated with scepticism. Alternative methods of powering sensors, i.e. energy harvesting, are then examined. The potential application of energy harvesting methods to the hospital logistics processes discussed previously was analysed. It was decided to use thermal energy harvesting and thermogenerators as a power source for sensors, considering that each surgical instrument undergoes a sterilisation process, usually with steam at high temperature. The theoretical basis of the Peltier and Seebeck processes and the operation of the thermogenerator modules have been analysed. A literature review of the available technologies and a review of the solutions available on the market have also been carried out. It was decided that a thermogenerator based on bismuth telluride should be chosen. After reviewing the available technologies, the technical and business requirements of the industrial partner, Aesculap AG, were defined. A physical model of the power module was then developed. A module of this type consists of an aluminium housing to which a thermal generator is attached from the inside. A Heat Storage Unit (HSU) is attached to the other side of the thermogenerator. The inside of the module is insulated with aerogel; therefore, the heat flow from outside (during the sterilisation process) to the inside of the prototype will only pass through the thermogenerator, causing an electromotive force to develop. After the development of the physical model, the next step was the construction of a virtual model and then the identification of the parameters of the physical model. For the thermogenerator, an analogous process of building a virtual model was carried out. For this purpose, the Kubov model based on SPICE environment was used. On the basis of the manufacturer's technical documentation, corrected with laboratory measurements, the thermogenerator was also parameterised. Finally, the energy consumption of the planned electronic sensor module was studied. This was done to define the minimum requirements for the power supply module to be developed. The measurements and simulations needed to validate the virtual models were then carried out. Finally, to answer the question of whether the proposed technical solution was likely to provide sufficient power to the sensors, a simulation of the steam sterilisation process was carried out. These simulations showed that the prototype was capable of powering the planned sensors. In addition, there was a fairly large power reserve. Therefore, there was a decision to do an optimisation process for the miniaturisation of the whole prototype. This process showed that the size of the HSU was the key to the performance of power generation. On the other hand, it was possible to reduce the thickness of the thermal insulation. This allowed the size of the entire prototype to be significantly reduced to the size of 7.5 mm of HSU height and 5 mm of thermal insulation. Several international patent applications have also been filed as a result of the research and development work to which this thesis belongs.

Streszczenie

Niniejsza praca dotyczy tematyki zasilania czujników wbudowanych w urządzenia i kontenery chirurgiczne, które regularnie poddawane są procesowi sterylizacji parą wodną. Celem pracy było opracowanie metody zasilania czujników, która pozwalałaby na ich działanie podczas sterylizacji parą wodną. Pozwoliłoby to na zbieranie danych użytecznych w środowisku Internet of Medical Things. Pierwsze rozdziały przedstawiają cele badawcze, ekosystem internetu rzeczy medycznych oraz analizę logistyki szpitalnej i procesów, przez które przechodzą narzędzia chirurgiczne. Przeanalizowano wpływ różnych metod sterylizacji stosowanych w placówkach medycznych na elektronikę i elektrochemiczne urządzenia magazynujące energię. Do dalszej analizy wybrano sterylizację parową, ponieważ jest to najpopularniejsza metoda sterylizacji. Następnie przeanalizowano możliwość wykorzystania elektrochemicznych źródeł energii w środowisku sterylizacji parowej. Przeprowadzona analiza wykazała, że zastosowanie elektrochemicznych źródeł zasilania jest niemożliwe biorąc pod uwagę wymagania dotyczące bezpieczeństwa (możliwa reakcja samozapłonu) jak i użyteczności (szybka degradacja i utrata pojemności), dodatkowo, zdaniem autora, w najbliższej przyszłości należy sceptycznie podchodzić do perspektywy wprowadzenia na rynek wysokotemperaturowych źródeł energii. W kolejnym rozdziale przeanalizowano alternatywne metody zasilania sensorów – tj. "energy harvesting odzyskiwanie energii. Przeanalizowano wcześniej poruszone procesy logistyki szpitalnej pod kątem możliwego zastosowania tych metod. Biorąc pod uwagę fakt, że każde narzędzie chirurgiczne przechodzi proces sterylizacji – najczęściej parą wodną w wysokiej temperaturze – zdecydowano się na wykorzystanie thermal energy harvesting i termogeneratorów jako źródła zasilania dla sensorów. Następnie przeanalizowano teoretyczne podstawy zjawisk Peltiera i Seebecka a także działanie modułów termogeneratorów. Dokonano także przeglądu literaturowego dostępnych technologii budowy ww. modułów oraz przeglądu rozwiązań dostępnych na rynku. Zdecydowano się na wybór termogeneratora opartego na tellurydzie bizmutu. W kolejnym kroku zdefiniowano wymagania techniczne oraz biznesowe pochodzące z firmy Aesculap AG. Opracowano prototyp modułu zasilającego. Moduł taki składa się z aluminiowej obudowy do której przymocowany jest od wewnątrz termogenerator. Do drugiej okładki termogeneratora przymocowana jest masa termiczna (*Heat Storage Unit - HSU*). Jest ona zaizolowana aerożelem, stąd przepływ ciepła z zewnątrz (podczas procesu sterylizacji) do wewnątrz modułu jest możliwy jedynie przez termogenerator powodując wytworzenie się na nim gradientu temperatur. Po opracowaniu modelu fizycznego zbudowano model wirtualny, a następnie dokonano identyfikacji parametrów modelu fizycznego. Analogiczny proces tworzenia wirtualnego modelu dokonano dla termogeneratora. Wykorzystano do tego model Kubova opracowany w środowisku SPICE. Dokonano także parametryzacji modelu termogeneratora na podstawie dokumentacji technicznej producenta. Wreszcie, przebadano projektowany moduł czujnika elektronicznego pod kątem zużycia przez niego energii celem zdefiniowania minimalnych wymagań dla opracowywanego modułu zasilającego. Kolejnym krokiem było przeprowadzenie niezbędnych pomiarów oraz symulacji celem walidacji modeli wirtualnych, oraz przeprowadzono symulację procesu sterylizacji parą wodną aby odpowiedzieć na pytanie czy zaproponowane rozwiązanie techniczne ma szansę zapewnić moc wystarczającą do działania czujników. Symulacje te dowiodły że prototyp jest w stanie zasilić planowane do użycia czujniki, a dodatkowo występuje dość duża rezerwa mocy. W związku z tym zdecydowano się na przeprowadzenie procesu optymalizacyjnego pod kątem miniaturyzacji całego modelu fizycznego. Proces ten wykazał, że kluczowa dla wydajności generowania energii jest przede wszystkim wielkość HSU, natomiast jeśli chodzi o izolację termiczną to jest możliwe zmniejszenie jej grubości. W rezultacie rozmiar całego modelu mógł być znacząco zmniejszony do 7.5 mm wysokości HSU oraz 5 mm grubości izolacji termicznej. W ramach pracy zgłoszono także szereg wniosków patentowych międzynarodowych.

Contents

1. Research Aims 12
2. Broad View - Place for the PhD Thesis in the IoMT Ecosystem 14
3. Introduction 16
3.1. Aim and Scope 17
3.2. Structure of the Dissertation 17
3.3. Visual Map of the PhD Thesis Research 19
4. Work Environment 20
4.1. Surgical Instrument Lifecycle 20
4.2. Sterilisation 22
4.2.1. Moist Heat Sterilisation 22
4.2.2. Dry Heat Sterilisation 25
4.2.3. Ethylene Oxide Sterilisation 25
4.2.4. Chlorine Dioxide 25
4.2.5. Vaporised Hydrogen Peroxide 26
4.2.6. Hydrogen Peroxide Gas Plasma 26
4.2.7. Gamma Ray 26
4.2.8. Electron Beam 27
4.3. Implications for Electronics and Energy Harvesting 27
5. Energy Storage Systems - State of the Art 29
5.1. High Temperature Batteries 32
5.1.1. High Temperature Primary Batteries 33
5.1.2. High Temperature Secondary Batteries 35
5.2. Electrochemical Capacitors 38
5.2.1. High Temperature Supercapacitors 39
5.2.2. Lithium-Ion Capacitors 40
5.3. High Temperature Energy Storage Systems Summary 40
6. Energy Harvesting in Surgical Tool Workflow 42
6.1. Hospital Context for Energy Harvesting 42
6.2. Thermal Energy Harvesting 44
6.2.1. Thermoelectric Generator - What Do We Talk About 44
6.2.2. Thermoelectric Effect and Heat Transfer 45
6.2.3. TEG Model in Steady State 49

6.2.4. Commercial Available Thermoelectric Generators ... 57
6.3. Thermal Energy Harvesting - Applications ... 58
6.4. Energy Harvesting Summary ... 59
7. Initial Requirements ... 60
7.1. Business Requirements ... 60
7.2. Hardware Requirements ... 62
8. System Prototype ... 64
8.1. Prototype Concept ... 64
8.2. Research Concept ... 66
8.3. Sensor Electronics Concept and Power Requirements ... 67
8.3.1. Power Benchmark ... 71
8.3.2. ADC SD14 Power Consumption Measurements ... 76
8.3.3. Power Consumption Measurements of Exemplary Low Power Sensing Program ... 77
8.4. TEG Selection ... 78
8.5. Thermal Insulation Material ... 81
8.6. Prototype Enclosure Selection ... 82
8.7. Prototype Assembly ... 83
9. Physical Model and TEG Characterisation ... 85
9.1. Prototype Characterisation ... 85
9.1.1. Temperature Measurement System ... 86
9.1.2. Thermal Measurements Procedure ... 93
9.1.3. Thermal Measurements Results ... 94
9.2. TEG Validation Measurement System ... 95
9.2.1. TEG Characterisation Results ... 97
10. Simulations ... 101
10.1. CAD Modelling ... 102
10.2. Thermal Simulation Setup ... 102
10.2.1. Material Parameters ... 103
10.2.2. Meshing ... 104
10.2.3. Boundary Conditions ... 108
10.2.4. Numeric Setup ... 109
10.2.5. Simulation Run Setup ... 110
10.3. TEG Modelling ... 111
10.3.1. TEG Model Selection ... 111
11. Results and Validation ... 117
11.1. Virtual Model Validation Results ... 117
11.2. TEG Model Validation ... 120
11.3. Steam Sterilisation Boundary Conditions ... 124
11.4. Sterilisation Simulation Results ... 125
11.4.1. Effect of insulation thickness on temperature gradient ... 125

11.4.2. Effect of HSU size on temperature gradient 131
12. Simulated Power Generation during Steam Sterilisation 135
12.1. Methodology and Simulation Setup 135
12.2. Results 136
12.2.1. Scenario 1 - Using ESS 137
12.2.2. Scenario 2 - No ESS 146
13. Summary 164
13.1. Research Questions Answers 164
13.2. Thesis Summary 165
13.2.1. Original Input 168
13.2.2. Further Research 168
13.3. Published Patent Applications 169
13.4. Published Articles Related to the Thesis 169
Appendices 170

Nomenclature

Abbreviations and Definitions

AC	Active carbon material
ANSI	American National Standards Institute
BLE	Bluetooth Low Energy
CAD	Computer aided design
CAE	Computer aided engineering
CFD	Computational fluid dynamics
DCL	Direct current leakage
DNA	Deoxyribonucleic acid
DUT	Device under test - a device which is undergoing testing procedure
EC	Electrochemical Capacitor
EDLC	Electrolytic double-layer capacitors
EDLC	Electrostatic double-layer capacitors
EESS	Electrochemical Energy Storage Systems
EH	Energy harvesting
EMF	Electromotive force
EPA	United States Environmental Protection Agency
ESD	Electrostatic discharge
ESR	Equivalent Series Resistance, internal resistance
ESS	Energy Storage System
ETO	Ethylene Oxide
FDA	Food and Drug Administration
FEA	Finite element analysis
HSU	Heat Storage Unit - A unit for storing heat from outside the module during steam sterilisation

IC Industrial constraint

IC Integrated circuit - an assembly of electronic components, fabricated as a single unit

IEC International Electrotechnical Commission

IIOT Industrial Internet of Things

IoMT Internet of Medical Things

LTC Lithium-Thionyl-Chloride cells

MAPE Mean absolute percentage error

MCU Microcontroller unit

MUMPS Multifrontal Massively parallel sparse direct solver

NFC Near Field Communication - set of communication protocols that enables communication between two electronic devices over a distance of up to 4 cm

NRMSE Normalised root mean square error

OCV Open-circuit voltage

OEM Original equipment manufacturer

PID Proportional-integral-derivative regulator

PTFE Polytetrafluoroethylene

RF Radio-frequency

RFID Radio-frequency identification - technology that uses electromagnetic fields to automatically identify and track tags attached to objects

RNA Ribonucleic acid

SEI Solid-electrolyte interface

SPICE Simulation Program with Integrated Circuit Emphasis - a general-purpose, open-source analog electronic circuit simulator

TE Thermoelectric element

TEC Thermoelectric cooler

TR Thermal Runaway

VHP Vaporised Hydrogen Peroxide

Zigbee Zigbee is an IEEE 802.15.4-based specification for a set of high-level communication protocols that are used to build personal area networks using tiny low-power digital radios.

Constants

A_{RTD}	A coefficient from european norm *EN 60751*	$3.9083 \times 10^{-3}\ °C^{-1}$
B_{RTD}	B coefficient from european norm *EN 60751*	$-5.775 \times 10^{-7}\ °C^{-1}$

Symbols

α_n	Seebeck coefficient of n-type material	$V \cdot K^{-1}$
α_{pn}	Relative Seebeck coefficient between p-type material and n-type material	$V \cdot K^{-1}$
α_p	Seebeck coefficient of p-type material	$V \cdot K^{-1}$
χ	Power generation safety margin	
$\dot{Q}_C$	Conduction heat	W
$\dot{Q}_J$	Joule heating	W
$\dot{Q}_P$	Peltier heat absorbed or generated (depending on the flow of the current I).	W
$\dot{Q}_{TEGc}$	Heat dissipated on the cold side of the TEG	W
$\dot{Q}_{TEGh}$	Heat absorbed on the hot side of the TEG	W
$\dot{Q}_T$	Thomson heat	W
$\dot{W}_{TEG}$	Power output of the thermoelectric module (TEG)	W
$\frac{\Delta T}{\Delta x}$	Temperature gradient, where where x is the distance along the heat flow path	$K \cdot m^{-1}$
π_n	Absolute Peltier coefficient of n-type material	$J \cdot C^{-1}$
π_p	Absolute Peltier coefficient of p-type material	$J \cdot C^{-1}$
π_{pn}	Relative Peltier coefficient between p-type and n-type material equals to the difference between Peltier coefficient of p-type material π_p and Peltier coefficient of n-type material π_n	$J \cdot C^{-1}$
ρ	Electrical resistivity	$\Omega \cdot m$
ρ_n	Electrical resistivity of n-type pellet	$\Omega \cdot m$
ρ_p	Electrical resistivity of p-type pellet	$\Omega \cdot m$
ρ_{pn}	Electrical resistivity of TE pair, $\rho_{pn} = \rho_p + \rho_n$	$\Omega \cdot m$
τ	Thomson coefficient of a material	$V \cdot K^{-1}$
τ_{pn}	Thomson coefficient of the TE pair equals $\tau_p - \tau_n$, where τ_p is a Thomson coefficient of p-type pellet, and τ_n is a Thomson coefficient of n-type pellet of TE pair	$V \cdot K^{-1}$
Θ	Thermal resistance	$K \cdot W^{-1}$
Θ_{np}	Thermal resistance of the couple of pellets	$K \cdot W^{-1}$
Θ_{TEG}	Thermal resistance of the thermogenerator	$K \cdot W^{-1}$
ξ	Compensation factor for boost converter efficiency	
A	Heat transfer area	m^2
A_n	Heat transfer area of the n-type pellet in TE pair	m^2

A_p	Heat transfer area of the p-type pellet in TE pair	m^2
A_{pn}	Heat transfer area of the TE pair equals to sum of cross-sectional area of p-type pellet and n-type pellet ($A = A_p + A_n$)	m^2
C_p	Specific heat	$J \cdot kg^{-1} \cdot K^{-1}$
C_{th}	thermal conductance - the ability of a material to conduct heat, it is the reciprocal of thermal resistance	$W \cdot K^{-1}$
d	Density of the material	$kg \cdot m^{-3}$
E_{Tc}	Absolute error of thermocouple readout	°C
I	Electric current	A
I_{ADC}	Current consumed by the analog-digital converter (ADC) during the readout procedure.	A
I_{MCU}	Current consumed by the microcontroller unit (MCU)	A
k	thermal conductivity	$W \cdot m^{-1} \cdot K^{-1}$
k_n	Thermal conductivity of n-type material	$W \cdot m^{-1} \cdot K^{-1}$
k_p	Thermal conductivity of p-type material	$W \cdot m^{-1} \cdot K^{-1}$
k_{pn}	The thermal conductivity of the TE pair	$W \cdot m^{-1} \cdot K^{-1}$
L	Height of the TE pair	m
m	Measured value of voltage, current and power	
N	Number of TE pairs (pellets)	
P_{ADC}	Power consumed by ADC	W
$P_{MCU_{LPM0}}$	Power consumed by MCU working in active mode	W
$P_{MCU_{LPM3}}$	Power consumed by MCU working in passive mode	W
r	Measurement range of voltage, current and power	
R_m	Electrical resistance of the specific material	Ω
R_{pn}	Electrical resistance of a single TE pair	Ω
R_{TEG}	Internal resistance of the TEG module equals $R_{TEG} = N \cdot R_{pn}$	Ω
s	Simulated value of voltage, current and power	
T	Temperature in Kelvin	K
T_{cold}	Temperature on the cold side of the thermoelectric generator or thermoelectric pair.	K
T_{hot}	Temperature on the hot side of the thermoelectric generator or thermoelectric pair.	K
T_{Pt100}	Temperature value registered using Pt100 RTD	°C
T_{Tc}	Temperature value registered using thermocouple	°C

V_S	Voltage induced due to the Seebeck effect	V
V_{TEG}	Voltage across the Thermoelectric Generator	V
ZT	Dimensionless form of thermoelectric figure of merit (*see* Z)	
Z	Thermoelectric figure of merit characterising the performance of a material or device	K^{-1}

1. Research Aims

Abstract

This chapter defines the main topic of the Ph.D. thesis and formulates the research questions related to the Ph.D. thesis topic. Second, it also defines the basic design constraints coming from industrial partner B.Braun Aesculap AG, Tuttlingen, Germany.

Outcomes of this chapter: Defined research questions which will be addressed in this Ph.D. thesis, as well as industrial constraints limiting the flexibility of the design.

This Ph.D. thesis is related to the concept of Hospital 4.0 - an idea in which the hospital infrastructure interacts with smart medical devices and tools that allow better maintenance and asset management. The thesis explores in particular the topic of powering the low-power sensor nodes for surgical devices with special attention paid to the process of steam sterilisation. Steam sterilisation is the most popular method of sterilising surgical goods in European hospitals. It is also very harmful to energy storage devices and portable electronics as a result of the high temperature and pressure inside the sterilisation chamber. It makes it impossible to use regular rechargeable battery-driven devices for surgical instruments undergoing steam sterilisation. Using primary batteries is also not an easy task (need for constant maintenance); moreover, high-temperature primary cells have a relatively high cost, which limits the applicability of such solutions in hospital environment.

Due to these reasons, this Ph.D. thesis focused on the following research question:

Is it possible to provide a reliable power source for sensors in smart surgical tools during steam sterilisation?

This research question was divided into the following subquestions that have been formulated in the process of developing possible solutions.

1. **RQ1** What are the possibilities of powering low-power electronics in the steam sterilisation chamber using energy storage devices?
2. **RQ2** Is it possible to design a maintenance-free power solution for sterilisable medical tools using energy harvesting solutions, what are the design constraints?
3. **RQ3** What is the energy balance of the proposed design, what are the main constraints and possibilities for size optimisation?
4. **RQ4** What are the limitations in terms of sensor design related to power consumption?

In addition to the research questions listed above, this PhD thesis had to deal with the requirements from industrial partner Aesculap AG. The main industrial constraints (IC) were:

1. **IC1** Applicability in mass production,
2. **IC2** Robustness of the design,
3. **IC3** Maintenance-free nature of the target solution,
4. **IC4** Compatibility with the concept of the Internet of Medical Things (IoMT) system,

During the whole PhD thesis research process, these requirements were strict and were not disputable.

2. Broad View - Place for the PhD Thesis in the IoMT Ecosystem

Abstract

This chapter presents the idea of the Internet of Medical Things. This concept involves a network of connected medical devices and instruments which are stored and utilised in hospitals and other medical facilities. The chapter explains an idea of an IoMT system concept from the industrial partner Aesculap AG, shortly describes its data layers as well as presents an overview of the system in relation to hospital infrastructure.

Outcomes of this chapter: Presentation of Internet of Medical Things concept and defining the area where in the IoMT ecosystem this PhD thesis is placed.

The topic of this Ph.D. Thesis, a power system for low-power sterilisable sensor electronics, was developed and researched in the context of the Medical Internet of Things. IoMT systems usually have several layers and integrate hospital infrastructure, cloud systems, and data collection nodes (sensor nodes). According to industrial constraints **IC4** the power system developed in this thesis was part of a broader concept presented in figure 2.1. This fact affected the initial industrial requirements for the prototype. As shown in Figure 2.1 the whole system can be described from three main perspectives: information flow perspective, power perspective, and usability perspective. From the information flow perspective, the system consists of three layers. The first layer is the data collection layer and it is made up of distributed small autonomous sensor nodes. The second layer - the gateway layer - is designed as a set of data readout points or data readout devices (e.g. smartphone) which read the acquired data from the sensor nodes, validate it, and forward it to the third layer, the cloud analysis system. From the power supply perspective, we have two different areas involved in the system. The first is the area where autonomous sensor nodes perform their tasks. Here, the nodes need to be self-sufficient and maintenance-free in terms of power supply. The second area is the area of readout gateways and cloud systems, where power supply can be provided from external sources. The third perspective is a user experience perspective. Due to the extreme work environment according to time management, the sensor nodes must be maintenance-free and autonomous. Data collection gateways have been designed as semi-automatic (smartphone) or automatic. Finally, the cloud data analysis layer can be automatic or manual depending on the business case. Taking into account all these perspectives, the initial requirements for the sensor node and for the sensor node power supply module have been defined.

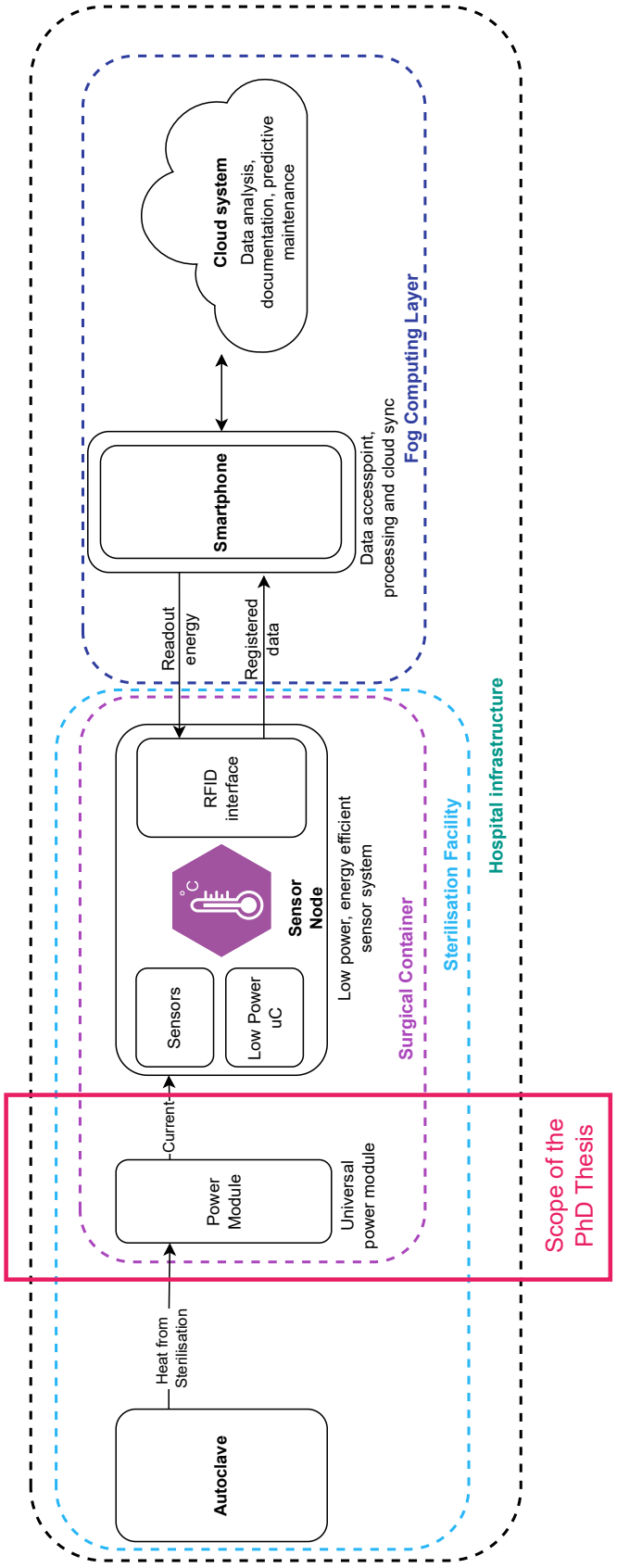

Figure 2.1. Broad view of the whole concept of the Internet of Medical Things and placement of the topic of this PhD thesis. During steam sterilisation in the autoclave, high temperatures and pressures are generated, which affect the power module and sensor electronics inside the surgical container. The power module must withstand the steam sterilisation environment and provide enough power for the sensor electronics. The sensor module registers the temperature and stores data in memory. After steam sterilisation, data can be read using a smartphone or any other access point with a radio communication interface and sent to cloud data storage.

3. Introduction

Abstract

This chapter briefly introduces the issue addressed in this dissertation: the power supply of electronic sensors embedded in medical containers, part of the IoMT system, which can be sterilised by steam. This requirement is driven by the technological cycle of surgical instruments in the hospital and is a factor that prevents the use of electrochemical energy storage systems. The plan for the entire dissertation is then presented, and each chapter of the dissertation is briefly described. Finally, a visual representation of the dissertation is presented along with a diagram of the research methodology.

Outcomes of this chapter: The outcome of this chapter is an outline of the topic of the dissertation and motivation for the dissertation, a description of the different chapters of the dissertation, and a visual representation of the research methodology presented in this dissertation.

Digital healthcare is a very fast-growing area of the medical industry with a huge potential to deliver secure and high-quality patient care and drive greater business efficiency. Many reports suggest that digitalisation is becoming a new business opportunity for the healthcare industry involving the Internet of Medical Things, Big Data and automatization. This could allow the connection between patients, healthcare professionals, manufacturers and providers [1]–[3]. There are strong indications that bringing the idea of traceable and connected devices to the operating room can significantly improve the efficiency and safety of surgical procedures [4], [5]. Moreover, some papers highlight the direction towards digitalisation in hospital management systems to create "Smart Connected Hospitals" with sensor nodes and tracking systems. To make this possible many different technologies are suggested for IoMT, such as radio frequency identification (RFID), ZigBee , Narrow-band Bluetooth and Bluetooth Low-Energy (BLE) [6]. Medical and surgical tools incomparably differ from other IoT-enabled devices for consumer markets due to the need for sterilisation. However, each of these devices and technologies requires a power source. In the case of surgical tools and containers, the power source must stand for sterilisation procedures. However, the steam sterilisation process is very harmful to conventional electrochemical energy storage systems (EESS) . In this dissertation, multiple possible EESS has been analysed, like primary and secondary cells, supercapacitors, and hybrid capacitors. In the case of primary cells, there are solutions on the market that will endure the conditions of steam sterilisation, however, they are economically inefficient and require constant maintenance. In contrast, secondary (rechargeable) cells are in most cases not suitable for steam sterilisation conditions at all. In the case of supercapacitors and hybrid capacitors, there are some solutions on the market which are suitable for steam sterilisation; however, their price and need for maintenance make it difficult to consider them as a desired solution for low-power sensor electronics. Thus, the aim of this PhD dissertation is to find a solution to the problem of maintenance-free powering of sensor electronics inside surgical sterilisable container.

3.1. Aim and Scope

The subject of this dissertation concerns the power supply of electronic sensors intended for medical devices that undergo the steam sterilisation process. The aim of the thesis was to find a solution that allows the unattended operation of sensors for the purposes of the medical Internet of Things inside an autoclave, i.e. in conditions extremely unfavourable for electrochemical energy storage systems.

3.2. Structure of the Dissertation

This PhD thesis consists of 13 chapters, the first of which presented the thesis and related scientific issues, the second focused on describing the context in which the thesis is set, and the third presented the structure of the thesis. The following chapters are listed and described below.

Chapter 4 focusses on the conditions that determine the technical requirements for surgical instrument supply systems. It presents the working environment of surgical instruments, their life cycle inside the hospital, and discusses the types of sterilisation to which devices and surgical instruments may be subjected.

Chapter 5 is devoted to an analysis of the available scientific and technical developments in the field of electrochemical energy storage. The available technologies of primary cells, secondary lithium-ion based cells, supercapacitors, and hybrid capacitors are systematically analysed for their use in high-temperature environments such as the steam sterilisation process. An economic analysis of each solution and a safety analysis of each technology were performed. As a result of the analysis, the lack of the ability to use these technologies to realise the topic of this thesis was identified. An analysis of the potential development of these technologies in the near future was also done.

In **chapter 6**, in the absence of traditional power technology capable of operating under steam sterilisation conditions, the focus is on alternative technologies as energy harvesting. Different types of energy harvesting were analysed and their application in the context of surgical instrument logistics was examined. Thermal energy harvesting technology based on Peltier-Seebeck modules was selected as particularly useful. The theoretical basis for the operation of such modules was then analysed and the technologies and solutions available on the market were reviewed to prepare recommendations for future steps in the design of the power supply system.

Chapter 7 outlines the requirements for the prototype being developed by the industrial partner Aesculap AG. The chapter describes the essential business and technical requirements that are critical factors in creating a new technical solution.

Chapter 8 presents the concept of both the system and the planned research design. This included the selection of an electronic sensor, which would be a sort of sample application to be fed into the system that is being developed in the thesis. The procedure for selecting the thermoelectric generator, the insulation materials, and the overall conceptual design of the prototype was also described.

Chapter 9 describes the characterisation of the physical model. The characterisation procedure is defined, and the selection of appropriate sensors used for the characterisation registration is proposed. This selection was made based on previously defined requirements. The selected sensor, a K-type thermocouple, was then

validated for accuracy using a reference resistance temperature detector and the entire procedure and the test bench are described. The expected measurement error of the measuring system was then calculated. The procedure for characterising the thermal response of the prototype using a thermal chamber and previously selected sensors is also presented. The second part of the chapter presents the characterisation procedure for the thermogenerator selected in Chapter 8. The measurement bench, the procedure, and software specially built for this purpose in the LabView environment are described. The chapter also presents the results of the collected measurements, which will be used to validate the simulation models of both the prototype and the selected thermogenerator.

Chapter 10 Chapter 10 describes the creation of simulation models of both the prototype and the thermogenerator. The creation of the prototype simulation model started with creating a 3D model of the prototype and its adaptation to the needs of the FEM simulation software. Next, the selection of the necessary physical parameters to be carried out and the selection of the values of these parameters for each material are described. In the next step, the preparation of the FEM simulation is described. First, the construction of a suitable mesh was analysed, the procedure of creating the mesh and its evaluation and refinements were described, and finally, the mesh results obtained and its parameters were presented graphically. These parameters were within the recommended limits, guaranteeing the correctness of the numerical simulations. In the next step, the selected boundary conditions are described. These conditions were the surface temperature of surgical instruments previously measured in an autoclave. These conditions were applied to the surface of the virtual prototype. The next step describes the numerical settings of the simulation and the possible impact on the results of each parameter. Finally, the settings of the simulation run and the parameters that can affect the accuracy of the simulation are described.

The second part of this chapter describes the modelling of a thermogenerator using the SPICE environment. First, a literature review of the available thermogenerator modelling technologies was made. Then criteria were formulated to select a specific model that allowed its practical use in the R&D departments in the industry. Then, the Kubov model was selected, described, and implemented in the LTSpice environment. Then, its parameters were selected based on the technical documentation of the thermogenerator, the theoretical basis described in Chapter 6 and the measurements of the thermogenerator characteristics described in Chapter 9. Finally, the results of the thermogenerator simulation are presented in the table and graph.

Chapter 11 compares the results obtained experimentally with the results of numerical simulations. The simulation results coincided with the experimental results from the experiments described in Chapter 9. This allowed to conclude that it is possible to use simulation models to simulate the entire steam sterilisation cycle and to validate the efficiency of extracting electricity from the proposed prototype. Next, on the basis of these results, several optimisations have been made to answer the question of how much the prototype can be miniaturised, with the assumed energy consumption by sensors and electronics. The results of these optimisations are presented at the end of the chapter and commented on accordingly.

Chapter 12 describes the simulation of the sterilisation process and the optimisation of the size of the prototype. In this chapter, a series of simulations of the steam sterilisation process was carried out for different sizes of the model. Based on the thermal simulations, electrical simulations were carried out to estimate the amount of power generated by each variant of the model. This chapter aimed to estimate the smallest possible size of the model that would generate sufficient power to supply the sensor module with the specified minimum power consumption.

Chapter 13 summarises all the work carried out in this dissertation. It discuss the problems identified during the development work, the methods used to overcome these problems, and the results of the research and development work. The chapter also describes the results of the work carried out in the form of international patent applications and discusses potential next steps and scientific challenges related to powering IoT devices in a steam sterilisation environment.

3.3. Visual Map of the PhD Thesis Research

In order to better illustrate the contents of this dissertation, a visual content map has been created, as shown in Figure 3.1.

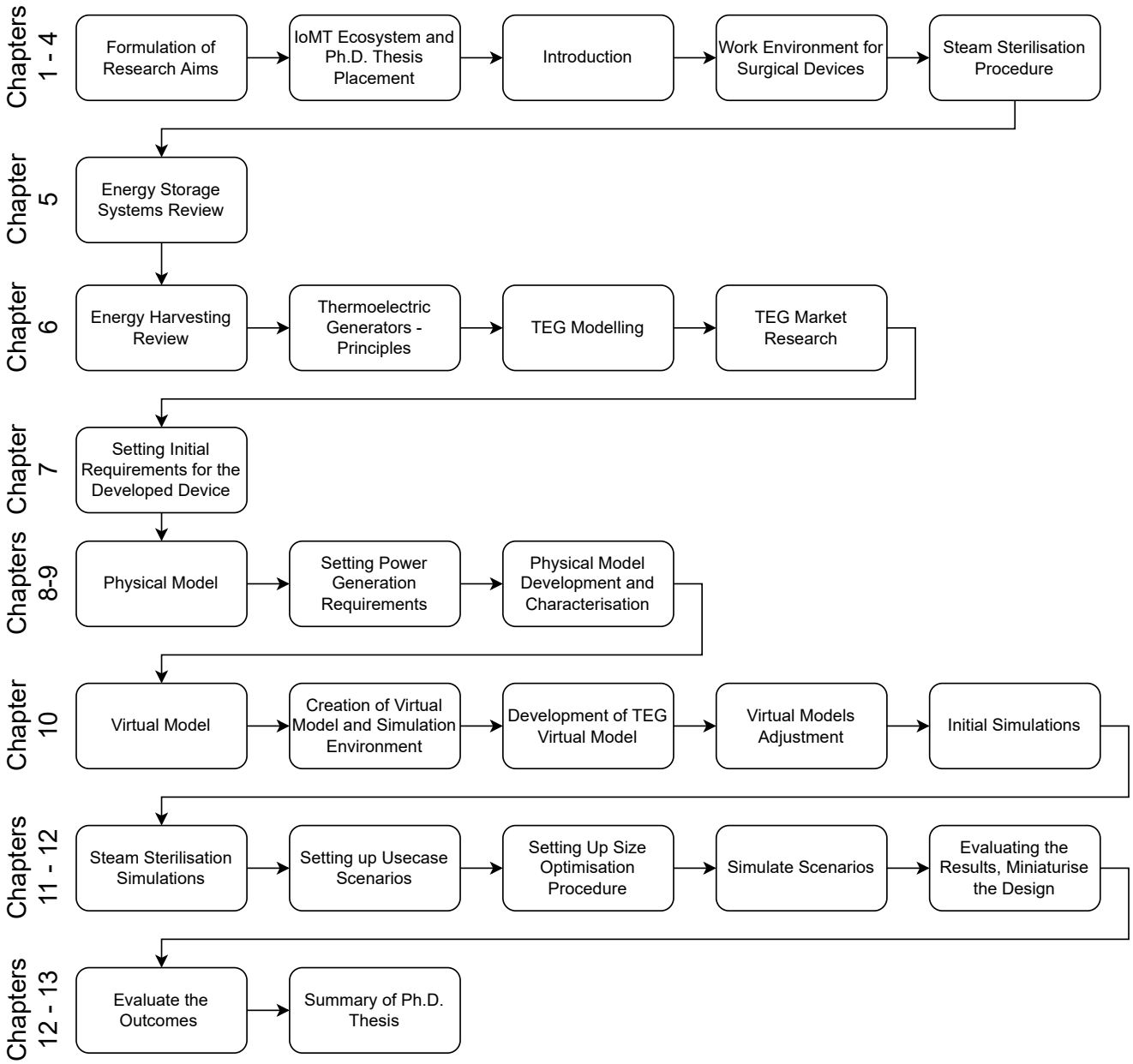

Figure 3.1. Ph.D. Thesis content map visualisation.

4. Work Environment

Abstract

This chapter describes the work environment of sterile medical devices. It describes a surgical instrument life cycle starting from the stock management phase, through delivery to use in the operating room, washing, quality control, packing, and sterilisation for the next use. The most critical part of the cycle is sterilisation. This can be done using several different methods, which are described in this chapter. The most popular is steam sterilisation because of its simplicity and low cost. This method involves heating the sterilisation chamber to 134 °C for at least 4 min. Finally this chapter discusses the influence of each method on electronic devices and lists the related design challenges.

Outcomes of this chapter: Presentation of surgical device lifecycle, presentation of surgical goods sterilisation methods, discussion on their influence on surgical electronic devices and their design.

One of the key requirements for surgical electronic devices is to ensure their reliability in daily use in the environment of a healthcare facility. Every single surgical instrument has its life cycle: from the storage room to the operating theatre, and to the central cleaning and sterilisation area. This is to assure the safety and efficiency of the delivery of sterile goods in the environment of a healthcare facility. It is necessary to take a deeper look at this cycle, as it determines the very specific requirements for surgical devices and their power sources.

4.1. Surgical Instrument Lifecycle

In the hospital environment, surgical electronic devices are usually part of larger surgical instrument sets. Proper handling and decontamination of these sets is an essential requirement for patient safety, as they can provide a potential route for the transmission of pathogens and bacteria into the body of a patient [7], [8].

Every set needs to be managed appropriately, which is usually termed the lifecycle of surgical instruments as it is presented in Figure 4.1. It is an essential requirement if the hospital needs to deal with a large number of surgical procedures and needs to ensure the availability of instruments in each operating room. The cycle usually starts in a warehouse where the instruments are stored and can be picked up for the operation, and finishes when the instruments are stored again to be ready for another operation. Instruments are stored in surgical containers and transported with medical carts throughout the process, as shown in the Figure 4.2.

Usually, literature shows that the management of surgical instruments in a hospital is carried out in the following phases [10]–[12]:

1. **Stock Management** - The stock management phase is performed in storage areas. Different surgical containers containing the instruments are transported from the sterilisation facility on case carts and inserted into shelving. This must be carried out very carefully so as not to damage the surgical containers

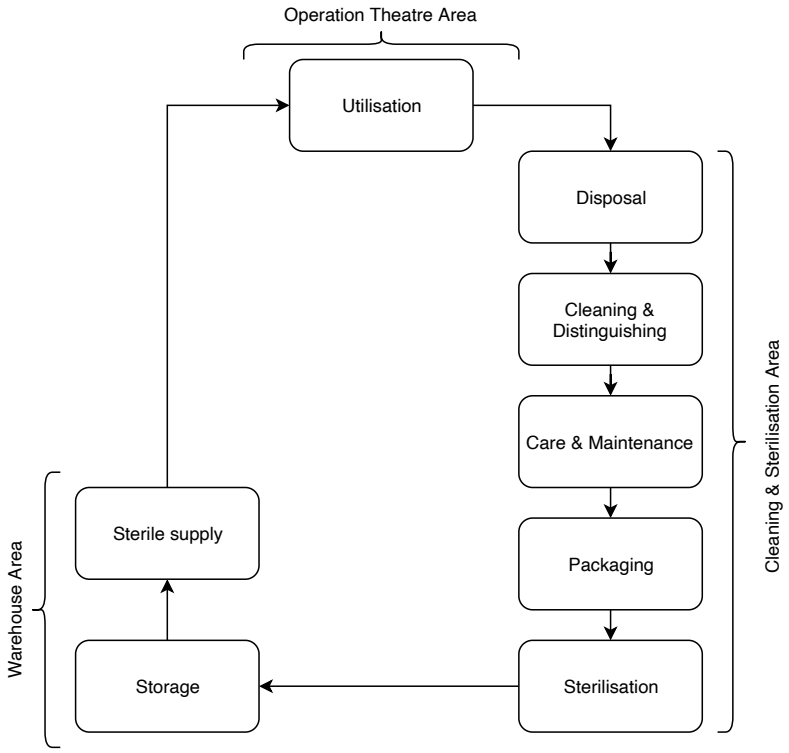

Figure 4.1. Instrument lifecycle process diagram.

and not to expose their contents to contamination. Each container is inventoried and placed in a suitable place where it remains until the request from the operating room. When this happens, the appropriate containers are collected and stacked on previously prepared case carts. These carts are available according to the daily schedule of the surgical procedures.

2. **Operation Room** - Upon arrival in the operating room where the patient is operated, the containers are opened and their contents are transferred to the surgical trays from which they are taken and used during the operation. When the operation is complete, all instruments are placed back in the containers and transported to the decontamination room. Reusable surgical instruments are then transported for cleaning, while disposable instruments are placed in special boxes to be disposed of.

3. **Washing** - Reusable instruments are washed after the operation. This process consists of prewashing (automated or manual, depending on the type of instrument and available resources) and washing in a washing machine. The instruments are first washed to ensure that all organic and inorganic residues are removed from their surface. The instruments are then subjected to an ultrasonic bath which removes dirt and surgical residues from microcracks and difficult-to-reach areas. The final step is washing in a washing machine to remove microorganisms and detergents remaining on the surface.

4. **Quality control and Packaging** - After washing the instruments, each of them is visually checked. To be packaged for sterilisation, it must be dry and clean. If any debris is noticed, it is sent for washing again. All clean instruments are then packed in containers for sterilisation.

5. **Sterilisation** - After packing, surgical instruments are ready for sterilisation. Sterilisation is defined as the technological process of destroying all the forms of microbial life. The sterilisation process usually takes between 10 and 60 minutes, depending on the technology used. The issue of sterilisation of surgical

Figure 4.2. Example of surgical instruments tray being inserted into surgical container on the transporting cart in the central sterilisation facility [9].

instruments will be discussed later in this chapter. Once sterilisation is complete, the containers with the instruments are placed in a case cart and transported to the storage rooms.

When designing electronic surgical devices, each of the described processes must be considered. Conditions during sterilisation can be particularly severe for electronic devices, so the types of sterilisation will be discussed in detail later in this chapter.

4.2. Sterilisation

Use of inadequately sterilised surgical devices and instruments involves a high risk of transmitting pathogens. However, documented transmission of pathogens associated with an inadequately sterilised critical item is exceedingly rare. This is probably due to the sterilisation processes used in healthcare facilities. Sterilisation plays a key role in the decontamination of surgical devices. It destroys all microorganisms on the surface of an article or in a fluid to prevent the transmission of disease associated with the use of that article [13]. Medical devices that have contact with sterile body tissues or fluids are considered critical items. These items should be sterile when used because any microbial contamination could result in disease transmission. Such items include surgical instruments, biopsy forceps, and implanted medical devices. If these items are heat resistant, the recommended sterilisation process is steam sterilisation, because it has the largest safety margin due to its reliability, consistency, and lethality. Most medical instruments and devices used in healthcare facilities need to be made from materials that are heat stable. This requirement comes from the sterilisation. There are several different methods of sterilisation, described and evaluated in the literature [13]–[16] as it is shown in the figure 4.3.

4.2.1. Moist Heat Sterilisation

According to the European standards *EN ISO 17665-1:2006* and *EN 285:2015+A1:2021* steam sterilisation involves directly exposing sterilised products (e.g. surgical instruments, implants) to steam at the required

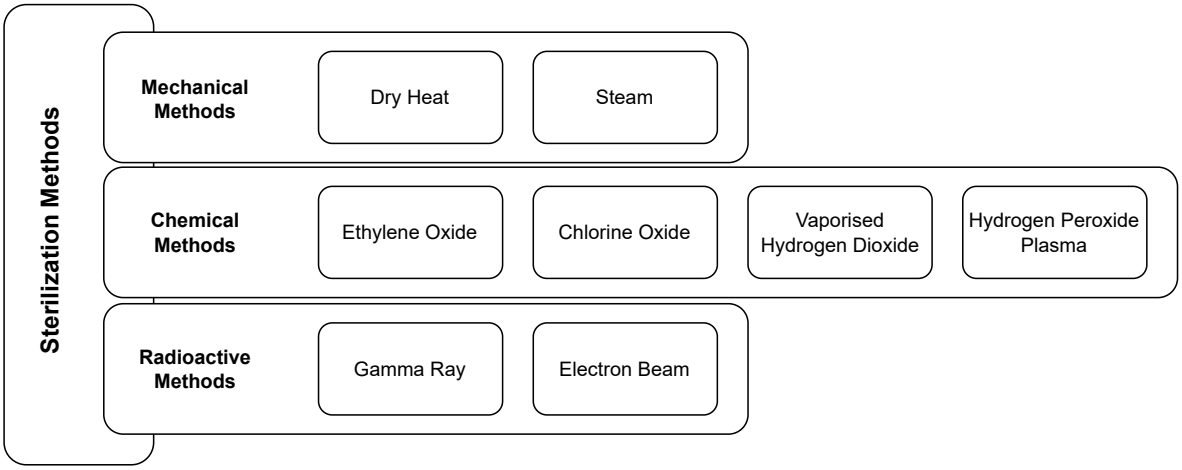

Figure 4.3. Different types of sterilisation used in healthcare facilities around the world.

temperature and pressure for a well-defined period of time. All three parameters (pressure, temperature, time) depend on the specific autoclave model, the specific sterilisation programme, and the type of product being sterilised. Two sterilisation temperatures are commonly used: 121 °C and 134 °C. The exposure time for a given temperature is 30 min minutes for 121 °C degrees and 4 min minutes for 134 degrees, respectively. There are two basic types of sterilisers (autoclaves) in use – a steriliser with a gravity vent system and a steriliser with a forced vent system.

In the **gravity vent system**, the sterilisation process consists of three phases. The first is the heating phase. In this phase, with the vent open, saturated steam is admitted into the steriliser chamber. After reaching a certain temperature level (usually a level defined by the device manufacturer), the vent opening is closed and the infused steam causes the pressure inside the chamber to increase until it reaches the appropriate level to ensure the sterilisation temperature specified in the standard. The second phase is the so-called plateau phase, a phase in which both pressure and temperature are maintained at a level that ensures effective sterilisation. The plateau phase can last from 4 to as long as 45 minutes, depending on the sterilisation temperature, the type and weight of products to be sterilised, and the size of the sterilisation chamber itself. The third phase is the cooling phase, where steam is discharged through the outlet valve and air is admitted into the sterilisation chamber, slowly cooling its interior. It is this slow heating and cooling that is a desirable feature in this type of sterilisation, which is used to sterilise solutions, among other things. A schematic of the steam sterilisation process using gravity venting is shown in Figure 4.4.

The second type of steam sterilisation is sterilisation using forced air removal systems and is presented in Figure 4.5. This type of sterilisation is used in cases where gravitational air removal may be difficult, for example, in porous materials or packaged items. The sterilisation process in this case consists of six phases. The first of these is the air removal phase. It involves the pulsed vacuum generation in the sterilisation chamber in alternation with a pulsed increase in pressure. It happens by mechanically pumping air out of the chamber and then introducing steam at a pressure above atmospheric pressure. The value of the pressure depends on the manufacturer and the specific model of the autoclave, but is usually within the limit of up to 3 bar. The next phase is the filling phase, in which saturated steam is introduced into the steriliser chamber until the pressure and temperature in the chamber reach the values assumed by the given sterilisation programme.

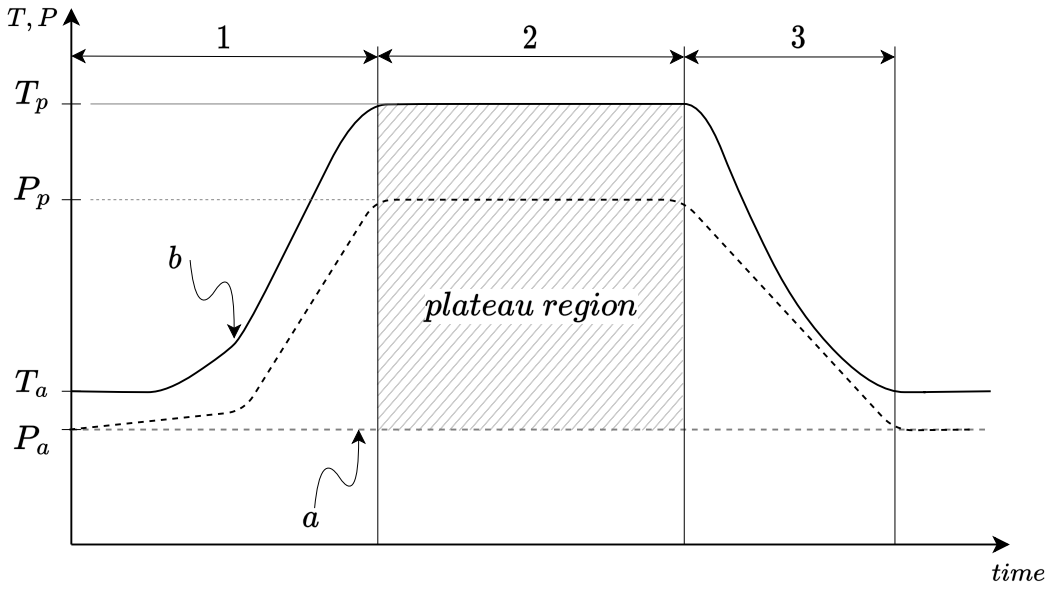

Figure 4.4. Gravity venting steam sterilisation procedure diagram. Temperature changes are presented with a solid line, while pressure changes are presented with a dotted one. The process consists of three phases: **1)** heating phase, **2)** plateau phase, **3)** drying phase. With letter **b** a moment of closing the ventilation valve is depicted, while letter **a** indicates the level of atmospheric pressure.

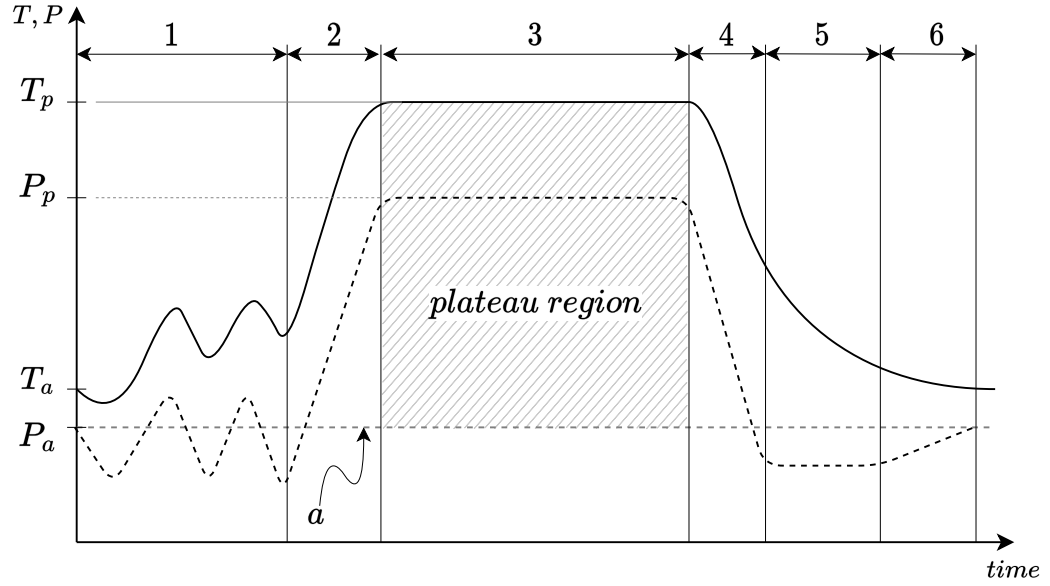

Figure 4.5. Forced venting steam sterilisation procedure diagram. Temperature changes are presented with a solid line, while pressure changes are presented with a dotted one. The process consists of six phases: **1)** air removal phase, **2)** filling phase, **3)** plateau phase, **4)** removal phase, **5)** drying phase, **6)** vacuum removal phase. Letter **a** indicates the level of atmospheric pressure.

The third phase is the plateau phase, which, exactly as in the case of the previously described gravity method, consists of maintaining the assumed level of temperature and pressure for a certain period of time. The fourth phase is the evacuation phase, in which steam is removed from the sterilisation chamber, causing

a vacuum. In the fifth phase, the drying phase, the predetermined drying temperature and the vacuum are maintained in the sterilisation chamber for a specified time. Finally, the last phase is the vacuum elimination phase, in which air is admitted into the sterilisation chamber and the pressure is levelled to atmospheric pressure.

4.2.2. Dry Heat Sterilisation

Dry Heat sterilisation is used in the case of materials and devices that cannot handle moist (i.e. powders or very sharp surgical instruments due to corrosion). Among several types of dry heat sterilisers described in the literature [17], two of them are widely used: static air and forced air. The first one has heating coils at the bottom of the sterilisation chamber, so the hot air is coming up, heating the whole space and instruments inside. The second type is equipped with a motor-driven blower that circulates air throughout the chamber. The advantage of this type is that the temperature distribution is more equal. There are two parameters used in this method: temperature and time. Depending on the mode, we can distinguish sterilisation in 170 °C for 60 minutes, 160 °C for 120 minutes and 150 °C for 150 minutes. The main advantages of this method are low installation and operating costs, use of nontoxic sterilisation agent (hot air), and that it is noncorrosive for the metals, but still the penetration grade is satisfying. However, it is also a time-consuming method, involving the exposure of surgical instruments to high temperatures. In case of embedded devices the high temperature is a main disadvantage, as it is in the range of most commercially available semiconductors and energy storage systems; thus, the good thermal insulation needs to be implemented into such devices.

4.2.3. Ethylene Oxide Sterilisation

Ethylene Oxide sterilisation is performed with heat or moisture sensitive devices and materials. This method is using Ethylene Oxide (ETO) - a colourless flammable and explosive gas. ETO shows microbicidal activity by alkylation (replacement of a hydrogen atom with an alkyl group) of protein, DNA and RNA . This prevents normal cellular metabolism and replication. The whole process of sterilisation involves five stages: preconditioning and humidification, gas introduction, exposure, evacuation, and air washes [13]. It takes approximately two and a half hours. The problem is that ETO is absorbed by many materials, and to provide safety for medical staff, the sterile equipment must undergo aeration. Aeration is performed to remove residual ETO, and it takes 6-12 hours. The main disadvantages of ETO sterilisation are the lengthy cycle time, potential hazards to patients and healthcare staff, the flammability of the gas, and its cost. Thus, ETO sterilisation is used in healthcare facilities only if the steam sterilisation is not possible and remains the second popular method in hospitals, however not in the entire medical industry [18].

4.2.4. Chlorine Dioxide

Chlorine Dioxide sterilisation is one of the chemical based methods which have been registered by United States Environmental Protection Agency (EPA) in 1988 as a sterilising agent. Chlorine dioxide (ClO_2) acts as an oxidising agent on amino acids [19]; however, the exact mechanism by which free chlorine destroys microorganisms still needs to be studied [13]. The whole sterilisation process consists of five stages: humidification preconditioning, conditioning, generation of ClO_2, exposure of the sterilised utensils, and finally aeration. This method is used mainly in laboratories as it is still not approved by the Food and Drug Administration (FDA) for use in healthcare facilities, however, it could still be considered a technical possibility. The procedure involves only low temperatures from 15 °C until 40 °C. Most importantly, chlorine dioxide

is nonflammable and not carcirogenic. All of these factors make it very convenient for embedded electronics and batteries.

4.2.5. Vaporised Hydrogen Peroxide

Vaporised Hydrogen Peroxide (VHP) sterilisation of medical equipment has been developed in the mid-1980s [20]. There are two main methods of VHP delivery to the sterilisation chamber. In the first method, a deep vacuum is used to pull liquid hydrogen peroxide (30 - 35 % concentration) from a disposable cartridge through a heated vaporiser and then, after vaporisation, into the sterilisation chamber. A second approach to VHP delivery is the flow-through approach, in which the VHP is carried into the sterilisation chamber by a carrier gas such as air using either a slight negative pressure (vacuum) or a slight positive pressure. VHP sterilisation has many advantages including rapid cycle time (e.g. 30 to 45 minutes), low temperature, environmentally safe by-products, good material compatibility, and ease of operation [21]. This method of sterilisation is safe for embedded electronics due to its low temperature (from 25 °C to 50 °C) however, the vacuum generated throughout the process may not be acceptable for embedded batteries and energy storage systems. The penetration capabilities of VHP are less than those of ETO [13].

4.2.6. Hydrogen Peroxide Gas Plasma

Invented and patented in 1987 the Hydrogen Peroxide Gas Plasma sterilisation is one of the newest methods with FDA approval [13]. In this method, the gas plasma is generated inside a closed chamber, in deep vacuum, by radio frequency and microwaves. The microwaves excite the gas molecules so that they become free radicals. Free radicals generated in the plasma field are capable of interacting with essential cell components (e.g., enzymes, nucleic acids) and thereby disrupting the metabolism of microorganisms [22]. The method consists of two cycles; first the hydrogen peroxide is difused into a chamber, and in the second stage the plasma is generated. The whole cycle takes from 1 to 3 hours with a temperature range of 37 °C to 44 °C which makes it compatible with more than 95% of the medical devices available on the market. Hydrogen peroxide plasma sterilisation is suited for objects that cannot sustain the high temperature and moisture necessary for steam (autoclave) sterilisation. The required vacuum is not as deep as with VHP sterilisation. Although the low process temperature of 40 °C to 65 °C is appealing, the 13.56 MHz RF energy in the range of 200 W to 400 W during the plasma discharge phase is problematic for embedded electronics. Hydrogen peroxide plasma sterilisation should not be used for objects containing semiconductors [23].

4.2.7. Gamma Ray

Use of gamma ray sterilisation method is increasing in recent years, and more and more temperature-sensitive devices are being sterilised using this method [24]. The objects to be sterilised are put on a conveyor that transports them to the area of strong gamma radiation. The conveyor stops exposing a particular object to a defined amount of gamma radiation. Then, the conveyor moves on and exposes the next object. The ionising radiation causes excitations, ionisations, and, where water is present, free radical formation. All three processes cause the disintegration of essential cell components, such as enzymes and DNA, resulting in cell death. According to the literature the dose of 25 kGy is perceived as a gold standard in gamma ray sterilisation method [25], this dose is also recommended by the ISO 11137-2:2013 norm. In addition to affecting living cells, gamma radiation also affects polymers and semiconductors. The effect on electronics depends on the dose and the dose rate. In the extreme, a total ionisation greater than 5000 rads in silicon delivered over seconds

to minutes degrades semiconductor materials for long periods. In practise, however, such high doses are not present in medical industrial sterilisation.

4.2.8. Electron Beam

In this sterilisation method, the accelerator generates an electron beam – a concentrated, highly charged electron stream. The objects which need to be sterilised are put on a conveyor, which transports them through a window where they are exposed for the electron beam. The conveyor speed is set so that the proper dose of radiation is applied to each object. Reaching the penetration needed for sterilisation requires energy levels of the magnitude of 5 to 10 MeV [26], [27]. In this sterilisation method the electron beam radiation forms free radicals that react with macromolecules, damaging cellular DNA which leads to cell death. It destroys all types of pathogens, including viruses, fungi, bacteria, parasites, spores, and moulds. This method is faster than gamma ray sterilisation, it does not produce nuclear waste, however electron beam radiation does not penetrate as deep as gamma radiation. When it comes to embedded electronics, this method can cause charge build-up (Electrostatic Discharge – ESD) which can cause damage; thus, objects containing semiconductors should not be sterilised with this method.

4.3. Implications for Electronics and Energy Harvesting

As was shown, the surgical instrument life cycle defines the requirements for electronic embedded devices. It also provides opportunities for energy harvesting on the other side. Steam autoclave sterilisation and ethylene oxide are two of the most popular methods of sterilisation among hospitals. From these two, steam sterilisation has the most harsh conditions for embedded devices. It's high temperature, humidity and presence of vacuum leverages the design requirements for the sterilisable electronics. However, it also makes possible the thermal energy harvesting, one of the most reliable methods for supplying the low power sensors and actuators. The second method with a great potential for thermal energy harvesting is dry heat sterilisation. However, this method is not as effective and efficient as wet heat (steam) sterilisation and therefore is not so spread around healthcare facilities [14]. Due to this, in the frame of this Ph.D. thesis, only the steam and dry heat sterilisations are being considered. The summary of the impact on electronics and possible energy harvesting from different sterilisation methods is shown in the Table 4.1.

Table 4.1. Summary of different sterilisation methods, their impact on embedded electronics and potential for energy harvesting, based on [23].

Method	Critical Parameters	Compatibility	Energy Harvesting
Steam	- High temperature, - Humidity, - Vacuum	- Can affects the electronics, - Reduces lifetime of the embedded primary battery, - Causing exothermic chemical reaction in lithium-based secondary batteries	Probably possible
Dry Heat	- Very high temperature	- Can affects the electronics, - Reduces lifetime of the embedded primary battery, - Causing exothermic chemical reaction in lithium-based secondary batteries	Probably possible
Ethylene Oxide	- Flammability, - Carcinogen	- Vacuum environment can affect embedded ESS	Probably impossible
Chlorine Dioxide	-	- There is no critical parameters for embedded electronics or ESS	Probably impossible
Vaporized Hydrogen Peroxide	- Vacuum	- Vacuum environment can affect embedded ESS	Probably impossible
Hydrogen Peroxide Plasma	- Vacuum, - Plasma discharge	- Radio field energy required to generate the plasma may not be compatible to semiconductors	Probably impossible
Gamma Ray	- Radiation, - Nuclear waste	- The semiconductors and ESS may be damaged by radiation, if they are not designed for exposure.	Probably impossible

5. Energy Storage Systems – State of the Art

Abstract

In this chapter, energy storage systems (ESS) for high temperature applications are discussed. First, the overview and development challenges of the ESS in the medical field are presented. Next, primary cells, secondary rechargeable lithium-base cells, electrolytic double layer capacitors (EDLC) and lithium-ion capacitors are preselected for further investigation. As the first, high temperature batteries are being investigated. Despite several different technologies which are usable in the temperature range up to 220 °C their main disadvantage is the need of replacement and accelerated degradation in high temperatures. Next, the li-ion-based secondary cells have been investigated. This technology has the main thermal limitation coming from several factors related to the chemistry of the anode, cathode and separator making it almost impossible to bare temperatures higher than 60 °C and resulting in the exothermic reaction of thermal runaway. There is, however, one solution on the market which is designed for medical use and temperatures up to 135 °C, its disqualifying disadvantage is however high price, availability and manufacturer's requirements towards full disclosure of R&D process. The electrochemical and lithium-ion hybrid capacitors have been analysed next. Here, a high-temperature-resistant models are available; however, they need to be recharged very often due to limited capacitance, thus the requirement of maintenance-free has not been met and these technologies were not considered for further development. As a result of the research on possible ESS for high-temperature maintenance-free sensor node, it was decided to not choose any of the technologies in the ESS domain and search for alternative power sources.

Outcomes of this chapter: As a result, an analysis of the available high-temperature ESS has been created. On the basis of the analysis and technological limitations of available technologies, it was decided to select the lithium-ion supercapacitor as a potential power buffer and to continue investigation for alternative power sources such as energy harvesting technologies.

One of the key components of the Internet of Medical Things node power module is the energy storage system. To select the optimal solution, a market analysis was performed to select the appropriate technology. Electrical energy drives most modern devices and appliances. The same is true for medical devices where energy storage systems are usually a bottleneck in the design process, due to the harsh working environment of surgical devices mentioned in the chapter 4. Energy Storage Systems can be defined as a system that converts electrical energy from the power network to a portable form that can be converted back to electricity and used later [28]. Every ESS is designed for a given application, and it is a result of several compromises. Usually there are two drivers of the design process of a given storage system: power requirements and working environment. The diverse requirements resulting from this lead to the diversity of ESS technologies being used today. Each of these technologies has its own performance characteristics that make it suitable for a specific application. To continue the discussion, some basic definitions describing energy storage systems need to be introduced first. There are two main parameters which allow us to compare different types of ESS in terms of application requirements - specific power and specific energy. Specific power, also known as the

gravimetric power density, indicates the loading capability. It is a relationship between the power delivered by the storage system and its weight. Unit is $W \cdot kg^{-1}$. High specific power is important for applications with weight limitations and high power demand. Specific energy, or gravimetric energy density, defines the energy capacity in a given weight of a particular ESS. The unit is $Wh \cdot kg^{-1}$ [29]. It is important factor for devices with low power consumption but with the requirement of long life. According to these two parameters, it is possible to describe and compare different energy storage systems regardless of their chemistry. Only the systems applicable to portable devices have been selected for comparison in this thesis. Electrochemical systems offer a wide selection of available technologies, including primary and secondary battery cells, supercapacitors, and hybrid capacitors. To have an overview, the most important technologies are listed in the figure 5.1.

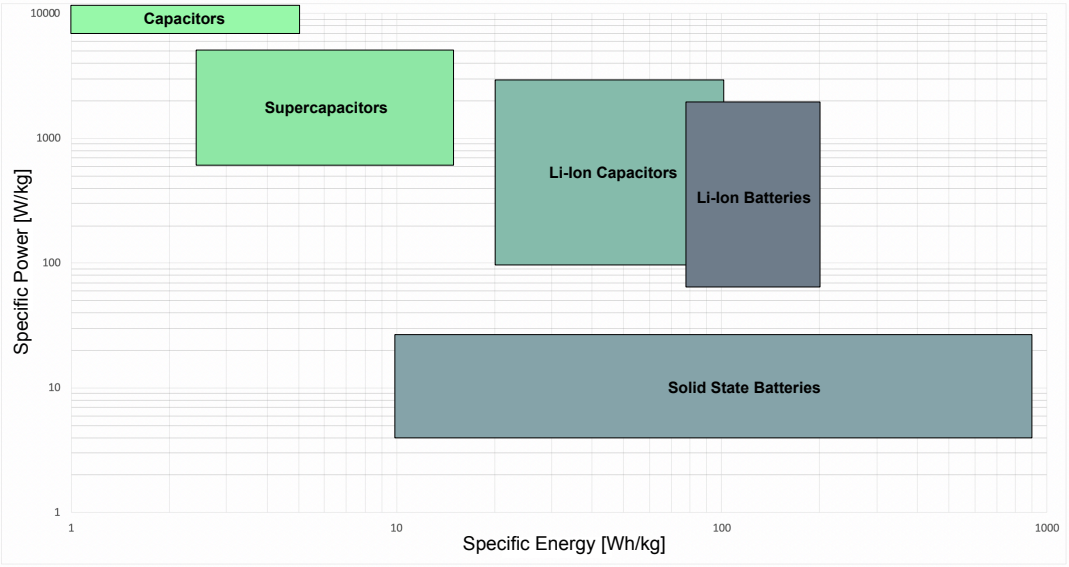

Figure 5.1. Overview on electric energy storage systems potentially usable for medical technology applications. Based on [30]–[34].

As mentioned in chapter 4 temperature is a main issue in adaptation of energy storage systems to the environment of steam sterilisation. It affects the structure and properties of the materials comprising the device, as well as its chemistry and efficiency. Currently each ESS is designed for a very specified temperature range as is shown in Figure 5.2. In industry it is possible to distinguish devices operating at low temperatures (0 °C), room temperature (0 °C to 40 °C), elevated temperatures (40 °C to 80 °C), high temperatures (80 °C to 300 °C) and very high temperatures - above 300 °C [33]. This classification should not be perceived as a strict one, as in different industrial areas the definition of temperature ranges may differ and overlap suggested borders. It is worth mentioning that the adaptation of new energy storage systems is closely related to market size. Devices designed for the biggest market, consumer electronics, usually operate from –20 °C to 60 °C [29], [37]. The availability of ESS operating in this temperature range is usually good. Every other system designed for different temperature range shall be considered as a specialised system. For such devices, availability and price can differ and are highly dependent on current market situation and the possible ordering quota.

It is also worth mentioning that there are several challenges that limit the fast development of high-temperature energy storage systems, especially those based on electrolytes. Most of the materials used for the development and production of ESS are those that are stable and nominally function in the range of room temperatures. It may be also caused by R&D costs optimisation, by adoption the materials and technologies from the consumer-electronics market. The other problem is related to the safety issue. As mentioned in several papers [33], [38]–[41], despite the design of sophisticated safety systems, some ESS still suffer from

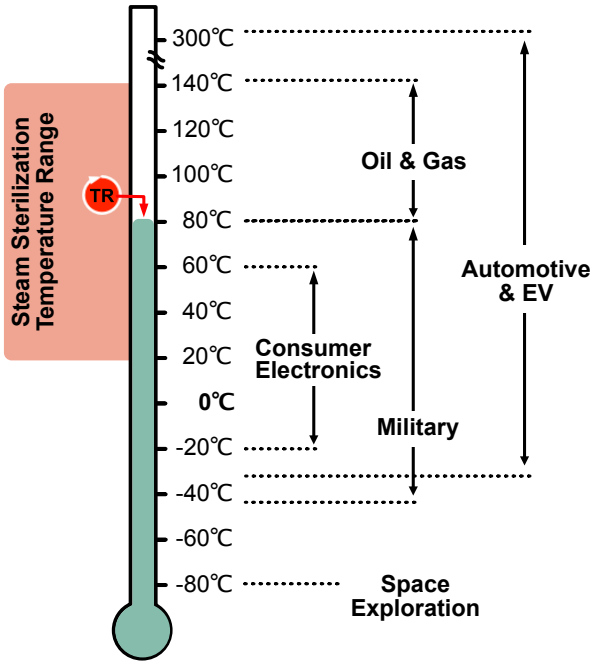

Figure 5.2. Overview of the temperature ranges of specific industrial grade batteries in comparison to steam sterilization environment. Thermal runaway phenomenon (TR) in Li-Ion batteries starting at 80°C is a main limitation for using rechargeable batteries in high temperatures environments [33], [35], [36].

high temperature under various circumstances. Such a rapid heating of a single cell in a power pack and reaching a certain onset temperature can lead to a chain reaction called thermal runaway (TR) and serious safety incident [42]. Mitigation of TR outcomes might be reduced by using low-flammable materials; however, their development is still in its infancy and most materials, especially elecrolytes, are flammable and have low boiling points [33], [43], [44]. Also covering the cell with non-flammable thermal resistant material is only a partial solution as the main problem is that chemical reactions during the TR are mostly exotermic. Each ESS is combined from several different materials. Each of them has it's own work characteristics and can function separately as well as interact with the others to achieve the design goals of the ESS. As a result many different chemical reactions, side effects, and transfer phenomena may occur. All of these are thermally controlled according to the Arrhenius equation [45]–[48]. At high temperatures, the desired reaction kinetics and charge carrier mobility are faster. The behaviour of protective layers on the cathode and anode may also be influenced [49], [50]. On the other hand, the intensity of side reactions, interface deterioration internal resistance, heat accumulation and self discharge is increased. The chemical compatibility of materials in the energy storage device is thus altered, causing possible uncontrollable exotermic chemical reactions. Even if safety issues are solved by changing materials, there are still challenges associated with the life cycle of the ESS. Elevated temperature causes corrosion processes on the nonactive materials of the device such as packaging, circuits, insulators, and current collectors (which blocks the access to the active material of the electrode)[51]. Finally, the overall performance of the ESS is a result of the synergy between its components, and what is more important - replacing the single component with a thermally stable alternative does not guarantee the overall thermal resistance enhancement of the whole device. All of the issues mentioned above cause the design process of the high-temperature ESS to be very sophisticated and holistic. Thus, there is a shortage of

technologies on the market that are capable of withstand high and elevated and high temperatures. Each of these ESS technologies will be described in detail in this chapter.

Before reviewing of the ESS types and chemistries, it is important to define the parameters and factors critical from the project perspective. In case of described power system in this dissertation the predicted working environment and conditions are as follows:

- **Environmental resistance** - the ESS applied to the system needs to withstand an environmental challenges during the whole surgical container lifecycle, from storage through washing procedure, steam sterilization, drying and on the use in the operating theatre.
- **Easiness of use and maintenance** - ESS needs to be rechargeable, ensuring it is maintenance-free, and it needs to be replaceable in an easy and robust way.
- **Self Discharge Rate** - It should have a possibly low self-discharge rate, as it is not possible to guarantee the regular recharging interval due to the complexity and diversity of applications in the clinical environment. Based on internal data on surgical instrument usage statistics collected by the company Aesculap AG, it was assumed that the device can be in the idle state for a maximum of 3 months.
- **Discharge Current** - It does not to have a high discharge current, as the predicted use will be for powering from ultra-low-power to low-power devices and sensors. The ultra low power device can be defined as device with energy consumption less than 0.1 mW and low power in this case can be defined as device with energy consumption less than 5 mW.

Due to these requirements following ESS have been analysed: primary cells, secondary rechargeable lithium based cells, electrostatic double-layer (super)capacitors (EDLC) and lithium-ion capacitors.

5.1. High Temperature Batteries

Batteries, both those with a standard operating temperature range and those designed to operate in an extended temperature range can generally be divided into three types: primary, single use batteries; secondary (rechargeable) multi-use and reserve batteries which are single use and need to be activated before usage. Each battery can be defined as an assembly of one or more cells (unit cell). A cell is a basic electrochemical unit, that converts chemical energy into electrical energy and, in case of rechargeable cells, vice versa. It should also be mentioned that both batteries and cells are commercially available, except that batteries are available to individual consumers, while training is often required to purchase and work with the component cells, and the cells themselves are not offered to the mass market.

Each cell is composed from several different components depending on the manufacturer and the detailed technology, however, there are some elements which are shared by all types of cells:

- Anode - an electrode that lithium ions flow out and is oxidized during discharge (electrochemical definition); however in battery industry we refer to the anode as a negative electrode (no matter if it is charged or discharged),
- Cathode - an electrode that accepts the lithium ions and is reduced during discharge (electrochemical definition); however in battery industry we refer to the cathode as a positive electrode (no matter if it is charged or discharged),
- Separator - an ion permeable, electrically non-conductive material which prevents electronic contact between electrodes in the cell,

– Electrolyte - the non-conductive medium (usually liquid) which provides the ion transport mechanism between the positive and negative electrodes of the cell.

All of these elements are depicted in Figure 5.3.

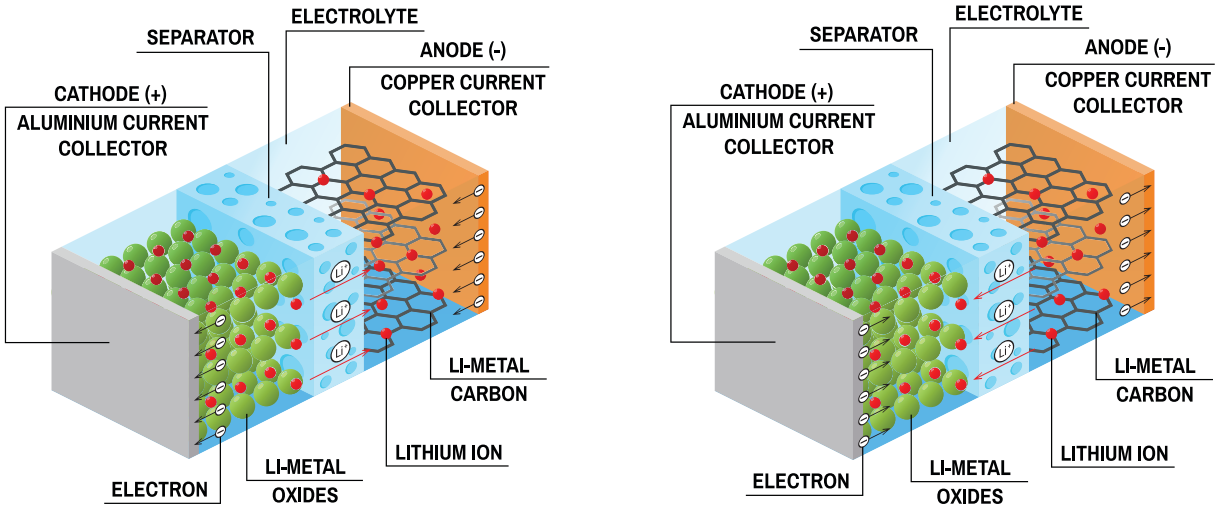

(a) Charging mechanism of Li-ion cell.

(b) Discharging mechanism of Li-ion cell.

Figure 5.3. Lithium-ion battery cell during charging (a) and discharging (b) [52].

Physical and chemical parameters of each of these components affects heavily the performance and operating ranges of the cell, and thus of the battery itself. The composition of the anode and cathode materials can be named as cell chemistry. There are many different chemistries under development at the universities; however, only very few of them have their market release. Due to the practical aspect of this dissertation, only cells available on the market or in pre-release phase will be taken under consideration.

5.1.1. High Temperature Primary Batteries

Primary batteries, or nonrechargeable batteries, are widely used due to their high performance, great convenience, ease of use, and very good shelf life. Primary batteries have usually higher energy density in comparison to the rechargeable secondary batteries. This is caused by the lack of need for design compromises to accomodate charging functionality. In situations where consistent power is required without charging, primary batteries are adequate as they do not exhibit voltage delays even after long storage periods. However, the biggest disadvantage of primary cells is that, at the end of their life, they need to be maintained and replaced. It should be taken into account that the low initial cost of the cell is compensated by costly maintenance in the long run.

Primary cells can be divided into four main chemistries [29], [37], [53], [54]:

– **Alkaline Manganese Dioxide (Zn / MnO_2)** - Introduced to the market in 1960, with 1.58 V open circuit voltage (OCV), with low to moderate discharge rates and with operating temperature from –10 °C to 55 °C. Having varying sizes including AAA, AA, C, D and 9V sizes, it is very popular both in industrial and consumer applications. Despite it's low cost and established market position, it is not applicable due to the low operating temperature and possible damages caused during the steam sterilisation procedure.

– **Silver-Oxide (Zn / Ag_2O)** - With 1.6 V - 1.86 V OCV (depending on the model and manufacturing technology) and high energy per unit weight combined with long operating range they might be

considered as a good choice for low power electronics. Due to the high cost of a silver they are available mainly in very small sizes as button cells. Their main markets are consumer electronics, hearing aids, and medical devices. Despite of their high chemical stability, safety and flat discharge curve they cannot be used in sterilizable electronics, as their operating temperature ranges from –10 °C to 55 °C

- **Zinc-Air** - A main competitor to Alkaline and Silver-Oxide batteries. In Zinc-Air batteries the electrical power is generated by an oxidation process of zinc and oxygen from the air. These types of batteries can have 1.65 V OCV. Batteries with lower OCV (1.4 V) achieve a longer lifetime. This battery needs a removal of a sealing tab that enables airflow, and reaches a full operational voltage within 5 seconds. Their main advantages are high energy density (300 – 400 Wh/kg), flat discharge curve, and low cost. Their main disadvantages are limited power output, short life after activation and being dependent on environmental conditions. Due to its chemistry and need for airflow, this type of batteries cannot be considered as useful for sterilisable electronics.

- **Lithium-based chemistries** - Lithium-based cells are composed of metallic lithium anode, electrolyte made of different compounds and cathode made of different materials determining the type and application of a whole cell. The performance of lithium-based cells depends on their electrochemical system, size, and internal design. The advantages of lithium-based cells are high energy densities (up to 1300 Wh/l or 760 Wh/kg), high power density (2200 W/l or 970 W/kg), high OCVs (1.8 V - 4.1 V), wide current capabilities (1 µA to 130 A) and what is most important, a wide operating temperature range, from –65 °C to 220 °C, low weight, flat discharge curve, very long shelf and operating life. It is also worth to mention that it's yearly operation cost is relatively low, even if their unit price is high. However, like all of the chemistries, lithium-based chemistry has limitations such as safety concerns in a case of a safety event, passivation during restart, high heat dissipation, and high unit price. We can distinguish the following main lithium chemistries for primary cells:

  Lithium-Sulphur-Dioxide (Li / SO_2) - Lithium sulphur dioxide battery uses lithium as the anode and a porous carbon cathode with sulphur dioxide as the active cathode material. With 3.0 V OCV high discharge rates and wide operating temperature range from –60 °C to 70 °C it is a good candidate for extended temperature and power applications such as military and space. It also has a specific energy of 260 Wh/kg and an energy density of 415 Wh/l.

  Lithium-Thionyl-Chloride (Li / $SOCl_2$) - The Lithium-Thionyl-Chloride (LTC) cell contains a metallic lithium anode and a liquid cathode comprising a porous carbon current collector filled with $SOCl_2$. It has OCV of 3.6 V and very high specific energy and energy density of 590 Wh/kg and 1100 Wh/l respectively. The end-of-discharge cut-off voltage is 3.0 V. The biggest advantage of LTC cells is a very wide operating temperature range from -55 °C to 220 °C, and ability to withstand very strong vibrations. A strong passivation effect in this type of chemistry ensures long shelf-life. Unfortunately, there are limitations in a load which can be connected to the LTC cells. A constant current is a preferable way of draining the LTC cell, as it ensures a longer cell lifetime. LTC chemistry is very commonly used in oil & gas drilling applications as well as in some of the medical devices. As a result of safety reasons, it is not present in consumer electronics. This type of cell chemistry (and the respective battery models) could be a possible candidate for energy storage system for sterilisable electronics. However, safety considerations, high unit cost, and the need for maintenance are limiting factors for practical use of LTC chemistry and cell as a solution for the problem adressed in this Ph.D. thesis.

  Lithium-Manganese-Dioxide (Li / MnO_2) - This type of cell is composed of a lithium-based anode, an electrolyte containing lithium salts in an organic solvent, and the heat-treated form of MnO_2

(electrolytic manganese dioxide - EMD). This type of chemistry is similar to LTC, however, its specific energy and energy density are lower, reaching 280 Wh/kg and 588 Wh/l respectively. Lithium manganese dioxide cells have in general 3.25 V OCV, having many different forms, i.e. bobbin, spiral, coin, prismatic and cylindrical, they are one of the most universal and popular primary cell chemistry. In some cases, the cell is pre-discharged to lower the OCV, resulting in corrosion reduction. Having a flexible range of discharge rates, from low to high, and a wide temperature range, from –20 °C to 60 °C, with the possibility to reach 125 °C in some coin cell designs (specially developed materials for coin cell gasket and separator), they are a very good choice for sensor systems exposed to variable environmental conditions. High-temperature coin cell designs have very low continuous discharge current (usually less than 1 mA). The disadvantage of such a cell is a low passivation that may lead to capacity loss over time. This type of battery could be used as an energy storage system in the case of steam sterilisable sensor nodes, however, as in the case of LTC batteries, it raises the need of replacement and a design of special battery holder with safety mechanisms. Also, extended temperature versions of this cell chemistry cannot be used and handled by not trained personnel.

Lithium-Sulfuryl-Dioxide - The chemistry of this cell is similar to LTC containing lithium anode, a carbon cathode, and the electrolyte of $LiAlCl_4$ in SO_2Cl_2, resulting in an OCV of 3.95 V, placing this technology as one with the highest OCV delivered. It has also one of the highest energy density of 1040 Wh/l and a specific energy of 480 Wh/kg. A strong passivation effect in this technology ensures long shelf-life; however, the self-discharge rate is higher than that in LTC-based systems. This cell chemistry is also sensitive to temperature, OCV might depend and change on environment temperature variations. This behaviour and safety concerns prevent this technology from reaching the wide market, and the number of manufacturers and offered models is due to this fact very limited.

Lithium Carbon Monofluoride (Li/CF_X) -This cell chemistry has an active component made of lithium for the anode and polycarbon monofluoride (CF_X) for the cathode. Such chemistry assures high chemical stability. Li/CF_X based cell is a solid cathode system, with a specific energy of 250 Wh/kg - 820 Wh/kg and 635 Wh/l - 1180 Wh/l of energy density depending on the cell size (bigger cells are more efficient and energy rich). Compared to LTC chemistry, it has a low passivation effect and, because of this, a higher discharge rate. Another drawback of this type of battery is a low nominal voltage of only 2.6 V and very low possible constant current drain (usually not higher than 0.5 mA in coin-size cells and not higher than 5.0 mA in the case of the bobbin type.

Lithium-Iron-Disulphide (Li / FeS_2) - This type of chemistry is using solid cathode of FeS_2 mixed with carbon and Polytetrafluoroethylene (PTFE), an anode of lithium alloyed with aluminium and polyethylene separator. The electrolyte is a 0.75 mol solution of LiI in an organic solvent blend. These cells, with 1.78 V OCV, have a nominal voltage of 1.5 V and therefore can be used as a replacement for Alkaline batteries. Disulphide electrode discharges in two steps, resulting in two distinctive voltage plateaus in the discharge curve. This might be helpful for the low-drain applications (like sensors) allowing the easy fuel gauge implementation. Li/FeS_2 chemistry offers specific energy of 310 Wh/kg. The operating temperature range varies from –40 °C to 60 °C, however, applications for high-temperature (90 °C) and high-temperature separators (>150 °C) are under development [55].

5.1.2. High Temperature Secondary Batteries

Secondary batteries have been the leading technology of energy storage in recent years. Due to the dry heat and steam sterilisation technologies, there is a need for secondary batteries able to cope with elevated temperature ranges. Despite its limitations the leading technology in this area is still lithium-ion chemistry.

There is also a growing number of alternative chemistries and their variations in the development phase; however, it is a very fast growing area on the market and further developments in these technologies are predicted to happen.

High-temperature lithium-ion batteries are key technologies in areas like space industry, automotive, emergency roadside systems, container and cargo tracking, military communication batteries, and deep-space applications. In addition, in the medical industry, there is a high demand for reliable and cost-effective lithium-ion secondary batteries. Due to the different chemistries we can distinguish following types of secondary li-ion batteries:

- Lithium Cobalt Oxide (LCO),
- Lithium Manganese Oxide (LMO),
- Lithium Nickel Cobalt Manganese Oxide (NCM),
- Lithium Nickel Cobalt Aluminum (NCA),
- Lithium Iron Phosphate (LPF),
- Lithium Sulfur-Lithium Metal (Li-S),
- Lithium Titanate (LTO),
- Lithium with nano-structure Silicon Anode (Li-Si),
- High temperature Lithium-based microbatteries.

Only very few of these cell chemistries, such as $LiFePO_4$ [54], are safe for operating in extended temperature.

To talk about extended-temperature batteries, it is important to define the standard operating temperatures for storage, charging, and discharging of the cell. All of these processes involve different chemical reactions and thus have different temperature ranges. For storage, as a standard temperature range, based on the datasheets of the cell manufacturers and work by Leng et al. [37], [56], we can consider temperatures from 10 °C to 35 °C. During the charging procedure, cells may face high temperatures and high charging voltage, causing the cell chemicals reaction to accelerate. That might lead to a higher potential for performance degradation and raises a safety concern. For this reason, cell manufacturers usually recommend a narrower temperature range for charging, usually in the limits of 0 °C to 45 °C. However, in the low temperatures a Li-plating, which is the formation of metallic Li on the anode particle surfaces, might occur. This is causing a dendritic growth and can cause an internal short, thus charging currents can already be limited for temperatures around 5 °C. For discharge, the operating temperature limits are usually wider, from –20 °C to 60 °C due to the less heat generated by the cell itself while discharge.

Operating at extended temperature involves multiple negative phenomena to a cell such as, low cycle, calendar and shelf life; increased internal pressure causing cell packaging expansion, shrinkage of the separator; chemical damage - electrode passivation, corrosion and emission of combustible gases; higher safety risk for thermal runaway. However, the discharge capacity is increased, as the literature suggests [57]. There are two major problems with Lithium-ion secondary batteries in elevated temperature: ageing and thermal runaway. While the first mechanism only causes damage to the cell itself, the second usually results in a violent release of flammable gases, often ending in the explosion of the battery pack and the entire device. In a standard consumer-grade cell, the thermal runaway mechanism starts in the temperature from over 80 °C and is evolving as listed below[35], [58]–[60]:

- 60 °C - Maximum operating temperature,
- 80 °C - Solid electrolyte interface, (SEI) layer breaks down,
- 90 °C - Separator pores close preventing ions from passing,
- 100 °C - 120 °C - Electrolyte breaks down and begins producing flammable gases,
- 120 °C - 130 °C - Separator melts causing electrodes to short circuit,
- 130 °C - 150 °C - Cathode breaks down and begins generating oxygen,
- 180 °C - Melting point of lithium, after this point the reaction becomes self sustaining.

The main problem with high-temperature secondary batteries is the lack of industry standards for the manufacturing and testing of the batteries for extended temperatures. To the best knowledge of the author, such a standard does not exist (neither IEC standard nor ANSI standard, state for 2023). Without an official standard, it is very hard, and sometimes even not possible, to compare between cells and select the right one for the specific needs. However, market research has been done by the author to combine possible candidates for the sterilisable energy storage system. The results of the market research are available in the Table 5.1. Due to the specifics of the application, two different scenarios are being considered - battery is charging while steam sterilisation and the battery is charging before or after steam sterilisation. In the first scenario, only one cell model has been found that fulfils this requirement, it is a Tadiran Israel TLI-1550HT cell. In the second case, there are multiple cells available on the market; however, only one, Saft VL25500-125 could be a possible candidate for a power storage in the sterilisable electronic device.

Table 5.1. Batteries available on the market, state on 2022.

Manufacturer	Model	Nominal Voltage	Operating Temperature	Capacity
High-Power China	14500AT-800	3.7 V	–20 °C to 85 °C	800 mAh
High-Power China	18500AT-1500	3.7 V	–20 °C to 85 °C	1500 mAh
High-Power China	32650DT-4000	3.7V	–20 °C to 85 °C	4000 mAh
Tadiran Israel	TLI-1550A	4.1 V	–40 °C to 85 °C	330 mAh
Tadiran Israel	TLI-1550HT	4.1 V	–40 °C to 135 °C	500 mAh
Saft Batteries	MP176065	3.65 V	–40 °C to 85 °C	5600 mAh
Saft Batteries	MP174565 XTD	3.65 V	–40 °C to 85 °C	4000 mAh
Saft Batteries	VL25500-125	3.6 V	up to 125 °C	2000 mAh
LG Chem	INR18650HG2	3.6 V	–40 °C to 75 °C	3000 mAh

Despite the presence of so-called "safe" technologies, such as Lithium-Iron-Phosphate batteries, it is very unlikely that even this kind of batteries will be approved for medical use in the steam sterilisation environment in the near future. Also it needs to be mention, that consideration of Lithium-Iron-Phosphate batteries is more like a marketing slogan for sales. The LFP batteries does not ignite as easy as other Li-base rechargeable cells, however that means that toxic and flammable gasses accumulate rather than burn. That shifts the risk towards explosion, especially in a confined space (e.g. battery pack with metal casing).

Perspectives on high temperature batteries

As a summary of this subchapter it was essential to answer a question if the new high-temperature batteries have a chance to be released on the market in the near future, or is it needed to look for some other, alternative technologies. Author of this dissertation would like to perform a short analysis of this issue. Despite the high demand for high-temperature batteries, its wide use in the near future might be limited. The main factors limiting the use of batteries in the medical industry are the battery ageing mechanisms depicted in the figure 5.4. Ageing mechanisms are very closely related to base chemistry and electrochemistry, material properties, and physics. In the author's opinion, it is very unlikely that all of these issues will be addressed in the near future, tested, evaluated and put into production, so alternative power sources need to be researched to allow powering the electronic sensors inside the autoclave.

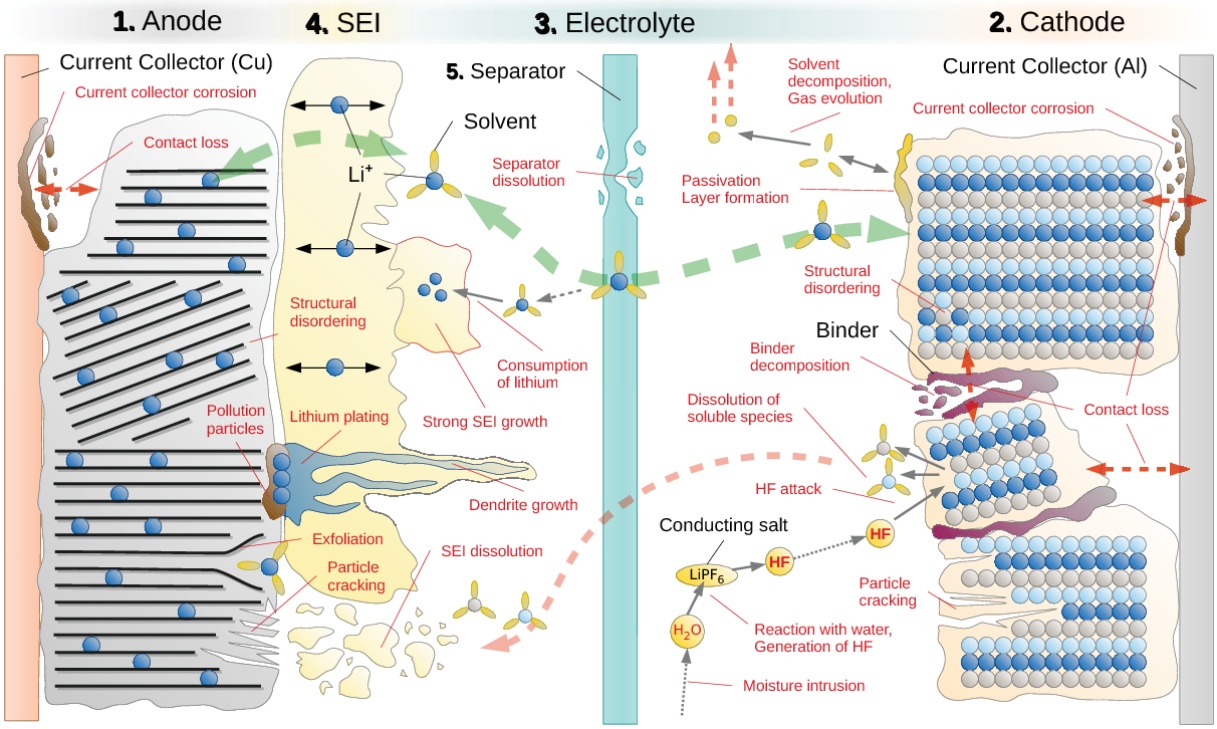

Figure 5.4. Battery aging mechanisms depicted in single figure [61].

Batteries have a lot of advantages, but they also have some drawbacks, which cause severe design limitations. First of all, due to the faradic type of chemical reactions most of them have safety concerns; they are composed of corrosive, flammable, and toxic electrolytes that can be especially dangerous at elevated temperatures. The other problem with the batteries is that only $LiFePO_4$ chemistry is chemically stable (in LFP the phosphate (PO_4) is more stable and the oxygen is not released as easily as in NCM chemistries) and does not have as rapid self-heating effect that causes thermal runaway. Finally, for some applications, batteries have a low power density, which, however, does not apply to the desired application in this Ph.D. thesis. Unfortunately, low cycle life (especially in elevated temperatures) beside the safety concerns is the main limitation factor to use batteries in sterilisable electronic devices.

5.2. Electrochemical Capacitors

The second most popular energy storage device beside the battery is an electrochemical capacitor (EC). Capacitors are electrolytic components made up of two conductors separated by an insulator. One type of

capacitors are electrolytic capacitors, where one of the electrodes is an electrolyte. Capacitors usually have a very low capacity in relation to the battery. A special type of high capacity capacitors are called supercapacitors. They are electrolytic capacitors in which the electrodes are made of materials with very high porosity, mainly based on activated carbons, carbon and carbon aerogels [54]. However, an EC distinguishes from a battery by the charge-storage mechanism, which is typically capacitive rather than faradaic [54], [62]. This means that there is a reversible adsorption of ions on the electrode surface during charging and discharging; on the contrary, in faradic processes there is a redox reaction at the anode and the cathode. Such capacitive mechanism has improved safety contrary to the faradic one. However, there are more differences in contrary to battery systems such as shorter charging time, very low internal resistance, very high power density, and very long shelf life. All these differences are summarised in Table 5.2.

Table 5.2. Comparison between supercapacitors and lithium-ion rechargeable batteries, based on [63], [64]

Function	**Supercapacitor**	**Li-Ion battery**
Charge time [s]	5	4000
Internal resistance (ESR) [Ω]	0.01	0.2
Energy Density [$Wh \cdot kg^{-1}$]	5	150
Instantaneous power density [$W \cdot kg^{-1}$]	10000	2000
Operating temperature [°C]	-40 to 200	0 to 60
Shelf life [h]	1000000	3000
No. of charging cycles	1000000	500 to 10000

As can be seen, the difference in energy storage mechanism implies a number of differences in the performance of capacitors relative to lithium-ion batteries. For IoT systems, that is, low voltage, low humidity sensors together with a communication module, the most important capacitor characteristics are the equivalent series resistance (ESR) (as low as possible, to enable high power delivery) and leakage current (DCL) . For the application described in this Ph.D. thesis, additional parameters that will critically influence the choice of technology are the operating temperature range and high capacitance. The form factor plays also a role, however, it is not as critical as other parameters mentioned above due to the desired use of the sensor node (surgical containers).

5.2.1. High Temperature Supercapacitors

For electrolytic super capacitors, the operating temperature range is usually up to 65 °C. Solutions that allow operation at temperatures of up to 75 °C - 85 °C are generally referred to as high-temperature supercapacitors[65]. Over these ranges, we deal with so-called "elevated temperature applications". Elevated temperature has a negative impact on the EDLC capacitor. One of the most critical factors is electrolyte degradation. Most of the electrolytes in commercially available EDLC supercapacitors have organic electrolytes that cannot withstand temperatures greater than 100 °C. High temperature also accelerates solvent decomposition, electrolyte ion intercalation into the electrode, and reaction of the impurities with the electrolyte [46]. All of these factors may lead to cell production of gaseous products causing package deformation and danger of explosion, but even though there is no gasation effect, ESR increase and capacitance loss might occur. As mentioned above, most commercially available products do not withstand temperatures over 65 °C. In recent years, however, efforts have been made to develop an electrolyte and production technology for EDLC supercapacitors capable of operating at temperatures up to 200 degrees Celsius. One example of such technol-

ogy, already commercialised, are FastCap Systems supercapacitors capable of operating at temperatures up to 150 °C. Unfortunately, this technology, despite its advantages, is so far relatively unattractive economically, and it is not possible to use these devices to build a low-cost IoMT module.

5.2.2. Lithium-Ion Capacitors

A lithium ion capacitor consists of a cathode (usually carbon), a predoped lithium anode, and an organic electrolyte containing lithium ions. These properties can be altered by the appropriate doping and selection of materials for a particular application. The charging and discharging mechanism adopted in LIC technology consists of adsorption or desorption of anions to and from the surface of the positive electrode (as in EDLC capacitors) and intercalation and deintercalation of Li+ ions on the negative electrode (as in lithium ion batteries, this process involves reversible incorporation of lithium ions into the structure of transition metals and graphite constituting the anode material). This combination of EDLC capacitor and battery properties makes lithium-ion capacitors with EDLC solutions features such as higher specific power and higher cycle life, and lithium-ion batteries features such as higher specific energy and voltage compared to EDLC. It is worth adding that specific energy and specific power increase with the square of the voltage. Lithium-ion capacitors have a much higher operating temperature than lithium-ion batteries because of their design. In some cases, this temperature reaches 105 °C. Unfortunately, the vast majority of lithium-ion capacitors are sensitive to high temperatures. As the ambient temperature increases, their chemical and electrical parameters deteriorate. With the number of cycles at high temperature, the capacitance of the capacitor decreases. This is due to active carbon (AC) material utilisation, SEI formation, anode lithium storage consumption, and change in pre-lithiation capacity [62]. The increase in temperature also accelerates the electrolyte evaporation intercalation of ions from the electrolyte on the electrodes, as well as the reaction of production impurities with the electrolyte. This in turn leads to the formation of gaseous products causing an increase in pressure inside the capacitor, the formation of solid deposits blocking the pores of the electrodes, which in turn leads to a decrease in capacitance, and an increase in ESR. These phenomena cause, on the one hand, deterioration of the device's operating parameters and, on the other hand, lead to the risk of a safety incident. At present, a lot of work is being carried out on electrolytes enabling their operation at high temperatures. Compounds based on ethylene carbonate and dimethyl carbonate seem to be particularly promising; however, the only commercialised solution (to the best knowledge of the author) is the Taiyo Yuden capacitor capable of operating at 105 °C. This capacitor is the only one on the market that can be a candidate for sterilisable electronic sensors, but it must be insulated due to the steam sterilisation temperature exceeding the maximum operating temperature recommended by the manufacturer. Therefore, admittedly, it can be used as an auxiliary solution and as an energy reservoir from energy harvesting.

5.3. High Temperature Energy Storage Systems Summary

This chapter analyses available and commercialised electrochemical energy storage technologies. A number of parameters relevant to the designed application, a power module for low-energy high temperature sensors, were selected. The analysis was done in terms of thermal endurance, safety, ease of use, and economy. Batteries, rechargeable batteries, supercapacitors, and lithium ion capacitors were considered. This selection was dictated by the commercial availability of products in these technologies. Only a few of the available technologies demonstrated the ability to operate at temperatures above 100 °C. The vast majority had an operating range of up to 85 °C, which still exceeds consumer-grade batteries that can operate at temperatures of 50 °C or less. The most widely available solutions are primary batteries, which can operate in temperatures as

high as 170 °C. Unfortunately, the nature of their operation determines the need for technical supervision and battery replacement in case of depletion. This implies the need to develop logistics at the hospital level, which is the criterion that disqualifies this technology from the application considered in this dissertation. Rechargeable batteries (based on secondary cells) and especially lithium ion batteries, are generally not adapted to work at temperatures that prevail in the autoclave. Another problem with lithium-ion batteries is their life time at elevated temperatures, which is usually low, estimated at a maximum of 500 cycles. Suppose a scenario in which the device is sterilised daily, this is less than a year and a half of product life. There is only one battery model available on the market that is suitable for sterilisable medical device applications, but unfortunately, due to availability risks and the manufacturer's requirements (contact and specification of the device in which the model is to be used), it is not suitable for the purposes of this dissertation. Among the EDLC supercapacitors, only a few are capable of handling sterilisation in an autoclave. The only manufacturer of such supercapacitors is FastCap Systems (this is a technology patented in 2018). Due to the innovative character of this solution and patent rights, this solution is economically unjustified in the context of a low-cost power module - the subject of this dissertation. Additional disadvantages also arise from the very characteristics of EDLC technology: a significant leakage current would have to be compensated in some way. Finally, parts availability can be an issue here, due to the fact that these capacitors are not offered at retail but only by the manufacturer directly. This is an additional risk factor against this solution. The fourth type of ESS considered was lithium-ion capacitors. This solution, which combines the selected features of EDLC capacitors and lithium-ion batteries, is one of the most promising energy storage technologies available on the market. The increased safety characteristic of EDLCs compensates for the disadvantages of lithium-ion batteries, while taking over their positive features, such as very low leakage current. At present, the market for high-temperature lithium-ion supercapacitors is dominated by Taiyo-Yuden, although it is not the only manufacturer, which is important from the point of view of supply and production security. The models available on the retail market can operate at temperatures up to 105 °C. In combination with thermal insulation, it is possible to use this technology in sterilisable applications. For the reasons mentioned above, it was decided to consider this solution as an energy storage. However, to ensure maintenance-free operation of the entire module, it was decided to use energy harvesting technology to supplement the energy consumed by the measuring equipment and compensate for leakage current.

6. Energy Harvesting in Surgical Tool Workflow

Abstract

The chapter reviews energy harvesting methods with a view to their use in the hospital environment. Thermal energy harvesting was then decided on as the method of choice. A description of the thermal energy harvester and the physical phenomena occurring in it was made. The available technologies are described. A market review was carried out and then the Bismuth telluride based thermoelectric generator was chosen as a technology of choice.

Outcomes of this chapter: This chapter provides a review of the available energy harvesting technologies and selection of thermoelectric energy harvesting as the technology of choice for further development. A solid theoretical background of TEG working principle is presented, maximum power point requirements are presented and factors affecting power generation efficiency are defined. Finally, a technological and market analysis is performed providing input for initial requirements of the device model developed in this PhD thesis.

The process of recovering energy from the environment is called energy harvesting (EH) . In the context of today's applications, energy harvesting involves not only recovering energy from the environment but also storing it for low-power electronic sensors and applications. Many different approaches to this topic have evolved over the years, and energy harvesting itself is possible from sources such as fluid flow, the sun, vibrationx, strain, electromagnetic radiation, thermostatics and thermodynamics, changes in atmospheric pressure or from such a non-obvious source as blood sugar. In the context of Internet of Things sensors and electronics, the most common energy harvesting methods are mechanical or piezoelectric, electromagnetic, solar, thermoelectrical and wind energy harvesting. Their applications range from agriculture sensors to wearable technologies and eventually to nuclear power station applications. All of the EH techniques are presented in the Figure 6.1.

6.1. Hospital Context for Energy Harvesting

Based on the workflow presented in the figure 4.1, the feasibility of different types of energy harvesting technologies was analysed. Technologies that use energy sources based on fluid mechanics, i.e. hydro energy harvesting and wind energy harvesting, have been rejected. This is because it is not foreseen in this study to use the equipment outside the hospital building environment. It is also not possible to use hydroturbine technology because during the life cycle of a surgical instrument it is not part of the processes that use laminar flowing fluid under high pressure. The second type of energy analysed is mechanical energy. As the designed module is intended to be used in a medical container, the possibility of using kinetic energy from human physical activity was rejected. By combining the two remaining energy sources, vibration and pressure changes, they were both analysed with regard to the logistics of medical containers in the hospital. The container is exposed

to vibrations and impacts during its transfer from place to place, either manually or on a special transport trolley. This phenomenon, which is detrimental to the construction of the container itself, occurs throughout its entire life cycle – from the sterilisation room via the warehouse to the operating theatre. This is desirable from the point of view of energy harvesting based on vibrations – piezoelectric harvesters or electrostatic harvesters. The third potential energy source analysed was light energy. Energy harvesting based on light energy inside buildings is applicable to some IoT sensor applications, however, the medical container logistics process does not guarantee that a given container will be exposed to light energy long enough to store the energy needed to power the sensors during the sterilisation process. In addition, if the sensor is located inside the medical container, the energy harvesting system of that sensor would have to be integrated into the container itself. Otherwise, the energy harvesting of indoor light would not be possible. Energy harvesting from electromagnetic waves was also considered; however, the efficiency of such solutions, the fact that medical container are usually made out of metal which limits the radio field available and the possible amount of energy harvested compared to the average demand of IoT sensors made it impossible to choose this method. The last of the energy harvesting methods analysed is thermal energy harvesting. During the steam sterilisation, the container is exposed to high temperatures, up to 134 °C. Furthermore, the temperature gradients that occur in the autoclave during the sterilisation process are significant, as shown in Fig. 4.4 and Fig. 4.5. Moreover, it can be assumed that each of the containers will undergo the sterilisation process with a frequency adequate to its use. Generating electricity from a thermal source – the temperature inside the autoclave – brings with it another advantage in the context of supplying power to sensors supervising the sterilisation process – if the thermogenerator is properly designed, the sensors will be powered even when their energy storage system is discharged. These factors were the reason why thermoelectric energy harvesting using peltier modules was chosen for further analysis. All energy harvesting methods, and the potential energy yield of each are summarised in Table 6.1.

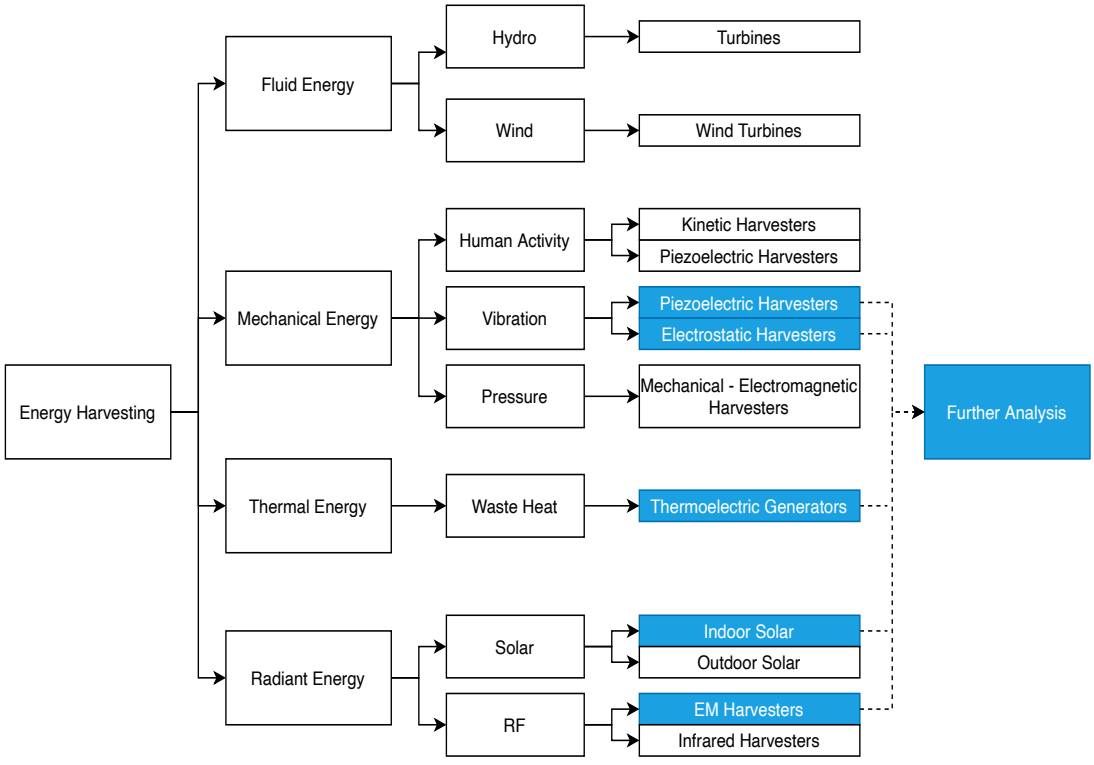

Figure 6.1. Overview on energy harvesting technologies. Technologies pre-selected for further analysis in the context of hospital environment are marked in blue [66], [67].

Table 6.1. Comparison and summary on different energy harvesting methods preselected to use in a hospital logistics environment [68]–[70]

Harvester	Physical Phenomena	Power Density	Efficiency
Photovoltaic	Photovoltaic Effect	Outdoors: 15 $mW \cdot cm^{-2}$	40 %
		Indoors: 10 – 100 $\mu W \cdot cm^{-2}$	
Piezoelectric	Piezoelectric Effect	330 $\mu W \cdot cm^{-3}$	30 %
Electromagnetic	Faraday's law	306 $\mu W \cdot cm^{-3}$ per kHz	67 %
Electrostatic	Vibration-dependent capacitors	50 – 100 $\mu W \cdot cm^{-3}$	23.5 %
Thermoelectric	Seebeck effect	100 $mW \cdot cm^{-3}$	10 % – 15 %
RF	Ubiquitous radio transmitters	0.01 – 0.1 $\mu W \cdot cm^{-2}$	50 % – 70 %

6.2. Thermal Energy Harvesting

Due to the practical implications of energy harvesting in a hospital environment, thermal energy harvesting have become a technology of choice. In this chapter, basics of the thermoelectric effect will be introduced, its practical implementation both as a single P-N pair and as a whole module will be discussed, as well as basic parameters describing a single thermoelectric generator module. Finally, a short review of thermoelectric technologies considering their operating temperatures and market research will be conducted.

The generation of electricity from heat has been known since the 19th century, when in 1821 the scientist Thomas J. Seebeck discovered that in a circuit built out of two different metals, the heating of one of the junctions in the circuit creates an electromotive force (potential difference). We call this effect the Seebeck effect. Thirteen years later, the opposite of the Seebeck effect was discovered by Jean Peltier. It involves the release or absorption of heat energy when an electric current passes through a junction. In 1856 another physicist, William Thomson, discovered that when a current flows through a homogeneous conductor with a temperature gradient, heat is absorbed or dissipated. This effect is called the Thomson phenomenon. These phenomena were not understood until the late 19th century, when electrons were discovered. Thermal energy can release e.g. certain amounts of electrons from their atomic bonds, even at room temperature, causing them to move to areas where they can move. However, when we apply different temperatures to two different areas of a conductor, the area with the higher temperature will release more free electrons. These electrons then diffuse to the cooler area where there are fewer of them. The difference in electron concentration between the warm and cool areas of the conductor also causes an electric field to occur which, through the action of Culomb's forces on the electrons, causes them to move towards the cooler area. Consequently, an electric current flows opposite to the temperature gradient, causing an electromotive force to occur. This phenomenon is reversible – i.e. current flow in a given direction generates a certain opposing temperature gradient. The mechanisms described are used in devices called thermogenerators and thermocoolers.

6.2.1. Thermoelectric Generator – What Do We Talk About

In thermal energy harvesting a device of choice is thermoelectric generator (TEG). It is a solid-state device that produces electrical energy from the thermal gradient across the device. TEGs are usually build from thermoelectric (TE) elements. TE element is composed from a pair of p-type and n-type semiconductors connected in series with a copper connector, while being placed between two ceramic plates in a form of a sandwich. This structure forms so called TE pair which is connected electrically in series and thermally in

parallel. Each pair, when applied a thermal gradient across, is generating a given voltage, due to the Seebeck effect. To increase the efficiency and output power TE pairs are connected forming a TEG. In a standard TEG it can be multiple TE pair, usually from 100 to 200. Overview on a single TE couple as well as a TEG is presented in the Fig. 6.2. The physical principles of TEG will be discussed shortly.

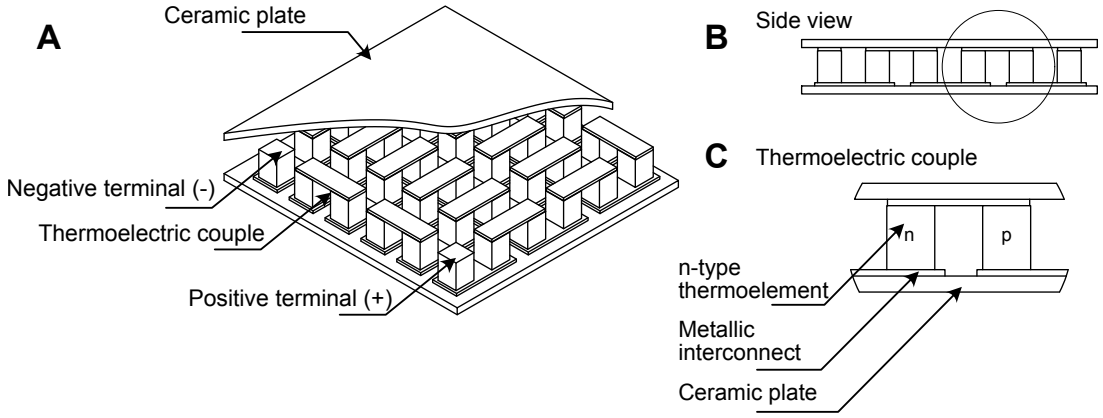

Figure 6.2. 3D model of the thermoelectric generator (A), cross-section of the TEG with visible thermoelectric couples (B), cross-section through a single thermoelectric couple (C).

6.2.2. Thermoelectric Effect and Heat Transfer

The fundamental principle of TEGs is based on thermoelectric effect that can be described as direct conversion of temperature differences to electric voltage and vice versa via a thermocouple. It is a physical phenomenon which is a basic mechanism used in thermogenerators. The thermoelectric effect is composed from three different phenomena: Seebeck effect, Peltier effect and Thomson effect [71], [72].

Thermal conduction

Thermal conduction is the transfer of energy from one particle to another, mediated by the oscillatory motion of these particles. This process continues until the body temperature is equalized throughout the volume under consideration [73]. An example to illustrate conduction would be heating one end of a copper wire over a flame. The wire heats up gradually and heat flows from its hot end (over the flame) to the cold end. In the case of thermogenerators, heat transfer by conduction occurs from the heat source, through the hot ceramic cover of the thermogenerator, through the TE vapour to the cold cover of the thermogenerator and on to the heat sink. It is possible to quantify the amount of heat transfer using Fourier's law, which for a one-dimensional object takes the form:

$$\dot{Q}_C = -kA\frac{\Delta T}{\Delta x} \tag{6.1}$$

where:

$\dot{Q}_C$ - heat transfer through the conduction [W],

k - thermal conductivity [$W \cdot m^{-1} \cdot K^{-1}$],

A - heat transfer area [m^2],

$\frac{\Delta T}{\Delta x}$ - temperature gradient, where where x is the distance along the heat flow path [$K \cdot m^{-1}$].

When considering the conductive heat transfer through TEG pellet, equation ((6.1)) can be formulated as follows [74]:

$$\dot{Q}_C \approx -k\frac{A}{L}\Delta T = -\frac{\Delta T}{2\Theta_{np}} \tag{6.2}$$

where:

L - height of the TE pellet [m],

A - heat transfer area, in this case cross-sectional area of the TE pellet [m^2],

T - temperature in Kelvin [K],

Θ_{np} - thermal resistance of the couple of pellets [$K \cdot W^{-1}$].

Thermal resistance Θ_{np} of the couple of pellets can be expressed as:

$$\Theta_{np} = \frac{1}{k}\frac{L}{2A} \tag{6.3}$$

When considering the thermogenerator as a whole, we will be dealing with N (multiple) thermal pellets connected in parallel. Therefore, the overall thermal resistance of the thermogenerator will be equal to:

$$\Theta_{TEG} = \frac{\Theta_{pn}}{N} \tag{6.4}$$

Joule heating

Another physical phenomenon taking place during the operation of thermoelectric module is Joule heating. Joule heating is a physical effect in which the flow of current through a conductor produces heat energy [72], [75]. This can be seen as the transformation of electrical energy into thermal energy. Considering an electrical conductor of length L and cross-sectional area A, made of a material with electric resistivity ρ, one can calculate its electrical resistance using the formula:

$$R_m = \frac{\rho L}{A} \tag{6.5}$$

Having an electrical resistance R_m it is possible to calculate the estimated Joule heating using the well known formula:

$$\dot{Q}_J = I^2 R_m \tag{6.6}$$

Where:

I - electric current [A]

R_m - electric resistance of the specific material [Ω]

The Joule heating $\dot{Q}_J$ will be referenced later, in equations (6.28) and (6.29).

Seebeck Effect

Seebeck effect plays a major role in thermoelectric energy harvesting and the most straightforward way to describe it is the conversion of a temperature difference into an electric current. Suppose we have a TE pair composed of two different materials, the p-type and n-type, electrically in series and thermally in parallel. After applying a thermal gradient by heating one side of the pair, it can generally be found that a potential difference, or voltage V_S, will appear on the TE pair [72], [75], [76]. The voltage V_S can be defined as:

$$V_S = \alpha_{pn}\Delta T \tag{6.7}$$

where:

ΔT - temperature difference between hot side temperature (T_{hot}) and cold side temperature (T_{cold}) of the TE pair equals $\Delta T = T_{hot} - T_{cold}$,

α_{pn} - relative Seebeck coefficient equals to the difference of Seebeck coefficient of p-type pellet and Seebeck coefficient of n-type pellet according to the equation: $\alpha_{pn} = \alpha_p - \alpha_n$.

Relative Seebeck coefficient α_{pn}, also called thermopower, can be defined as the ratio of electromotive force to temperature difference and it is measured in $V \cdot K^{-1}$ or $\mu V \cdot K^{-1}$. However, measurement of absolute thermopower is difficult to perform, as voltage meter always reads the relative Seebeck coefficient between materials *p* and *n*.

Peltier Effect

Peltier effect is the reverse phenomenon of the Seebeck effect. When a current flows throught the junction connecting two materials (e.g. p-type and n-type inside TE pair), it will emit or absorb heat. The heat is proportional to the current flow and it changes the sign according to the current flow direction. We can express this relationship as follows [72], [74]:

$$\dot{Q}_P = (\pi_p - \pi_n)I = \pi_{pn}I \tag{6.8}$$

where:

$\dot{Q}_P$ - Peltier heat absorbed or generated - depending on the flow of the current I [W],

π_{pn} - Peltier coefficient between p-type and n-type material equals to the difference between Peltier coefficient of p-type material π_p and Peltier coefficient of n-type material π_n [$J \cdot C^{-1}$].

Peltier coefficient can be defined as the heat energy per electron per unit time carried to the junction and depends on using two different materials with a large difference between their Peltier coefficients [77].

Thomson Relationship and Thomson Effect

The third thermoelectric phenomenon described is the Thomson effect. As *Encyclopædia Brittanica* defines [78]:

> Thomson effect, the evolution or absorption of heat when electric current passes through a circuit composed of a single material that has a temperature difference along its length.

Its influence on the operation of a thermoelectric module is usually negligible, but it should be mentioned because it represents a link between the Seebeck effect and the Peltier effect. Through thermodynamic analysis, Thomson has shown a direct relationship between the Peltier and Seebeck effects [72], [76], [79], [80]:

$$\pi_{pn} = \alpha_{pn}T \tag{6.9}$$

$$\tau_{pn} = T\frac{\mathrm{d}\alpha_{pn}}{\mathrm{d}T} \tag{6.10}$$

and

$$\dot{Q}_P = \alpha_{pn} T I \tag{6.11}$$

where:

α_{pn} - relative Seebeck coefficient between p-type material and n-type material [$\mu V \cdot K^{-1}$],

π_{pn} - relative Peltier coefficient between p-type material and n-type material [$J \cdot C^{-1}$] ,

τ_{pn} - relative Thomson coefficient [$V \cdot K^{-1}$],

T - absolute temperature of a pellet [K],

I - electric current [A].

This is one of most important thermoelectric equations and it's full deduction can be found in [72] and [81].

In addition, Thomson showed that heat release or absorption also occurs when current flows through a material that has a temperature gradient along its length, as shown in equation (6.12), the sign of τ is negative if the heat is liberated from the material and positive when the heat is absorbed [82], [83]. This phenomenon is referred as Thomson effect, and is defined as:

$$\dot{Q}_T = \pm \tau I \frac{\Delta T}{x} \tag{6.12}$$

where:

τ - Thomson coefficient of a material [$V \cdot K^{-1}$],

I - electric current [A].

Thomson effect can be illustrated by the example of a copper wire through which current flows and which is heated at a point such that we can distinguish between its hot and cold points. In this situation, heat is absorbed when the conventional current approaches the hot point and transferred to the copper just after the hot point - towards the cold points. In practise, the Thomson effect is smaller by order of magnitude from Joule heating, which overlays it, and it can be neglected in the simulations [74], [84].

Figure of Merit

In order to be able to compare different types of thermoelectric materials, it became necessary to introduce a thermoelectric figure of merit [72], [74], [76], [85], [86]. The figure of merit characterises the performance of a material or device. In the case of thermoelectric devices, the figure of merit, with units 1/K can be defined as:

$$Z = \frac{\alpha^2}{\rho k} = \frac{\alpha^2}{R C_{th}} = \frac{\alpha^2 \Theta}{R} \tag{6.13}$$

where:

α - Seebeck coefficient [$\mu V \cdot K^{-1}$],

ρ- electrical resistivity [$\Omega \cdot m$],

k - thermal conductivity [$W \cdot m^{-1} \cdot K$],

C_{th} - thermal conductance [$W \cdot K^{-1}$],

R - electrical resistance [Ω],

Θ - thermal resistance [$K \cdot W^{-1}$].

Figure of merit can be also dimensionless, having a form of ZT, where T is the absolute temperature in K. It is also worth mentioning that there are no universally accepted measurement procedures for α, C_{th} and R for thermoelectric materials; therefore, the methods and results shown in the literature might slightly differ. Thus, it is widely accepted that ZT value of the thermoelectric module can be averaged [86].

The ZT value is directly correlated with the energy conversion efficiency of a given thermoelectric material. However, obtaining high ZT values and thus high efficiency of these materials is a complex task. This is because in order to achieve high ZT values, the Seebeck coefficient and the electrical conductivity must be maximised, while the thermal conductivity should be minimised. All three requirements are very difficult to meet. Considering the performance of thermoelectric materials, we can speak of three generations. The first generation from the late 1950s and early 1960s achieved a ZT factor of 1.0, which translates into an efficiency of 5%. The second generation of thermoelectric materials began in the 1990s with a ZT of 1.3 to 1.7 and an efficiency of up to 15%. The third generation of thermoelectric materials developed today enables efficiencies of up to 20% to be achieved with a ZT between 1.8 and 2.2 [72], [87]. It should also be mentioned that the parameters of the materials, and therefore their ZT, depend on the operating temperature. This is not always possible, as not all known solutions and materials are commercialised.

6.2.3. TEG Model in Steady State

As was mentioned before, a thermoelectric device, which is in this case a thermoelectric generator, is made up of p-n junctions connected thermally in parallel and electrically in series. These p-n junctions are covered with ceramic plates on both sides, forming a sandwich structure. This is shown in the picture 6.2 which depicts the structure of the TEG, and in the figure 6.3 a scheme of a single thermoelectric pair is presented.

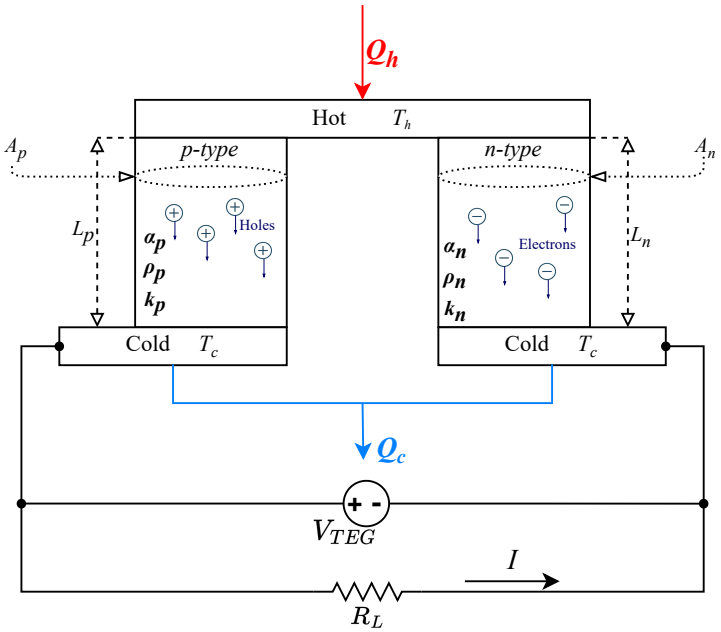

Figure 6.3. Thermoelectric pair scheme with the flow of the heat and current generated. Based on [72], [74], [88]–[90].

As stated in [83], each TE pair is composed of p-type and n-type semiconductor pellets. These pellets are usually made from a similar material, for example, p-doped Bismuth Telluride (Bi_2Te_3) for the p-type

pellet and n-doped for the n-type pellet, respectively. The Seebeck coefficient of TE pair can be defined as in equation (6.14)

$$\alpha = \alpha_p - \alpha_n \tag{6.14}$$

where:

α_p - Seebeck coefficient of p-type material [$\mu V \cdot K^{-1}$],

α_n - Seebeck coefficient of n-type material [$\mu V \cdot K^{-1}$].

The electrical resistivity of the TE pair can be defined as a sum of electrical resistivities of both n-type and p-type pellets as they are connected electrically in series. This is expressed in Equation (6.15).

$$\rho_{pn} = \rho_p + \rho_n \tag{6.15}$$

where:

ρ_p - electrical resistivity of p-type material [$\Omega \cdot m$],

ρ_n - electrical resistivity of n-type material [$\Omega \cdot m$].

The thermal conductivity k_{pn} of the TE pair can be defined as the sum of the thermal conductivities of the TE pellets, as shown in equation (6.16):

$$k_{pn} = k_p + k_n \tag{6.16}$$

where:

k_p - thermal conductivity of p-type material [$W \cdot K^{-1}$],

k_n - thermal conductivity of n-type material [$W \cdot m^{-1} \cdot K^{-1}$].

By doping a basic material with p and n impurities it is possible to achieve the relation of the material parameters between the p-type and the n-type pellets, which is defined in equations (6.17), (6.18) and (6.19).

$$\alpha_p \cong -\alpha_n \tag{6.17}$$

$$\rho_p \cong \rho_n \tag{6.18}$$

$$k_p \cong k_n \tag{6.19}$$

Based on existing literature [72], [74], let us consider step by step how the thermoelectric generator works. This is needed for further mathematical modelling of the TEG behaviour. Let us consider a situation where across the TEG a thermal gradient ΔT is applied, so T_h stands for higher temperature applied and T_c for the lower temperature applied on the other side of the TEG. The first effect which will be under consideration is the heat flow through the TEG caused by the thermal convection. As was mentioned in Equation (6.2) the thermal conduction is equal:

$$\dot{Q}_C = \frac{k_{pn}}{L} A_{pn} \Delta T \tag{6.20}$$

where:

k_{pn} - the thermal conductivity of the TE pair [$W \cdot m^{-1} \cdot K^{-1}$],

L- height of the TE pair (or single pellet) [m],

A_{pn} - heat transfer area of the TE pair equals to sum of cross-sectional area of p-type pellet and n-type pellet ($A = A_p + A_n$) [m^2].

Such a heat flow through thermoelectric material leads to the occurrence of an electromotive force (EMF), caused by the Seebeck Phenomenon. The thermoelectric material EMF can be expressed as the electric field strength vector (6.21):

$$V_{TEG} = -\alpha \frac{\Delta T}{\Delta L} \tag{6.21}$$

where:

α - Seebeck coefficient of the thermoelectric material [$\mu V \cdot K^{-1}$],

$\frac{\Delta T}{\Delta L}$ - thermal gradient [K].

In engineering practice, based on the equation (6.7), this can be referred as Seebeck voltage (V_S) as in the equation (6.22):

$$V_S = V_{S_p} + V_{S_n} = (\alpha_p - \alpha_n)\Delta T = \alpha_{pn}\Delta T \tag{6.22}$$

where:

V_{S_p} - Seebeck voltage of p-type pellet [V],

V_{S_n} - Seebeck voltage from n-type pellet [V],

α_p - Seebeck coefficient of p-type material [$\mu V \cdot K^{-1}$],

α_n - Seebeck coefficient of n-type material [$\mu V \cdot K^{-1}$],

α_{pn} - Seebeck coefficient of the TE pair, equals $\alpha_p - \alpha_n$ [$\mu V \cdot K^{-1}$].

Normally, the TEG works connected to a energy harvesting system. It can be stated that this system, from the TEG perspective, is a load, with a given resistance R_L. This causes an electric current I to flow and causes joule heating which affects the thermal balance of the TEG. Assuming that $\rho_p \cong \rho_n \cong \rho_{pn}$, based on equation (6.18), the joule heating of a single TE pair can be expressed as shown in Equation (6.23):

$$\dot{Q}_J = I^2 \left(\frac{\rho_p L_p}{A_p} + \frac{\rho_n L_n}{A_n} \right) = I^2 \rho_{pn} \frac{2L}{A_{pn}} \tag{6.23}$$

where:

I - electrical current [A],

ρ_p, ρ_n - electrical resistivities of p-type and n-type pellets materials respectively [$\Omega \cdot m^{-1}$],

L_p, L_n - height of p-type and n-type pellets respectively [m],

A_p, A_n - heat transfer area equals to cross-dimensional area of the p-type and n-type pellet in TE pair respectively [m^2],

L - height of p-type and n-type pellets, in TE pair $L_{pn} = L_p = L_n$ [m],

A_{pn} - cross-section area of p-type and n-type pellet, $A_{pn} = A_p + A_n$ [m^2],

ρ_{pn} - electrical resistivity of TE pair, $\rho_{pn} = \rho_p = \rho_n$.

It is also possible to define the resistance of a single TE pellet as follows:

$$R_{pn} = \rho_{pn} \frac{2L}{A_{pn}} \tag{6.24}$$

Most of the researchers agree that it can be assumed that half of the joule heating is added to the cold side, and the other half to the hot side, however, some papers do not agree with this assumption, stating that it is not accurate enough [91] and others neglect the Joule heating [92]. As this thesis is not focused on evaluation or development of thermoelectric pair mathematical models, the common assumption that Joule heat dissipates half to the hot and cold side is taken for further consideration.

When current flows through the p-n junctions of the TE pair another effect, opposite to Seebeck's, needs to be considered - a Peltier effect, expressed as:

$$\dot{Q}_P = \pi_{pn} I = (\pi_p - \pi_n) I \tag{6.25}$$

where:

$\dot{Q}_P$ - Peltier heat flow between hot and cold sides.

Taking into account the Thomson relation from Equation (6.9):

$$\dot{Q}_P = \alpha_{pn} T I = (\alpha_p - \alpha_n) I T \tag{6.26}$$

The last thermoelectric phenomenon considered in the TE pair model is the Thomson effect, as shown in the Equation (6.12). For the TE pair's pellet, the Thomson effect is as follows [82], [88]:

$$\dot{Q}_T = -\tau I \frac{\partial T}{\partial L} = -T \frac{\partial \alpha}{\partial T} I \frac{\partial T}{\partial L} \tag{6.27}$$

Where:

τ - Thomson coefficient of the TE pellet [$V \cdot K^{-1}$],

I - electric current flowing through the TE pellet [A],

T - temperature of the TE pellet [K],

α - Seebeck coefficient of the TE pellet [$\mu V \cdot K^{-1}$],

L - length of the TE pellet [m].

The Thomson heat is usually neglected because it overlays with the internal Joule heating, being smaller by order of magnitude.

These five effects occur in the steady operation state of the TE pair. Taking all of them under consideration, it is possible to form two equations describing a heat flow balance on the hot and cold sides:

$$\dot{Q}_h = \dot{Q}_{C_h} + \dot{Q}_{P_h} - \frac{\dot{Q}_J}{2} \tag{6.28}$$

$$\dot{Q}_c = \dot{Q}_{C_c} + \dot{Q}_{P_c} + \frac{\dot{Q}_J}{2} \tag{6.29}$$

Taking into account the heat on the cold and hot side of the whole TEG it is needed to adapt the Equations (6.28) and (6.29) for a given number of pellets in the TEG which we define as N:

$$\dot{Q}_{TEGh} = N \left[\underbrace{\frac{k_{pn}}{L} A_{pn} \Delta T}_{\dot{Q}_{Ch}} + \underbrace{\alpha_{pn} T_h I}_{\dot{Q}_{Ph}} - \underbrace{\frac{1}{2} I^2 R_{pn})}_{\frac{1}{2}\dot{Q}_J} \right] \tag{6.30}$$

the same for the cold side:

$$\dot{Q}_{TEGc} = N\left[\underbrace{\frac{k_{pn}}{L}A_{pn}\Delta T}_{\dot{Q}_{Cc}} + \underbrace{\alpha_{pn}T_c I}_{\dot{Q}_{Pc}} + \underbrace{\frac{1}{2}I^2R_{pn})}_{\frac{1}{2}\dot{Q}_J}\right] \tag{6.31}$$

Having a heat balance on both sides of the TEG, it is possible to calculate the power output of the module. Applying the first law of thermodynamics, for the thermoelectric module the power output is:

$$\dot{W}_{TEG} = \dot{Q}_{TEGh} - \dot{Q}_{TEGc} \tag{6.32}$$

The total power output of the TEG can be described using internal properties of the TEG as follows:

$$\dot{W}_{TEG} = N\left(\alpha_{pn}I(T_h - T_c) - I^2R_{pn}\right) \tag{6.33}$$

From the external load with the resistance of R_L perspective, the power output can be stated as:

$$\dot{W}_{TEG} = N \cdot I^2R_L \tag{6.34}$$

Assuming that:

$$\dot{W}_{TEG} = I \cdot V_{TEG} \tag{6.35}$$

we can calculate the total voltage of the module as:

$$V_{TEG} = \underbrace{N \cdot I \cdot R_L}_{\substack{\text{Load}\\ \text{perspective}}} = \underbrace{N \cdot \left[\alpha_{pn}(T_h - T_c) - IR_{pn}\right]}_{\text{Module internal perspective}} \tag{6.36}$$

From Equation (6.36), it can be stated that the current flowing from the TEG is defined as:

$$I = \frac{V_{TEG}}{R_L + R_{pn}} = \frac{\alpha_{pn}(T_h - T_c)}{R_L + R_{pn}} \tag{6.37}$$

It is worth to note, that current I is independent of the number of TE pairs. Inserting the equation (6.37) into equation (6.36) gives the voltage across the TEG dependent only from thermal material and electrical characteristics of the module, and the thermal gradient:

$$V_{TEG} = \frac{N \cdot \alpha_{pn}(T_h - T_c)}{\frac{R_L}{R_{pn}} + 1}\left(\frac{R_L}{R_{pn}}\right) \tag{6.38}$$

The produced electrical power can be calculated by inserting equation (6.37) into equation 6.35 which gives the following formula:

$$\dot{W}_{TEG} = \frac{N \cdot \alpha_{pn}^2(T_h - T_c)^2}{R_{pn}} \frac{\frac{R_L}{R_{pn}}}{\left(1 + \frac{R_L}{R_{pn}}\right)^2} \tag{6.39}$$

The thermal efficiency is defined as the ration of the power output over the heat absorbed at the hot junction:

$$\eta_{th} = \frac{\dot{W}_{TEG}}{\dot{Q}_h} \tag{6.40}$$

Inserting equations (6.30) and (6.39) into equation (6.40) gives a conversion efficiency defined as follows:

$$\eta_{th} = \frac{\left(1 - \frac{T_c}{T_h}\right)\frac{R_L}{R_{pn}}}{\left(1 + \frac{R_L}{R_{pn}}\right) - \frac{1}{2}\left(1 - \frac{T_c}{T_h}\right) + \frac{1}{2Z\overline{T}}\left(1 + \frac{R_L}{R_{pn}}\right)^2\left(1 + \frac{T_c}{T_h}\right)} \tag{6.41}$$

Where the average temperature is defined as $\overline{T} = \frac{T_h + T_c}{2}$.

Maximal parameters of the thermoelectric module

Estimation of maximum parameters of the thermoelectric module is essential for choosing the right TEG for the application. Maximum TEG parameters can be calculated as it was shown in [72]. The maximum current of the TEG module obviously occurs when the shortcircuit occurs; in such a situation, the load resistance R_L is close to 0. By applying this assumption to Equation (6.37) we can state that the maximum current of the TEG is equal:

$$I_{max} = \frac{\alpha(T_h - T_c)}{R_{pn}} = \frac{N \cdot \alpha(T_h - T_c)}{N \cdot R_{pn}} = \frac{N \cdot \alpha(\Delta T)}{R_{TEG}} \tag{6.42}$$

where:

R_{TEG} - internal resistance of the TEG module equals $R_{TEG} = N \cdot R_{pn}$ [Ω].

The maximum voltage of the TEG occurs when there is an open circuit, so $I = 0$. Having such situation it is possible to apply it to the equation (6.36) and calculate OCV as follows:

$$V_{max} = N \cdot \alpha_{pn}(T_h - T_c) \tag{6.43}$$

The maximum power output can be estimated by by maximizing $\dot{W}_{TEG}$ with respect to current. The detailed explanation of the formula can be found in [93] and [94].

$$\dot{W}_{max} = \frac{n\alpha^2(T_h - T_c)^2}{4R_{pn}} = \frac{V_{TEG}^2}{4R_{pn}} \tag{6.44}$$

By differentiating the conversion efficiency in equation (6.41) with regard to the proportion of the load resistance to the internal resistance and setting it to zero, the maximum conversion efficiency may be attained. The end outcome is a connection of $\frac{R_L}{R_{TEG}} = \sqrt{1 + Z\overline{T}}$ The highest conversion efficiency is then:

$$\eta_{max} = \left(1 - \frac{T_c}{T_h}\right)\frac{\sqrt{1 + Z\overline{T}} - 1}{1 + \sqrt{1 + Z\overline{T}} + \frac{T_c}{T_h}} \tag{6.45}$$

Not only conversion efficiency is essential for building energy harvesting systems, but also a maximum power efficiency. It is obtained by letting the $R_L/R_{TEG} = 1$ in equation (6.41). The maximum power efficiency η_{mp} is then expressed as follows:

$$\eta_{mp} = \frac{\left(1 - \frac{T_c}{T_h}\right)}{2 - \frac{1}{2}\left(1 - \frac{T_c}{T_h}\right) + \frac{2}{Z\overline{T}}\left(1 + \frac{T_c}{T_h}\right)} \tag{6.46}$$

Normalized Parameters of the TEG

Normalised characteristics of the TEG might be obtained by dividing the given parameter by its maximal value, and its very useful in characterization of commercial modules, the normalized plots of power, voltage,

current, and efficiency against normalized load are depicted in Figure 6.4. As it can be seen, the maximum power output is given when R_L equals R_{TEG}, and the maximum energy efficiency when R_L equals 1.5 R.

The normalized power output $\frac{\dot{W}}{\dot{W}_{max}}$ can be obtained from the equation:

$$\frac{\dot{W}}{\dot{W}_{max}} = \frac{4\frac{R_L}{R_{pn}}}{\left(\frac{R_L}{R_{pn}}+1\right)^2} \tag{6.47}$$

Normalized currents obtained from equations (6.37) and (6.42) are as follows:

$$\frac{I}{I_{max}} = \frac{1}{\frac{R_L}{R_{pn}}+1} \tag{6.48}$$

Normalized voltage onbtained from equations (6.36) and (6.43):

$$\frac{V_n}{V_{max}} = \frac{\frac{R_L}{R_{pn}}}{\frac{R_L}{R_{pn}}+1} \tag{6.49}$$

Normalized thermal efficiency is obtained from the equations (6.41) and (6.45):

$$\frac{\eta}{\eta_{max}} = \frac{\frac{R_L}{R_{pn}}\left(\sqrt{1+Z\overline{T}}+\frac{T_c}{T_h}\right)}{\left[\left(\frac{R_L}{R_{pn}}+1\right)-\frac{1}{2}\left(1-\frac{T_c}{T_h}\right)+\frac{1}{2Z\overline{T}}\left(\frac{R_L}{R_{pn}}+1\right)^2\left(1+\frac{T_c}{T_h}\right)\right]\left(\sqrt{1+Z\overline{T}}-1\right)} \tag{6.50}$$

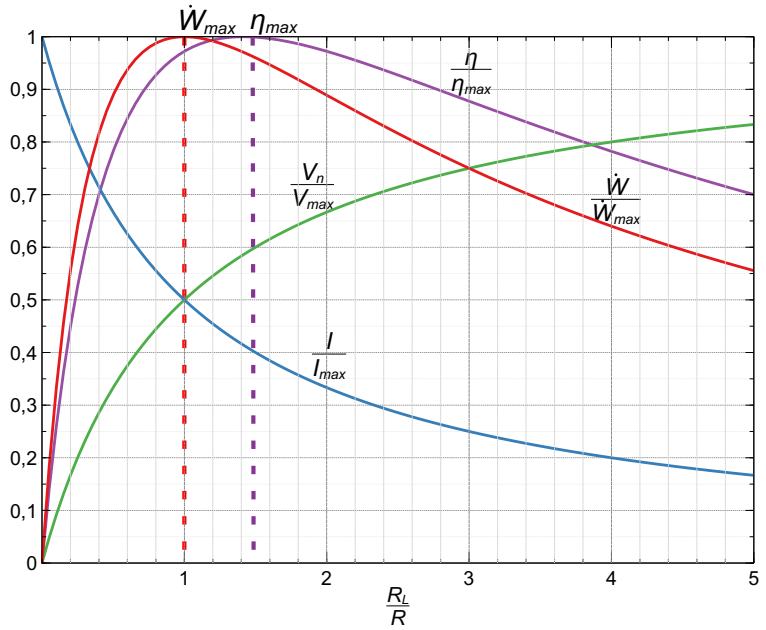

Figure 6.4. Normalized parameters of Power, Efficiency, Voltage and Current as a function of load resistance (R_L) to TEG internal resistance (R) ratio.

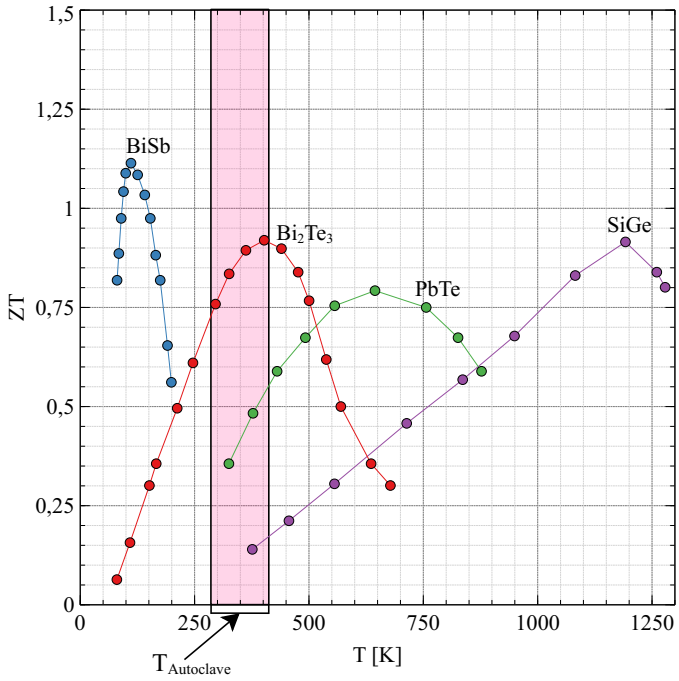

Figure 6.5. Overview of commercialized TEG materials and their ZT values depending on the ambient temperature. The thermal range of steam sterilization in the autoclave is marked in red and depicted as $T_{Autoclave}$. Diagram based on the data from [86], [88], [95]–[98].

Thermoelectric Materials Review

As mentioned earlier, we can conventionally distinguish three generations of thermoelectric materials [72]. Their ZT or figure of merit differs depending on the thermoelectric material, its additives, the technology in which it was made and the temperature. To maximise the performance of a thermoelectric device, the thermoelectric material must be selected in such a way as to achieve the highest possible ZT in the expected operating temperature range.

In addition, when considering the potential implementation of the entire system into production, it is important to focus on as many commercially available materials as possible. Although autoclave temperatures are in the range of 20 °C to 140 °C, which in the context of consumer electronics is the high temperature range, for thermoelectric materials, this range is the low temperature range. An overview of the ZT dependence of the operating temperatures of commercially available thermoelectric materials can be seen in Figure 6.5 and their commercial embodiments in the Table 6.2. As we can see in the figure, the material that achieves maximum performance in the specified temperature range is Bismuth Telluride. It is also the oldest thermoelectric material. Its undoubted advantages include wide product availability: 70% of thermoelectric devices available on the market are based on Bi_2Te_3. Unfortunately, it also has a number of disadvantages.

Bismuth Antimony (BiSb): Bismuth Antimonide (Antimony) is the only material with unique thermoelectric properties in the temperature range below room temperature. It is used mainly in the range of liquid nitrogen (80 K where its ZT reaches 0.4 [75]. The maximal ZT of these types of materials can be achieved by appropriately doping and in the presence of a magnetic field at a temperature of 120 K, where its ZT reaches values over 1.0 [100]–[103]. However, one of its main disadvantages is its poor mechanical stability[75].

Bismuth telluride (Bi_2Te_3): As shown in Figure 6.5, bismuth telluride is the preferred material for the low-temperature domain (between 0 °C and 200 °C). It has the highest figure of merit for p and n-type material

Table 6.2. Comparison of different thermoelectric materials used for thermoelectric generators, with respect to its market availability [99]. **C** – material commercialized, **R** – material in research, **P** – prototypes available, **+** – positive assessment, **-** – negative assessment, **?** – no data or contradictory data

Materials	BiSb	Bi_2Te_3	PbTe	SiGe	$MnSi_{1.73}$	Mg_2-SiSn	$CoSb_3$	Oxides	Half-Heuslers
Market status	C	C	C	C	R	R	P	P	P
Figure of Merit	< 1.2	< 1.0	< 1.0	< 1.0	> 1.0	> 1.0	≥ 1.0	< 1.0	> 1.0
Operational Temperature	80	300	500	900	550	550	520	700	550
Long-term Stability	?	+	+	+	?	?	?	?	+
Mechanical Stability	?	-	+	+	+	+	-	-	+
Thermal Stability	+	?	+	+	+	+	+	+	+
Chemical Stability	+	?	?	?	?	?	?	-	+
Toxicity	+	-	-	+	+	+	?	+	?
Environmental Aspects	+	-	-	+	+	+	-	+	?
Raw Material Availability	?	-	-	-	+	+	?	+	?
Large Scale Manufacture	+	+	+	+	+	+	+	+	+

in this range. It is now the most widely used thermoelectric material. ZT's recognised average value ranges from 0.8 to 1.1.

Lead Telluride (PbTe): Lead telluride is widely used for power generation in mid-temperature range starting from 200 °C and going up to 600 °C. It's ZT in a room temperature is only about 0.1 but in the operating temperature range the peak ZT is about 0.8. Additionally, the addition of suitable admixtures might increase the ZT to more than 1. Unfortunately, assuming the steam sterilisation temperature range, this material does not have sufficient ZT [104], [105].

Silicon-germanium (SiGe): The silicon germanium matherial is a preferred TE material for power generation at elevated temperatures as high as 1200 K. The ZT reaches values from 0.7 to 1.1 at optimal temperature. This type of material has been used in deep space NASA missions; however, its desired operating temperature prevents it from use in the application of steam sterilisation.

6.2.4. Commercial Available Thermoelectric Generators

The industrial nature of this PhD indicates the need for market analysis in terms of suppliers and available technologies. Despite the commercialisation of four thermogenerator technologies, i.e. BiSb, Bi_2Te_3, PbTe and SeGe, the only TEG modules available on a mass scale are those based on bismuth telluride. A total of 69 suppliers of thermoelectric modules have been identified offering different types of technology. Table 6.3 shows the leaders in each technology and the companies that had their product offerings available generally. As can be seen, the technology based on bismuth telluride (Bi_2Te_3) has received the most commercial attention. This is due to its operating temperature range that covers room temperatures and applications operating below 200 °C, and the fact that it can easily be used to cool consumer and speciality electronics. This makes the technology applicable in the wearables segment, the mining industry, heavy industry, and the automotive industry, among others [106]–[109].

Table 6.3. Summary of main TEG manufacturers divided on different technologies

Manufacturer	Materials	Δ T	Power	T_{max}
HiZ, Thermonamic, Lairdtech, Marlow, European Thermodynamics, Ferrotec Nord, Kryotherm, AMS Technologies, CUI, Crystal Ltd, Kelk Ltd, P&N Tech, RMT LTD, Wellen Tech, Thermonamic, Micropelt	Bi_2Te_3	300K	20W	200 °C - 300 °C
TEGNology	Zn_4Sb_3/Mg_2SiSn	105K	9mW	125 °C
TECTEG MFR	Calcium/Manganese oxide	750K	12.3W	800 °C
TECTEG MFR	Calcium/Manganese oxides with Bi_2Te_3	435K	11W	600 °C
Hotblock Onboard	Silicon Based Alloy, SiGe	500K	Multiple variants available	600 °C / 800 °C

6.3. Thermal Energy Harvesting - Applications

Thermoelectric generators have both advantages, such as their reliability and consistency of operation, and disadvantages, such as relatively low energy conversion efficiency. As a result, they find their application in specific conditions [106] such as:

- generating current in extreme environments - heat sources are specially adapted to work with thermo-generators (for example Radioactive-thermo-generators used, among others, in radio beacons located in inaccessible terrain, another example is space exploration),
- generating electricity from waste heat - where the aim is to extract electricity from objects that normally lose heat during their scheduled operation, this increases their energy efficiency,
- decentralised power generation systems,
- microgenerators for IoT sensors, microelectronics, sensors operating in extreme conditions.

Given the context of this dissertation, a more detailed analysis of the medical application of thermogenerators is in order. Most of the applications in the medical industry focus on wearable devices. This is because the human body can be treated as a constant source of heat. Taking into account that the ambient temperature usually differs from the human body temperature, it can be considered that there is a temperature gradient implying the use of just TEG. On average, such a gtadient is 13 °C, while the minimum amount of energy required for wearable devices is usually less than 5 mW. The second domain where TEG is used in medicine is implantable devices like pacemakers and sensors. Their main advantage is that there is no need to change or

recharge batteries, which could involve a number of health risks and hazards for the patient. Medical wearables is also a growing niche, where thermogenerators can be used [109], e.g. to power electrocardiograms [110], heartbeat monitoring devices [111], electroencephalograms [112], monitoring wristbands [113], smart watches [114], pulseoximeters [115]. Due to the growing importance of fog computing (decentralised IT infrastructure in which data, its processing and storage, and applications are distributed in optimal locations between the data source and the cloud) and edge devices (distributed computing devices, where data are processed at the edge of the network, as close as possible to the sources of origin) of IoT in hospital and medical environments [116], wireless sensor networks are also expected to grow in importance, and hence the increasing demand to power such sensor networks with TEGs. One of the main problems of such networks is the need for their unmanned operation. A solution can be low-cost energy harvesting modules [117], as shown by Markiewicz et al. [118] the cost of such a module is about 9 euro, which makes it economically comparable to a battery-based solution. So far, despite the best intentions of the author, it has not been possible to find any publications describing the use of a thermoelectric generator in the context of surgical instruments or energy recovery from hospital logistics. This work and the papers published within it [119], [120] are the first attempts of such solution in the field.

6.4. Energy Harvesting Summary

The chapter outlines the topic of energy harvesting in the context of the surgical instrument environment in a hospital. The applicability of several energy harvesting methods was analysed in the hospital logistics process. The analysis has shown that the only repeatable energy harvesting method is the recovery of energy from temperature during the sterilisation process in an autoclave, and the repeatability of this process, regulated by appropriate standards, guarantees the invariability of the recovered energy. In the following section, the theoretical basis of thermoelectricity and thermogenerators was analysed, which will be used in further chapters of this work for the modelling and optimisation process. Finally, the technologies available on the market were analysed, and an overview of the suppliers of the individual modules was made. As a result, it was decided to choose Bi_2Te_3-based module technologies due to their optimum performance at steam sterilisation temperatures and mass market availability.

7. Initial Requirements

Abstract

In this chapter specific business and hardware requirements are defined and described. Following requirements have been defined:

Business Perspective:

- Low Cost,
- Robustness,
- Of-the-shelf components,
- Maintenance free,
- Universality.

Hardware Perspective:

- Steam Sterilisation Resistant,
- Optimize for the Steam Sterilization Procedure,
- Minimum Power Requirement,
- Size, Shape and Weight Compatibility,
- Safety.

Outcomes of this chapter: Defined business and hardware requirements for the development of energy harvesting modules.

Due to the specific operating environment, the device design had to meet a number of prerequisites. These requirements were divided into business requirements and technological requirements. The business requirements were defined by the industrial partner, Aesculap AG. The technological requirements, on the other hand, are defined by the working environment of the device inside the sterilisation chamber.

7.1. Business Requirements

From a business perspective, the power supply system had to meet a specific set of requirements defined by the company Aesculap AG.

- **Low Cost** - The price of the new digitised version of the medical container should not increase by more than 10% of the value of the current model on sale. For the purposes of the project, the average price

of the medical container with all accessories was assumed to be up to EUR 1,000. Therefore, the price of the energy acquisition module should not exceed EUR 100. After taking into account a margin of 30%, the budget for such a module should be up to 70 EUR, assuming mass production.

- **Robust** - The requirement for robustness comes from the entire product life cycle and the company philosophy to produce reliable and long-lasting products. A single container might be in service for as long as 15 years of work in the harsh environment of sterilisation facilities inside the hospital. Containers and their contents are constantly exposed to vibrations, mechanical impacts, falls, and large fluctuations in temperature and pressure from the sterilisation process. It must also be taken into account that the end user might handle them without due care and usually in a hurry. This makes it necessary to provide a design that is robust and resistant to all these factors. Furthermore, the design of the module itself must be adapted to the processes already present in the company, so that its production does not require deep modifications to the production lines and processes currently in use. The desired material for the enclosure from the perspective of company's production facility would be steel enclosure, and the non-steel parts shall be made from medical grade plastic. However, a detailed analysis of this issue is not the subject of this thesis.

- **Build from the of-the-shelf components** - Another requirement, important from the business point of view, is to build the module from components possibly available on the market, not requiring time-consuming and costly processes of joint R&D, creation of specially modified original equipment manufacturer's (OEM) versions or introduction of new technologies to the market. The main reason for such assumptions is the necessity to keep the low price of the module (after all, it is only an addition to an existing product). The second reason, directly related to the current situation on the market, is the need to ensure the flexibility of deliveries in the situation of complication and extension of logistic chains.

- **Maintenance-free** - The maintenance-free requirement is closely related to the working environment of the entire device, namely the hospital. The staff working there, especially the technical staff, usually work under a strict time regime. A situation in which a digitised medical container would require additional handling by staff is unacceptable from the perspective of potential customers. It would also contradict the whole idea of digitisation and automation. Hence, the electronic module should be as autonomous and maintenance-free as possible and operate in a non-invasive manner on a "switch on and forget" basis.

- **Universal** - The universality of the module is a very desirable feature. It can be seen from two different perspectives: electrical engineering perspective and mechanical perspective. From the electrical engineering perspective, the universal module should be flexible enough to be able to operate with different loads (e.g. different types of sensors adjusted accordingly). From the mechanical perspective, the universality of a module comes down to its shape and size, which must fit into the widest possible range of medical containers offered by the company. Therefore, the aim should be to optimise the size and maximise the extracted electrical energy.

All business requirements can be ranked in order of importance in the pre-production phase and in the production phase. The most critical from a business perspective is the need for maintenance-free operation. From a production process perspective, there is a need to use commercially available components and adapt the materials to the company's production processes.

7.2. Hardware Requirements

The hardware requirements are directly related to the planned working environment of the module and are mainly derived from the business requirements.

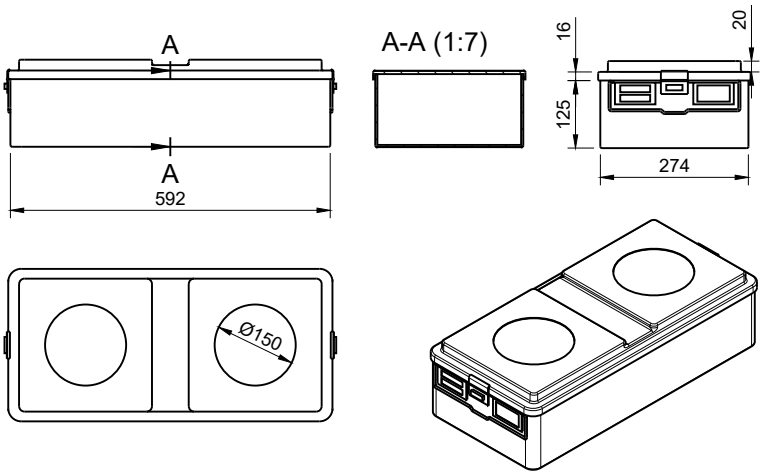

Figure 7.1. Medical container schematics and its dimensions in mm. The container consists of two parts - a bottom part with labels and closing mechanism and a cover with 150 mm diameter filters. Size of the container is the key size limiter for the energy harvesting module.

- **Needs to survive steam sterilisation conditions** - A fundamental requirement for the module with respect to its working environment is the ability to work in a steam sterilisation chamber. The outer casing must withstand the mechanical stresses of increased pressure and be resistant to temperatures as high as 134 °C. Further work assumes the ability to work at temperatures up to 150 °C (12% safety margin) and at pressures up to 4 bar.

- **Needs to be optimised for the steam sterilisation temperature curve** - The energy harvesting module must be adapted appropriately to the operating environment. Especially in the case of steam sterilisation processes, the design of the module must force the appropriate heat flow to maximise the amount of electrical energy obtained and, consequently, to harvest enough energy to power the sensor module.

- **Minimum power requirement** In order to power the sensor module, the energy harvesting module must produce power sufficient for sensor node in 95 % of the plateau phase of the steam sterilisation procedure. This requirement is directly derived from the business requirement "maintenance-free". The sufficiently wide safety margin in power generation should be taken into account due to the need for high reliability. Measurement of the power requirement of the sensor module was performed on the benchmark software and benchmark operating architecture. The whole procedure will be described in Section 8.3 of this thesis.

- **Size and shape** Similar to the business requirement, the requirements for the shape and dimensions of the module are directly related to its usability for hospital staff and its working environment, the interior of the medical container. The module must fit into the surgical container and at the same time take up as little space as possible to minimise interference with the arrangement of the surgical instruments placed inside the container. An outline diagram of a standard surgical container with the marked potential arrangement of the module is shown in Figure 7.1.

- **Minimized weight** The weight requirements are directly related to hospital logistic processes. Taking into account the fact that medical containers are moved using human muscle power, the aim is to minimise their weight. For this reason, the energy harvesting module should weigh as little as possible to not contradict this trend and not significantly affect the weight of the entire toolkit enclosed in the container.
- **Safety** Safety is the key design requirement for the described module. By safety we mean chemical and mechanical stability of construction materials stability. The selection of materials must also take into account the so-called active mode scenario, i.e. a situation in which an unexpected event occurs that could lead to sudden damage to the module. The scenarios considered should include prolonged sterilisation (200% of the length of a standard sterilisation process), leakage of the module housing, higher than expected temperature (10% safety margin), and mechanical damage.

8. System Prototype

Abstract

In this chapter, the creation of the system prototype is described. First, a concept of the prototype has been established. The research plan has then been created, serving as a road map for the further development of the project. The next step was to formulate initial power requirements, as they will determine the key design constraints. For this, market research has been conducted to evaluate possible sensors and its capabilities in relation to the needs from the described business requirements. After performing a market research a sensor system serving as a benchmark has been selected. The selected sensor was then evaluated in terms of power consumption. The detailed procedure of power consumption measurements, hardware setup and software setup has been described. Several measurements were carried out in different sensor modes and, based on this, the minimum requirements for the power generated by the prototype were determined.

Outcomes of this chapter: The results of this chapter are related to the concept of the system and the physical model of the device. A concept of an energy harvesting device for the steam sterilisation procedure has been developed. Then the measurement procedures and the research plan have been established. Initial requirements based on the selection of the sensor electronics and its evaluation have been performed. Finally, a TEG selection procedure has been described, and the physical model assembly has been described. In summary, a TEG **TMG-127-0.4-1.6** has been selected for further investigation. The initial power requirements have been set as 1.674 mW for the active mode scenario and 0.353 mW for the passive mode scenario during the plateau phase of the sterilisation procedure.

8.1. Prototype Concept

The main technical challenge during the conceptual phase of the prototype development was to ensure an adequate temperature gradient throughout the TEG module. This is a complicated task, as the sterilised module is subjected to a specific temperature, which is the same at every point on the surface of the module. Each autoclave is built in a way that forces a uniform temperature distribution inside its sterilisation chamber. For this reason, it is not possible to use potential changes in the temperature distribution in geometrical space to create a gradient; however, there are temperature changes in time which can be used.

The solution investigated in this dissertation is to produce such a temperature gradient inside the energy harvesting module itself. The overall concept is based on the embedded thermal mass which is thermally insulated. For this purpose, certain conditions had to be met, namely:

1. The walls of the prototype should be constructed from a material that conducts heat well,
2. The thermal mass inside the prototype, isolated from its outer walls, should have as large a thermal capacity as possible,
3. The insulation between the thermal mass and the walls of the prototype should have the lowest possible thermal conductivity (comparable to air),

4. The connection between the outer walls of the prototype and the thermal mass should be provided by the TEG module, so that the only heat transfer route to and from the thermal mass is the one through the thermogenerator.

The concept and operation of the prototype is presented in Figure 8.1 and is based on the heat flow in two phases. In the first phase, shown in Figure 8.1a, when the prototype is sterilised by overheated steam, the heat flows from the autoclave sterilisation chamber to the insulated thermal mass located inside the module. During the process of heat flow through the TEG, electrical power is generated and used to power the sensors. After the sterilisation process, the container and the module inside it are removed from the autoclave. In this phase, the insulated thermal mass inside the module has a higher temperature than the surroundings of the module, and the heat flows the other way through the TEG, which generates electrical power, but with inverse polarisation than in the first phase. The energy generated in the first phase can be used directly to power the sensors, and the energy generated in phase two can be stored in an insulated high temperature energy storage system (e.g. a high temperature lithium-ion capacitor) and used in the start-up phase of the sensors and electronics before measuring the next sterilisation cycle in the autoclave.

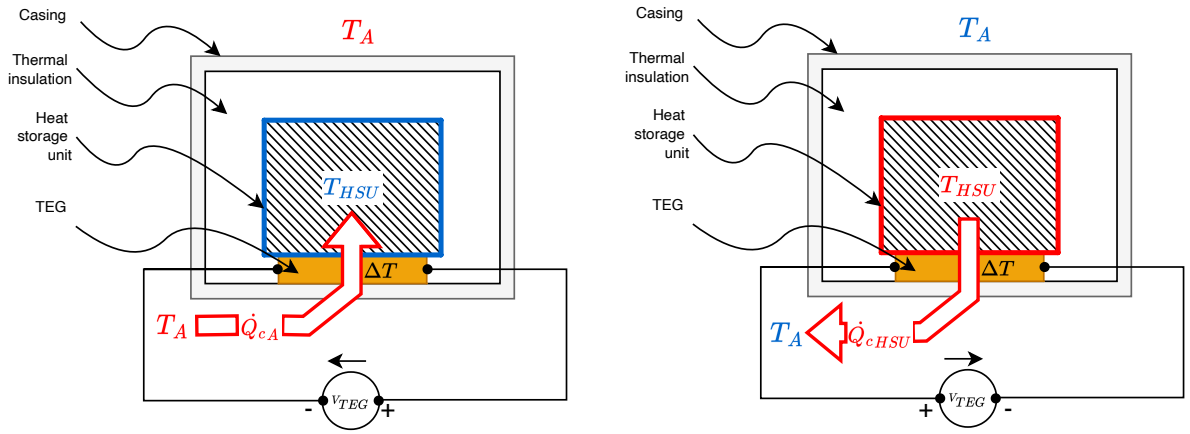

(a) Heat transfer and TEG operation during the steam sterilisation.

(b) Heat transfer and TEG operation after the steam sterilisation.

Figure 8.1. Concept of the energy harvesting module prototype working in the autoclave environment during the steam sterilisation **(a)** and after the steam sterilisation **(b)**. During the steam sterilisation module is place inside the autoclave. The temperature T_A is higher than the temperature of the heat storage unit T_{HSU}. Heat flow by conduction ($\dot{Q}_{cA}$) is from outside of the module, through the TEG to the HSU, inducing the voltage V_{TEG}. After the sterilisation **(b)**, when putting outside of the autoclave, the heat transfer is in the opposite way - from HSU towards outside of the module as T_{HSU} is higher than T_A.

8.2. Research Concept

Usually, the way from the first energy harvesting module concept to any proof-of-concept is long and leads through a series of studies and experiments. It is not different in this case. Based on the concept described in Section 8.1, a number of tests, simulations, and optimisations have to be carried out to find out whether the concept itself works and whether it has practical applications. In order to structure the further steps, the research plan shown below was constructed, consisting of a number of tests - both physical and virtual simulations.

1. **Establish power requirements of the sensor electronics** - the first step is to formulate the power generation requirement to be able to choose an appropriate TEG module and evaluate it.
2. **Development of an initial physical model of the prototype** - the next step is to build a physical prototype with selected TEG module and initial design assumptions to evaluate the concept of the prototype. This step will allow the prototype to be tested inside the thermal chamber and perform thermal distribution measurements inside the physical model.
3. **Development of its virtual equivalent using CAE tools** - Using computer-aided engineering (CAE) tools such as computer-aided design (CAD) and finite element analysis (FEA) is necesary to perform a further virtual simulations. A CAD digital twin of the physical device needs to be created and adjusted for the FEA software requirements.
4. **Identification of physical prototype parameters and build a simulation model** - Performing CAE simulations of the thermal unit step will allow to adjust the virtual model parametrisation based on physical model measurements.
5. **Development of a SPICE model of the TEG** - Based on the initial requirements, a TEG device needs to be selected, and its virtual model needs to be created for the purposes of the subsequent simulations of the steam sterilisation process.
6. **Model testing of the prototype and simulation on the virtual model and comparison of the obtained results** - the virtual models of the prototype as well as a SPICE model of the TEG needs to be evaluated by the comparison with the physical measurements in the heat chamber and TEG test bench.
7. **Simulation of steam sterilisation process in an autoclave** - After performing the model parametrization and developing a SPICE model of the TEG a simulated steam sterilization process could be performed to evaluate possible energy harvesting of the prototype.
8. **Optimization of the prototype dimensions on the basis of simulation data** - after performing the simulations of the initial prototype it is possible to perform size optimizations assuming the initial requirements for the prototype from the power generation perspective.

The whole research plan with highlights of each step and the data flow is presented in the figure 8.2

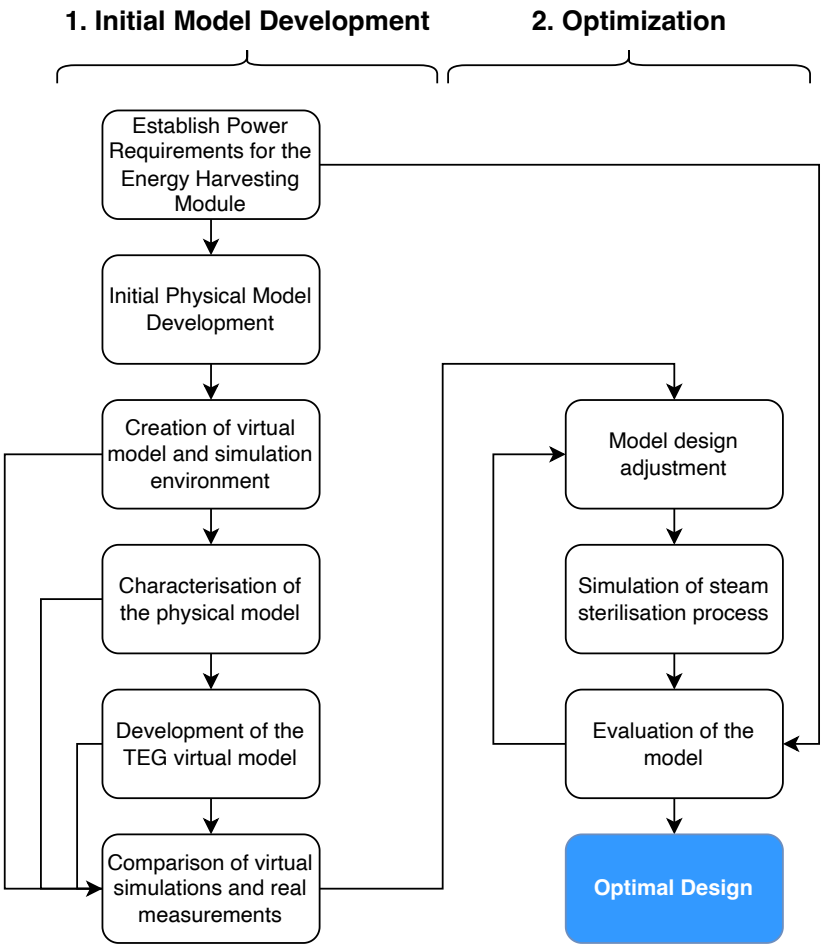

Figure 8.2. Research plan of the initial physical model preparation, creation of it's digital version and optimisation of the digital model.

.

8.3. Sensor Electronics Concept and Power Requirements

The problem of supplying power to the electronics inside the autoclave during steam autoclaving should be tackled from two angles. On the one hand, the aim should be the optimisation of the energy yield of the energy harvesting system with the assumed initial requirements for the module as a whole (i.e. dimensions, materials, etc.). - described in chapter 7). The problem is, however, the optimisation of the power consumption of the sensor module itself. Therefore, it was necessary to determine the power requirements as a prerequisite for the entire prototype prior to the research work. In other words, what is the minimum power the TEG energy harvesting module should generate to power the sensor module? In order to proceed with this task, it was necessary to consider the selection of a suitable sensor device (hardware) and then to optimise its power consumption and develop an algorithm for the lowest possible energy demand on the measurement side. Due to the specific nature of the application, a number of constraints were defined, as shown in the table below 8.1. One of the most important requirements is flexible power management, a prerequisite for a low-power application. The second requirement is an integrated radio frequency (RF) field energy recovery system, which is directly related to the passive and active mode requirement. In active mode, the device could collect data and perform calculations, and in passive mode it would be inactive, collecting data using an interrupt

routine until the RF field from the NFC/RFID (Near Field Communication/Radio Frequency Identification) reader is present. A wide supply voltage range was also identified as a necessary requirement so that the device could be installed in a variety of business applications.

Table 8.1. Initial requirements for sensor selection to evaluate possible energy consumption.

Initial Requirements				
Domain	No.	Requirement	Background	Importance
Power	1.1	Flexible power management, ultra low power modes	The device shall preserve any power to minimize the energy consumption to absolute minimum, to increase the robustness and to ease the requirements for energy harvesting	Very High
Power	1.2	Integrated Energy Harvesting	Energy harvesting circuit is needed for the passive operation data readout	Very High
Power	1.3	Wide operating voltage range	The device shall be prepared for powering both from battery, the energy harvesting solution and RF energy harvesting to maximize it's use cases	Very High
Power	1.4	Passive and Active mode operation	Device shall be able to work both in active mode (powered from energy harvesting module) and passive - powered from RFID antenna	Very High
Communication	2.1	Low Power Peripherals	It should be possible to easy extend the functionalities by adding a low power peripherals	High
Features	3.1	Bus	The device shall have a communication interface which is a well established standard, in best case allowing the power measurements and optimizations by JTAG programmer	Moderate
Features	3.2	Low Power ADC Integrated	Integrated ADC preserves the power and eases the overall module design	High
Features	3.3	Integrated thermistor or temperature sensor	Integrated thermistor preserves the power and eases the overall module design	High
Economic	4.1	Low Price	Part of business requirement of the whole business case - the device will be sold as an additional feature to the existing product, it cannot be expensive	Very High
Economic	4.2	Market position	Device shall be an well-established brand with mature development tools and support	Moderate

In order to select a suitable device model, market research was conducted on available low-power NFC/RFID integrated circuits (ICs). The research identified three major chip manufacturers producing so-called "smart" NFC tags, which are listed in Table 8.2. Taking into account the criteria described in Table 8.1, it was decided to select the RF430FRL153H device for further analysis as it met all the criteria.

RF430FRL152H is a chip that integrates three modules - a microcontroller module based on the MSP430 architecture, a NFC communication module and the FRAM memory module. The device block diagram is

shown in Figure 8.3. The key components from a power consumption perspective are highlighted in red. The modules used for active and passive power and data transfer are highlighted in yellow.

Table 8.2. Market Research Towards Off-The-Shelf Smart NFC Tags.

Market Research - NFC Smart Tags Off-The-Shelf Solutions			
Manufacturer	ST Micro Electronics	NXP	Texas Instruments
Model	ST25DV	NXP NT3H1101	RF430FRL152H
Operating Voltage [V]	1.8 - 5.5	1.72 - 3.6	1.5 - 3.0
MCU integrated	No	Yes	Yes
MCU Power Consumption	-	low	very low
Energy Harvesting	No	Yes	Yes
Power Management	Yes (good)	Yes (Very Good)	Yes (Very Good)
Passive and Active	No	Yes	Yes
Low Power Peripherals	Yes	Yes	Yes
Bus	I2C	I2C	I2C/SPI
ADC	No	No	Yes
Thermistor	No	Yes	Yes
Price [USD]	1.56	1.73	1.42
Market Position	Very good	Very good	Very good

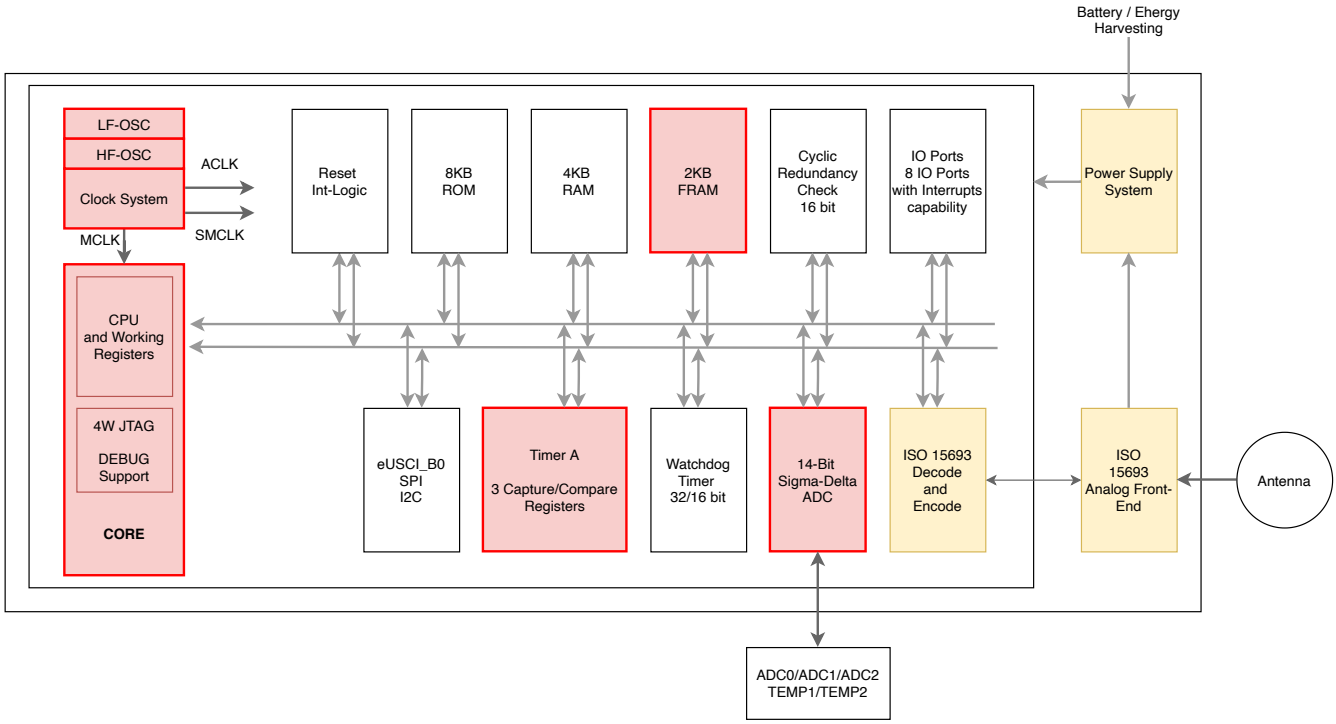

Figure 8.3. Functional Diagram of RF43FRL152H smart NFC Chip.

The RF430FRL152H is equipped with a number of key components for low-power applications [121]–[123]. First, it has a compact clock system module which includes an embedded 256-kHz low-frequency oscillator (LFOSC) and an embedded high-frequency oscillator (4 MHz, HFOSC) on board. The CCS module provides the following clock signals:

1. **Auxiliary Clock** - ACLK - sourced from the 256-kHz internal LFOSC,

2. **Main Clock** - MCLK - the system clock used by the CPU, sourced by the same sources as ACLK clock,

3. **Sub-Main Clock** - SMCLK - Used by peripherals, sourced by the same sources as ACLK clock.

The CCS clock system can be configured to save power; it is optimal to select the clock frequency to meet the minimum timing requirements of the application. Another element of the RF430 chip architecture used to optimise power consumption is the 14-bit analogue-digital converter (ADC) and Timer A. The ADC is responsible for converting the analogue signal from the sensors into digital signal. The SD14 (Sigma-Delta, 14 bit) ADC module consists of an on-chip temperature sensor, a resistive bias interface (for thermistor-based measurements), a programmable gain amplifier, and a sigma-delta analogueue-to-digital converter. The ADC can handle up to 8 inputs and is optimised for low power consumption. Third design feature for low-power applications is a Ferroelectric Random Access Memory (FRAM) which guarantees the data safety even when the entire chip has no power source. From the point of view of low-power applications, the low voltage, of only 1.5V, required for the read or write procedure in FRAM is crucial (in comparison, EEPROM requires 10-14V), and the procedure itself is very fast, taking only 1.5 µs. The FRAM controller can also be unplugged when not in use, additionally saving power. All of the possible setup configurations might be difficult to handle from a programmers perspective, thus the RF430 firmware offers several, Low Power Modes (LPMs) which sets the chip hardware components in one of several operating states according to the low power mode needed by the application. LPMs, as they are recommended way of handling the low power chip capabilities by the manufacturer, has been used also in the testing procedure for evaluation of minimal power requirement of the chip in the context of steam sterilisation surveillance. The power consumption of each of the RF430 chip modules is listed in Table 8.3. The same table also summarises the current consumption declared by the manufacturer in each of the LPMs. Each LPM affects the clock system differently due to power preservation. All LPMs and their capabilities related to the clock system are listed in Table 8.4. It is worth mentioning that the chip CPU is off in all of the LPMs, so every single operation needs to be based on the Interrupt Service Routines of the chip.

Table 8.3. RF430 power consumption in different low power modes, according to the technical specification of the module.

Active Mode Supply Current Into VDDB Excluding External Current							
Parameter	Execution Memory	VDDB	Frequency (fMCLK = fSMCLK)				Unit
			1 MHz		2 MHz		
			typical	max	typical	max	
$I_{AM\ (FRAM)}$	FRAM	1.5 V	330	420	480	580	µA
$I_{AM\ (RAM)}$	RAM	1.5 V	220	300	250	320	µA
$I_{AM\ (ROM)}$	ROM	1.5 V	220	300	230	300	µA
Low-Power Mode Supply Current Excluding External Current							
Parameter	VDDB	Temperature					Unit
		20 °C		45 °C		70 °C	
		typical	max	typical	max	typical	max	
I_{LPM0}	1.5 V	190	-	190	-	260	340	µA
I_{LPM3}	1.5 V	13	-	13	-	25	65	µA
I_{LPM4}	1.5 V	11	-	12	-	24	60	µA

Table 8.4. Summary of available low power modes (LPMs) and their consequences on selected clocks and CPU modules

Mode	**CPU**	**MCLK**	**SMCLK**	**ACLK**	**HFOSC**	**LFOSC**
Active	On	On	On	On	On	On
LPM0	Off	Off	On	On	On	On
LPM3	Off	Off	Off	On	On	On
LPM4	Off	Off	Off	Off	Off	On

Based on the architecture shown in Figure 8.3 and the "low power" mode data, a benchmark program was written to determine the initial power requirements for the RF430FRL152H chip.

8.3.1. Power Benchmark

After selection of the desired hardware sensor platform, it was necessary to determine the power requirements of the sensors that will then be used as the power generation requirement for the energy harvesting prototype. To determine a minimal power consumption with functional requirements, an energy benchmarking procedure had to be performed. This procedure consisted of a series of steps presented in Figure 8.4 which are as follows:

1. Hardware selection and setup for power measurements - The hardware selection was performed as the first step, the aim was to pre-select the hardware optimized for low power sensor applications. To accomplish this, literature research has been performed using the SCOPUS search engine, then a patent research has been made using the Google Patents search engine. The aim of such a selection was to get reliable data on possible sensor hardware platforms, which has already been proofed as useful in the context of research applications or low power sensor inventions. In this stage, pre-selected hardware from main manufacturers has been summarised, and the RF430 chip has been chosen for further analysis.

2. Development of the benchmarking program - Using the selected technology and chip a benchmarking program had to be written to evaluate the simulated use case and available low power modes of the chip itself. It was important to test the practical limitations of each of the power modes of the RF430 chip, as well as their usefulness for the possible sensor applications. Here, the connection capabilities of the RF430 chip have been evaluated as well.

3. Hardware/Software power measurements - After development of benchmark software, a power consumption of the chip with running program had to be made. For this procedure, a RF430FRL152HEVM development board was chosen. However, using the development board might affect the power consumption measurements of the RF430 chip. To compensate for the parasitic power consumption of the development board, a two-stage measurement procedure had to be developed.

   (a) Initial measurement of overall power consumption in the IDLE state of the RF430FRL152HEVM development board using TI MSP-FET programmer

   (b) Precise measurement of the power consumption of RF430FRL152H chip on the development board using the laboratory multimeter.

4. Power consumption measurements of each of LPMs using the MSP-FET programmer and compensate its measurements with the measurements acquired by the laboratory multimeter.

5. Setting up the power generation requirements.

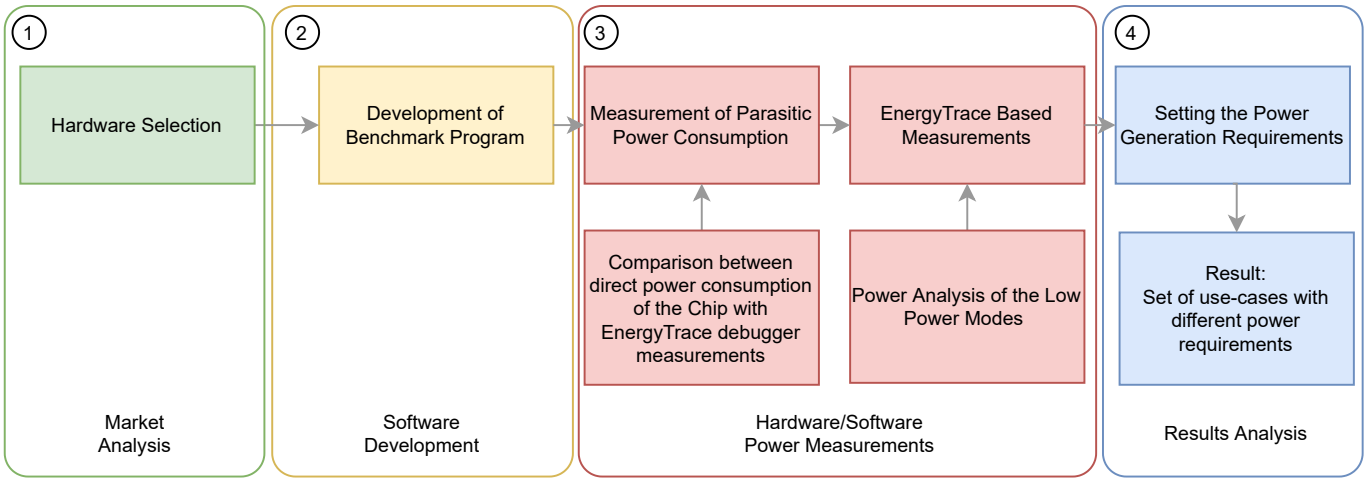

Figure 8.4. Overview of the benchmarking procedure.

By performing such a procedure, initial energy requirements will be created, and both passive mode scenario and active mode scenario can be developed. The passive mode scenario will be characterised by operating the electronics in the lowest power consumption mode for 100 % of the time, while the active mode scenario will assume that the device is operating in the active mode (no power-saving modes) for 100 % of the device's operating time. In both of these modes, it is assumed that the device will use its timer circuit and its ADC module.

Hardware Selection and Setup for Power Measurements

To perform tests on the RF430FRL152H chip, the RF430FRL152HEVM evaluation kit has been used. It is shown with a description of the main parts in Figure 8.5. This kit consists of the RF430FRL152H chip and associated circuitry such as voltage regulation circuits, photoresistor, battery holder, thermistors, and leads to connect other modules.

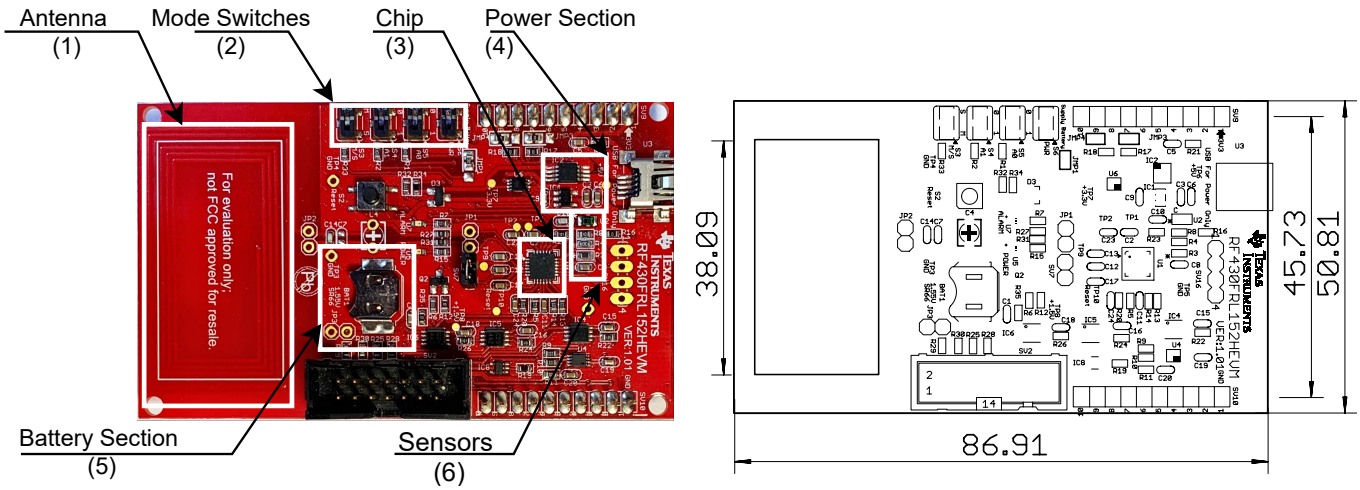

Figure 8.5. Photo of the RF430FRL152HEVM evaluation board (on the left) with described the main blocks on the PCB, as well as its design drawing (on the right).

The most important modules are described on the figure 8.5 and are as follows: Antenna (1), Mode Switches (2), Chip (3), Power Section (4), Battery Section (5), Sensors (6). All the modules are described

below:

1. **Antenna** - Integrated Antenna might be used both for data transmission and energy harvesting. The energy needed for transmission of the data stored in the FRAM is harvested from the RF field before the readout procedure, so it assures the data integrity. From the energy harvesting point of view such a solution is optimal, as data storage and readout does not need external power supply.

2. **Mode Switches** - The S3 - S6 mode switches handles multiple functions, such as putting the device into Master or Slave mode in the I2C communication. However, switch S6 is also responsible for power source selection, power might be taken from either the battery or programmer or USB port. The power mode selected here can affect the measurements results, as only the battery has a direct connection to the chip, and is not affected by parasite ICs.

3. **Chip** - The RF430FRL152H chip is placed on the board with all of its necesary components. As the chip operates on 1.5 V logic it was needed to provide also the voltage level translators, so the MSP-FET programmer working on 3.3 V logic can be used. In case of programming the bare chip, without the development board, it is needed to have voltage level translators designed in similar way.

4. **Power Section** - As the chip operates on 1.5 V logic the voltage both from USB port and from the MSP-FET programmer needs to be adjusted accordingly. This is done by two integrated circuits by Texas Instruments: TPS773 and TPS72215. Unfortunately, these ICs have their quiescent currents and power, which needs to be taken under consideration.

5. **Battery Section** - The board is equipped with the battery holder for SR66 type coin battery. Additionally it is possible to simulate the battery as there is a place for attaching the wires to mock the battery with laboratory power source (jumper JP3).

6. **Sensors** - On the board there are two thermistors and one phototransistor to measure the temperature and the light conditions, all of the sensors are connected to the ADC pins in RF430FRL152H chip. From the power measurements perspective it is worth to note, that these sensors are powered from the USB or MSP-FET device, so they might affect the power measurements, however in the benchmark application they are in use, so in this scenario their presence and power consumption is needed.

Power consumption measurements of selected low-power modes

Power consumption of the RF430 chips is directly affected by the programme running on it and by the settings of its internal modules. Thus, it was needed first to develop a benchmark programme to test each of the possible LPMs, and secondly to initialise the whole device appropriately. Before the whole procedure, the RF430FRL152HEVM board had to be prepared to mimic the behaviour of the real sensor node. This procedure is described in detail in Appendix E. Listing 8.1 shows the LPM testing programme. It remains inside the `void main()` function. First, a watchdog timer is turned off, as it would affect the measurements. Then, the ROM variable DS is initialised; this is the default step from the manufacturer's software guide. Then two assembly directives are called (also default, recommended by the manufacturer), and the device configuration is performed in functions `initISO15693(CLEAR_BLOCK_LOCKS)` and `DeviceInit()`. The main programme loop consists of only one directive `__bis_SR_register(LPM3_bits + GIE)` that enters the specified LPM, in this particular case - LPM3.

```
1 void main()
2 {
3   WDTCTL = WDTPW + WDTHOLD;       // Stop watchdog
4
```

```
    // ROM RF13M module setup ** The following three lines are needed for proper RF stack
    operation
    DS = 1;              // ROM variable needs to be initialized here
    asm ( " CALL #0x5CDA ");     // Call ROM function (Initialize function pointers)
    asm ( " CALL #0x5CAC ");     // Call ROM function ( Check part configuration)

  initISO15693(CLEAR_BLOCK_LOCKS);
  DeviceInit();

  while(1){
      __bis_SR_register(LPM3_bits + GIE); // Measured LPM Mode
  }
}
```

Listing 8.1. Benchmark code for power measurement in given low power modes.

The power consumption can also be affected by the proper setting of the chip's peripherals, hence it was necessary to use the `DeviceInit()` function, shown in the listing below, to ensure that the clock parameters do not change. In first two lines, we keep the JTAG interface off, to spare the power. JTAG interface is needed when debugging is ongoing and setting breakpoints in the programme flow is needed. This is, however, not such a case, so JTAG can be deactivated after programme starts. In next two lines the direction of PIN1 is set according to manufacturer's datasheet. Next, the configuration of the device clocks is performed, after unlocking the Compact Clock System (clock system module of RF430 chip) configuration. The intended application will be a sensor that operates in the environment of steam sterilisation and takes very low-frequency measurements. Thus, it is needed to lower the clocks frequency as much as possible and deactivate all not needed clocks. All of these operations are performed on the lines from 11 until 22 of the listing 8.2.

```
void DeviceInit(void)
{
    P1SEL0 = 0x00; // Keep primary function of the PIN, disable JTAG interface
    P1SEL1 = 0x00; // Keep primary function of the PIN, disable JTAG interface

    P1DIR &= ~0xEF;
    P1REN = 0;

    CCSCTL0 = CCSKEY;        // Unlock CCS

    CCSCTL1 = 1;             // half the clock speed

    CCSCTL4 = SELA_1 +       // ACLK Source - Low Frequency Clock
              SELM_0 +       // MCLK Source - High Frequency Clock HFCLK
              SELS_0;        // SMCLK Source - High Frequency Clock HFCLK

    CCSCTL5 = DIVA_5 +       // ACLK Source Divider set to divide by 32
              DIVM_1 +       // MCLK Source Divider set to divide by 2
              DIVS_3;        // SMCLK Source Divider set to divide by 4

    CCSCTL6 = XTOFF;         // Turns of the crystal if it is not being used
    CCSCTL8 = ACLKREQEN + MCLKREQEN + SMCLKREQEN; //disable clocks if they are not being used

  return;
}
```

Listing 8.2. Benchmark code for power measurement in given low power modes.

Power consumption measurement consisted of the two stages - current measurement of the RF430 chip itself using laboratory multimeter (Agilent 34410A), and using the MSP-FET programmer with EnergyTrace power consumption technology enabled. The difference is that MSP-FET measurements also have a bias power consumption and might be not accurate without compensation of this bias, however, it is very convenient to use this technology while working with software development. On the contrary, the measurement procedure with laboratory multimeter and appropriate hardware configuration provides very accurate results; however, it is very problematic during the software development process. Thus, it was necessary to compare these two methods and estimate average bias existing in EnergyTrace based measurements. In order to determine the power consumption of the processor chip itself, powering only the chip itself with the disconnected MSP-FET programmer was used. For each of the LPMs, the same test procedure has been applied. First, the benchmark programme has been compiled and uploaded to the chip using the TI MSP-FET programmer. In the next step, the power measurement has to be performed using a simulated battery power source. To do this, the MSP-FET programmer has been disconnected. The development board has been switched to battery power mode. The battery holder on the board has been attached to the laboratory power supply to simulate the 1.5 V coin cell battery. Then, between the development board and the laboratory power source, the Agilent multimeter has been attached, measuring the current flow to the RF430 chip. After performing the measurements with the multimeter, the battery supply has been disconnected, the development board has been switched back to the powering from MSP-FET programmer, and the measurements using MSP-FET EnergyTrace technology has been performed to compare it with the measurements using a multimeter and to estimate the power consumption bias of the EnergyTrace measurements. After the measurements were completed, the programmer was connected, and the benchmark programme was modified to investigate another of the modes of operation. The measurement results are shown in Table 8.5. As it can be seen, there are very significant differences in the measurements performed with EnergyTrace and direct measurements using a multimeter. This difference comes from the way EnergyTrace works. This technology evaluates the pulse width of a DC-DC converter inside the FET, which generates the power supply of the target board. This measurement represents the total current consumption of all circuitry on the RF430FRL152HEVM (including level shifters, etc.). There is also no possibility to change the target voltage to 1.5 V to have a measurement setup comparable to direct measurements using multimeter. This is caused due to the fact that EnergyTrace is integrated with the MSP-FET programmer which adapts to the development board, which operates at 3.3 V and then the level shifters converts it to 1.5 V to power the chip itself.

Table 8.5. Power consumption measurements results of the chip operation modes of RF430FRL152H.

	Multimeter measurements			**Energy Trace Measurements**		
Mode	Voltage	Current	Power	Voltage	Current	Power
LPM4	1.5 V	12.90 µA	19.35 µW	3.29 V	125 µA	0.41 mW
LPM3	1.5 V	13.70 µA	20.55 µW	3.28 V	120 µA	0.40 mW
LPM0	1.5 V	136.00 µA	204.00 µW	3.28 V	240 µA	0.79 mW

However it is not enough to measure the chip operation modes power consumption itself, as it is shown in the Table 8.5 as each active peripheral of the chip increases the overal power requirements. That's why it was essential to select the possible active peripherals and measure their power consumption as well. For this an 14 bit sigma-delta ADC has been chosen as it can be used for temperature measurement inside the sterile container.

8.3.2. ADC SD14 Power Consumption Measurements

When measuring the power consumption of the SD14 ADC, the dynamic phenomena accompanying the SD14 module's switching on and off also had to be taken into account. For this purpose, the CurrentRanger precision current adapter for oscilloscopes from LowPowerLabs was used. In general the current adapter device converts the current to the voltage based on the very precise shunt resistors folowed by set set of bandpass amplifiers [124]. The device's architecture is based on two MAX4239 ultra-low offset auto-zero 6 MHz bandpass amplifiers configured in non-inverting 10x gain each, using high precision resistors. The device allows operation in 3 measurement ranges (nA, µA, mA), which are selected by adjusting the precision shunts at the input of the amplifiers accordingly. In such a way, the current measurements could be performed using an oscilloscope which allowed to observe dynamic changes in current flow. CurrentRanger parameters are presented in the Table 8.6.

Table 8.6. Selected parameters of the LowPowerLabs CurrentRanger current meter [125].

Range	Current range	Burden Voltage	Accuracy	Bandwidth
nA	0 to 3300	10 µV/nA	± 0.05 %	300 kHz (-3dB)
µA	0 to 3300	10 µV/nA	± 0.05 %	300 kHz (-3dB)
mA	0 to 3300	17 µV/nA	± 0.1 %	300 kHz (-3dB)

The schematic of the measurement setup is presented in Figure 8.6. The voltage measurement was performed using the Siglent SDS1104X-E oscilloscope. The DC laboratory power source Siglent SPD3303X-Eis set up according to the RF430FRL152H voltage requirements (1.5 V). The CurrentRanger device has been connected in series between the power source and the device under test (DUT). The oscilloscope Siglent 1104X-Ewas connected to the CurrentRanger device and set up to DC voltage mode. RF430FRL152H device has run a testbench program. Testbench program has been designed from two stages. In first stage the device stayed in pre-selected low power mode (LPM0 or LPM3), then periodically the device entered the ADC readout stage and after this procedure has been finished it went back to the low power mode. The overall time plot of the benchmark programmeme can be seen in Figure 8.7.

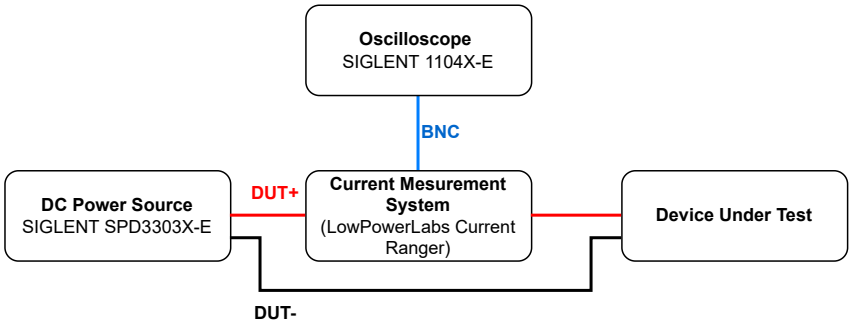

Figure 8.6. Schematic diagram of current measurement system composed from DC power source (Siglent SPD3303X-E), current measurement system (LowPowerLabs CurrentRanger) and digital oscilloscope (Siglent 1104X-E). RF430FRL152H chip served as DUT.

.

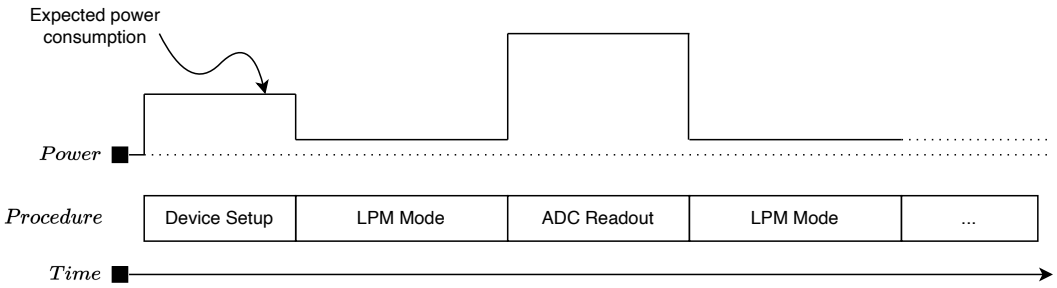

Figure 8.7. Diagram of the power consumption benchmark program running on the RF430FRL152H with the expected power consumption of each of the procedures in the program.

The measured current is presented in Figure 8.8 As it can be seen, the procedure of ADC readout takes 2 s and consumes on average 35 µA of the total current. However, it is worth to mention that during the ADC readout the consumed current equals the sum of the current consumed by the MCU (I_{MCU}) and by the ADC itself (I_{ADC}) as depicted in Figure 8.8.

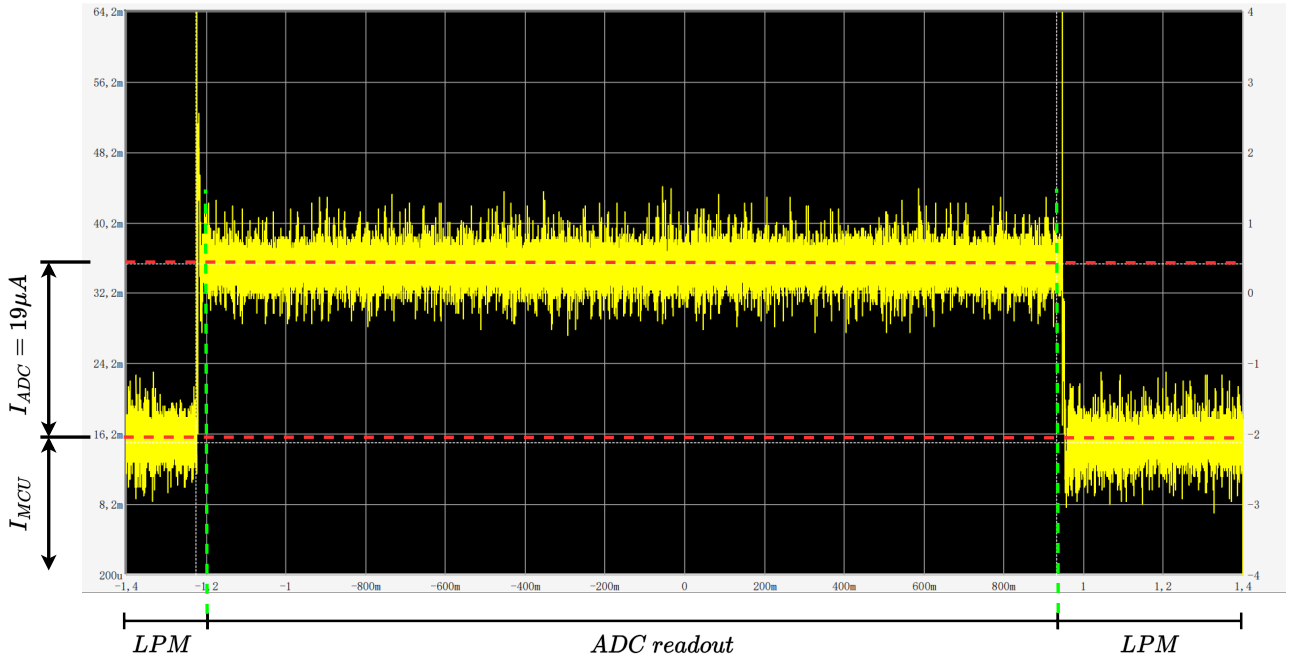

Figure 8.8. Measurement of the current flow while performing ADC data acquisition by RF430FRL152H chip, where 1 mV corresponds to 1 µA of current.

8.3.3. Power Consumption Measurements of Exemplary Low Power Sensing Program

Measurements described in Section 8.3.1 and summarised in Table 8.5 allow us to set the power generation requirements for the prototype of the energy harvesting module. For defining the minimal power needed for sensor modules, it was assumed that the software run on the RF430 chip will use only LPM0 or LPM3 modes, which allows the minimal capabilities for performing the measurement procedure with custom algorithm. According to the business requirements of Chapter 7.1, a safety margin should be taken into consideration. The estimated power consumption, assuming that the device will work in LPM0 mode is 204 µW, in addition the power of 28.5 µW consumed by the ADC must be added, resulting in 232.5 µW of power consumed by

the sensor device. However, it was assumed that the sensor will not be connected directly to the TEG as some of the power conditioning electronics need to be added in between. Currently, the efficiency of DC-DC boost converters ranges from a couple of percents to values as high as 80 % depending on the use case. Here a active mode scenario has been assumed, that the boost converter efficiency will be as low as 25 % giving an anticipated power requirement of 1.395 mW. However, including the safety margin level, it was increased by 20 % to 1.674 mW. Such a level of safety margin as well as initial requirements increases the power safety of the whole system from one side, and provides a wide area for further optimisations on the other side in case such optimisations would be needed. It also assures that change in hardware to different manufacturer, but from the same power-efficiency class, will not cause the need for a re-work of the entire energy harvesting module prototype. It is worth to mention that it is considered as an active mode scenario. In the passive mode scenario the device will work in a LPM3 mode. For LPM3 mode the overall power consumption drops to 49.05 µW and assuming boost converter efficiency of 25 % and 20 % of safety margin results in 353.4 µW (≈0.353 mW). Summary of power consumption calculations is presented in Table 8.7. For **LPM0** mode, the calculation of power requirements has been calculated according to the equation 8.1

$$P_{LPM0} = (P_{MCU_{LPM0}} + P_{ADC}) \cdot \xi \cdot \chi \tag{8.1}$$

where ξ is a compensation factor for the boost converter efficiency equal to 4.0, χ is the power generation safety margin of 20 % while P_{MCU} and P_{ADC} is the power consumed by MCU and ADC, respectively.

The power requirements for the second scenario - **LPM3** scenario - have been established based on the equation 8.2 presented below.

$$P_{LPM3} = (P_{MCU_{LPM3}} + P_{ADC}) \cdot \xi \cdot \chi \tag{8.2}$$

where ξ is a compensation factor for the boost converter efficiency equal to 4.0, χ is the power generation safety margin of 20 % while P_{MCU} and P_{ADC} is the power consumed by MCU and ADC, respectively.

Table 8.7. Two scenarios considered for establishing minimal power generation requirements for the energy harvesting module.

Scenario	MCU	ADC	Boost Converter Efficiency Compensation	Safety margin	Overall
LPM0	306 µW	42.75 µW	4.0 (for 25% efficiency)	20%	1.674 mW
LPM3	30.83 µW	42.75 µW	4.0 (for 25% efficiency)	20%	0.353 mW

8.4. TEG Selection

After having minimal power generation requirements, it is possible to select the appropriate TEG. The selection of a thermoelectric generator for a specific application is a basic prerequisite for an effective thermal energy harvesting process. The selection of TEG should start with the selection of the thermoelectric technology and materials which are the active part of the module itself. As shown in Chapter 6 in the Figure 6.5, for temperatures prevailing in the autoclave, i.e. in the range from 20 °C to 130 °C. The optimal thermoelectric material will be bismuth telluride (Bi_2Te_3). This is the most common material from which commercially available thermoelectric generators are manufactured, and hence the number of manufacturers

and models is wide. Consequently, it was necessary to narrow down the available models in terms of their optimal performance under the assumed temperature conditions. In addition, it should be taken into account that the thermoelectric generator will not operate under typical conditions - i.e. during a steady, constant heat flow from the heat source side through the warm side of the thermoelectric generator, the cold side, up to the heat sink from where the heat will be dissipated in the air. In the application described in this work, heat will be stored in the Heat Storage Unit during the sterilisation process and will flow in the opposite direction afterward. Therefore, unlike in classical applications, we cannot speak of an infinite-capacity heat source with an input temperature to the TEG that is only affected by the finite thermal conductivity of the source structure and not by the energy loss through the TEG. In such cases, maximisation of energy production is usually sought, and it is well documented in the literature ([82], [83]) that this occurs when the thermal resistance of the TEG approximately matches the thermal resistance of the remaining thermal path between the heat source (the warm side of the TEG) and the environment (the cold side of the TEG). On the contrary, in thermoelectric heat storage devices (which is what is considered here), the total available thermal energy is limited, and the heat flow through the TEG is also limited. Heat flows from the enclosure through the TEG to the heat storage unit until the HSU temperature is equal to the outside temperature. Once the outside temperature drops, the heat flow occurs in the other direction, i.e. heat flows out of the HSU, flows through the TEG and the housing and is dissipated to the outside. Heat flow that occurs slightly through the thermal insulation layer should also not be overlooked. A good analogy here is an electrical system in which we charge and discharge a capacitor. Such an arrangement is shown in the figure 8.9. The thermal resistances of the individual elements were modelled using resistors. In such a system, the voltages on the individual elements will be equal to their temperatures. Here we do not care about the highest available power, but rather the highest possible conversion efficiency in a given thermal cycle. As can be seen, to ensure the highest possible temperature difference in the TEG, we need to choose a TEG with the highest possible thermal resistance. The upper limit of the TEG resistance here is the length of the thermal cycle - we want the heat to flow all the time in the HSU direction until the temperatures are completely equalised and back again when the cycle is complete. When selecting a TEG, you should also pay attention to the material in which the HSU is made. In the absence of other constraints, the HSU should be made of a material with as large thermal capacity as possible and possibly good thermal conductivity (so that the temperature distribution inside the HSU is uniform). In turn, the insulation material should have a much higher thermal resistance than the TEG resistance. Efforts must be made to minimise the escape of heat from or to the environment through pathways other than through TEG. Therefore, among other things, a good match between the surface of the TEG and the HSU should be sought - parts of the HSU that protrude beyond the TEG should be minimised. In general, from the heat flow path perspective, a good module design should have a high thermal conductivity of the casing, of the casing/TEG interface, of the TEG/HSU interface, and the HSU. The thermal conductivity of thermal insulation should be significantly lower than the thermal conductivities of all other elements (k_{TEG}, k_{HSU}, $k_{interfaces}$ and k_{casing}). Furthermore, k_{TEG} should be matched with the desired heat cycle, so as to ensure the thermal gradient as long as possible. A complete list of requirements for the selection of TEG and the thermal design of the prototype is presented in Table 8.8 according to all significant elements in the heat flow path.

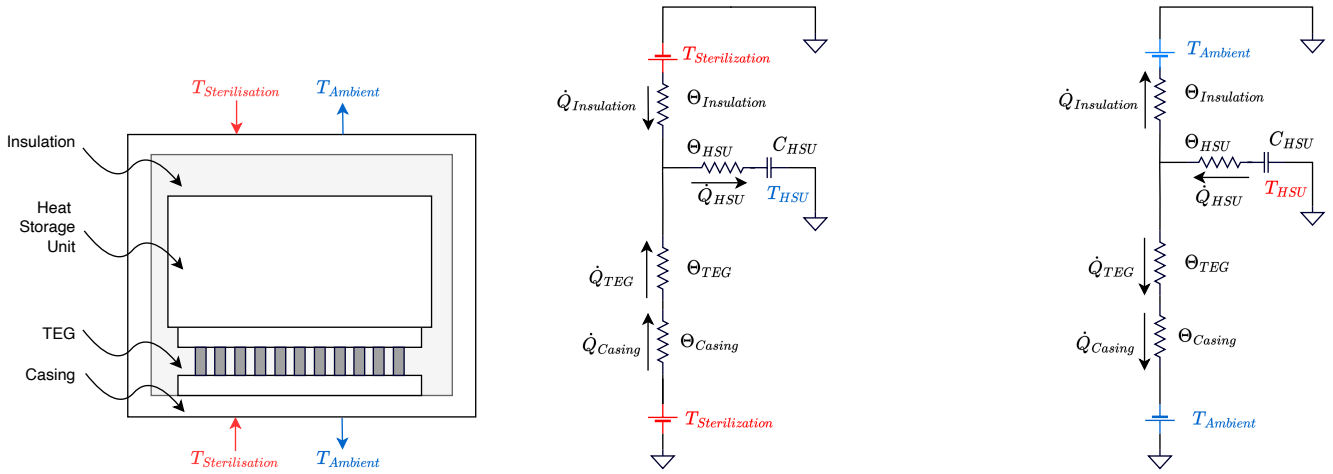

(a) Shematic of the prototype idea, $T_{Sterilisation}$ indicates the temperature of the steam sterilization, while $T_{Ambient}$ indicates room temperature after the sterilisation.

(b) Electrical model representation of the heat flow during the steam sterilisation. The heat flows from the autoclave with $T_{Sterilisation}$ temperature, through casing, TEG, towards HSU where the heat is stored until thermal gradient between outside of the module and HSU is > 0.

(c) Electrical model representation of the heat flow after the steam sterilisation. The heat flows from the HSU with T_{HSU} temperature, through TEG, casing, towards outside of the module, until thermal gradient between HSU and outside reach 0.

Figure 8.9. Prototype schematic and its electrical equivalent in the terms of heat transfer. (**a**) - schematic drawing of the prototype construction, (**b**) - heat transfer while steam sterilization (heat transfers towards HSU), (**c**) - heat transfer after the steam sterilization (heat transfers from the HSU to outside of the module).

Table 8.8. Design requirements towards the TEG model and other prototype elements related to heat path and heat transfer, k - thermal conductivity.

Prototype element	Requirement
Heat Storage Unit	High Heat Capacity High thermal conductivity
Thermo-Electric Generator	High efficiency at low temperature gradients $k_{TEG} \ll k_{HSU}, k_{interfaces}$ $k_{TEG} \gg k_{insulation}$ k_{TEG} small $\rightarrow R_{TEG}$ high k_{TEG} high enough for full heat cycle
Insulation	$k_{insulation} \ll k_{TEG}, k_{HSU}$
TEG interfaces	$k_{interfaces} \gg k_{TEG}, k_{insulation}$

After a market review, it was decided to choose a Ferrotec Nord TMG-127-0.4-16 generator for an initial prototype. This TEG has been chosen due to its very small size (16 mm x 16 mm x 3.5 mm) and appropriate power generating capabilities. Also, its size and thickness determined relatively low thermal conductivity. The basic technical parameters of the thermogenerator are shown in Table 8.9.

Table 8.9. Technical data of the Ferrotec Nord TMG-127-0.4-16 thermoelectric generator. V_{oc} - maximal open circuit voltage, R_{load} - matched load (correspondent to the maximal electric power), V_{load} - maximal voltage under the matched load, I_{load} - maximal current under the matched load, , W_{load} - maximal electric power output under the matched load, ACR - module AC resistance, Θ_{TEG} - module thermal resistance, α_{TEG} - module Seebeck coefficient, in simulations marked as *Se*.

Technical Data			
V_{oc}	2.8 V	I_{load}	0.044 A
V_{load}	1.4 V	R_{load}	32 Ω
W_{load}	0.063 W	ACR (at 25 °C)	26 Ω
Θ_{TEG}	27 K/W	α_{TEG} (Se)	56 mV/K

8.5. Thermal Insulation Material

Materials selection has been carried out according to the technical and business requirements described in Chapter 7. The most important factor was a proper selection of insulation materials. Adequate thermal insulation is a key factor in generating a thermal gradient through a thermogenerator. Therefore, a literature and patent search was conducted for insulating materials suitable for use in a steam sterilisation environment. As the most critical component of an electronic system is the electrochemical storage device, much work has focused on the thermal protection of these devices. The work of George et al. [126] analysed the use of two epoxy resins and high-temperature silicone to protect batteries from sterilisation. In this work, 225 sterilisation cycles were carried out. Unfortunately, in most of them mechanical damage, microcracks, and leaks of the insulation appeared, leading to disintegration of the thermal insulation. This was probably due to the lack of flexibility of the epoxy resin. The same results were achieved by Bohler et al. in their work. The same result was achieved with a specially constructed epoxy resin commissioned by Aesculap AG. The results of this work are also described in publications by Boehler et al [127].

For this reason, the use of traditionally used insulation could not be considered, and Boehler et al. proposed the use of Aerogel, a material traditionally used in construction and industry for insulation. The use of this material in medical applications was not known until now. Aerogels are a group of materials which can be divided into inorganic, the most common, organic, and inorganic-organic. The combination of alkoxides with metal oxides such as silicone leads to the formation of a nanoporous structure with pore sizes ranging from 5 nm to 100 nm. As a result, the material consists of 99.8% air, providing excellent insulating properties. Typically, aerogel materials are applied in the form of blocks or sheets. Other forms of aerogel, although developed in laboratories, have not reached the market stage and were not commercially available until recently. However, *ActiveAerogels* has developed the first aerogel foam that can be used in applications requiring precise thermal insulation. Because of the excellent thermal properties mentioned above and the possibility of using the foam to insulate small electronic components, it was decided to use this material in this prototype. Table 8.10 contains a list of insulation materials analysed, while Table 8.11 contains detailed parameters of the material selected for the thermal insulation of the prototype.

Table 8.10. Insulation material parameters most important for the design of the prototype – maximal operating temperature and thermal conductivity.

Material Parameters	Henkel FP4460 Epoxy	Epotek OD2002 Epoxy	Mold Max 60 Silicone	Active Aerogels Aerogel Foam
Maximal operating temperature [°C]	150	225	294	250
Thermal Conductivity [$W \cdot m^{-1} \cdot K^{-1}$]	0.68	0.3	0.21	0.027

Table 8.11. Physical parameters of selected insulation material – ActiveAerogels Aerogel Foam (Silfoam).

Parameter	Value
Density	$120\,kg \cdot m^{-3}$
Thermal Conductivity	$0.027\,W \cdot m^{-1} \cdot K^{-1}$
Specific Heat	$1.5\,kJ \cdot kg^{-1} \cdot K^{-1}$
Operating Temperature	–196 °C to 250 °C
Compressive Strength	41 kPa
Compressive Modulus	947 kPa

8.6. Prototype Enclosure Selection

The prototype enclosure serves two main functions: the function of protecting the interior of the prototype from moisture and autoclave pressure, and the function of conducting heat from the outside to the thermogenerator. Therefore, it was necessary to choose a material that is characterised by appropriate resistance to pressure and that conducts heat well. Additionally, we had to take into account the rapidly changing temperature inside the autoclave, which could adversely affect the material from which the casing would be made. While in the tests carried out in this dissertation the experiments were conducted in terms of heat flow, without placing the entire prototype in a real autoclave, it was necessary to select a material that could be used to build a fully hermetic casing adapted to the steam sterilisation process. Finally, the enclosure itself should have a relatively simple design and should allow easy access to its interior. This is due to the need to house the thermogenerator, HSU and fill the remaining space with insulation material. Do not forget about the proper protection of the thermogenerator current leads and thermocouples used to measure the temperature inside the prototype. For this reason the Hammond Electronics 1590Z110 enclosure was chosen. The housing has internal dimensions of 75 x 80 x 52 mm and is made of Aluminium. It is IP66 rated and the schematic is shown in Figure 8.10.

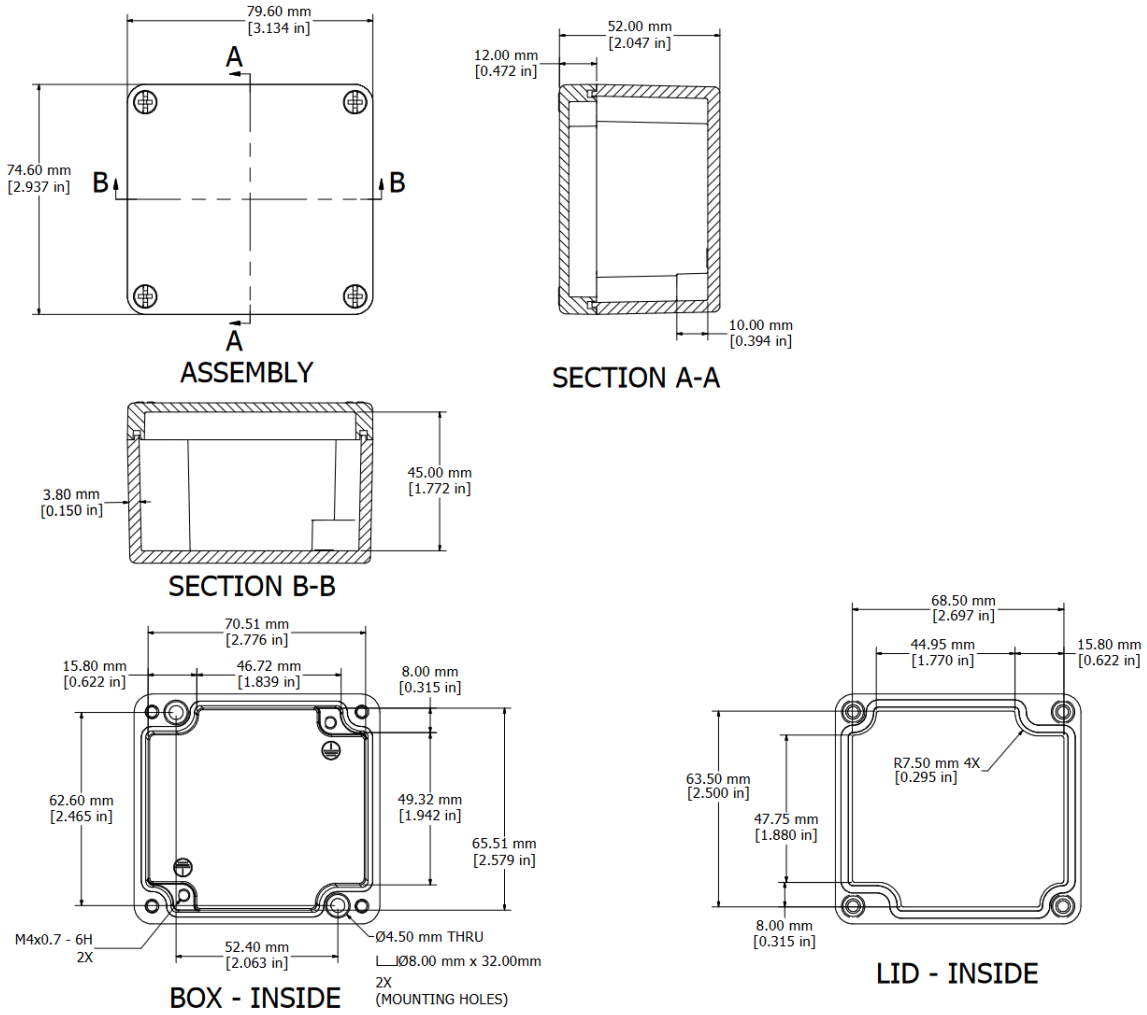

Figure 8.10. Schematics of the prototype IP66 enclosure Hammond Electronics 1590Z110 [128].

8.7. Prototype Assembly

Once the appropriate parts were selected, construction of the prototype began. A thermogenerator was attached to the aluminium housing at the centre point of the bottom of the housing. The thermogenerator was connected to the casing with a thin layer of thermoelectric paste in which a thermocouple was embedded. The thermogenerator wires were then insulated and led through the casing wall to the outside. A heat storage unit was placed on the thermogenerator. A thin layer of thermally conductive paste was spread between the thermogenerator and the heat storage unit, where the thermocouple was embedded. On the top wall of the HSU the third thermocouple was glued, which measures the temperature in the HSU. Then, the remaining space was filled with Active Aerogels Silfoam insulation. The prototype was allowed to dry for 5 days in a dry and warm environment at approximately 27 °C. The enclosure lid was then screwed on, further sealing it with heat-insulating silicone. Thermocouples measuring the temperature of the enclosure were additionally placed to the top and bottom of the enclosure (in a place corresponding to the location of the TEG). The entire assembly schematic is presented in Figure 8.11.

The sizes of the TEG and HSU are as follows (width, length, height):

- HSU: 25 mm x 25 mm x 15 mm
- TEG: 15.5 mm x 15.5 mm x 3 mm

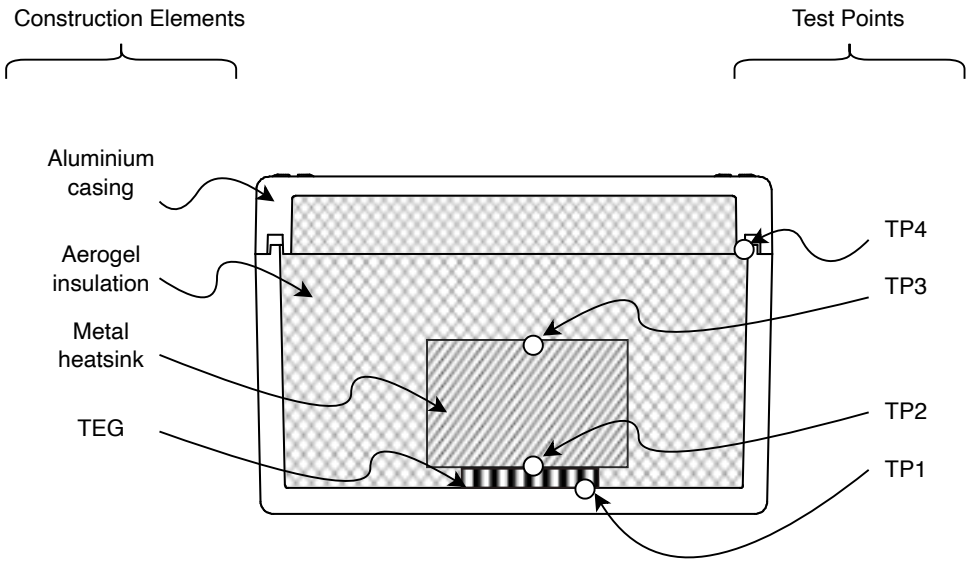

Figure 8.11. Schematic of prototype assembly. The construction elements are marked on the left side of the schematic, while the test point locations are marked on the right side of the schematic.

9. Physical Model and TEG Characterisation

Abstract

In this chapter a physical model and the chosen TEG is characterised. First, a model characterisation procedure is described. The procedure involves annealing the model in a thermal chamber and then removing it from the chamber to room temperature, forcing it to respond to a temperature step and measuring temperature changes inside the model. To perform this, a measurement system had to be assembled and characterised towards possible measurement errors. Type K thermocouples were selected for temperature measurement, which were previously validated using Pt100 RTD. The results have been registered for over 17,500 [s] and are presented in the diagram. The second part of the chapter describes the characterisation of TEG with OCV and the matched load resistance to validate the electrical parameters declared by the manufacturer. It was revealed that the TEG in reality has around 10% worse Seebeck coefficient than declared by the manufacturer.

Outcomes of this chapter: As a result of this chapter a physical models temperature step response has been registered and processed for further comparison with simulated data. A TEG efficiency has been measured using designed measurement system, revealing that the Seebeck coefficient of the TEG is aorund 10% less than declared by the manufacturer. Voltage, current, and power generated by the TEG have been registered for further comparison with simulations.

In this chapter a characterisation of the physical prototype as well as the selected TEG model is described. Both procedures are needed for further development of virtual device model for CAE simulations and TEG SPICE based model. To perform physical model characterisation, a measurement system has been built for measurement the temperature values inside the physical model. To make the characterisation of the physical model useful in the context of CAE simulations, the response to a thermal step had to be investigated. To do this, a thermocouple-based measurement system was built and its accuracy was identified by comparison with a class A Pt100 thermoresistor. The temperature was measured at a number of locations inside the model, starting from the surface of the Heat Storage Unit, through the hot and cold sides of the TEG, and finally at the model housing. The results of this procedure will be used in the next chapter to validate the accuracy of the CAE simulation model. The second stage was to perform measurements and parameterisation of the TEG, which were necessary to evaluate its SPICE model. To perform this procedure, a special test bench has been developed, which is also described in this chapter. Finally, the results of the TEG parametrisation have been registered and will be used in the next chapter to compare it with the simulation model.

9.1. Prototype Characterisation

In order to create the virtual model, the thermal characteristics of the physical model had to be collected. For this purpose, the physical model was subjected to a thermal step response test, and temperature measurements were collected at appropriately selected points inside the prototype. The test was designed to investigate the dynamic response of the prototype which would then be used for validation of CAE simulations.

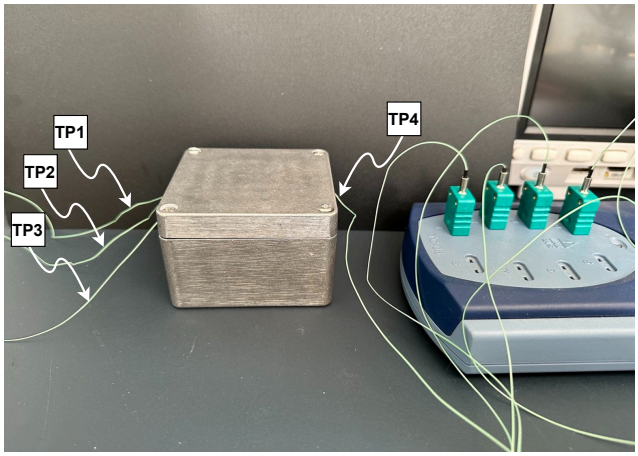

Figure 9.1. Assembled physical model with marked thermocouples.

The test procedure has been developed as follows:

1. The temperature measurement system has been built and validated using the selected thermocouple-based sensors. A sensor selection procedure has been described. The sensor accuracy has been established by comparison with class A Pt100 sensor. The accuracy of the system measurement has been calculated.

2. Four thermocouples have been placed inside and outside of the physical model: between the thermogenerator and the casing, between the thermogenerator and the heat storage unit, on the heat storage unit, and on the model casing. Thermocouples have been attached to the model parts using thermal-conductive glue, while their tip has been covered with a thin layer of thermo-conductive grease.

3. The model with connected thermocouples was placed in the thermal chamber, which was heated to 102 °C (± 0.5 °C, coming from the proportional-integral-derivative (PID) temperature controller of the thermal chamber), a special attention has been paid to the whole model equally, so the thermal gradients between all 4 thermocouples have been minimised.

4. The model was removed from the thermal chamber to a specially designed stand, ensuring heat transfer from the prototype to the environment being as uniform as possible.

5. Measurements from thermocouples were collected until thermal equilibrium was reached across the prototype - all of the thermocouples reached the temperature values within defined range.

The assembled physical model is presented in figure 9.1

9.1.1. Temperature Measurement System

In order to carry out the thermal measurements, it was necessary to build a measurement system using temperature sensors, a data acquisition device, and software for data recording. Two main requirements for the system were that it should be characterised by a good dynamic response, accuracy within the range of 3.0 °C and allow for archiving the collected measurement data in real time.

Selection of temperature sensors

Before the development of a measurement system, available temperature sensors were reviewed according to initial requirements. Three available technologies were considered: the thermocouple, the resistance ther-

mometer (RTD), and the thermistor. A summary of all these sensors in terms of the design of the measurement system is summarized in the Table 9.1.

Table 9.1. Comparison of three types of temperature sensors: thermocouple, temperature-dependend resistor and thermistor in according to the measurement system requirements [129].

Characteristic	Thermocouple	RTD	Thermistor
Temperature Range [°C]	-210 to 1760	-240 to 650	-40 to 250
Linearity	Fair	Good	Poor
Sensitivity	Low	Medium	Very High
Response Time	Medium to Fast	Medium	Medium to Fast
Stability	Fair	Good	Poor
Accuracy	Medium	High	Medium
Susceptible to self-heating	No	Yes, minimal	Yes, highly
Durability	Excellent	Good	Poor
Cost	Lowest	High	Low
Dimensions	Very small	medium	medium
Signal Conditioning Requirements	Cold-junction compensation, amplification, open-thermocouple detection, scalling	Excitation, lead resistance correction, scaling	Excitation, scalling

A sensor that could be used in the described measurements should be characterized by:

- High dynamic response,
- As small as possible tip size (large size could increase measurement inertia and could negatively influence the whole system, it could also cause problems with mechanical assembly of the prototype),
- Easy interference compensation and high reliability,
- High accuracy.

Due to the characteristics of the measurements, it was decided to choose the type K thermocouple as the optimal sensor for the planned measurement system. This was primarily determined by the high dynamic response rate and the small size of the thermocouple tip; moreover, the accuracy of the thermocouple measurement has been within the defined range (3.0 °C). However, due to the measurement characteristics with a K-type thermocouple, it is important to remember the necessary accuracy validation of the sensor used.

Validation of K-type thermocouple accuracy

As can be seen from the Table 9.1 thermocouples are characterized by relatively low measurement accuracy in comparison with other measurement methods - e.g. using a thermal resistor. According to the european norm *EN 60584-1* [130], the inaccuracy of thermocouple readings can range from 1.5 °C to 4.0 °C in contrary

to the precision of the RTD of class A which is in the range of 0 to 100 °C it has an inaccuracy of ±0.35 °C. Therefore, it was necessary to validate the measurement accuracy of the selected thermocouple.

The validation method involved measuring the temperature at a well-defined point using a Pt100 RTD and using a thermocouple. The two results were then compared, and the measurement inaccuracy of the thermocouple relative to the Pt100 sensor was determined. To carry out the measurements, the test bench shown in Fig. 9.3 has been built. It consisted of an aluminium plate of size 48 mm times 98 mm on which Thermo TECH 3326100 75 W, 24 V heating foil has been attached. The heating plate was placed on four thermally insulated legs attached to the measurement table. The heating foil was powered by a laboratory power supply Siglent SPD3303X-E. Thermocouples and a PT100 sensor were placed inside the copper block which was placed on the heating plate. The distances and arrangement of the sensors is presented in Figure 9.2. According to the used materials, the copper block, the temperature value in both points is assumed to be the same. Both the thermocouples and the Pt100 sensor have been placed inside the drilled holes filled with conductive grease. Pt100 sensor was connected to the Agilent 34410A laboratory multimeter with two-wire connection with length of 50 cm. Then, the temperature of the heating plate was adjusted in the range from 35 °C to 100 °C with the step of 5 °C. After each step, when the temperature has been set, the readout of both the thermocouples and the Pt100 has been performed.

Table 9.2. Parameters of LT-1-1000-K-TF/TF40-1K-type thermocouples.

Parameter	Value
Thermocouple type	K
Measurement tip diameter	<0.5 mm
Wire diameter	2 x 0.08 mm
Wire material	NiCr/NiAl
Wire length	100 cm
Measurement range	-190 °C to 260 °C
Declared accuracy	± 1.5 °C (class 1 according to EN 60584-1:2014-07)
Insulation type	PTFE-Teflon, 260 °C
Insulation max temperature	260 °C

For the design of the measurement system a thermocouple LT-1-1000-K-TF/TF40-1 by Therma Thermofuhler GmbH has been selected and its parameters are presented in the Table 9.2. As mentioned above, a Pt100 RTD was used to validate the accuracy of the thermocouple. For this purpose, a TEWA TT4PT100BT180C312 RTD has been chosen. Its biggest advantages are relatively small size (only 12 mm of length and 3 mm of diameter) and high accuracy (tolerance class B). The technical parameters of the chosen sensor are presented in the Table 9.3.

Table 9.3. Parameters of TEWA TT4PT100BT180C312 RTD [131].

Parameter	Value
No-load resistance at 0 celsius	100 Ω
Tolerance class	B
Tolerance range	-40 °C to 180 °C
TCR	3851ppm/°C

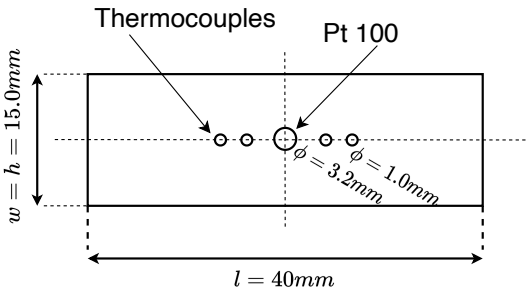

(a) Placement of the Pt 100 reference sensor and thermocouples being validated - top view.

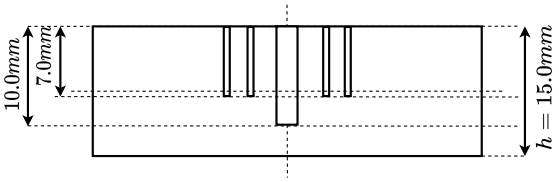

(b) Placement of the Pt 100 reference sensor and thermocouples being validated - side view.

Figure 9.2. Placement of the Pt100 sensor and thermocouples during the thermocouples validation procedure. Positions of the test probes are approximate with a tolerance od 1.0 mm due to the inaccuracies during the drilling process.

The resistance of the Pt100 RTD was registered. The resistance measurement range of the device has been set to 1 kΩ. In this range the measurement accuracy is 0.01 % of reading added to 0.001 % of measurement range [132].

The collected resistance values has been saved to a file. The correlation of temperature versus sensor resistance is described by the Callendar-Van-Dusen equation (9.1):

$$R_{RTD} = R_0 \cdot (1 + (A_{RTD} \cdot T) + (B_{RTD} \cdot T^2)) \tag{9.1}$$

where:

R_{RTD} - RTD resistance at given temperature in given testpoint Ω,

R_0 - RTD resistance at 0 °C [Ω],

T - temperature value in given test point [°C],

A_{RTD} - A coefficient from european norm *EN 60751* equals $3.9083 \cdot 10^{-3}[°C^{-1}]$,

B_{RTD} - B coefficient from european norm *EN 60751* equals $-5.775 \cdot 10^{-7}$ $[°C^{-1}]$.

Transforming the equation yields the temperature as a function of the resistance of the Pt100 sensor:

$$T = \frac{-A + \sqrt{A_{RTD}^2 - 4B_{RTD} \cdot (1 - \frac{R_{RTD}}{R_0})}}{2B_{RTD}} \tag{9.2}$$

In this equation, constants A_{RTD} and B_{RTD} are used. Parameter R_0 for Pt100 sensors is 100 Ω. Pt100 sensors are also characterised by a low variation of parameters; this means that there is not much variation between units of a given series. The accuracy of the Pt100 sensor is defined in IEC 60751 industrial standard and depends on the sensor accuracy class [133]. In the Table 9.4 accuracy classes according to IEC 60751 are listed.

Table 9.4. Selected tolerance classess of RTDs according to IEC 60751.

Tolerance Class	Tolerance Values [°C]	Resistance at 0 °C [Ω]	Error at 100 °C [°C]
IEC class C	± 0.6 + 0.01 • |T|	100 ± 0.24	± 1.60
IEC class B	± 0.3 + 0.005 • |T|	100 ± 0.12	± 0.80
IEC class A	± 0.15 + 0.002 • |T|	100 ± 0.06	± 0.35
IEC class AA	± 0.1 + 0.0017 • |T|	100 ± 0.04	± 0.27

After temperature registration an absolute error of thermocouples have been calculated using following equation:

$$E_{Tc} = |T_{Pt100} - T_{Tc}| \tag{9.3}$$

where:

E_{Tc} - absolute error of thermocouple readout [°C],

T_{Pt100} - temperature value registered using Pt100 RTD [°C],

T_{Tc} - temperature value registered using thermocouple [°C].

The results of the measurements and the comparison between the Pt100 and a thermocouple are shown in Table 9.5 and Figure 9.4, while the measurement stand is presented in Figure 9.3. As can be seen from the comparison with the Pt100 readout, the different thermocouples have different inaccuracies, ranging in average from 0.11 °C for the thermocouple TP1 to 0.56 °C for the thermocouple TP4. This is confirmed by the thermocouple datasheet, where the manufacturer declares the measurement inaccuracy of 1.5 °C. Standard deviations ranged from 0.05 °C for the TP1 thermocouple to 0.22 °C for the TP3 thermocouple. On the basis of these results, it is needed to take this into consideration in the prototype thermal measurements.

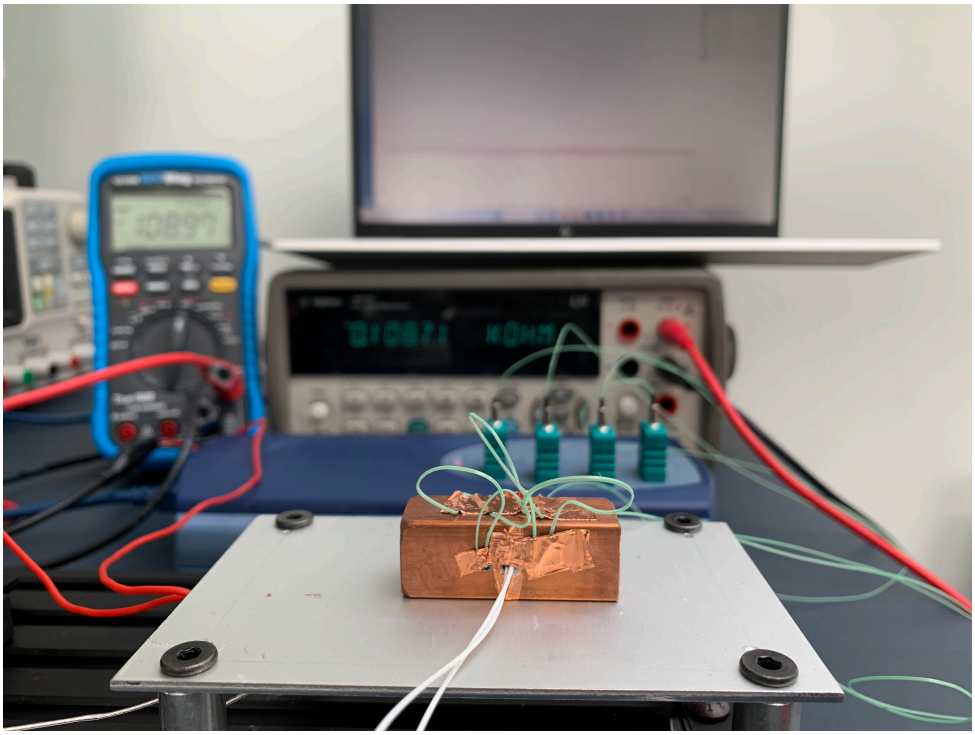

Figure 9.3. Test stand of the thermocouples accuracy validation. Thermocouples placed inside a copper block beside the Pt100 RTD, secured with the copper tape. Pt100 resistance has been acquired with Agilent 34410Amultimeter, the temperature of the heating foil has been validated using Pt100 RTD attached to the portable multimeter EEVBlog GW121and thermocouples readout have been acquired using TC-08 logger attached to the laptop.

Table 9.5. Resistance and calculated temperature of Pt100 sensor compared with thermal measurements taken by K-Type thermocouples (TP1 - TP4).

R_{Pt100} [Ω]	T_{Pt100} [°C]	T_{TP1} [°C]	T_{TP2} [°C]	T_{TP3} [°C]	T_{TP4} [°C]
108.83	22.67	22.59	22.49	22.33	22.11
111.75	30.20	30.17	30.12	30.02	29.80
115.44	39.74	39.66	39.57	39.50	39.34
119.69	50.76	50.61	50.45	50.36	50.23
124.01	62.00	61.88	61.69	61.61	61.51
129.20	75.56	75.45	75.19	75.12	75.07
133.97	88.06	87.94	87.64	87.60	87.60
138.62	100.30	100.48	99.95	99.73	99.66
144.39	115.55	115.64	115.02	114.83	114.79
145.48	118.44	118.25	117.62	117.50	117.58
	Avg. Inacc. [°C]	0.11	0.35	0.47	0.56
	Std. Dev. [°C]	0.05	0.20	0.22	0.14

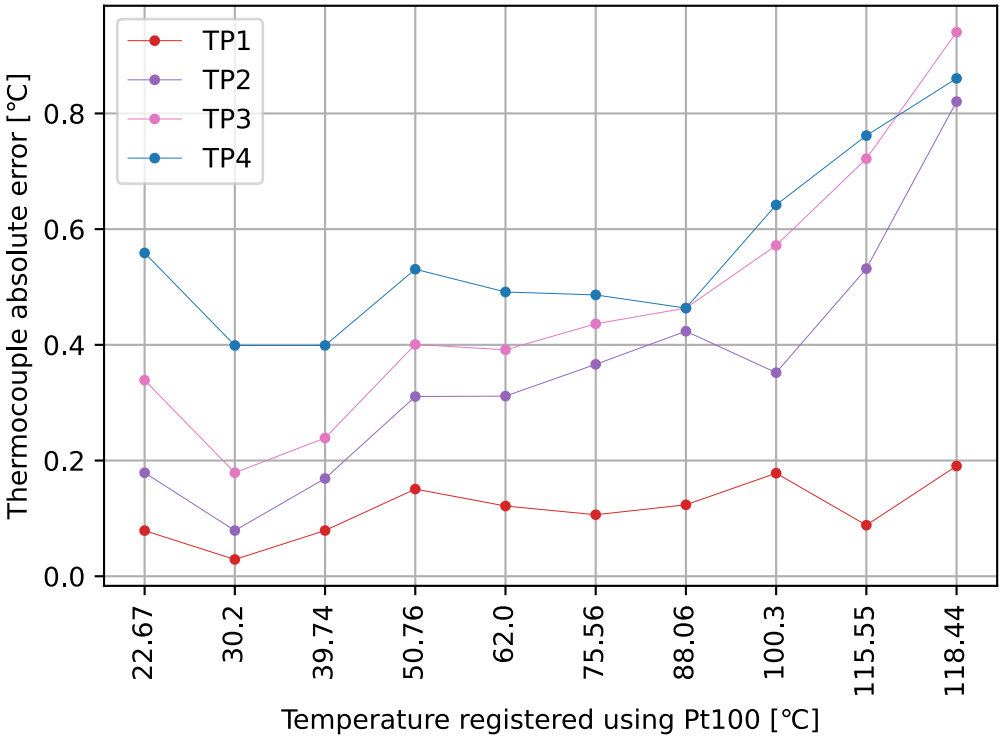

Figure 9.4. Results of the thermocouples validation in comparison to the reference Pt100 RTD.

Measurement system parameters and potential measurement error

The measurement system used for the prototype thermal step response measurement consisted of a Pico TC-08 USB thermocouple data logger and 4 LT-1-1000-K-TF/TF40-1K-type thermocouples. The technical parameters of the thermocouples used in the experiment are shown in Table 9.2. Pico TC-08 is a USB-powered 8 channel thermocouple data logger with built-in cold junction compensation circuit. It's biggest advantage is that it offers 20-bit resolution and it comes with integrated software as well as integration with

LabView and Matlab software packages possible. The parameters of Pico TC-08 are shown in Table 9.6. The LT-1-1000-K-TF/TF40-1type K thermocouples are one of the thinnest thermocouples available in the market, which could be used for measurements inside the prototype without significantly affecting its design. The PicoLog 6 software has been used for data acquisition from the TC-08 device. It allows data registration with selected frequency, creating the so-called Math Channels with a given mathematical function, e.g. substracting one thermocouple channel from another. This feature has been used to determine the thermal gradient across the entire prototype to control if the heat distribution is equal in the prototype body.

Table 9.6. List of critical parameters of PICO TC-08 temperature logger [134].

Parameter	Value
Hardware	
Number of channels	8
Conversion time	100 ms per thermocouple channel
Temperature Accuracy	Sum of 0.2 % of reading and 0.5 °C
Voltage Accuracy	Sum of 0.2 % of reading and 10 µV
Overvoltage Protection	±30 V
Input Impedance	2 MΩ
Input range (voltage)	70 mV
Resolution	20 bit
Noise-Free resolution	16.25 bit
Thermocouples types supported	B, E, J, K, N, R, S, T
Input Connectors	Miniature Thermocouple
Features	Built in cold-junction compensation
General	
Connectivity	USB 2.0
Power Requirements	USB Port
Temperature range (for quoted accuracy)	20 °C - 30 °C
Safety Approvals	2014/35/EU: Low Voltage Directive
EMC Approvals	2014/30/EU: Electromagnetic Compatibility Directive

It was also necessary to determine the measurement uncertainty. It is especially important for the further validation of the developed simulation models. The inaccuracy of the measurement of the TC-08 can be as shown in equation (9.4) [134].

$$E_{TC08} = 0.2 \cdot \frac{T_{max} - T_{ambient}}{100} + 0.5°\mathrm{C} \tag{9.4}$$

where T_{max} is maximal predicted temperature measured and the $T_{ambient}$ is an ambient temperature of the TC08 datalogger - in this case the temperature of the laboratory room.

The measurement uncertainty of the K-Type IEC584-2 standard compliant thermocouples (according to the standard and the manufacturers datasheet) has been taken as:

$$E_K = \pm 1.5°\mathrm{C} \tag{9.5}$$

The overall thermal measurement error has been calculated:

$$E_m = \sqrt{E_{TC08}^2 + E_K^2} = \sqrt{(0.2 \cdot \frac{105 - 25}{100} + 0.5)^2 + 1.5^2} = \pm 1.64°\text{C} \tag{9.6}$$

9.1.2. Thermal Measurements Procedure

After the calculation of potential measurement errors and inaccuracy of the thermocouple, it was possible to perform a thermal step response measurement of the prototype. The first step was to place the thermocouples at the particular locations inside the prototype. These locations are presented at Fig. 8.11 and are listed as follows:

- TP1 - The external side of the thermogenerator (connecting with the casing of the prototype),
- TP2 - Internal side of the thermogenerator (connecting with the heat storage unit),
- TP3 - Heat storage unit surface,
- TP4 - The outer wall of the prototype.

The entire prototype was then placed in a thermal chamber with a set temperature of 100 °C. This temperature was monitored with an additional thermocouple placed in the vicinity of the prototype. The procedure of heating the prototype lasted 60 minutes until the readings of all thermocouples indicated 102 °C (taking into account the measurement error). A convergence factor of 1 °C has also been defined.

Once the physical model was heated to the selected temperature and convergence was achieved (temperature values differed less than the convergence factor of 1 °C over time), it was removed from the thermal chamber and placed at room temperature, allowing uniform cooling with convection from the solid state to the air. In this way, a thermal step was forced which was then reproduced in the simulation environment. The whole procedure is presented in Fig. 9.5.

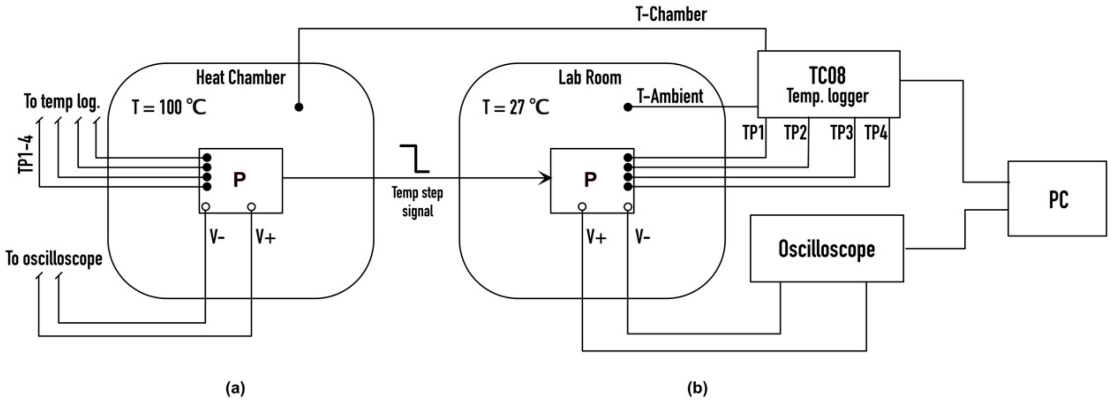

Figure 9.5. Schematics of thermal measurements of the prototype. The prototype is denoted as **P**.

9.1.3. Thermal Measurements Results

The data collected while performing the thermal step response measurements are presented in Fig. 9.6. The figure is composed of three main parts. As shown in the part 9.6a, the overall testing procedure lasted almost 5 hours and can be divided into three main stages: heating, stabilisation, and step enforcement. In the figure there are four data sets with the names reflecting the test points TP1 - TP4. In the first stage the whole prototype has been heated up, and this stage lasts for first 84 minutes (5000 seconds). It can be seen clearly that the heat comes from the outside of the prototype to the inside - the TP3 thermocouple heats up the fastest, then the heat is transferred through TP1 and TP2 and finally reaching the TP4 - the top of the HSU. It is also worth to mention that the top of the HSU is heated also from the top of the prototype, which is visible on the diagram, where the TP3 line exceeds TP1. This is caused by the imperfect insulation capabilities of the aerogel layer on top of the prototype. After reaching 100 °C it was necessary to stop the heating phase and try to set the thermal equilibrium across the prototype. This, a second phase of the procedure, can be seen from the minute 84 untill the minute 200 (12000 seconds). In this time, the temperature has been stabilised around the value of 103 °C. The difference in temperature between TP4 and TP2 might be caused by unequal heat transfer to the TEG and to the heat storage unit. Despite the best efforts to reach the same temperature in all parts, a small difference of 0.8 °C can still be observed. A detailed view on the equilibrium state has been presented in the figure 9.6c and in the Table 9.7. As can be seen, the difference between the highest temperature and the lowest temperature measured is within the accuracy level of the thermocouples. It can also be observed that a thermal chamber temperature regulation algorithm causes small thermal fluctuations, as well as initial thermal overshoot, which also caused the higher temperature of the prototype HSU (testpoint TP4 shown in Figure 8.11). In the third phase, the thermal step response has been applied. A detailed view of the thermal step response is presented in Figure 9.6b. This phase took around 115 minutes, and can be classified as relatively slow process in comparison to the response time of the thermocouples, so the dynamic characteristics of the thermocouples should not limit the accuracy of the readout. During the step response phase, a heat flow opposite to that of the heating phase can be observed. The TP3 thermocouple has the steppest response characteristics, which is caused by exposure of TP3 to ambient temperature in the laboratory. The TP1 curve strictly follows the TP3. The temperature observed in TP1 drops slower, since TP1 is connected to TEG on one side, so the heat from HSU is constantly flowing through TP1, causing an increased temperature in relation to TP3. TP2 and TP4 curves are dropping significantly slower, as both test points are connected to the HSU, which accumulated a significant amount of heat during the heating phase of the experiment. The results obtained have been classified as satisfactory and confirm the initial concept of the prototype. TP4 thermal curve in the response phase has been used as input for thermal step response simulation of the virtual prototype.

Table 9.7. Temperatures readout from the thermocouples attached to the measurement points in the prototype.

Thermocouple	Temperature
Casing Top (TP4)	102.30 °C
HSU (TP3)	103.20 °C
TEG Top (TP2)	102.40 °C
TEG Bottom (TP1)	102.40 °C
Casing bottom	102.40 °C

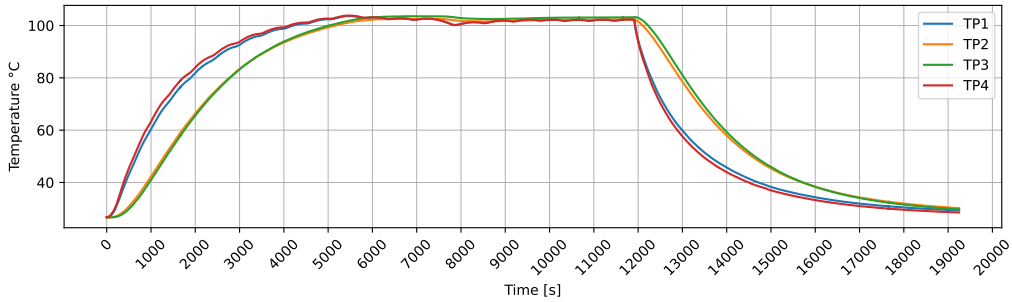

(a) Overview on the whole procedure including heating phase (seconds 0 to 11000) and step response phase (seconds 11000 - 19000)

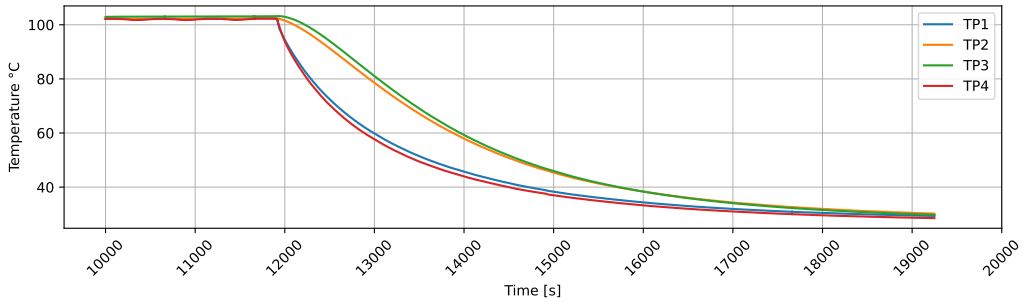

(b) Detailed view on the whole step response phase.

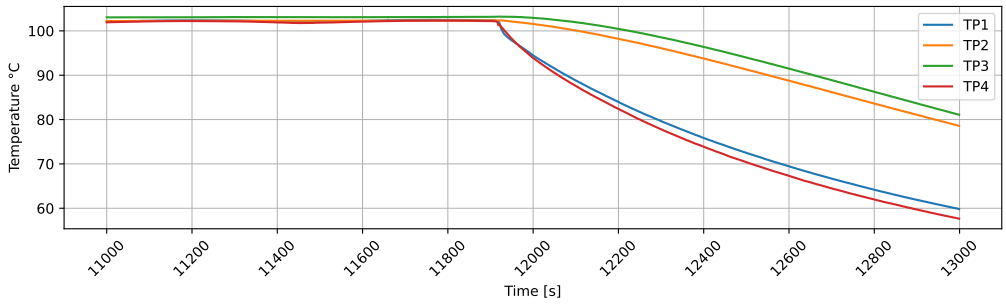

(c) Detailed view on the initial moment of the step response phase, just after model was placed outside of the thermal chamber. Differences between I-st order response (TP1 and TP4) and II-order response (TP2 and TP3) is visible.

Figure 9.6. Prototype thermal step response experiment.

9.2. TEG Validation Measurement System

In order to measure and characterise TEG, the measurement system shown in Figure 9.7 has been developed. The system consisted of a heating plate, connected to the Agilent E3631A laboratory power supply that operates in constant voltage mode. The plate was insulated from the bottom with a layer of thermal insulation foam. A TEG was placed on the plate. Between the plate and the TEG there was a layer of thermal conductive paste and a thermocouple that measured the temperature of the hot side of the TEG. On the other side of the TEG there was a heat sink attached using thermal conductive paste. In between the heatsink and the cold side of the TEG the second thermocouple has been placed. The thermal gradient formed by such assembly caused the TEG to generate the electric power which shall be then measured and evaluated. To accomplish this,

a resistive load has been connected to the TEG. A precise variable resistor with a resistance selection range of 1 to 100 Ω was used as the load and its value has been set to the value of internal resistance of the TEG. Between the TEG and the load, an Agilent 34410A laboratory multimeter was connected to measure the current, and at the output of the thermogenerator a Keithley DMM6500 benchtop multimeter was attached to monitor the TEG voltage. Finally, the thermocouple temperature readout was collected using the Pico TC-08 temperature logger. The whole system has been synchronised and has worked under the control of software developed in LabView. The general block diagram of the software is shown in Figure 9.8. The first stage is the pre-setup of the system system, i.e. opening the ports and establishing the connection with the devices connected to the system and the PC on the other side. When this is finished successfully, the setup of the measuring devices takes place where the measured values, number of channels, operation mode, measuring range, and other critical parameters are set. After this stage is done, the measurement process starts. The programme enters a loop, with a frequency of 1Hz. Such a low frequency is sufficient, as the TEG generates the DC voltage, and the thermal gradient changes are also relatively slow (the whole testing procedure can last over 2 hours), as we deal with the unforced heat transfer from metal to air. During each iteration of the loop the temperature of the hot side of the TEG, the temperature of the cold side of the TEG, the voltage and the current flowing into the load are read simultaneously. Those data are recorded along with the timestamp immediately after the acquisition in the same loop iteration. The user can stop the measurements with the "STOP" button. When this event occurs, the connections to the devices are terminated, and the ports are closed. The access to the file is also closed. The detailed programme block diagram is shown in Appendix A.

```
1
2
3 Setup: Load 31.6 Ohm, Power Supply: Agilent E3631A, Multimeter (current): Agilent 34410A,
      Voltage: NI MyDAQ, Temperature: TC08
4 Timestamp   |    T Cold      |    T Hot     |    Voltage    |    Current
5 ------------------------------------------------------------------------
6 1:18:59 PM     52.416542      34.221493       0.429497       0.015199
7 1:19:00 PM     52.344925      34.240261       0.427216       0.015086
8 1:19:01 PM     52.298420      34.251583       0.426076       0.015023
9 1:19:02 PM     52.269905      34.259232       0.423796       0.014969
10 1:19:03 PM     52.255825      34.274158       0.423796       0.014946
11 1:19:04 PM     52.230927      34.278160       0.422655       0.014920
12 1:19:05 PM     52.238728      34.289680       0.422655       0.014923
13 1:19:06 PM     52.217430      34.297325       0.422655       0.014942
```

Listing 9.1. Example of the thermal data logged while the measurement procedure of the TEG.

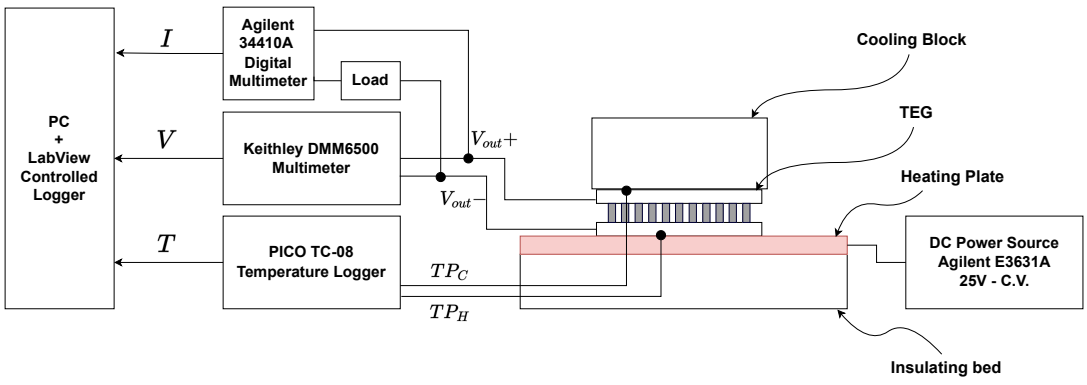

Figure 9.7. Functional schematics of the TEG testing stand.

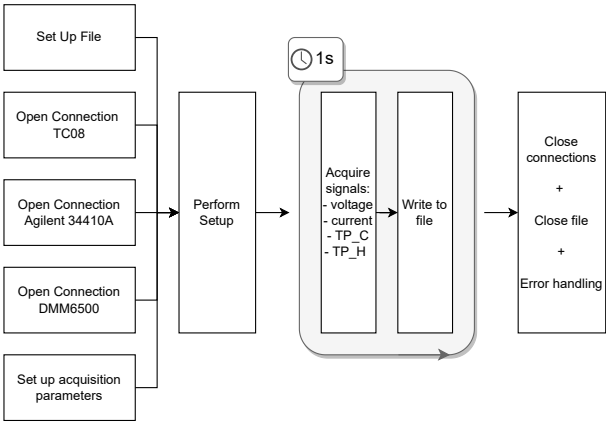

Figure 9.8. Schematics of Labview Program used for Logging the data.

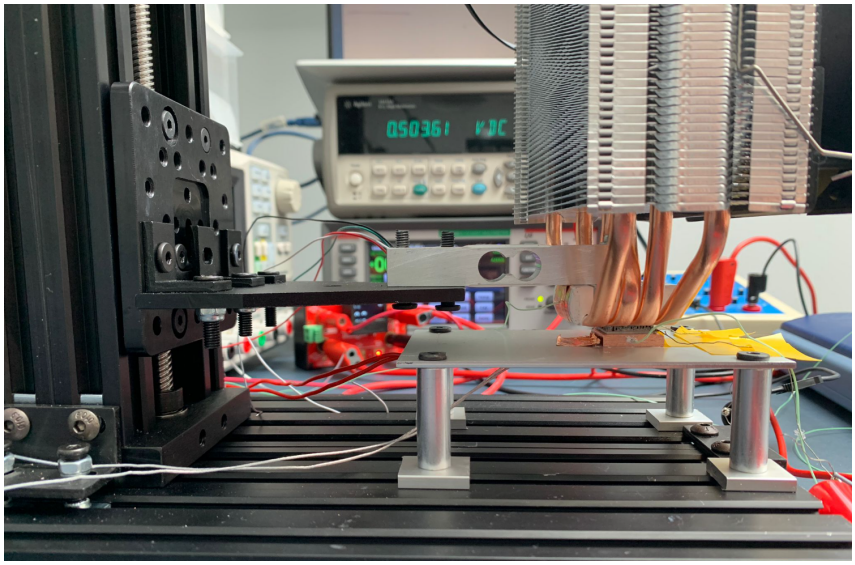

Figure 9.9. Test bench for parametrizing TEG.

9.2.1. TEG Characterisation Results

In this section, the results of the TMG-127-0.4-1.6 TEG characterisation are presented. As a first step, the open-circuit voltage as a function of the thermal gradient has been measured. This is presented in Figure 9.10. These data have been used next to calculate the Seebeck coefficient of the TEG. In the next step, a resistive load of R_L = 32Ω was connected to the TEG. With the load connected, the voltage across the thermogenerator (Figure 9.11a), and the current flowing from the thermogenerator to the load have been measured (Figure 9.11b). On the basis of this data, the generated power by the TEG has been calculated as a function of the given thermal gradient.

As can be seen in Figure 9.10 relation between voltage and the thermal gradient at the TEG is linear, reaching 3.99 V at 75 °C gradient. Based on the OCV measurement, a Seebeck coefficient of the TMG-127-0.4-1.6 module has been calculated according to the equation (9.7), where ΔT is a thermal gradient between the hot and cold sides of the TEG and ΔV is the voltage measured at the TEG terminals. This equation can be derived from equation (6.21). According to the manufacturer data presented in the Table 8.9 the Seebeck coefficient should be close to 0.056 $V \cdot K^{-1}$, however, it is always good to measure its actual value, as it can differ

in a particular application setup and in the particular piece of the given TEG model. The average real Seebeck coefficient is calculated using the data presented in the Figure 9.10 and using the formula as in equation (9.7):

$$Se_{real} = \frac{\Delta V}{\Delta T} = 0.0533 \tag{9.7}$$

It is worth mentioning that the average measured Seebeck coefficient differs from the declared value by the manufacturer by 0.0027 which is over 4.8%. The reason of such difference might be difficult to investigate, as multiple parameters can play a significant role here. First, the manufacturing process of the TEG might be imperfect causing the assembled module to be less efficient. Second, the materials from which this particular TEG is composed are not insulated from the environment, and after storage under different conditions the thermoelectric material might degrade to some extent. The third reason is that the material properties of the TEG tend to degrade with increasing number of work cycles.

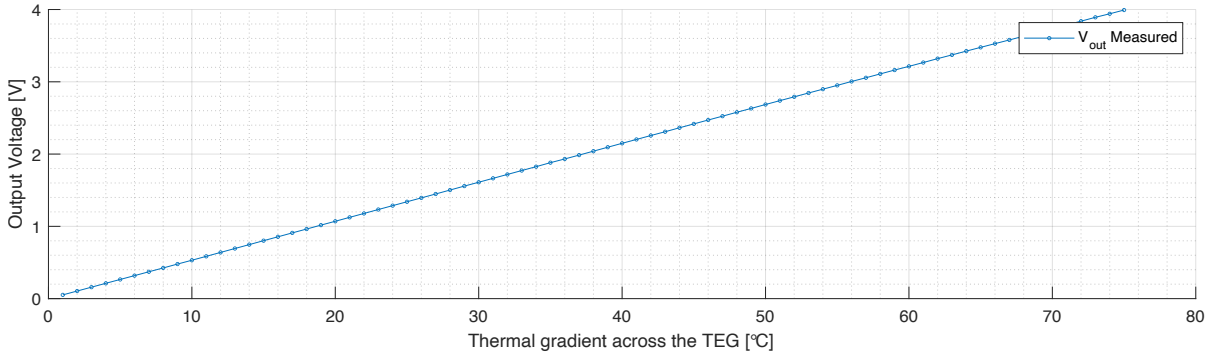

(a)

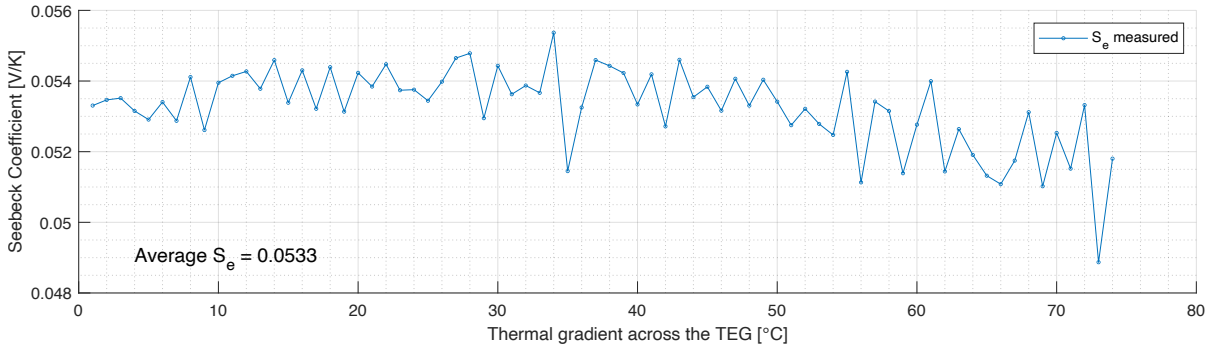

(b)

Figure 9.10. Open circuit voltage in relation to thermal gradient applied to the TEG (a), and it's Seebeck coefficient calculated from the equation (9.7) (b).

Figure 9.11a shows the voltage on the thermogenerator with a 32 Ω load connected as a function of the thermal gradient. As expected, the voltage increases nearly linearly with increasing gradient to reach 1.63 V at a gradient of 75 °C.

In addition to voltage measurement, the current flowing from the thermogenerator to the load was also recorded. The dependence of the current of the temperature gradient across the thermogenerator is shown in Figure 9.11b. As expected, this dependence is also nearly linear.

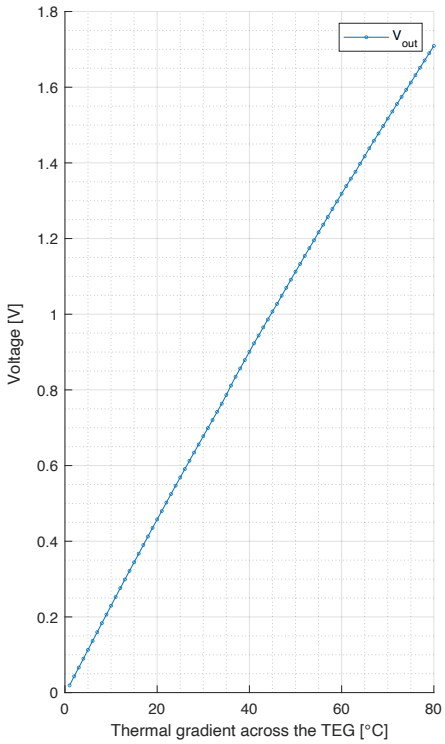

(a) Output voltage V_{out} of the TEG as a function of thermal gradient across the TEG

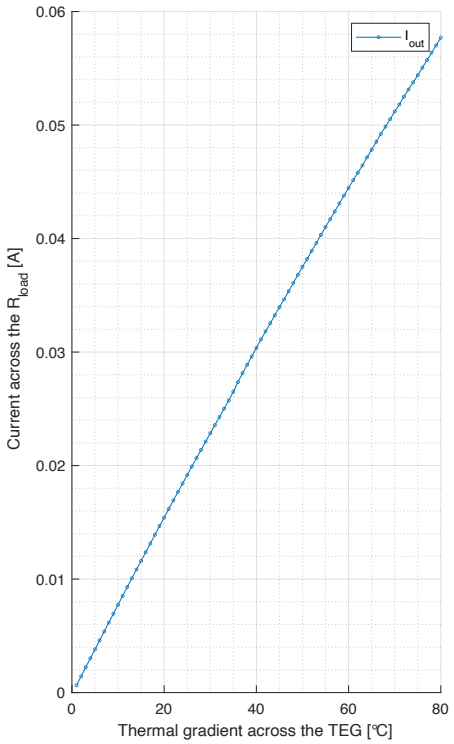

(b) Output current I_{out} of the TEG as a function of thermal gradient actoss the TEG

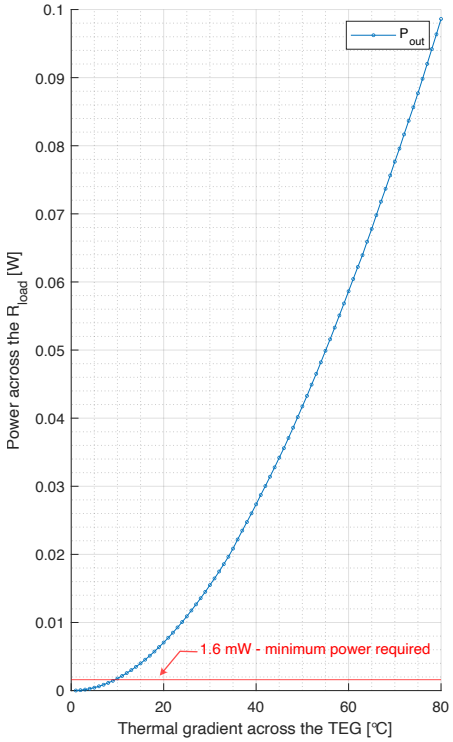

(c) Output power P_{out} of the TEG as a function of thermal gradient across the TEG

Figure 9.11. TEG voltage (a), current (b) and power (c) output characterisation under a load of $R_L = R_{TEG}$.

Based on voltage and current measurements, the power generated by the TEG was calculated as a function

of the temperature gradient and is shown in Figure 9.11c. As expected, this dependence is exponential in character. Based also on these measurements, the minimum thermal gradient that ensured sensor operation was determined taking into account the minimum power requirements of 1.67 mW defined in section 8.3.3 for LPM0 mode.

According to the literature on thermogenerators [135], their internal parameters, and in particular the internal resistance, can change with the operating temperature of the thermogenerator (and thus with the temperature gradient). Measurements of the internal resistance of the thermogenerator were made for temperature gradients in the range of 12 °C - 70 °C using the technical method according to the formula [136]:

$$R_{TEG} = \frac{V_{oc} - V_s}{I_s} \tag{9.8}$$

where:

R_{TEG} - internal resistance of the TEG [Ω],

V_{oc} - TEG open circuit voltage at given gradient [V],

V_s - TEG voltage with 0.6 Ω load [V],

I_s - TEG current with 0.6 Ω load [A].

Table 9.8. TEG internal resistance measurements results for different thermal gradients.

Gradient [°C]	V_{oc} [V]	V_s [°C]	I_s [A]	R_{TEG} [Ω]
12.0	0.65	0.020	0.016	39.00
20.0	1.08	0.038	0.027	40.07
32.5	1.75	0.057	0.042	40.31
41.0	2.20	0.067	0.052	41.02
50.0	2.72	0.079	0.062	42.59
60.0	3.30	0.092	0.073	43.95
70.0	3.82	0.102	0.084	44.26

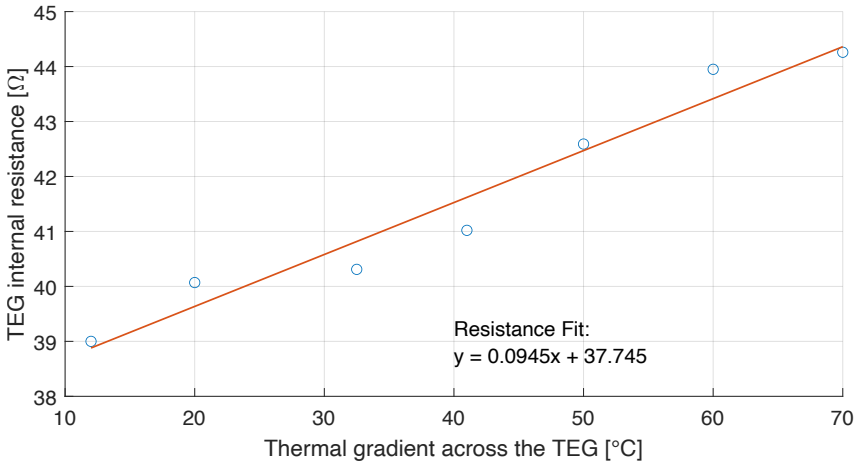

Figure 9.12. Internal resistance of the TEG in the conditions of different thermal gradients across the TEG.

As can be seen in Figure 9.12 the internal resistance of the thermogenerator increases with temperature and differs significantly from the AC resistance declared by the manufacturer (32 Ω). The internal resistance trend line was also determined to be a linear function, with a directional coefficient of 0.0945. For the purpose of further simulations, the internal resistance was selected for a gradient of 40 °C equal to approximately 41 Ω.

10. Simulations

Abstract

This chapter describes the virtual models of the device and the TEG and their setup for validation. First a CAD model of the physical model is created. Next the finite element modelling procedure is described in details. As first the material parameters are selected for each of the physical model parts - aluminium, aerogel, steel, Bi_2Te_3 and Al_2O_3. Next a meshing procedure is applied to 3D CAD model and mesh refinements are made in critical simulation areas. Each of the meshing parameters is described and evaluated, as it can have a significant influence on simulation results. Finally, the boundary conditions and numeric setup of the simulation are described. In the second part of the chapter a TEG modelling is described in detail. Due to simplicity and intuitiveness, a SPICE simulation method for the TEG has been selected. Several different models have been reviewed, and Kubov's model has been selected for further evaluation. After that, a set of parameters based on the TEG characterisation and manufacturer's datasheet have been applied to the model, and the simulation environment has been prepared.

Outcomes of this chapter: As a result of this chapter a detailed procedure of heatflow simulation in the virtual model has been described. Additionally, a TEG SPICE model has been selected and parametrised using the parameters obtained through physical measurements and taken from the TEG datasheet.

In this chapter a simulation setup and a steam sterilisation simulation procedure for the virtual model of the device will be presented. To perform any FEA simulation, the first step is to build a virtual CAD model of the device. Such a model has been created in the PTC Creo software and the FEA model simplification procedure has been applied. After having a model geometry, the material parameters have to be selected. This was made based on the literature values, taking the average value of the selected parameters. In all cases density, conductivity direction and thermal conductivity, as well as specific heat, have been selected. Having a CAD model and material parameters, the next step was to prepare a mesh. This was done in accordance with the good practises of the FEA modelling procedure and with respect to the software limitations and requirements. After generation of the initial mesh and inspecting its parameters, the mesh refinements have been applied to optimise it. Having a good quality mesh allowed us to go to the next step and set up the boundary conditions. Here the data acquired during the thermal step response experiment served as a boundary conditions of the simulation. Finally a numerical and simulation setup has been performed. The simulation used a Multifrontal Massively Parallel sparse direct Solver (MUMPS) solver with SCOTCH renumbering method and with Theta parameter of 0.5. After preparation of FEA simulation a setup for TEG simulation hase been made. In this thesis a Kubov SPICE model has been used, and initial TEG parameters has been chosen based on the methodology from the literature.

10.1. CAD Modelling

In order to carry out thermal simulations, it was necessary to construct a CAD model of the physical device. The CAD model represented a simplified version of the prototype, details not relevant to the simulation were omitted. The CAD model of the real object consisted of an aluminium housing, internal insulation, a thermogenerator module, and a HSU. The TEG model consisted of two ceramic plates and P-N pairs between them. It was modeled in a simplified manner with the electrical connections between the P-N pairs omitted. This model is shown in the figure 10.1. In part A of the figure 10.1, it can be seen the top view along with the dimensions. Part B of the Figure 10.1 presents the side view with its dimensions, while part C of the Figure 10.1 presents the isometric view on the whole CAD model. In part D a detailed view of the modelled TEG is presented.

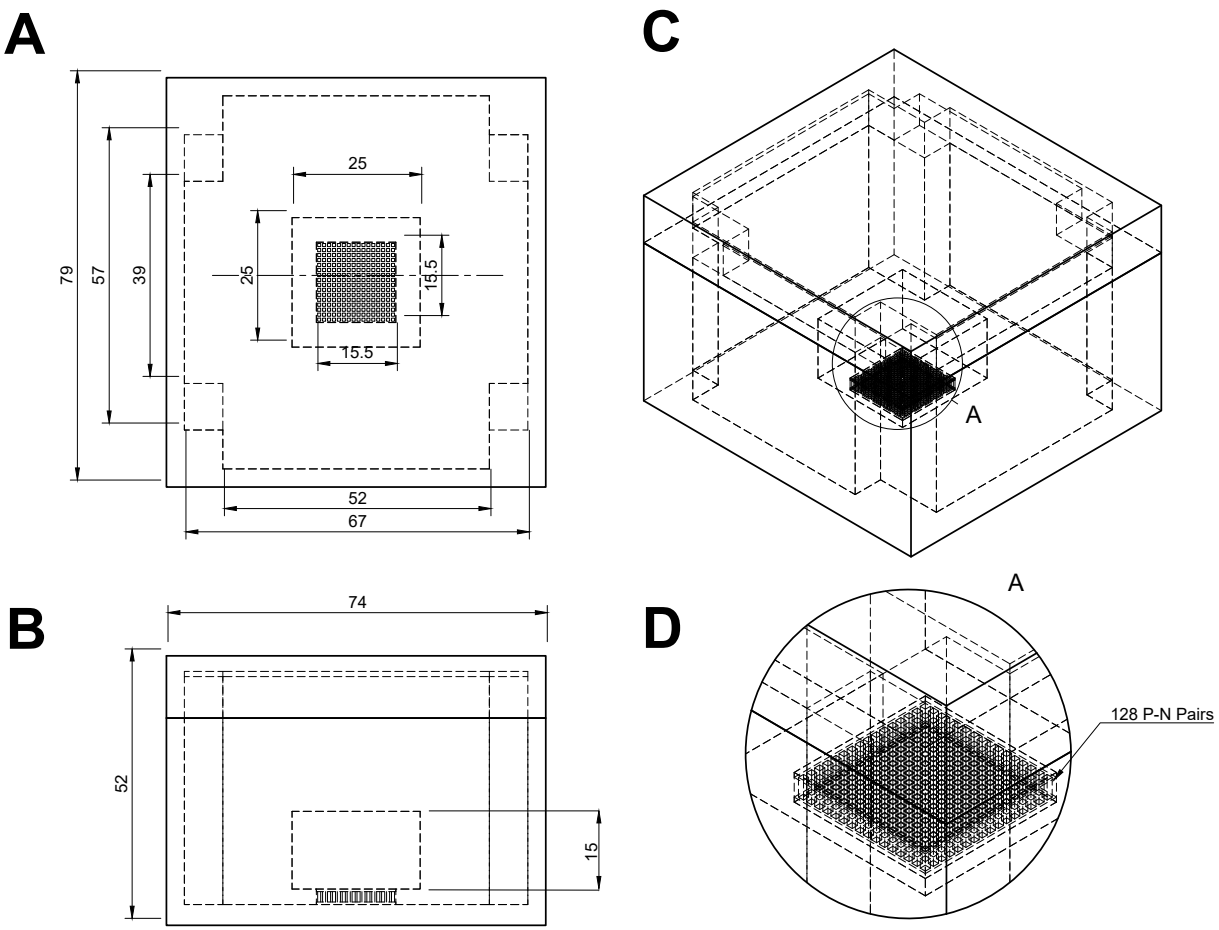

Figure 10.1. CAD model of the physical module.

10.2. Thermal Simulation Setup

The Simscale software package was used to perform the thermal simulations. This is a cloud-based simulation solution developed by SimScale Gmbh that allows for computational fluid dynamics, finite element analysis, and thermal simulations. The software consists of a web-based interface and a computational back-end. The back-end is based on open-source solutions such as Code_Aster and CalculiX for FEA calculations and OpenFOAM CFD software for computational fluid dynamics (CFD) calculations.

Code_Aster with the MUMPS solver was used for simulation studies. Code_Aster is a solution that allows for numerical and thermal analysis. MUMPS – a MUltifrontal Massively Parallel Solver is a parallel library for the solution of sparse linear equations. Multifrontal algorithms are popular for factorisation of linear systems, resulting in a mesh-based computations with the finite element method.

10.2.1. Material Parameters

To perform a simulation using the FEA method, it is needed to define the geometry (CAD model) that is a subject of simulation, as well as define and assign materials to the CAD model. They are the input data for the calculation and can have a great influence on the simulation results. Hence, the proper selection of material parameters is a very important part of the entire simulation process. The selection of these parameters also depends on the specific type of simulation.

In the thermal simulation process described in this chapter, three basic material parameters will be used: density, thermal conductivity, and specific heat, additionally it is also needed to define the type of conductivity – in the case of materials used in this simulation it is an isotropic type.

- Density – density is mass of a unit volume of a material substance, defined as $d = \frac{M}{V}$, where M is a mass, and V is a volume. Commonly expressed in $g \cdot cm^{-3}$ or in $kg \cdot m^{-3}$.
- Thermal Conductivity – Thermal conductivity of a material is a measure of its ability to conduct heat. It also defines the correlation between heat flux per unit area and temperature gradient defined as $Q = -k\Delta T$. Where Q is heat flux per unit area, k is thermal conductivity, and ΔT is thermal gradient. Commonly expressed in $W \cdot m^{-1} \cdot K^{-1}$
- Specific Heat – Specific heat is the energy required to raise the temperature of a unit mass of a substance by 1 K. Commonly expressed in $J \cdot kg^{-1} \cdot K^{-1}$

The material parameters used to build the simulation model are shown in Table 10.1.

Table 10.1. Material parameters selected for the simulation.

Material	d [$kg \cdot m^{-3}$]	Conductivity	k [$W \cdot m^{-1} \cdot K^{-1}$]	C_p [$J \cdot kg^{-1} \cdot K^{-1}$]	Source
Aluminium	2770	Isotropic	235	897	[137]
Aerogel	120	Isotropic	0.025	1500	[138]
Steel	8000	Isotropic	15.1	480	[72]
Bi_2Te_3 (n)	7740	Isotropic	1.5	180	[72], [139]–[143]
Bi_2Te_3 (p)	7740	Isotropic	1.5	180	[72], [139]–[143]
Al_2O_3	3720	Isotropic	25	880	[72], [144]

The material parameters were selected by averaging table values of reference materials, or where there was no table values available – a research on scientific papers has been made and average value has been established. It turned out to be problematic to select the appropriate parameters of the components of the thermogenerator itself. Unfortunately, TEG manufacturers provide very modest – approximate – data on it's construction and materials used. For example, in the Ferrotec Nord TMG-127-0.4-1.6 thermogenerator, the only information available is that it is a thermogenerator constructed on the basis of bismuth telluride (Bi_2Te_3), with ceramic covers based on (Al_2O_3). The manufacturer does not provide accurate material data or information on whether or what (Bi_2Te_3) is doped with. Therefore, a literature review was performed for the desired values of the material parameters. Thermal conductivity, examined in a number of publications

and entries, ranges from 1.25 to almost 2.11 $\mathrm{W} \cdot \mathrm{m}^{-1} \cdot \mathrm{K}^{-1}$. The specific heat, on the other hand, varies from 165 to nearly 200. Therefore, the values of 1.5 and 180 were chosen appropriately. The thermal parameters of (Al_2O_3) were similarly selected by analysing the tabular data available from specific commercially available materials. The Elsevier Knovel material database and the Total Materia database were used for this purpose.

10.2.2. Meshing

The basis for the operation of the finite element method is the division of continuous geometric space by discrete nodes that form geometric cells (discretization of space), these cells usually have a shape of tetrahedron. The number of such cells - and thus nodes - is limited, and by solving the equations describing the desired unknowns for each such node, an approximate solution for the entire geometric region is obtained. Creating a grid of nodes and cells is called meshing. Meshing is one of the most important parts of the FEA analysis process, and hence it must be optimised accordingly.

A well-made mesh is a compromise between computation accuracy and computation time. The denser the mesh, the more accurate the simulation results will be; on the other hand, fewer node points, so a sparser mesh, leads to faster calculations. The following procedure has been performed to generate an appropriate mesh:

1. The geometry of the CAD model has been studied,
2. CAD Cleaning procedure has been performed,
3. The appropriate type of mesh was selected,
4. Preliminary mesh creation was performed,
5. Mesh evaluation was performed,
6. Increase the mesh density in critical areas of the model (sharp edges, small parts).

The initial mesh has been generated using the automatic method provided by Simscale, and the initial simulation has been performed to check the accuracy of the procedure. After the successful initial results, the mesh refinement was performed. The refinements have been made by manipulating the following parameters:

1. Global element size reduction,
2. Local element size reduction,
3. Mesh adjustment,
4. Local mesh refinement.

The mesh quality indicators have been chosen as aspect ratio, non-orthogonality, edge ratio and volume ratio. Each of the parameters is described below.

- **Aspect Ratio** - The Aspect ratio quantifies the quality of the elements, where 1 is a perfectly shaped tetrahedral element and the shape of the element is worse with a higher aspect ratio. By definition the aspect ratio of a tetrahedron K is defined as $\frac{|K|_{max}}{2\sqrt{6}r}$, where $|K|_{max}$ and r, respectively, denote the highest edge length and the inradius of K. Figure 10.2 shows the placement of the tetrahedral cells with the highest aspect ratio in the meshed model.

Figure 10.2. Placement of the tetrahedral cells with the greatest aspect ratio.

– **Non-Orthogonality** - We define non-orthogonality as the angle made by the vector joining two adjacent mesh cells centers, across their common face and the face normal (as presented in the figure 10.3) [145]. It is one of the most critical parameters in both CFD and FEA analysis. High value of non-orthogonality might lead to the not-accurate results of FEA analysis or, in CFD, might cause convergence issues with the whole solution. However, many solvers can compensate this effect with a different methods depending on the solver type or setting. Thus it is important to minimize this parameters below the values specified by a given solver.

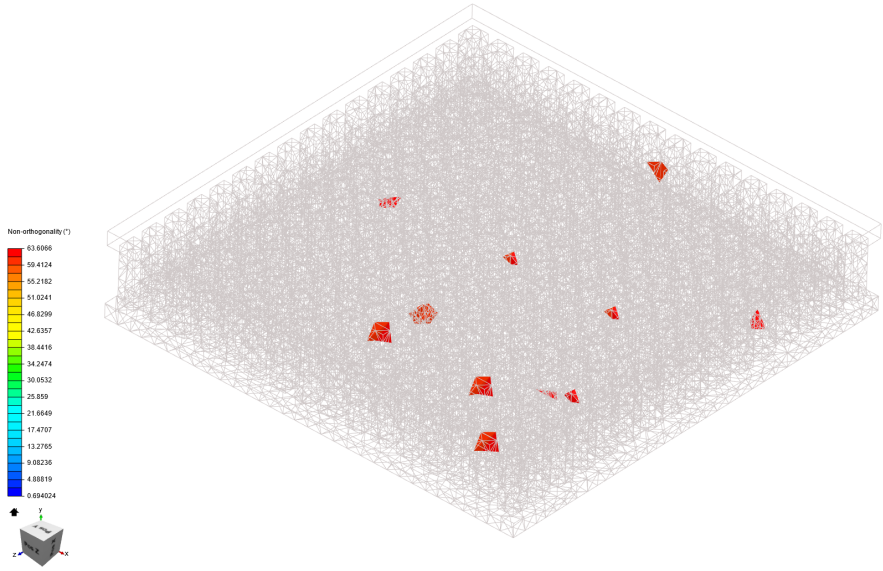

Figure 10.3. Placement of the tetrahedral cells with the greatest non-orthogonality.

– **Edge Ratio** - The edge ratio of a tetrahedron K is defined as $\frac{|K|_{max}}{|K|_{min}}$, where $|K|_{max}$ and $|K|_{min}$ respectively denote the greatest and the smallest edge lengths of K. The edge ratio is shown in Figure 10.4

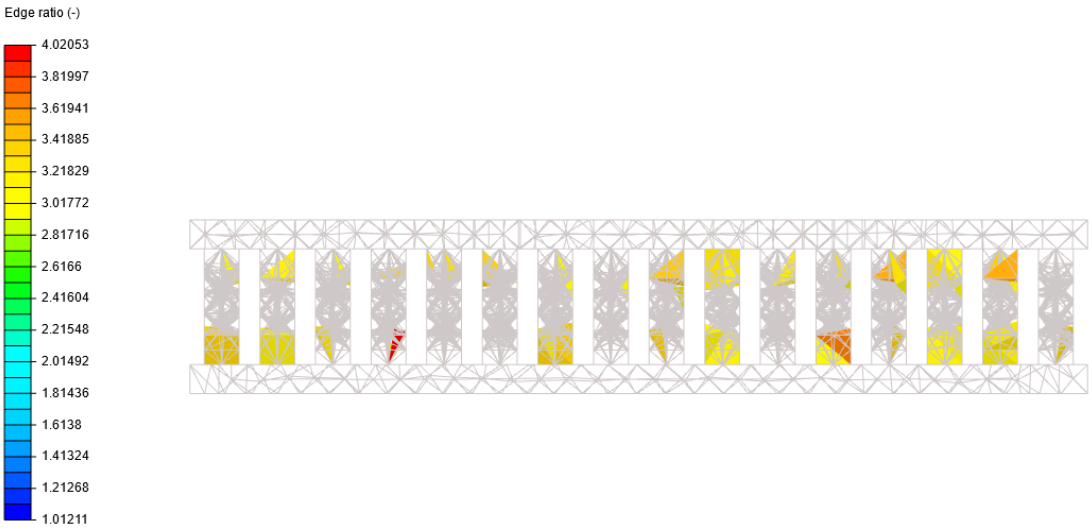

Figure 10.4. Placement of the tetrahedral cells with the greatest edge ratio.

– **Volume Ratio** - Volume ratio of the tetrahedron cell is defined as a maximal ratio between the volume of a given tetrahedron and each of the volumes of its neighbour cells. As an interpretation of volume ratio, it can be stated that it describes how smooth is the transition between small mesh cells and large ones. In the ideal case, this parameter shall be relatively small; however, it should be validated with solver documentation. Figure 10.5 denotes a cell with a volume ratio of 8, which means that its volume is 8 times greater than that of its smallest neighbour. Figure 10.6 presents the tetrahedral cells with the greatest volume ratio in the mesh of the model.

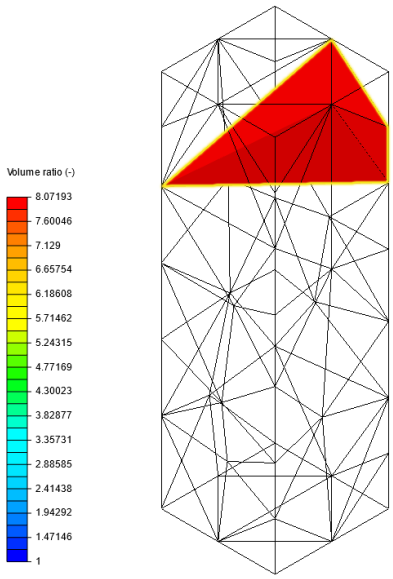

Figure 10.5. Example of a tetrahedron cell with a volume ratio of 8.07 (marked in red), meaning that its volume is over 8 times greater than the volume of its smallest neighbouring cell.

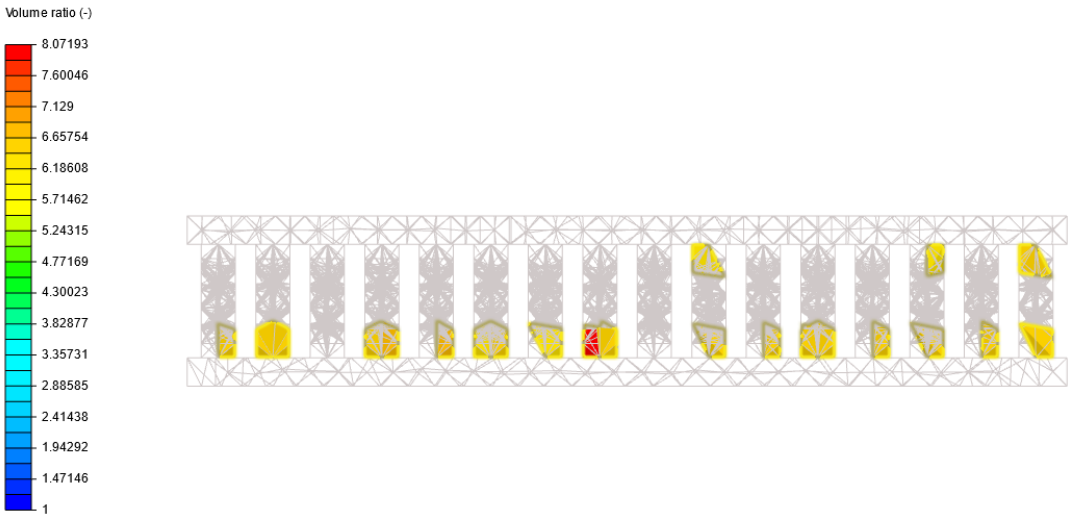

Figure 10.6. Placement of the tetrahedral cells with the greatest volume ratio.

As it is stated in the Simscale documentation, the mesh quality parameters shall be kept in a given range as it is presented in the Table 10.2. Thus, the initial mesh has undergone an mesh refinements to keep the quality factors according to the recommended values. The overall mesh is presented in the Figure 10.7. Figures 10.2 to 10.3 presents the mesh quality evaluation towards. It is worth to mention - all of the parameters are in range of the specification of Simscale [146].

Table 10.2. Recommended values of mesh quality parameters and the results of meshing refinements (maximal value, minimal value and average of each of the relevant parameters) [146].

Parameter	Recommended Value	Mesh value		
		Max	Min	Average
Non-orthogonality	Max. value <75	63	0	17.7
Aspect Ratio	Max value $\ll$ 100	2.9	1.0	1.56
Edge Ratio	Max value $\ll$ 100	4.02	1.01	1.69
Volume Ratio	Max value $\ll$ 100	8.07	1	1.29

While adjusting the parameters, the mesh convergence study has been performed. The parameters have been adjusted until the mesh convergence study showed that mesh converge. It means that the mesh did not produce significant differences in the result when mesh refinement was introduced. The summary of the final mesh used for thermal simulation is presented in the Figure 10.7.

(a)

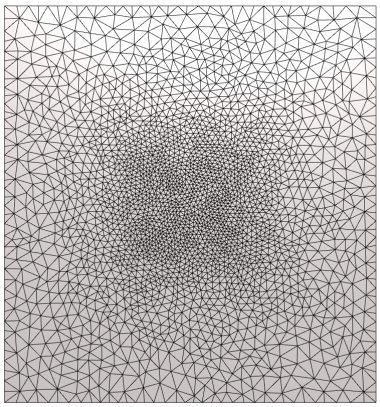

(b)

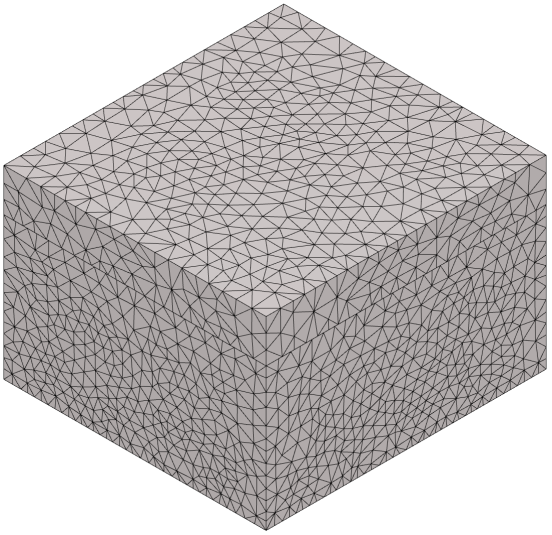

(c)

Figure 10.7. Overal mesh structure (a) - spatial view, (b) - bottom side, (c) - isometric view on the casing of the prototype 3D model

10.2.3. Boundary Conditions

Boundary conditions play a key role in FEA simulation. Their type and parameters define how a system (for example, the structure in which we simulate heat flow) interacts with its surrounding environment. In the case of steam sterilisation, the surface temperature of surgical instruments is a key parameter in terms of sterilisation

efficiency. This is also the boundary condition adopted in the simulations described here, where the boundary condition is the surface temperature of the prototype at its key points. Based on the measurements made in Chapter 9 of this thesis, the temperature of the prototype housing and its changes over time were adopted as the boundary condition. Figure 10.8 shows the temperature set as a boundary condition over time and compares it with the temperature collected from the prototype housing. The boundary conditions have been set to the fixed temperature of the walls of the virtual model.

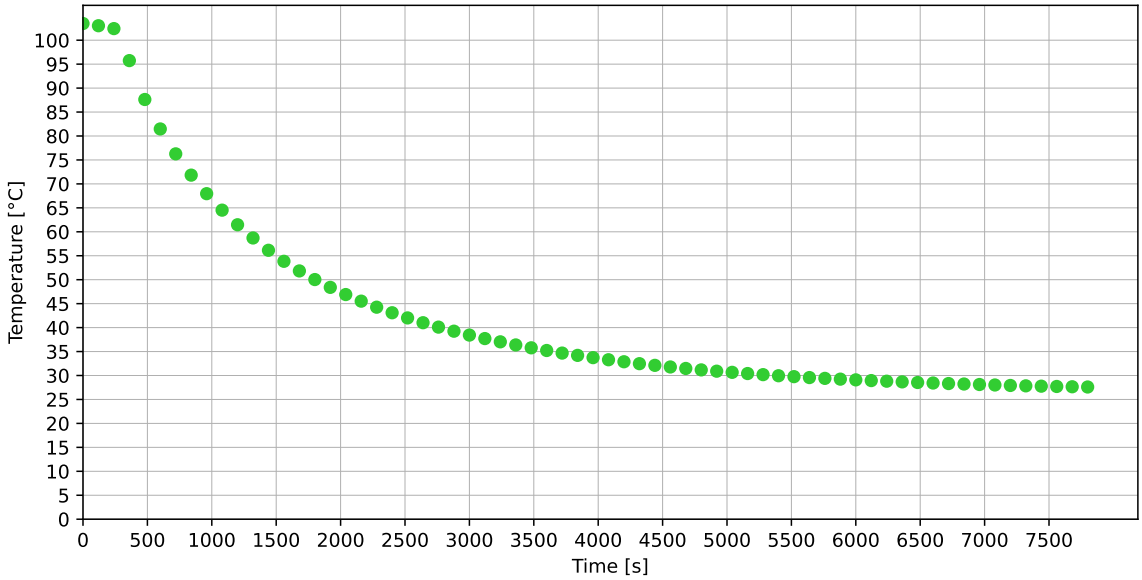

Figure 10.8. Temperature of the virtual prototype walls surface in time set as a boundary condition for temperature step response simulation for model parametrization.

10.2.4. Numeric Setup

Code_Aster offers a number of parameters that can affect the outcome of the simulation, so it is important to choose them appropriately and consciously. Based on the Simscale documentation [147] and literature [148], the parameters that should be properly set before starting the simulation are as follows:

- **Precision Singularity Detection** - Which defines the precision value for the detection of a singular matrix. A singular matrix is a square matrix that cannot be inverted, and thus matrix decomposition cannot progress any further. Such errors often occur when constraints to the analysis model are insufficient, and it is highly important to detect such cases. In the simulation setup, this value has been set to 8, meaning the detection with 10^{-8} precision.

- **Matrix Type** - This parameter determines if the stiffness matrix[1] related to the analysed problem is symmetric or asymmetric. This setting have been set to **Automatic** mode as Simscale documentation suggests.

[1] A matrix representing the linear equations that must be solved in order to ascertain an approximate solution to the differential equation.

- **Memory percentage for pivoting** - Define how much additional memory should be reserved for the pivoting operations. If MUMPS estimates that the necessary space for factorising the matrix would be 100, choosing a value of 20 would mean that MUMPS allocates a memory space of 120.
- **Linear system relative residual** - This settings allows to select the maximum relative residual for each linear system resolution compared to the exact solution. In a nonlinear calculation this setting can be deactivated by selecting a negative value since the quality of the solution is controlled within the Newton method.
- **Preprocessing** - It is possible to preprocess the stiffness matrix to make numerical factorisation cheaper in computing. The optimisations performed include: symmetric permutation, permutations to a zero-free diagonal, and row and column scalings. Each of the pre-processing methods is applied automatically, when needed [149].
- **Renumbering Method** - This option optimises the number of nodes so that the bandwidth of the matrix is as small as possible[2]. In the simulation setup, a SCOTCH renumbering algorithm has been used. SCOTCH is an algorithm build on a basis of the graph theory, with a divide-and-conquer approach, used for mesh optimisation in FEA analysis resulting in stiffness matrix bandwidth optimisation (but not only, it is used in many other scientific computing fields).
- **Memory Management** - This setting relates to the memory management of the MUMPS solver. The option is to use in-core memory - meaning a direct RAM memory in a given computation core will be used, out-of-core - meaning
- **Theta** - The parameter θ is used in Crank-Nicolson method must be ranging between 0.0 (explicit method) and 1.0 (completely implicit method). The standard value of $\theta = 0.57$ is chosen a little higher than $\theta = 0.5$ which would lead to the Crank-Nicolson scheme of order 2. The further explanation of the sense of the theta parameter is provided in Appendix B.

10.2.5. Simulation Run Setup

An important step in preparing the numerical simulation is to take care about the simulation run setup. In the heat transfer scenario, a linear static analysis setup is used. By definition, in this simulation type setup there is no time dependence of the material properties, boundary conditions, and results. The only nonlinearity allowed in the heat transfer simulation scenario is temperature dependency of the boundary conditions and material properties.

Simscale environment offers a set of settings that shall be adjusted according to the preferred simulation scenario. The parameters description and its values used for simulations in this dissertation are as follows:

1. **Pseudo time stepping** - A pseudo time stepping is a technique for solving for the steady-state solution of time-evolving partial differential equations (like theses used in heat transfer model) [150]. The technique is based on setting an initial guess and using a time-stepper to evolve the solution forward. This parameter has two possible settings: "Single Time Step" - indicating that only a single load case is run, and "Stepping List" - allowing to run a list of load cases, ordered by the pseudo time variable. In the transient heat simulation the "Stepping list" setup is chosen and locked, as it essential for transient simulation.

[2]The stiffness matrix of a typical finite element model has zeroes in most entries, except for a band about the diagonal. The bandwidth measures this "spread" of non-zeroes in the matrix. A smaller bandwidth means faster computation. It is usually measured as the maximum distance of any non-zero term in the matrix, from the leading diagonal.

2. **Simulation intervals** - In the transient simulation context it is the end value of the pseudo-time variable, meaning how long the simulation lasts and how long the transient effects should be taken under consideration. In the simulation setup this variable has been set to 9720 s.

3. **Time step length** - in transient simulation context it represents the incremental change in the pseudo-time variable. In the simulation setup this variable has been set to 120 s.

4. **Write control definition** - This setting indicates in which time steps the output result fields shall be written into the results database. During the simulation the selected option was "initial time steps" - meaning that the output is written on the time steps specified in Time step length field.

10.3. TEG Modelling

The second stage of the research after performing the thermal simulations is to simulate the power generation in the TEG with a given simulated thermal gradient. To perform this task, a set of steps must be performed. First, the TEG modelling techniques must be reviewed, and a given TEG modelling technique must be chosen, according to the application requirements. Then, the parameters needed by the model have to be extracted from the TEG datasheet, and finally, the model needs to be fed with the thermal gradients and the power output needs to be registered.

10.3.1. TEG Model Selection

The modelling of thermoelectric generators and thermoelectric coolers is not a new topic. The increasing popularity of energy harvesting techniques, especially thermal energy harvesting in the context of wireless sensor nodes and the industrial Internet of Things (IIoT) , drives the creation of new modelling approaches in this field. Thus, a short review of existing models needs to be done in this chapter, and particular model based on the given criteria needs to be selected. The selection criteria are as follows:

1. Simplicity - model needs to be as simple as possible still preserving the details important for simulation,

2. Accuracy - model needs to hold an accuracy within a low thermal gradients (0 °C - 20 °C) within a low overall temperature range (20 °C - 100 °C),

3. Ability to feed the model with the data extracted from the manufacturer's datasheet.

In case of modelling thermoelectric generators we can distinguish several different modelling techniques which approach the problem from several different points. First, we can model the thermoelectric phenomena itself, then the focus might be put into the modelling of the thermoelectric module only, and finally we can model the thermoelectric module from the system perspective, where it is used as an element of the whole energy harvesting system. Each of these approaches has several different techniques included. First, the modelling of the thermoelectric phenomena itself might be of different complexity. Starting from a simplified thermoelectric phenomenon model taking into consideration global balance of thermoelectric effects and heat transfer. In this simplified approach some of the TE effects are neglected, e.g. the Thomson effect, while the others are kept constant, e.g. the Peltier effect. Simplified models, however, might be improved by including the Thomson effect into the model, which results in better accuracy in the Thermoelectric Cooler application. Finally, the complex approach does not take into account the global energy balance but local energy balances, making the whole model much more complex, but also much more accurate [151]. The introduction to thermoelectric phenomena is presented in the chapter 6 of this thesis. However, this approach

is not within the scope of this chapter, as this chapter is focused on modelling of the TEG from the system perspective. Considering the usability of the model from a system perspective, we consider two approaches in general: analytical and numerical models. The analytical approach can be divided into two categories, and the difference is how we estimate the optimal load resistance of the TEG. In the first category, there is the assumption that the optimal load resistance is equal to the internal resistance of the TEG ($R_{TEG} = R_{load}$). This assumption is presented by authors such as Leonov, who describe a very interesting study on human body heat harvesting and its dependence on several factors such as wind speed, ambient temperature, or clothing [152], the second paper using this approach is the work of Sigrist et al. describing an energy harvesting system for the conversion of small bipolar thermal gradients into electrical energy [153]. Another application using this paradigm is presented in the work of Thielen et al. where authors analyse the energy scavenging from body heat and its processing in power conditioning circuits. The authors have put a great focus on comparing two different approaches, first having a high output voltage, low thermal resistance μTEG combined with a high efficiency active boost converter (LTC25504), secondly having a high thermal resistance, low electric resistance mTEG in combination with a low input voltage coupled inductors-based boost converter (LTC3108) [154]. The approach of matching the internal resistance and load resistance is also present in some of the books related to thermoelectricity [72].

The second category of the analytical modelling approaches assumes that load resistance should not only depend on the internal resistance of the TEG but also take under consideration the TEG's figure of merit. This can be described as $R_{TEG} = R_{load} \cdot \sqrt{Z \cdot \overline{T} + 1}$ where $Z\overline{T}$ is the thermoelectric figure of merit. This approach in analytical modelling is also presented by several authors [155]–[159].

In contrary to analytical models, the numerical models highly depend on the geometry of the thermoelectric generator and heavily use the FEM analysis. For these models, the research is focused mainly on shape, geometry or arrangement optimization of a given TEG/TEC module for a given applications [160]–[163].

An alternative approach for modelling the TEG is to use SPICE software, where the TEG module can be implemented as a transducer device. Such a model can capture both linear and non-linear properties such as material parameters depending on the temperature, leading to the increased prediction accuracy.

For the purpose of this dissertation, several concepts and approaches available in the literature for modeling a thermogenerator have been reviewed. They are described in Section 10.3.1 of this work. The choice of the appropriate method was dictated by the following requirements:

- The method must be simple to implement - This is a requirement driven by the need to make the model usable for industrial purposes, assuming it will be used by R&D personnel not necessarily in the thermoelectric specialty,
- The model must be based on parameters available from the thermogenerator catalog notes so that it can be easily adapted to evaluate new solutions in the market,
- The model must have a compensation mechanism so that adaptation is possible in the event of comparative testing with a real thermogenerator.

Based on the assumed criteria and taking into account the studies available in the literature, it was decided to choose the Kubov model as the model for SPICE analysis of the thermogenerator. Some papers suggest a relatively low overall accuracy of this model, however on the other side it's accuracy in the selected temperature range is satisfactory for this study. The model itself is presented in the Fig. 10.9.

Kubov's TEG Model and its Parameters

The Kubov's TEG model is presented in Figure 10.9. There is a main advantage of Kubov's TEG model – it is symmetric in the SPICE domain, and it is mapped directly with physical phenomena in the Peltier/Seebeck

module (TEG module). Thus, it is relatively easy to follow the process of creation of model itself and process of transfer the concepts and principles of the TEG into the electrical model. According to the paper of Kubov et al. [164] the model can be developed by combining thermal and electrical domains, as it is presented in Figure 10.9.

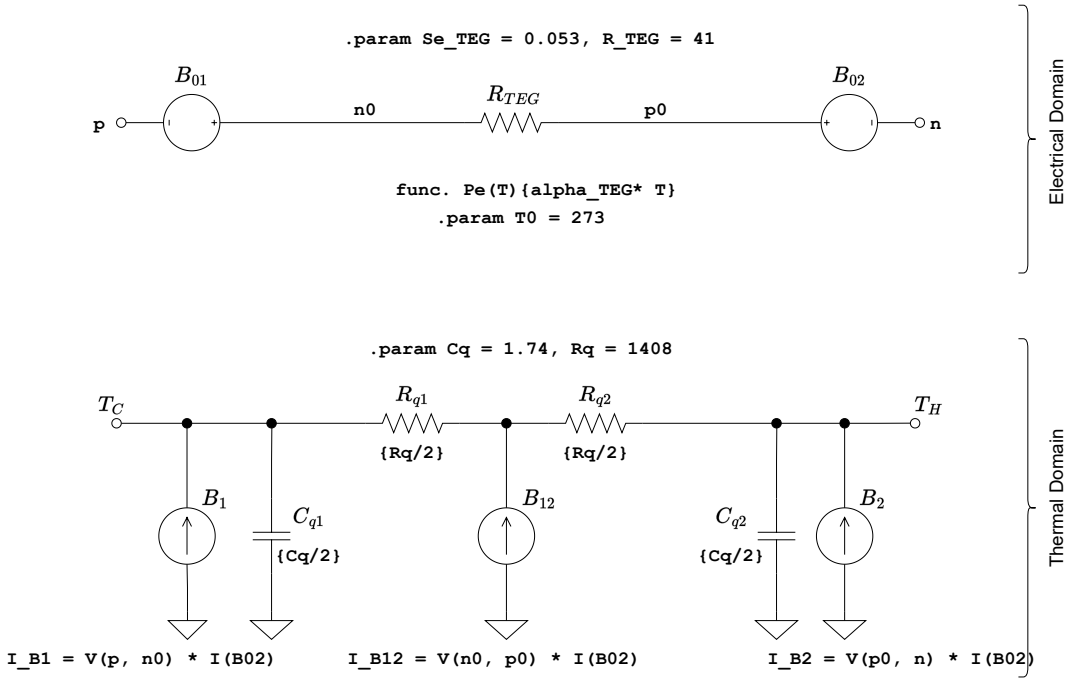

Figure 10.9. SPICE representation of Kubov's TEG model. Electrical domain (top of the figure) represents the electrical properties of the TEG module, while thermal domain (bottom of the figure) represents the thermal properties of the TEG model.

The model itself is relatively easy to understand and it can be described starting from the analysis of the corelation between the heat flow and current in the single Peltier element. As stated in Equation 6.8, in a Peltier element the heat that flows from cold to hot part is proportional to the current and the Peltier coefficient, as presented in Equation 10.1:

$$\dot{Q}_P = \pi_{pn} I \tag{10.1}$$

where π_{pn} represents a Peltier coefficient between p-type and n-type materials, and I represents a current.

This phenomenon can also be expressed as a balance equation of the thermal power, in such a case it would look as follows:

$$\dot{Q}_P = Q_c = -Q_h = \frac{Q_c - Q_h}{2} \tag{10.2}$$

When the hot and cold sides are connected with a thermoelectric material, this causes heat flow from a hot side to the cold side, and thus a generation of electromotive force depending on the Seebeck coefficient α and the temperature difference between the hot and cold side. This can be expressed as the following equation.

$$V_{TEG} = N \cdot (\alpha_{pn} \cdot (T_h - T_c) - I \cdot R_{pn}) \tag{10.3}$$

where R_{pn} is an electrical resistance of a single TE pair, thus the internal electrical resistance of the whole TEG can be defined as:

$$R_{TEG} = N \cdot R_{pn} \tag{10.4}$$

According to the thermoelectric model of the TEG described in chapter 6 Peltier coefficient and the Seebeck coefficient are connected to the Thompson equation as it was shown already in equation (6.9), and depend on absolute temperature T

$$\pi_{pn} = \alpha_{pn} T \tag{10.5}$$

Taking this into account and equation (6.8), it is possible to express the heat flux from the cold side to the hot side as follows:

$$\dot{Q}_P = (\dot{Q}_c - \dot{Q}_h)/2 = \alpha_{pn} \cdot (T_c + T_h)/2 \cdot I \tag{10.6}$$

Where $\alpha_{pn} \cdot (T_c + T_h)/2$ is an average value of Peltier coefficient for two contacts. Taking all of these into account it can be stated, that electromotive force for two opposite switched contacts will be determined by the temperature difference. It can be written down in the formula as follows:

$$V_{TEG} = N \cdot (\alpha_{pn} \cdot T_h - \alpha_{pn} \cdot T_c) = N \cdot \alpha_{pn} \cdot (T_h - T_c) \tag{10.7}$$

Taking into account the internal resistance of the TEG, the equation (10.7), can be formulated as follows:

$$V_{TEG} = N \cdot \alpha_{pn} \cdot (T_h - T_c) - I \cdot R_{TEG} \tag{10.8}$$

According to equations (10.6) and (10.8) an SPICE model has been implemented which consists of two parts representing the electrical domain and the thermal domain, respectively. The electrical domain part of the model consists of two current-driven voltage sources B_{01} and B_{02} representing the Seebeck potential on both sides of the module. Their values depend on the Seebeck coefficient and the hot and cold side temperatures, according to the equations:

$$V_{B_{01}} = \alpha_{TEG} \cdot T_c \tag{10.9}$$

$$V_{B_{02}} = \alpha_{TEG} \cdot T_h \tag{10.10}$$

The resistor R_e represents the electrical resistance of the module. The thermal domain consists of two resistors R_{q1} and R_{q2} representing the thermal resistance of the module, capacitors C_{q1} and C_{q2} representing the thermal capacitance of the module. The voltage-driven current sources B_1 and B_2 represent the heat consumed on the cold side of the module and the heat generated on the hot side of the module (when working as the thermoelectric cooler). The voltage-driven current source B_{12} represents the Joule heating from the electrical resistance of the module R_{TEG}. The parameter R_q represents the internal thermal resistance, while C_q represents the thermal capacitance of the whole module ($C_q = C_{q1} + C_{q2}$). With the letters **p** and **n** a positive and negative terminal of the module is marked, while T_c and T_h denote the low- and high-temperature sides of the module.

As mentioned above, all of the TEG parameters have been estimated on the basis of the only manufacturers data sheet and general material parameters. This method has been chosen to provide also a possibility to test any of the potential TEGs available in the manufacturers' offer. In the case where the most important parameters would be missing from the TEG datasheet, the needed calculations have been provided based on the work of Lineykin et al. [74]. The Kubov model requires to provide several parameters which can be calculated from the manufacurer's datasheet. All the parameters are both for thermoelectric generator (TEG) and thermoelectric cooler (TEC) as both devices can be used interchangeably. These parameters include:

1. $R_{TEG/TEC}$ - internal resistance of TEG or TEC module

2. $\alpha_{TEG/TEC}$ - Seebeck coefficient of the TEG or TEC module
3. $\Theta_{TEG/TEC}$ - thermal resistance of the TEG or TEC module

For each of the listed parameters equations using the manufacturer datasheet data are provided based on the work of Lineykin [74]. Equations (10.12), (10.14), (10.15) are usefull in the case of using TEC module, while equations (10.11), (10.13), (10.16) are useful in the case of TEG module.

Despite the electrical resistance of the TEG is usually given in the datasheet it can be also calculated from the TEG matched voltage and power at the matched load according to the equation:

$$R_{TEG} = \frac{V_{load}^2}{W_{load}} \tag{10.11}$$

where V_{load} is matched voltage and W_{load} is a power with the matched load attached. It might be a case, according to that instead of using Thermoelectric Generator, we would need to use thermoelectric cooler. In small thermal gradients, thermoelectric coolers might behave as thermoelectric generators. In such a case, it is possible to calculate the internal resistance of optimal performance and the maximum output voltage according to the following equation:

$$R_{TEC} = \frac{V_{max}}{I_{max}} \cdot \frac{T_h - \Delta T_{max}}{T_h} \tag{10.12}$$

Where:

V_{max} - DC voltage that will produce maximal possible ΔT, at the thermoelectric cooler (TEC) [A]

I_{max} - DC current that will deliver maximal possible ΔT, at the TEC [A],

T_h - estimated hot side temperature of the TEC [K],

ΔT_{max} - largest temperature difference that can be obtained between hot and cold side of the TEC [K].

The next parameter needed for the Kubov model is a Seebeck coefficient, expressed in Figure 10.9 as **`alpha_TEG`**. This parameter can be calculated as:

$$\alpha_{TEG} = \frac{2 \cdot V_{load}}{T_h - T_c} = \frac{2 \cdot V_{load}}{\Delta T} \tag{10.13}$$

In case of using thermoelectric cooler, Seebeck coefficient can be evaluated from equation as follows:

$$\alpha_{TEC} = \frac{V_{max}}{T_h} \tag{10.14}$$

One of the key parameters of the Kubov model is a thermal resistance of the TEC, Θ_{TEC}, depicted in Figure 10.9 in the thermal domain as **`Rq`**. Thermal resistance of the TEC can be calculated using following formula:

$$\Theta_{TEC} = \frac{\Delta T_{max}}{I_{max} \cdot V_{max}} \cdot \frac{2 \cdot T_h}{T_h - \Delta T_{max}} \tag{10.15}$$

For the TEG however, the thermal resistance can be derived with the following equation:

$$\Theta_{TEG} = \frac{R_{TEG}}{\alpha_{TEG}^2} \cdot Z \tag{10.16}$$

Where:

R_{TEG} - electrical resistance of the TEG [Ω],

α_{TEG} - Seebeck coefficient of the TEG [$V \cdot K^{-1}$],

Z - figure of merit of the TEG.

TEG model simulation setup

Simulations of the TEG module have been performed in the LTSpice software. The simulation setup is presented in the Fig.10.10 and the detailed SPICE netlist source code is presented in the listing in Appendix C. As can be seen in Figure 10.10, the TEG parameters have been calculated and set with Cq as a heat capacity, Rq as thermal resistance, Se as Seebeck coefficient, and R0 as internal resistance of TEG. Then two programmable voltage sources V_{TH} and V_{TC} have been attached simulating a temperature on the hot and cold side, respectively. Finally, the simulation parameters have been set to the operating point analysis (.op).

The simulation has been performed by applying given gradients across the thermal input of a model. The step was set as 1 °C. The simulations have been performed in three different configurations. In the first configuration, an open circuit voltage TEG setup has been simulated, the simulated value was only the voltage on the output of the TEG. In the second simulation setup, a load resistor of 32 Ω has been connected to the output of the TEG; this case simulated the optimal power matching scenario. Each setup has been then simulated with the thermal gradients from 1 °C to 75 °C.

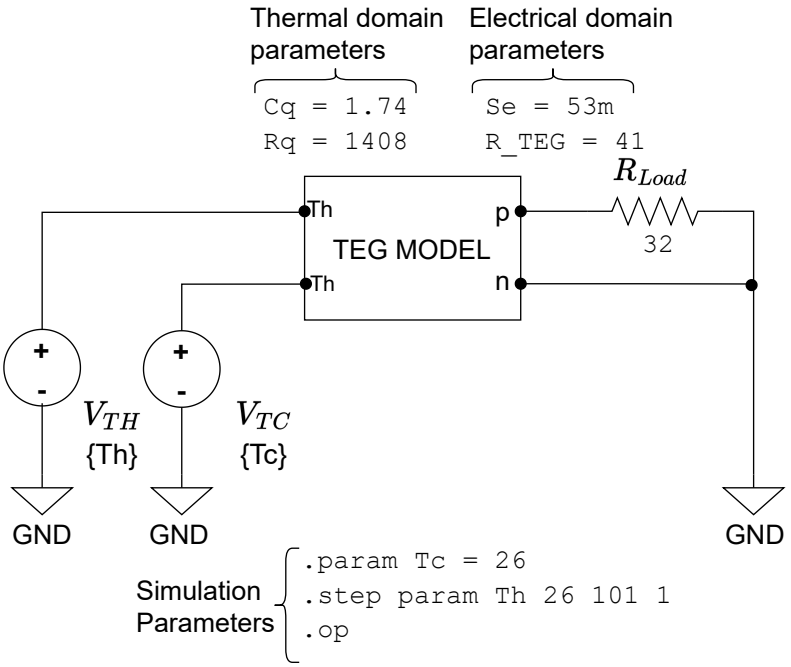

Figure 10.10. TEG simulation setup.

11. Results and Validation

Abstract

In this chapter, results from measurements of the physical model are presented and compared with the results of simulations to validate simulation accuracy. First a thermal simulation results of the virtual model are compared with the physical model measurements. The simulation inaccuracy remained within the bonds of the measurement error (± 1.64 °C). Next the simulation of the TEG with OCV and with a load resistance is presented and compared with the physical measurements. The Kubov model evaluation is performed, and the results are discussed. Finally, a set of simulations is performed to investigate the influence of the insulation thickness and HSU height on the thermal gradient possible to achieve across the TEG.

Outcomes of this chapter: In this chapter, the simulations are validated by comparison with the measurements acquired with the physical model of the energy harvesting system and from the TEG characterisation. Finally, it was investigated that the influence of the HSU height on the possible thermal gradient generated across the TEG is much higher than the influence of insulation thickness.

In this chapter, the results from physical prototype characterisation measurements and results of numerical simulations are compared.

First, a virtual model comparison with the physical prototype is performed to establish a reliable model for heat transfer inside the prototype. When the heat distribution inside the model is known, it is possible to simulate the TEG behaviour and estimate the generated electrical power. To do this, the results of the TEG virtual model have to be compared with the laboratory results gathered in the process of TEG characterisation. After this stage is completed and the results are comparable with the physical TEG model, a simulation of the full steam sterilisation cycle can be performed. On the basis of these data, it is possible to evaluate if the minimal gradient needed for the sensor electronics is achieved during the whole steam sterilisation process.

11.1. Virtual Model Validation Results

As it can be seen in the Figure 11.1 the results of the virtual simulation converges with the results of the laboratory measurements of physical model. Results of the simulations are not precisely the same as the measured temperatures in the laboratory, however, they stay within the measurement errors of the used thermocouples. On the basis of these results, it can be stated that virtual prototype model is accurate enough to proceed with the simulations. Other possible explanation of the small differences between the simulation and the laboratory measurements is numerical and mesh setup of the simulation, probably there is still a space for doing further optimisations in this area, however, the improvements are not expected to be significant. The other explanation could be the inaccuracies of the thermal measurements using thermocouples. It is worth noting that the thermocouples are not connected directly to the surface of the given prototype material, there

is a very thin layer of thermal paste in between, which could also affect the measurements. Finally, the material parameters could affect the simulation results as well, as the tabelary data can differ from the real material parameters, especially it is possible in the thermal properties of the TEG module, where the thermal conductivity and capacity of Bi_2Te_3 might significantly differ depending on the doping of the bismuth telluride, its manufacturing process and the manufacturers quality standards; also values taken from the literature differs relatively a lot. All of these factors could affect the quality of the simulation and improving each of them could lead to more accurate results. However, results obtained in this simulation, material, and measurement setup are accurate enough for the purposes of this Ph.D. dissertation project.

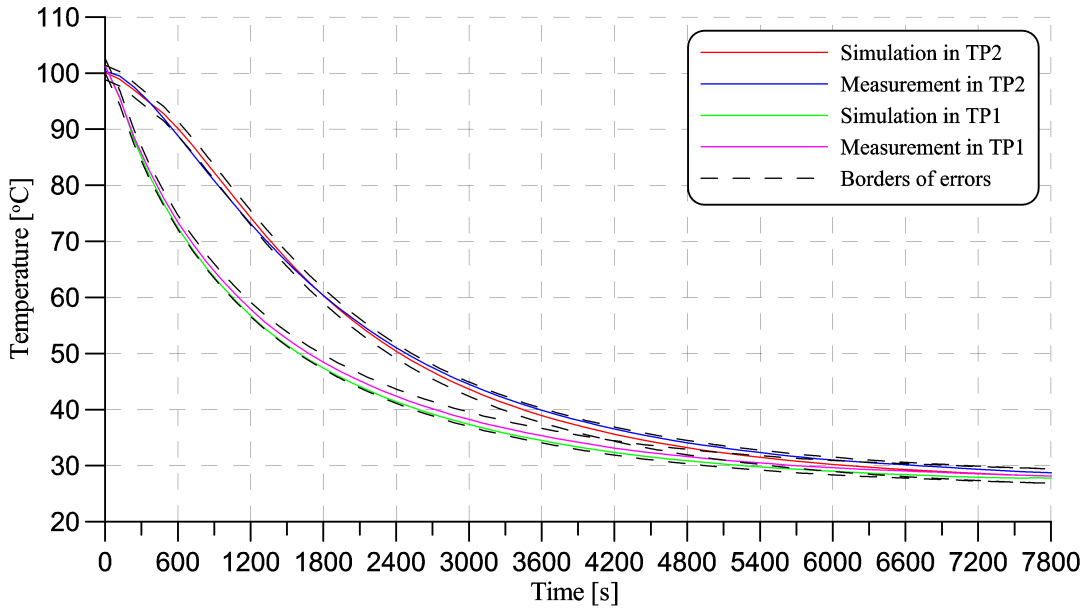

Figure 11.1. Validation of the virtual model compared with the measurements of physical prototype.

With the experimental and simulation data collected, the procedure for system identification and determination of time constants was carried out. To determine the transmittance function, we loaded the experimental data into Matlab and preprocessed. The constant component, which is the ambient temperature (26 °C), was removed from the experimental data to fit the Simulink step function. After this compensation, the temperature step was therefore in the range of 76 °C to 0 °C. A circuit was then built in Simulink software with two transmittances and a step enforcement on the input. The initial step parameters were adjusted accordingly so that, at equilibrium, the measured and simulated values coincided. The time constants of both transmittances were then manipulated to achieve results as close as possible to the measured values. The value of the normalised root mean square error (NRMSE), topped up to unity, was used as a validation criterion. In this assumption, 100 % represents a perfect fit.

As can be seen in Figure 11.2 for TP1, the accuracy of the fit function with the measurements is 94.49 %. This result is mainly due to the non-linearity seen in the initial stage of the temperature step response. This non-linearity was probably due to the measurement method and had to do with the transfer of the physical model from the thermal chamber to the rack on the laboratory table. Another reason for this non-linearity could also be the contact between the room-temperature rack and the heated module, which caused the module to lose heat rapidly during the initial phase of the temperature jump. Although the contact area between the rack and the module is minimised, this cause seems likely. Finally, a third possible cause of the nonlinearity could also be the thermoelectric phenomenon occurring in the thermogenerator, directly at which the thermocouple was located.

The fit in TP2 and TP3 already shows much better accuracy, since the NRMSE at these points is 96.24 % and 97.11 % respectively. At point TP1, there is one dominant time constant of T_{TP1} = 900 s. For measurement point TP2, there are two time constants, $T1_{TP2}$ = 2000 s and $T2_{TP2}$ = 330 s. In the case of the measurement point TP3, there are also two time constants of $T1_{TP3}$ = 1750 s and $T2_{TP3}$ = 700 s respectively. It is worth noting that at the TP3 point, the system has the highest inertia, which is in line with prediction and intuition. In the case of the time constant at TP2, it is worth noting that it is larger than the time constant at TP3, which is due to the heat flow from TP3 through TP2.

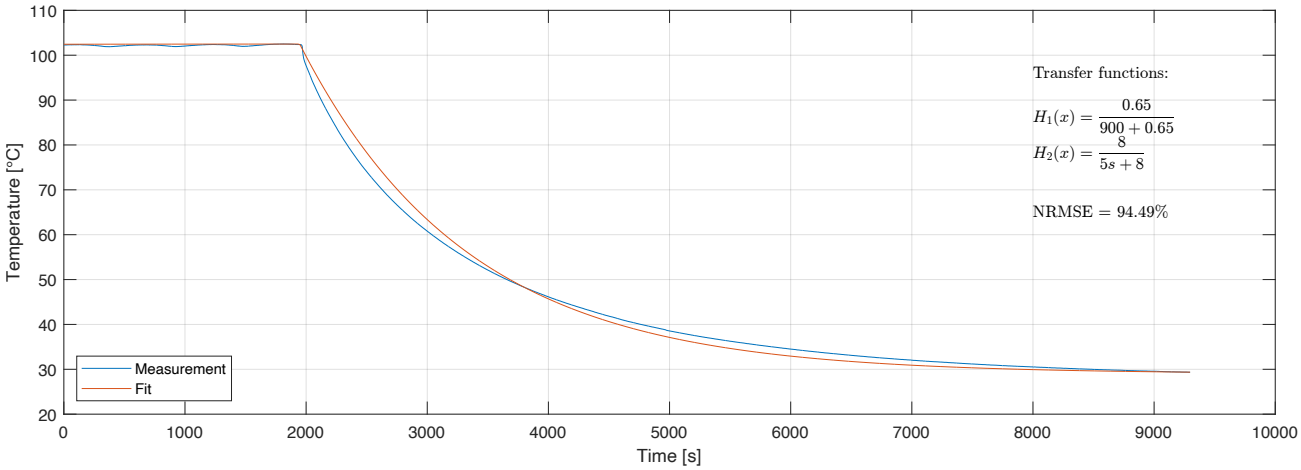

Figure 11.2. Identified transfer functions of the thermal step response in test point TP1 (between the physical model casing and the TEG).

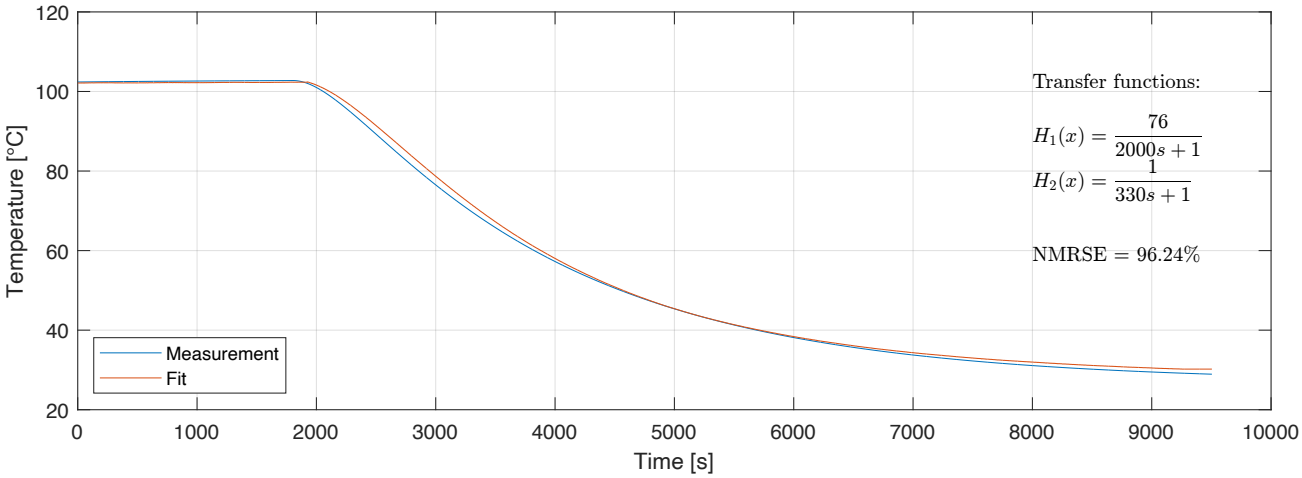

Figure 11.3. Identified transfer functions of the thermal step response in test point TP2 (between the physical model TEG and the HSU).

As it is visible in Figures 11.2 - 11.4, the character of the system response is as similar as it was anticipated, with small inaccuracies coming from non-linearity phenomena in the beginning of the step response. This, as well as general convergence of the thermal simulation step response results with measured real-world data, allows us to proceed with the validation of the TEG model itself.

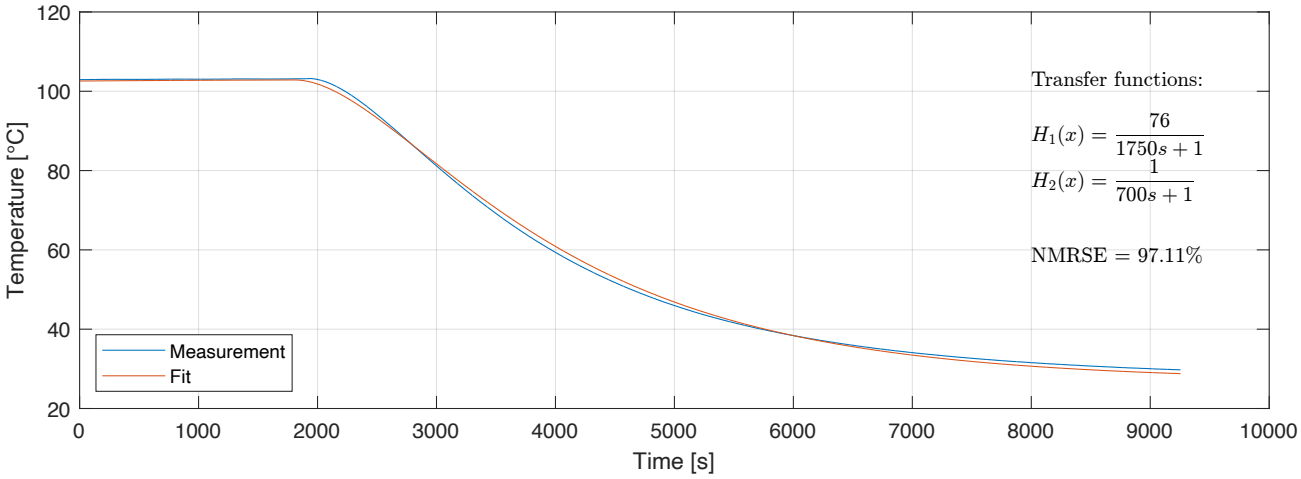

Figure 11.4. Identified transfer function of the thermal step response in test point TP3 (between the physical model HSU and the insulation layer).

11.2. TEG Model Validation

After having a virtual model of the whole device parametrised and evaluated (Chapters 8 – 10) the next step was to parametrize and evaluate the TEG SPICE model. The procedure involved creating a set of simulations using the Kubov's SPICE TEG model and performing a set of laboratory experiments using the selected TEG model. The validation procedure was divided into three steps. First a simulation using only the data acquired from the TEG datasheet (R_{TEG} = 32 Ω, α_{TEG} = 0.056 V · K^{-1}) have been compared with the physical measurements. In the second step, an internal resistance and Seebeck coefficient measured in the real device (R_{TEG} = 41 Ω, α_{TEG} = 0.053 V · K^{-1}) have been used for simulations. Finally, the results from both steps have been compared and the relative error calculations have been performed for the second step.

The acquired laboratory measurement data and the virtual simulation data are presented in Figure 11.5. As it can be seen the simulation is not satisfactory. It was prooven that the declared Seebeck coefficient on the manufacturer's datasheet differs from the Seebeck coefficient of the physical TEG device, the same applied with the internal resistance, leading to significant differences between the measured and simulated values as it is presented in Figure 11.6. After adjusting TEG internal resistance to the measured value (R_{TEG} = 41 Ω) and the Seebeck coefficient of the module to 0.053 V · K^{-1}, the simulation converged with the measured data within acceptable error range as presented in Figure 11.7. Despite this simulation is not a perfect one, it is accurate enough for the application needed in this Ph.D. dissertation.

The inaccuracies might be explained due to several reasons. First of all, the parameters declared by the manufacturer might differ from the reality, as it happened in this case and had to be adjusted. The second reason is that the measurement setup has its flaws and inaccuracies. The assembly of the measurement setup and a presence of thermal grease with the top of thermocouple between the radiator and the TEG and between the TEG and the heating plate could affect the measurements. The other reason is the quality of the TEG module, which might be affected by the different ageing mechanisms while being stored for a longer time. The third and possibly the most important factor affecting the quality of simulation in comparison to the laboratory measurements is the inaccuracies and limitations of the Kubov model itself. Although very simple and practical to implement the Kubov model has its limitations and it cannot be used in every temperature range, as was presented in the work of Posobkiewicz et al. [165].

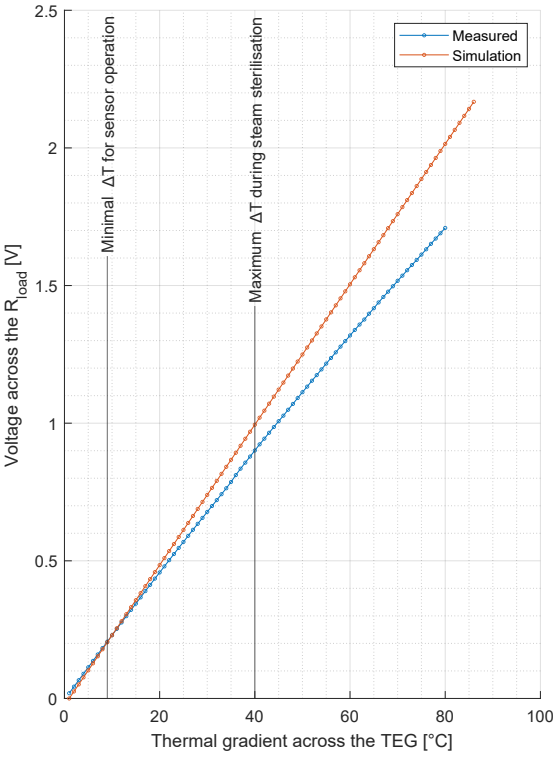

(a) Output voltage V_{out} of the TEG as a function of thermal gradient

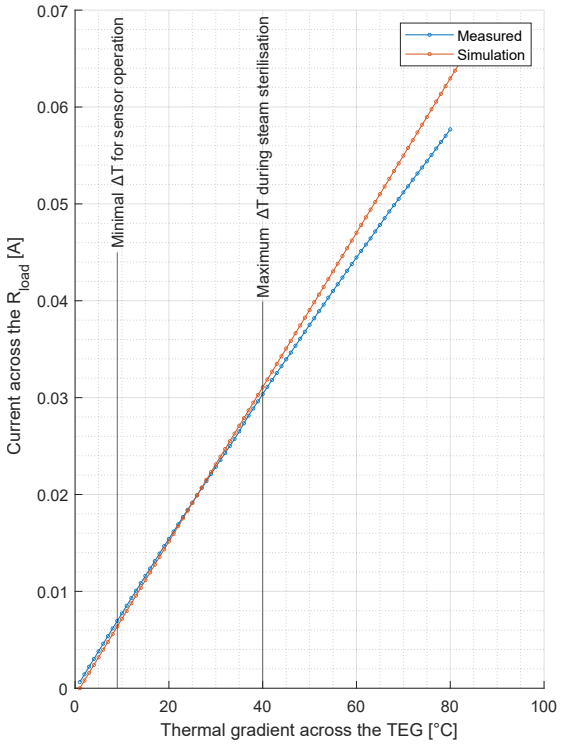

(b) Output current I_{out} of the TEG as a function of thermal gradient

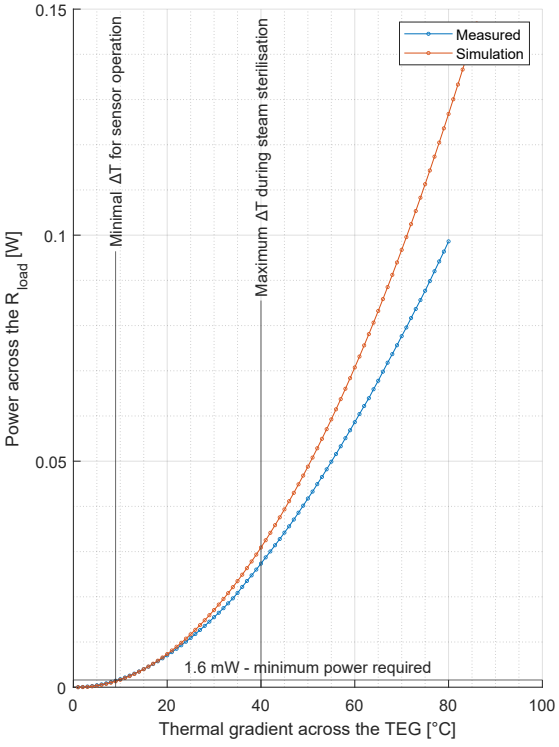

(c) Output current P_{out} of the TEG as a function of thermal gradient

Figure 11.5. Kubov's model validation under a load R_L = 32 Ω equal to the R_{TEG} of 32 Ω and α_{TEG} of 0.056 $V \cdot K^{-1}$ as declared in the manufacturer's datasheet. Kubov's model tends to be inacurrate in the thermal gradients higher than 40 °C.

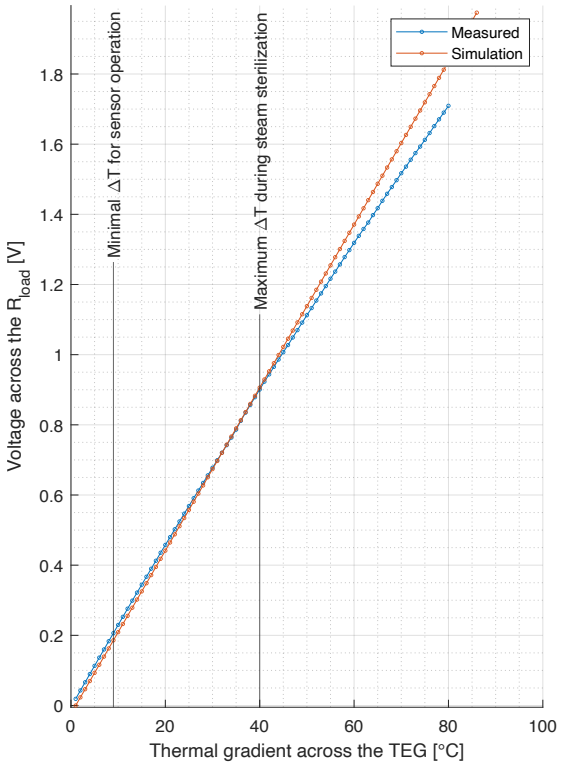

(a) Output voltage V_{out} of the TEG as a function of thermal gradient

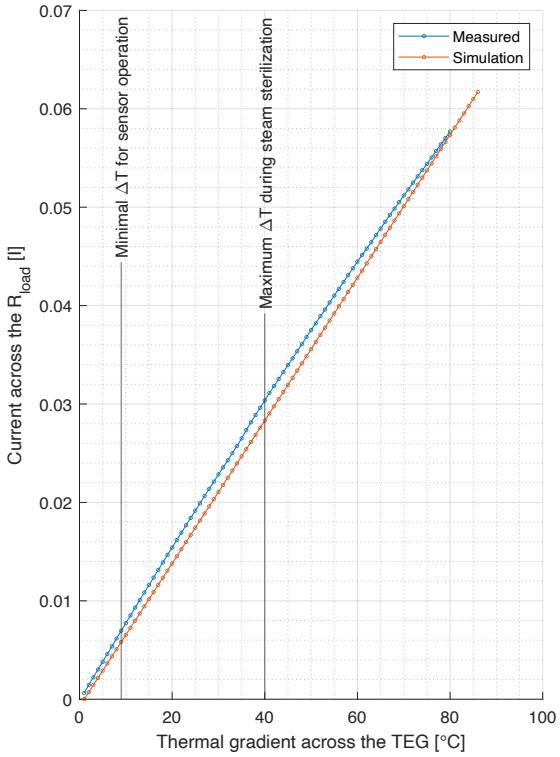

(b) Output current I_{out} of the TEG as a function of thermal gradient

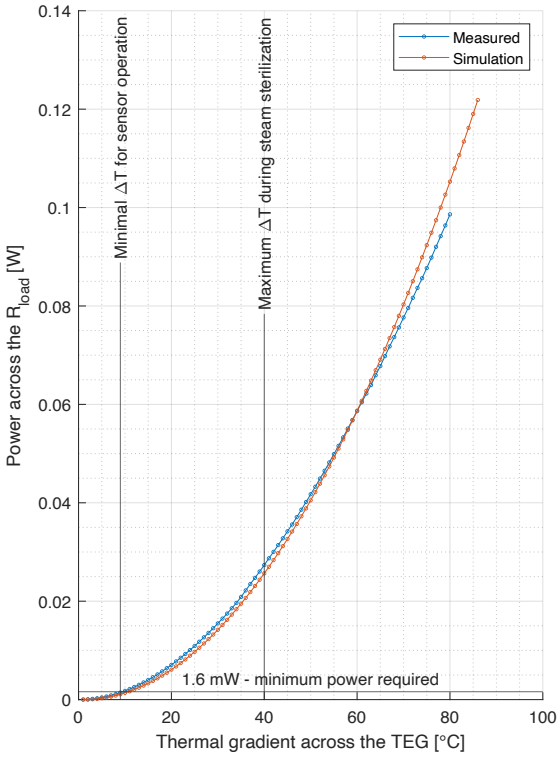

(c) Output current P_{out} of the TEG as a function of thermal gradient

Figure 11.6. Kubov's model validation under a load R_L = 32 Ω after adjustment of TEG internal resistance R_{TEG} to 41 Ω and the Seebeck coefficient α_{TEG} to 0.053 $V \cdot K^{-1}$.

There have been observed errors between the simulation and the TEG measurements performed on the test bench. This was expected due to the limited accuracy of the Kubov model and the inaccuracies of the physical parameters measurements. Thus, errors have been calculated for voltage, current and power simulated in comparison to the values measured. The simulation relative errors (in %) are given by the formula:

$$E_{s\%} = \frac{|m - s|}{r} \cdot 100 \tag{11.1}$$

Where:

m – measured value of voltage, current and power

s – simulated value of voltage, current and power

r – measurement range of voltag, current and power

All the errors are presented in Figure 11.7. Maximum errors and average values are summarised in Table 11.1.

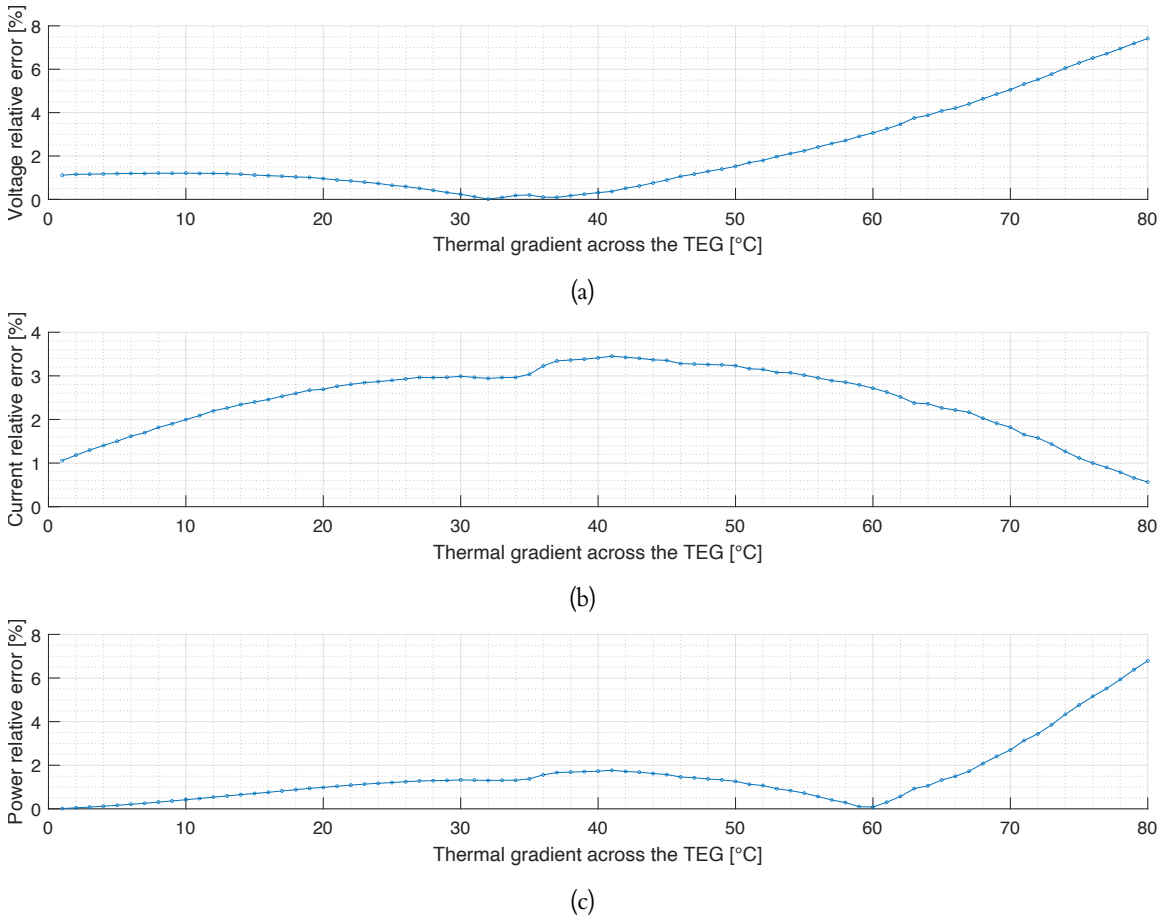

Figure 11.7. Modelling errors of voltage (a), current (b), and power (c) for the TEG simulation with adjusted parameters based on measured internal resistance and Seebeck coefficient, with load of 32 Ω attached.

Table 11.1. Comparison of modelling errors of TEG voltage, current and power.

Parameter	Max. Error [%]	Average Error [%]
Voltage	7.42	2.11
Current	3.45	2.46
Power	6.78	1.52

As can be seen in Table 11.1 the modelling error is the highest in the case of voltage reaching 8.78 %. However, this error occurs for the thermal gradient of 80 °C. According to the thermal simulations of steam sterilisation conducted, the maximum thermal gradient occurring throughout the TEG module is not greater than 70 °C. For such a gradient, the relative error in case of TEG voltage is 6.5 % which is an acceptable error for further simulations. The occurrence of such error was expected because the Kubov model does not take into account thermal dependency of the physical parameters of the TEG. As the literature [135] shows, these parameters can vary significantly. This was also observed in this work, while measuring TEG internal resistance that varied from 39 Ω to 44.26 Ω and for modelling an average value of 41 Ω has been selected. A similar phenomenon can be observed with the Seebeck coefficient and thermal resistance of the modules, according to the literature. All these factors are influencing the inaccuracies of the Kubov model; however, for the purpose of this thesis the maximal relative errors presented in the Table 11.1 are within an acceptable range. It is also worth mentioning that Kubov's model does not take into account the change in physical parameters under the influence of temperature, while it has been proven that such changes can be significant in the case of resistance and can be up to 80 % [135].

11.3. Steam Sterilisation Boundary Conditions

Boundary conditions play a key role in the FEA simulation. Their type and parameters define how a system (for example, the structure in which we simulate heat flow) interacts with its surrounding environment. In the case described, the environment that defines the boundary conditions for the simulation performed was the interior of a medical autoclave during steam sterilisation. The process of such sterilisation is regulated by appropriate standards in Europe: EN285, and therefore, the boundary conditions must have reference to these standards. In the simulations described here, such a boundary condition was the surface temperature of the tools inside the autoclave, and is presented in Figure 11.8.

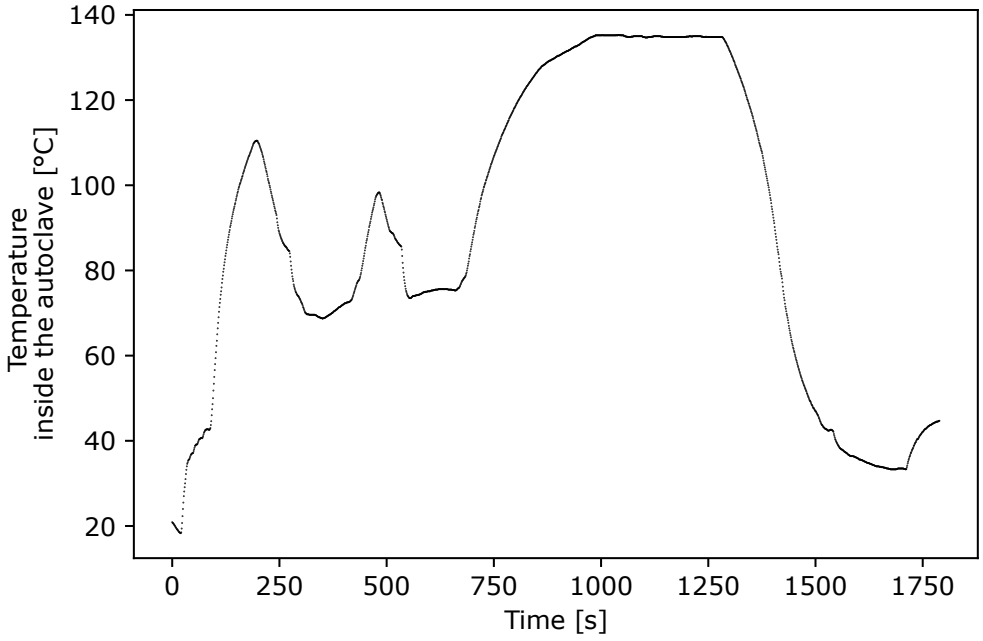

Figure 11.8. Steam sterilisation temperature as a boundary condition in the simulations.

11.4. Sterilisation Simulation Results

After parameterisation of both the prototype and the TEG the simulation of the whole sterilisation cycle was performed. As an input boundary condition, a temperature measured inside the autoclave has been applied. Then the temperature on both sides of the virtual model of the TEG has been registered. The simulation results are presented in Figure 11.9. As can be seen in the picture, the thermal gradient is positive in the first part (during the sterilisation phase) and negative after the device is withdrawn from the sterilisation chamber. With green lines, a minimal thermal gradient for operation of electronics is marked. The red line on the X-axis depicts the time when the gradient is sufficient to power the sensor electronics. As can be seen in the picture, for the entire steam sterilisation time, the minimal thermal gradient is achieved. What is more important, the thermal gradient is still present in the drying phase of the steam sterilisation, when the outside temperature is lower than the inside temperature of the prototype.

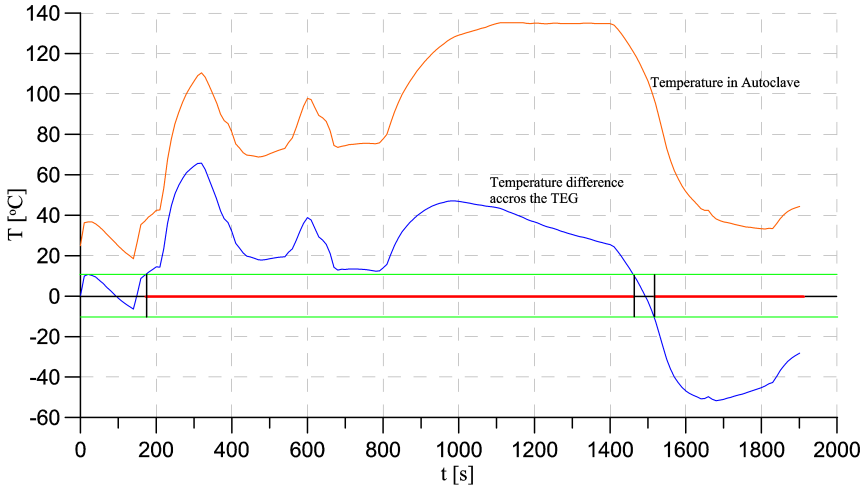

Figure 11.9. Thermal gradient across the TEG during the simulated steam sterilisation process.

11.4.1. Effect of insulation thickness on temperature gradient

After performing a simulation of an initial steam sterilisation procedure on a virtual model of the module, it was possible to investigate how the size of the HSU and the width of insulation affect the performance of gradient generation. A set of simulation experiments has been performed by analysing different insulation thicknesses and sizes of the heat storage unit.

The simulations carried out were preliminary. The aim was to see how the thickness of the insulation and the height of the HSU affected the amount of temperature gradient through the thermogenerator. On the basis of these results, detailed simulations of the amount of energy generated and the feasibility of powering the sensor module were carried out in subsequent steps.

In the first step, several simulations of the sterilisation process were performed for different versions of the virtual model, differing in the thickness of the thermal insulation with all other parameters unchanged. Simulations were carried out for four HSU heights: 5 mm, 10 mm, 15 mm and 20 mm. Four different thermal insulation variants were used for each:5 mm, 10 mm, 15 mm and 20 mm. For each simulation, the temperature gradient through the thermogenerator (the temperature difference between the two sides of the thermogenerator) was calculated. The purpose of the simulations was to see how the magnitude and course of the resulting gradient depended on the thickness of the thermal insulation. The results of each of these simulations are presented in Figures 11.10 - 11.13. In each figure, the temperature course of the steam sterilisation

process and the waveforms of 4 gradients for 4 different insulation thicknesses are marked with a dark grey line. Each figure is also divided into an area when the medical container with the module under examination is during the sterilisation process and during the drying phase. In addition, the green line indicates the size of the gradient at which the TEG generates the power necessary to power the sensor in active mode based on the power consumption calculated in Section 8.3.1. The quantitative analysis was performed at the six characteristic points (p1 – p6) marked at the top of the figure. These points correspond successively to the first temperature peak during the steam entry process (p1), the local temperature minimum (p2) during the air depressurisation process, followed by the second temperature peak (p3), the second local minimum (p4) and, finally, the temperature just before the start of the sterilisation plateau phase corresponding to the highest gradient and the temperature at the end of the sterilisation plateau phase (p5) and the start of the drying process (p6). At each of these points, the values of the temperature gradients were read and then compared with each other in a table (see Table 11.2 to 11.5).

The MAPE index (Mean absolute percentage error) was also used, which tells how the gradient curve differs from the autoclave temperature curve. MAPE have been calculated using following equation:

$$MAPE = \frac{1}{N}\sum_{n=1}^{n}\left|\frac{T_s - T_g}{T_s}\right| \cdot 100\% \tag{11.2}$$

where:

T_s – temperature value of sterilisation at a given point,

T_g – value of thermal gradient across the TEG,

n – given sample index,

N – number of samples.

The smaller the value of the MAPE index, the greater the overall gradient on the TEG and the better the power generation efficiency. Each figure also indicates in what percentage of the overall sterilisation process time the temperature gradient on the thermogenerator exceeds the minimum needed for the sensor to operate in active mode ($\Delta T_{A\%}$). This has been calculated for each of the thermal insulation thicknesses.

The first of the simulated variants was for a 5 mm HSU as presented in Figure 11.10. According to the simulation procedure, simulations were carried out for 4 different insulation variants. The first conclusion from the simulations is that, even with 20 mm insulation, the module is not able to generate the power needed to power the sensor in active mode during the entire length of the sterilisation procedure, but only for 56 % of its length. In the case of 5 mm thick insulation, this percentage drops to 50.97 %. Another observation is also that the thickness of the thermal insulation in the case of a 5 mm HSU only slightly affects the efficiency of the power generation process giving a difference of only 5.88 % in the length of time the sensor is powered.

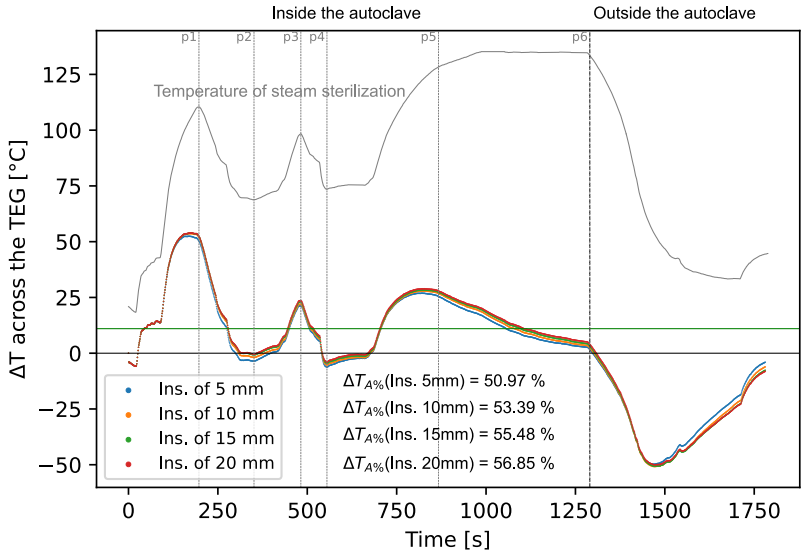

Figure 11.10. Heatsink of size 5 mm with different insulation thicknesses: 5 mm, 10 mm, 15 mm, 20 mm.

In addition, the differences in temperature gradients at points p1 – p6 appear to be negligible for different insulation thicknesses, as can be seen in the Table 11.2. The highest gradient obtained for point p1 was 52.3 °C, while the lowest at the same point was 50.2 °C. At point p2, larger differences in gradients were observed, ranging from –3.6 °C to –0.4 °C. At this point the effect of the insulation on the performance of the thermogenerator is more apparent, as it is undesirable for the thermogenerator to change polarity under the influence of a change in the direction of the temperature gradient. The next point of interest to consider is p4, where it is again undesirable to change the polarisation of the temperature gradient and where, unfortunately, this happens in the cases considered. It can also be seen that the differences in gradient values are much smaller than at point p2. This is due to the smaller temperature peak at p3 and its too short duration and therefore most likely incomplete heating of the HSU. Looking at the behaviour of the temperature gradient between points p5 and p6, it can be seen that for this size of HSU and insulation variants, it is not possible to achieve a gradient on the thermogenerator that allows the sensor module to be powered throughout the sterilisation plateau phase. At p6, the temperature gradient on the thermogenerator is only between 1.5 °C and 3.8 °C, which is far from the assumed minimum of 12 °C.

Table 11.2. Comparison of thermal gradients across the TEG for the heat storage unit with height of 5 mm with the different insulation thicknesses.

	Sterilisation Temperature	I5HS5	I10HS5	I15HS5	I20HS5
p1 [°C]	110.5	50.2	51.9	52.2	52.3
p2 [°C]	68.7	-3.6	-1.9	-0.8	-0.4
p3 [°C]	98.3	21.2	21.9	22.9	23.5
p4 [°C]	73.5	-6.2	-5.2	-4.5	-3.8
p5 [°C]	128.3	25.5	26.8	27.4	27.9
p6 [°C]	133.6	1.5	2.2	3.0	3.8
MAPE [%]		87	86	85	84

The second case study was a model with an HSU of 10 mm. Simulations were carried out according to

the simulation procedure for four different insulation thicknesses, and the results are presented in Figure 11.11 and Table 11.3.

The first noticeable difference in Figure 11.11 compared to the simulations carried out for the HSU with a height of 5 mm is the significantly higher temperature gradients achieved relative to both sides of the thermogenerator. This is also reflected in the percentage of sterilisation time where the gradient is above 12 °C. For the case described here, this time is already 77.98 % of the total sterilisation time for 5 mm thick insulation. For 20 mm thick insulation, however, the time is already 87.90 %. It is also worth noting that for the 15 mm and 20 mm insulation thicknesses in the case considered, they allow a gradient of more than 12 °C to be generated throughout the plateau phase of sterilisation. This is significant in the context of powering the sensor directly with energy from the thermogenerator, without the use of electrical energy storage.

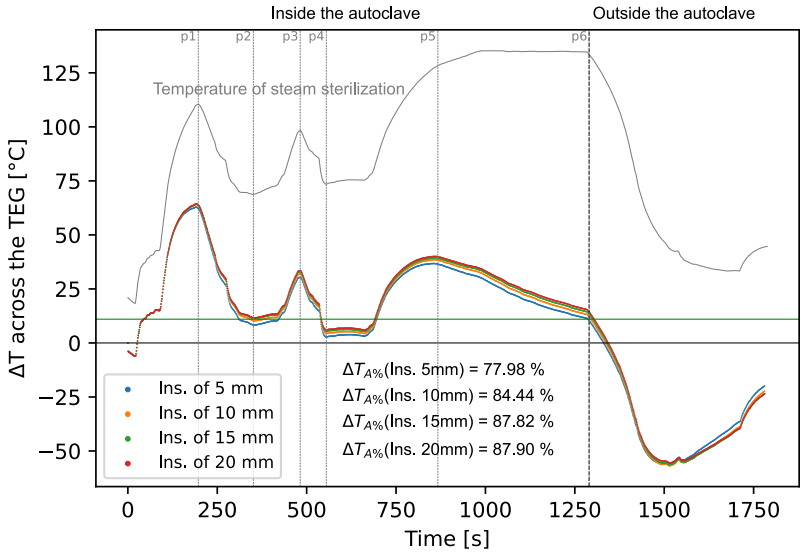

Figure 11.11. Heatsink of size 10 mm with different insulation thicknesses: 5 mm, 10 mm, 15 mm, 20 mm.

When analysing the temperature gradients at points p1-p6 presented in Table 11.3, it can be seen that in general the gradient values at p1 are higher compared to the variant with a 5 mm HSU. However, the difference in gradient values at point p1 is much smaller and only 1.7 °C between the 5 mm and 20 mm insulations. At point p2 all the gradients are positive, which is very important because the polarity of the thermogenerator does not change. At p3, which is the second local maximum during the process of pumping air out of the autoclave, the gradients reach values between 30.3 °C and 33.5 °C, while at p4 they drop to between 2.7 °C and 6.0 °C. Again, all gradients remain positive. Finally, on p5, the gradients reach values between 36.5 °C and 39.9 °C, which is well above the required minimum. However, it should be noted that at the end of the plateau phase, only two isolation variants, 15 mm and 20 mm, provide a gradient above the required 12 °C. The other two variants, 5 mm and 10 mm, provide gradients of 10.1 °C degrees and 11.9 °C respectively.

It is also apparent that there is a significant change in MAPE compared to the 5 mm HSU variant, indicating better performance in the generation of thermal gradients than the 5 mm HSU. Importantly, as in the previous case, different insulation heights result in a slight change in MAPE. However, their impact on the energy extraction process should not be underestimated, particularly during key phases of the sterilisation process, such as the plateau phase between points p5 and p6, where only some of the insulations considered provided a gradient above the expected minimum.

Table 11.3. Comparison of thermal gradients across the TEG for the heat storage unit with height of 10 mm with the different insulation thicknesses.

	Sterilisation Temperature	I5HS10	I10HS10	I15HS10	I20HS10
p1 [°C]	110.5	62.1	63.5	63.7	63.8
p2 [°C]	68.7	8.3	10.3	11.3	11.6
p3 [°C]	98.3	30.3	31.8	32.9	33.5
p4 [°C]	73.5	2.7	4.4	5.3	6.0
p5 [°C]	128.3	36.5	38.3	39.2	39.9
p6 [°C]	133.6	10.1	11.9	13.1	14.1
MAPE [%]		78	76	75	75

The third scenario examines the effect of 4 different insulations and a 15 mm HSU on the temperature gradient generated at the thermogenerator. As can be seen in Figure 11.12, in two cases a gradient above the minimum is maintained throughout the sterilisation process. These cases are 15 mm and 20 mm thick insulation. In the other cases, 5 mm and 10 mm thick insulation, the minimum gradient is maintained for 89.44 % and 99.19 % of the sterilisation time, respectively.

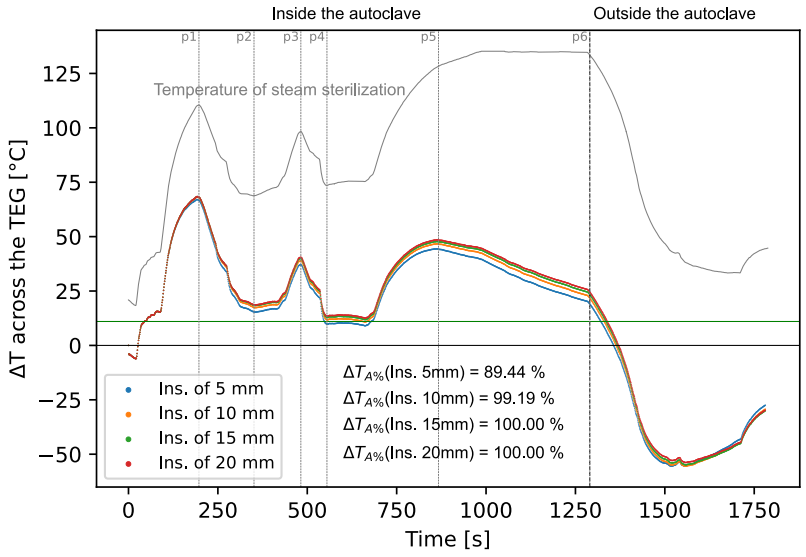

Figure 11.12. Heatsink of size 15 mm with different insulation thicknesses: 5 mm, 10 mm, 15 mm, 20 mm.

Analysing the characteristic points p1-p6 summarised in Table 11.4 it can be seen that the gradient achieved at p1 ranges from 66.6 °C to 68 °C. It can also be seen that the differences in the gradient values are very small. At point p2, which is the local minimum, the values of none of the gradients fall below 12 degrees and then reach values ranging from 37 °C to 40.5 °C at point p3. After the second temperature peak, there is a sharp drop to point p4 where the values of the gradients for the two insulation thicknesses are below the assumed threshold. For case I5HS15 the gradient value at p4 was 9.8 °C and for case I10HS15 it was 11.8 °C. Although this is below the assumed threshold, the difference in this case is only 0.2 °C. In the area of the sterilisation plateau, between points p5 and p6, all cases provide sufficient temperature gradients well above the established minimum.

Table 11.4. Comparison of thermal gradients across the TEG for the heat storage unit with height of 15 mm with the different insulation thicknesses.

	Sterilisation Temperature	I5HS15	I10HS15	I15HS15	I20HS15
p1 [°C]	110.5	66.6	67.8	68.0	68.0
p2 [°C]	68.7	15.4	17.4	18.4	18.6
p3 [°C]	98.3	37.0	39.0	39.9	40.5
p4 [°C]	73.5	9.8	11.8	12.8	13.5
p5 [°C]	128.3	44.3	46.6	47.7	48.4
p6 [°C]	133.6	18.9	21.6	23.2	24.3
MAPE [%]		71	70	69	68

The fourth case describes the use of a 20 mm high HSU with four different insulation thicknesses, according to the simulation scenario shown in Figure 11.13. This is an optimistic variant in terms of the dimensions of the module itself - it should be taken as a reference, as implementation-wise its large size and weight works against it. In this variant, all insulation thicknesses ensure that the minimum temperature gradient is achieved on the thermoelectric generator.

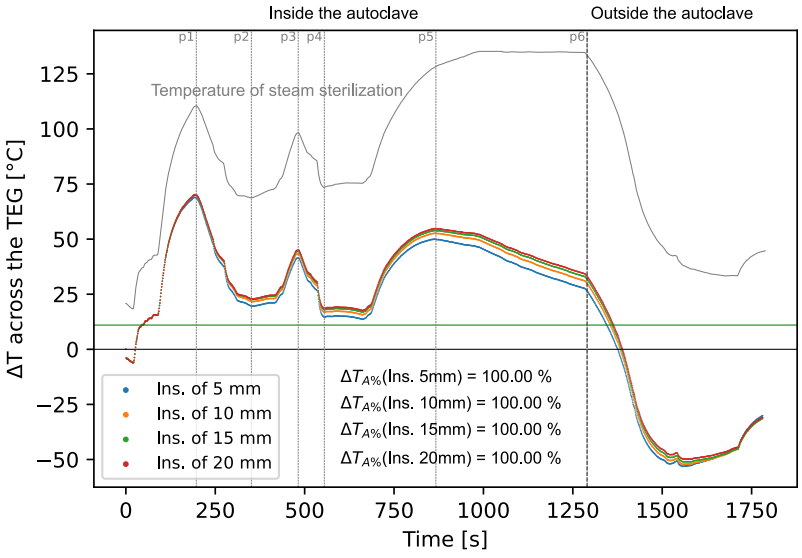

Figure 11.13. Heatsink of size 20 mm with different insulation thicknesses: 5 mm, 10 mm, 15 mm, 20 mm.

Analysing the values of the temperature gradient at the characteristic points summarised in Table 11.5, we see that they differ significantly from the other cases. The minimum gradient found in the I5HS20 variant of 14.6 °C significantly exceeds the assumed minimum. The gradient values at p1 and p3 also suggest that there are conditions for efficient energy harvesting. In the plateau phase of sterilisation (points p5 - p6) the gradients for all insulation thicknesses significantly exceed the assumed minimum and reach a maximum value of 54.7 °C. As expected, the MAPE values in this case are also the lowest of all simulated cases.

Table 11.5. Comparison of thermal gradients across the TEG for the heat storage unit with height of 20 mm with the different insulation thicknesses.

	Sterilisation Temperature	I5HS20	I10HS20	I15HS20	I20HS20
p1 [°C]	110.5	68.6	69.8	69.9	70.0
p2 [°C]	68.7	19.6	21.7	22.6	22.8
p3 [°C]	98.3	41.5	43.4	44.5	45.0
p4 [°C]	73.5	14.6	16.8	18.0	18.6
p5 [°C]	128.3	49.9	52.6	53.9	54.7
p6 [°C]	133.6	26.2	29.7	31.6	32.9
MAPE [%]		67	65	64	63

11.4.2. Effect of HSU size on temperature gradient

The next step was to investigate the effect of the height of the HSU on the temperature gradient between the thermogenerator covers. Four basic HSU heights (also 5, 10, 15 and 20 mm) were tested for each insulation thickness (5, 10, 15 and 20 mm). The simulation results are shown in Figures 11.14 - 11.17 and Tables 11.6 - 11.9.

The parameters tested remained the same as for the simulations described in section 11.4.1 and detailed measurements were taken at points p1, p2, p3, p4, p5, p6. Each figure and table is briefly analysed.

As can be seen in Figure 11.14 for the insulation of 5 mm only HSU with 20 mm height ensures the 100% time over the defined minimum gradient threshold. However, during the plateau phase the HSU heights of 10 mm, 15 mm and 20 mm ensure the minimum required thermal gradient. As can be seen in the Table 11.6, the differences in MAPE between each size of HSU are significant, ranging from 87% in the case of HSU of 5 mm to 0.67% in the case of HSU of height 20 mm.

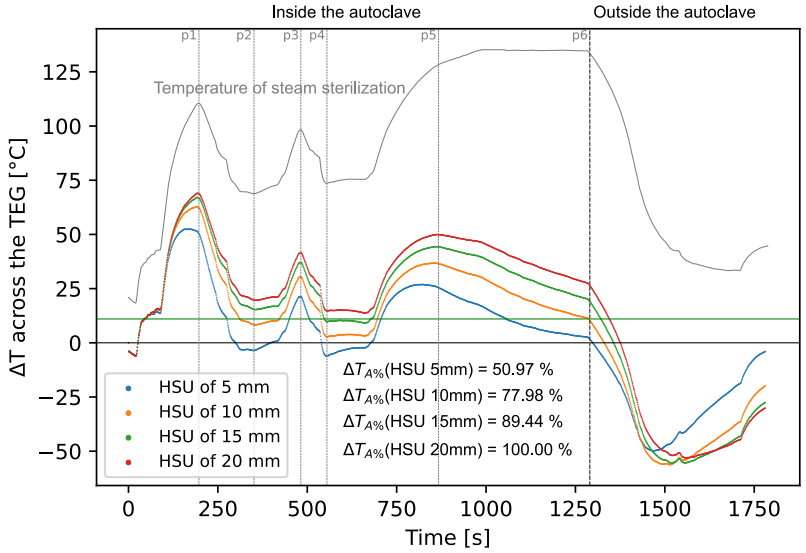

Figure 11.14. Insulation of size 5 mm with different HSU heights: 5 mm, 10 mm, 15 mm, 20 mm.

As can be seen both in the Figures 11.14 - 11.17 and in the Tables 11.6 - 11.9, the differences between the MAPE values increase with increasing thermal insulation, which is a logical consequence. The thicker

Table 11.6. Comparison of thermal gradients across the TEG for insulation thickness of 5 mm with different HSU heights.

	Sterilisation Temperature	**HS5I5**	**HS10I5**	**HS15I5**	**HS20I5**
p1 [°C]	110.5	50.2	62.1	66.6	68.7
p2 [°C]	68.7	-3.6	8.3	15.4	19.6
p3 [°C]	98.3	21.2	30.3	37	41.5
p4 [°C]	73.5	-6.2	2.7	9.8	14.6
p5 [°C]	128.3	25.5	36.5	44.3	49.9
p6 [°C]	133.6	1.5	10.1	18.9	26.2
MAPE [%]		87	78	72	67

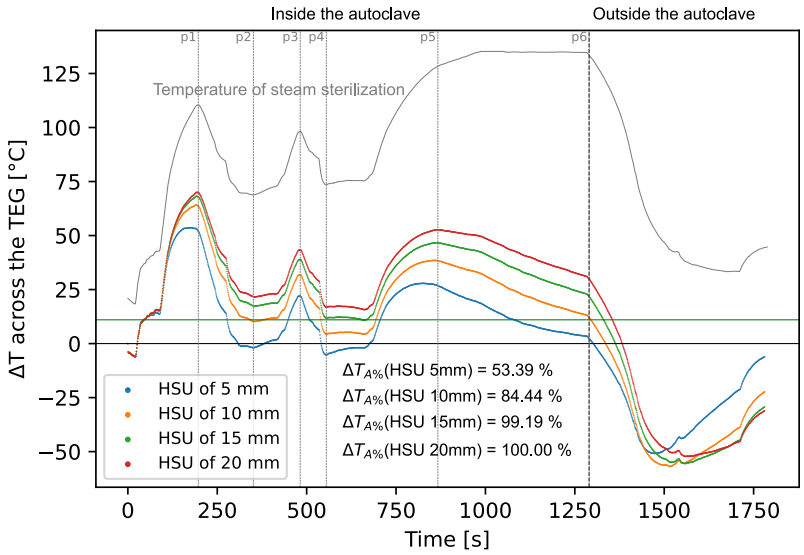

Figure 11.15. Insulation of size 10 mm with different HSU heights: 5 mm, 10 mm, 15 mm, 20 mm.

the insulation around the HSU, the less heat is lost by convection from the HSU directly to the enclosure and then to the environment. When considering the scenario where the thermal gradient must be maintained throughout the sterilisation process, it is particularly important to monitor the test point **p4** and to minimise the overall height of the device while maintaining the minimum thermal gradient. Such a situation can be achieved by combining either HSU of height 20 mm with insulation of 5 mm or HSU of height 15 mm with insulation of 15 mm. It's clear that in order to minimise the height of the device and reduce its size, the parameter to consider is the height of the HSU and not the thickness of the insulation, which may seem counterintuitive. However, based on the preliminary results, more detailed simulations of scenarios with different HSU heights need to be carried out in order to have a deeper insight into the minimisation of the device while preserving it's core functionalities.

Table 11.7. Comparison of thermal gradients across the TEG for insulation thickness of 10 mm with different HSU heights.

	Sterilisation Temperature	**HS5I10**	**HS10I10**	**HS15I10**	**HS20I10**
p1 [°C]	110.5	51.9	63.5	67.8	69.8
p2 [°C]	68.7	-1.9	10.3	17.4	21.7
p3 [°C]	98.3	21.9	31.8	38.9	43.4
p4 [°C]	73.5	-5.2	4.4	11.8	16.8
p5 [°C]	128.3	26.8	38.3	46.6	52.6
p6 [°C]	133.6	2.2	11.9	21.6	29.7
MAPE [%]		86	76	70	65

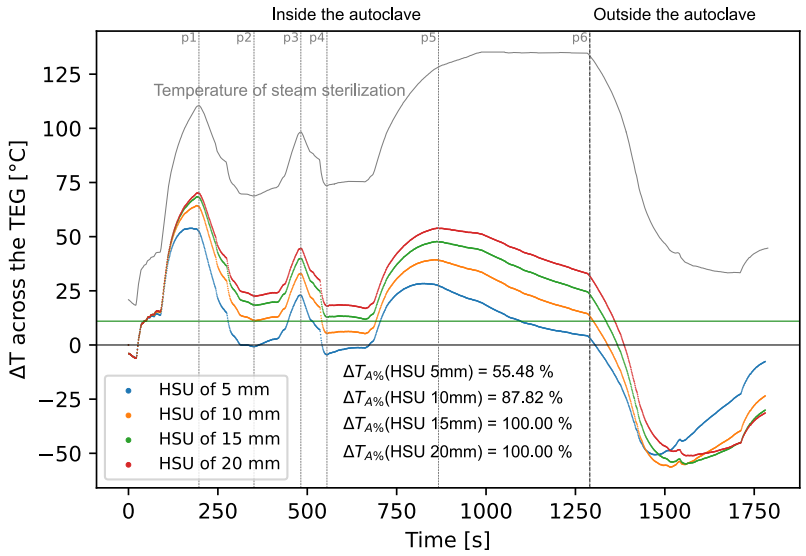

Figure 11.16. Insulation of size 15 mm with different HSU heights: 5 mm, 10 mm, 15 mm, 20 mm.

Table 11.8. Comparison of thermal gradients across the TEG for insulation thickness of 15 mm with different HSU heights.

	Sterilisation Temperature	**HS5I15**	**HS10I15**	**HS15I15**	**HS20I15**
p1 [°C]	110.5	52.3	63.7	68.1	69.9
p2 [°C]	68.7	-0.8	11.3	18.4	22.6
p3 [°C]	98.3	22.9	32.9	39.9	44.5
p4 [°C]	73.5	-4.5	5.3	12.8	18
p5 [°C]	128.3	27.4	39.2	47.7	53.9
p6 [°C]	133.6	3.1	13.1	23.2	31.6
MAPE [%]		85	76	69	64

Table 11.9. Comparison of thermal gradients across the TEG for insulation thickness of 20 mm with different HSU heights.

	Sterilisation Temperature	**HS5I20**	**HS10I20**	**HS15I20**	**HS20I20**
p1 [°C]	110.5	52.3	63.8	68.1	70
p2 [°C]	68.7	-0.4	11.6	18.6	22.8
p3 [°C]	98.3	23.5	33.5	40.5	45.1
p4 [°C]	73.5	-3.8	6.0	13.5	18.6
p5 [°C]	128.3	27.9	39.9	48.4	54.7
p6 [°C]	133.6	3.9	14.1	24.3	32.9
MAPE [%]		85	75	68	63

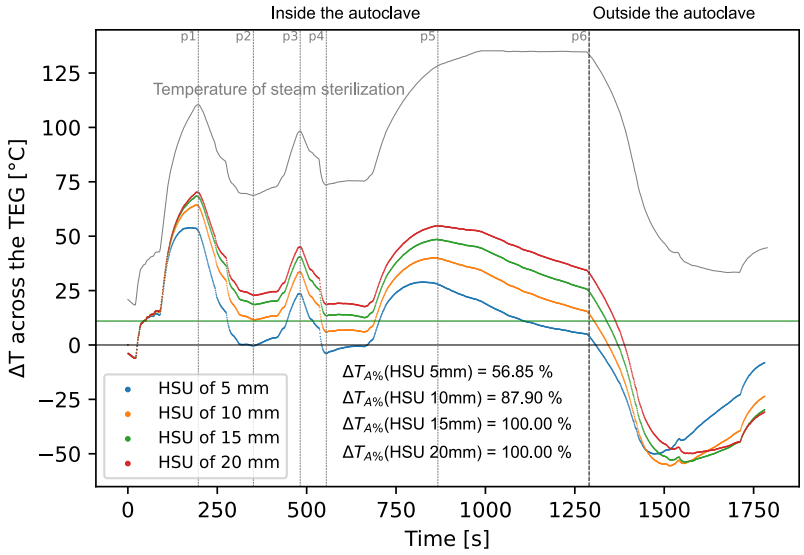

Figure 11.17. Insulation of size 20 mm with different HSU heights: 5 mm, 10 mm, 15 mm, 20 mm.

12. Simulated Power Generation during Steam Sterilisation

Abstract

This chapter presents the methodology and simulation results of the power generation by the TEG during the steam sterilisation process for different geometric configurations of the device model. Firstly, the methodology of the simulations carried out for each model variant is defined. Then, the results are summarised in relation to the minimum power requirements for the sensor operating in active mode and in passive mode. For both modes two scenarios have been analysed - scenario with a power buffer, where the energy balance has been calculated, and the scenario without any power buffer where the sensor electronics is driven directly from the DC-DC converter from the TEG. Finally, the most optimal design was selected to ensure that the design objectives were met while minimising the size of the overall module.

Outcomes of this chapter: The result of this chapter is a summary of the power and energy produced for different variations of the energy harvesting module design. Modules with HSU heights from 2.5mm to 20mm in 2.5mm increments and thermal insulation thicknesses from 5mm to 20mm in 5mm increments were considered. The 10mm HSU height and 5mm thermal insulation variant was selected as the optimum. It provided power to the sensor module for more than 94 % of the sterilisation time while minimising the module dimensions.

With a mechanical model of the module and a SPICE model of the TEG, it was possible to run a simulation of the steam sterilisation process to measure the power generated during the full steam sterilisation cycle.

12.1. Methodology and Simulation Setup

The power generation simulation during the steam sterilisation cycle was performed in two main steps. In the first step, a heat transfer simulation was performed to obtain the temperature of the hot and cold sides of the TEG module, which formed the simulation output. In the next step, the hot and cold side temperature values were used as input for SPICE simulation of TEG power generation using Kubov's model. The overall scheme is shown in Figure 12.1.

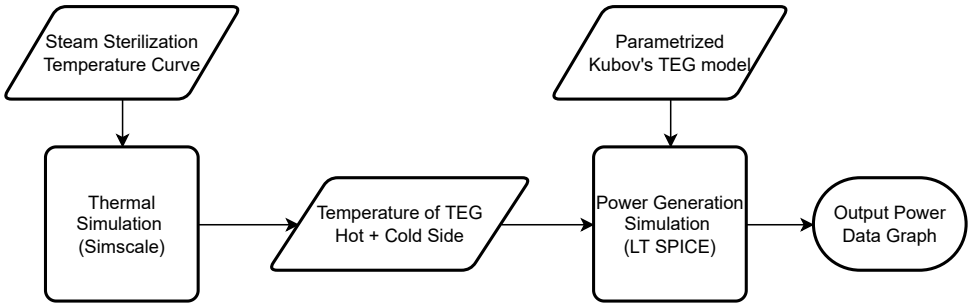

Figure 12.1. Schematic diagram of the power generation simulaton procedure.

All thermal flow simulations were performed in Simscale environment using parameters and CAD models described in detail in the chapter 10. SPICE simulations were performed in LTSpice using the SPICE script presented in the listing in Appendix D.

The simulation was performed for insulation thicknesses of 5 mm, 10 mm, 15 mm, and 20 mm and for HSU heights of 5 mm, 10 mm, 15 mm and 20 mm. After each simulation an average power generated during the whole cycle, as well as the total amount of energy harvested, has been calculated.

12.2. Results

The simulations were carried out for the entire steam sterilisation process, including all three phases of the process, but the most critical part is the second phase, known as the plateau phase, where steam sterilisation takes place. The analysis of the results reflects this. First, the results of the entire steam sterilisation process are analysed. Then the detailed analysis of the power generation during steam sterilisation is carried out. The results are analysed considering two possible scenarios for powering the sensor electronics:

- **Using Energy Storage System (ESS)** Although the use of the ESS is generally not desirable due to the problems with most of the available ESS solutions mentioned in chapter 5, a situation is considered where technological advances will allow the introduction of cost effective ESS to the market. In this situation it is considered that the sensor electronics are connected to the energy storage system which stores the energy generated during the entire steam sterilisation process.
- **Without ESS** In this scenario there is no energy storage system and the sensor electronics are powered directly by the thermoelectric generator. In this scenario the energy generated during the steam sterilisation phase of the steam sterilisation process was considered. The aim was to power the sensor electronics for at least 95 % of the steam sterilisation plateau phase.

The overview of the analysed scenarios is presented in the Figure 12.2.

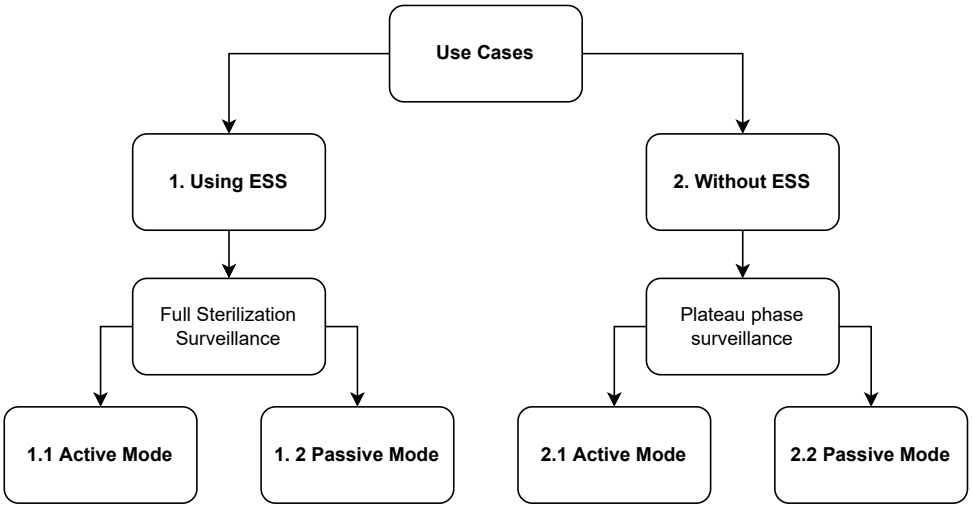

Figure 12.2. Schematic diagram of the power generation simulaton procedure.

12.2.1. Scenario 1 – Using ESS

The first case study considers the use of an ESS in the form of a high temperature hybrid capacitor connected to a power management system. The option considered assumes that the excessive energy generated by the TEG is stored in the capacitor and consumed by the measurement module when the energy generated by the TEG is insufficient. This assumption is favoured by the steam sterilisation process, where prior to the actual sterilisation phase (plateau), preliminary operations (pumping in and out of steam) are carried out which cause high temperature differences between the HSU and the module housing. This temperature difference generates a relatively high electromotive force in the TEG and thus electrical energy.

In the scenario described here, it is assumed that once sufficient electrical energy has been stored in the capacitor, the sensor module will switch on and draw an average power in active mode of 1.674 mW as calculated in section 8.3.3, while in passive mode the sensor will operate at 0.353 mW. For both cases, a cumulative energy balance was simulated and the amount of energy stored at the end of the sterilisation process was estimated. A number of design options were considered where the variables were the height of the HSU and the thickness of the thermal insulation. HSU thicknesses from 2.5 mm to 20 mm (in 5 mm increments) and insulation thicknesses from 5 mm to 20 mm (in 5 mm increments) were tested. This gave a total of 32 parameter combinations for which simulations were carried out.

Active Mode

The first case analysed is the one where the RF430FRL152H chip operates in LPM0 (active mode) and the energy from the TEG is stored in the energy storage system. All the results are summarised in the Table 12.1 and the selected simulation results are shown in the figures 12.3. - 12.12.

Each figure shows the complete steam sterilisation process including the preparation phase (venting air, releasing steam, preheating), the plateau phase and the drying phase. The plateau phase lasts 620 seconds in the simulation, which is indicated in each figure by the variable $T_{sterilisation}$. The figures are divided into three parts. The first part shows a graph of the power generated by the TEG operating throughout the process. In this graph, the area where the power generated by the TEG exceeds the assumed power consumption threshold of the sensor is marked in blue. In other words, in the areas marked in blue, the power generated by the TEG is sufficient to power the sensor electronics. The second graph shows the energy balance. The energy balance is the sum of the energy produced by the TEG and the energy consumed by the sensor

module. The energy balance diagram also shows the amount of energy produced by the entire sterilisation process (E_p) and the amount of energy remaining to be used at the end of the entire process (E_{BE}). The third subgraph shows, in simplified form, the graph of the power consumption of the sensor module that is switched on when entering the plateau phase of the sterilisation process. This graph also shows how much power the sensor consumed (P_s) and how much energy the sensor consumed during its entire cycle (E_s). Therefore, each graph shows the instantaneous power generated by the TEG, the energy balance, the operating state of the sensor and the energy balance at the end of the sterilisation process. This last data is important in the context of estimating the performance of other IoT systems that remain active at the end of the sterilisation cycle. For a better understanding of the data presented in the figures, Figure 12.3 is described in detail. In this figure it can be seen that the total energy produced during the sterilisation process is 7.63 J and the remaining energy to be used is 6.59 J. It can also be clearly seen that during the plateau phase, only in the first part of the plateau phase is the power generated by the TEG sufficient to power the sensor, this is also reflected in the inflection of the energy balance graph around the 900^{th} second. It can also be seen that after the plateau phase there is a significant increase in the power generated by the TEG. This is due to the rapid drop in temperature in the autoclave chamber, which causes a reverse flow of heat through the TEG, from the HSU to the module enclosure. It should be noted that the reverse heat flow also changes the polarity of the TEG voltage, which must be taken into account when designing the power conditioning system.

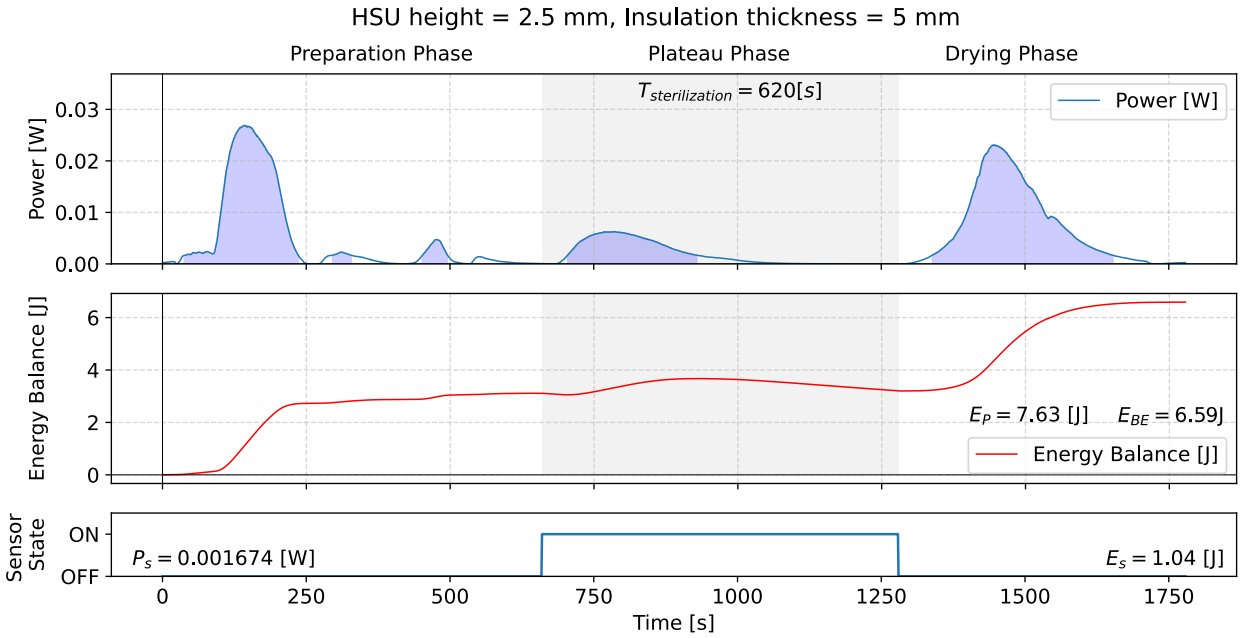

Figure 12.3. Generated power and energy balance during the preparation phase, plateau phase and drying phase of the steam sterilization procedure for a HSU of height 2.5 mm and insulation thickness of 5 mm. The sensor is turned on for the surveillance of sterilization phase, while remaining inactive in the preparation and drying phase.

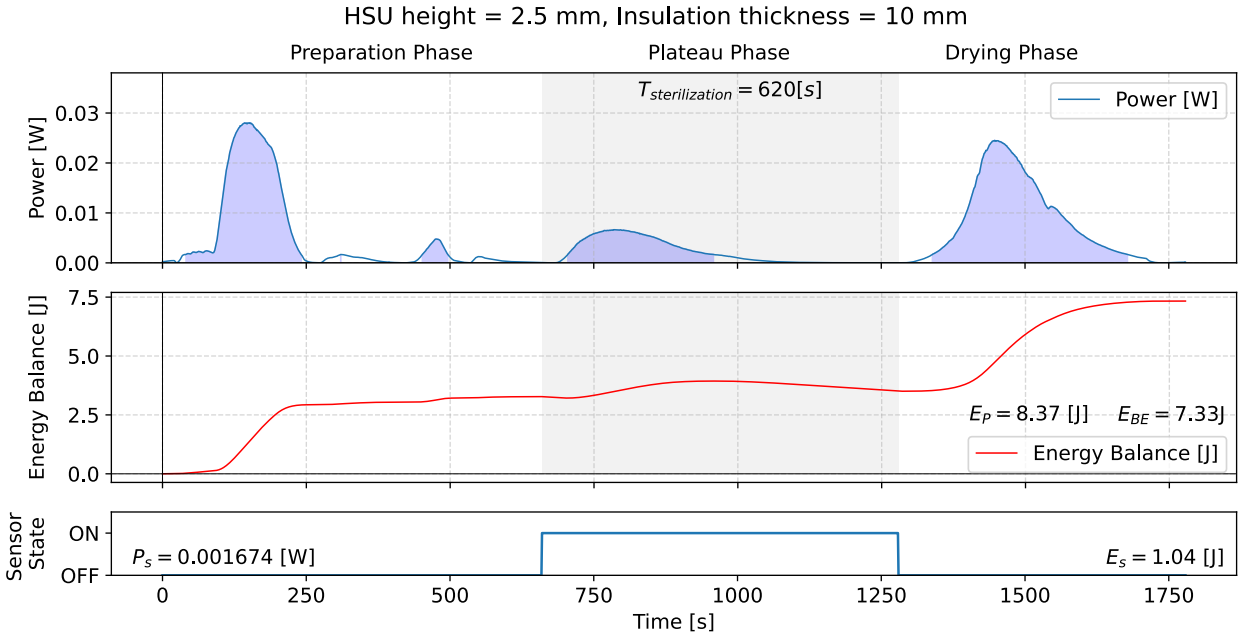

Figure 12.4. Generated power and energy balance during the preparation phase, plateau phase and drying phase of the steam sterilization procedure for a HSU of height 2.5 mm and insulation thickness of 10 mm. The sensor is turned on for the surveillance of sterilization phase, while remaining inactive in the preparation and drying phase.

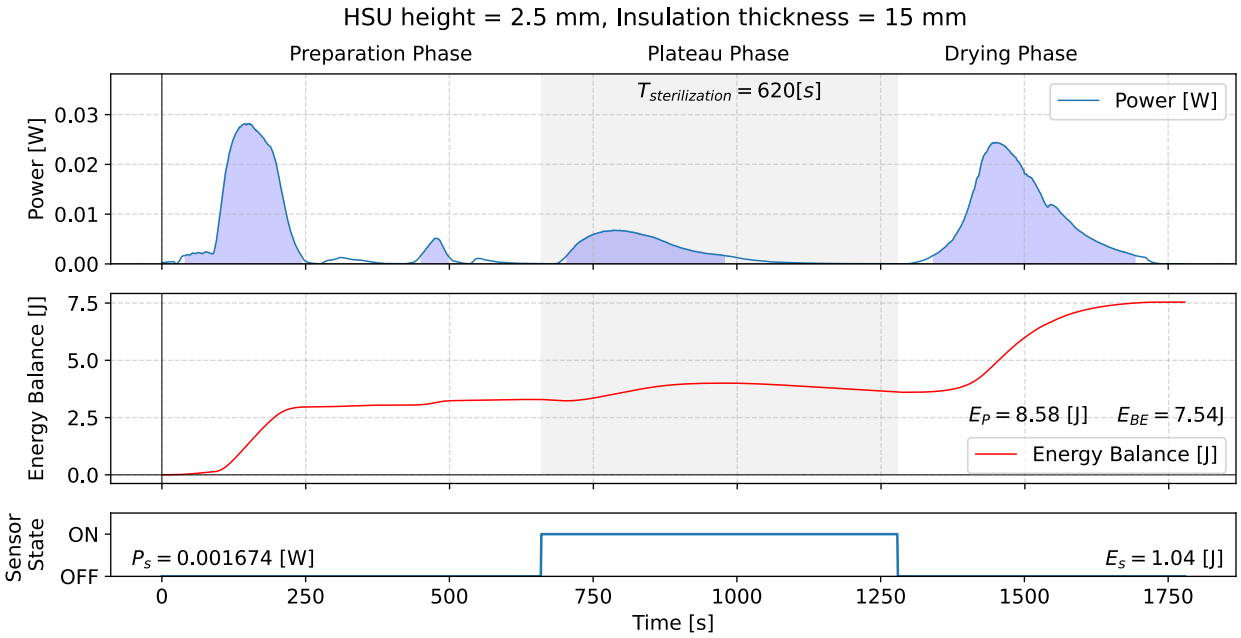

Figure 12.5. Generated power and energy balance during the preparation phase, plateau phase and drying phase of the steam sterilization procedure for a HSU of height 2.5 mm and insulation thickness of 15 mm. The sensor is turned on for the surveillance of sterilization phase, while remaining inactive in the preparation and drying phase.

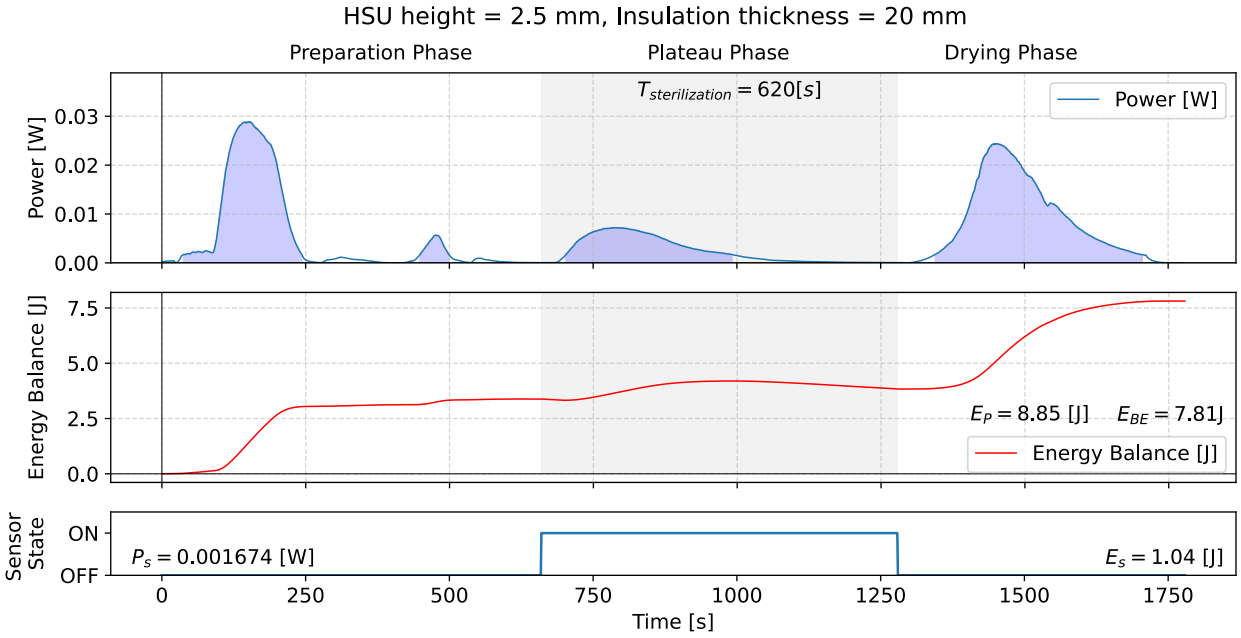

Figure 12.6. Generated power and energy balance during the preparation phase, plateau phase and drying phase of the steam sterilization procedure for a HSU of height 2.5 mm and insulation thickness of 20 mm. The sensor is turned on for the surveillance of sterilization phase, while remaining inactive in the preparation and drying phase.

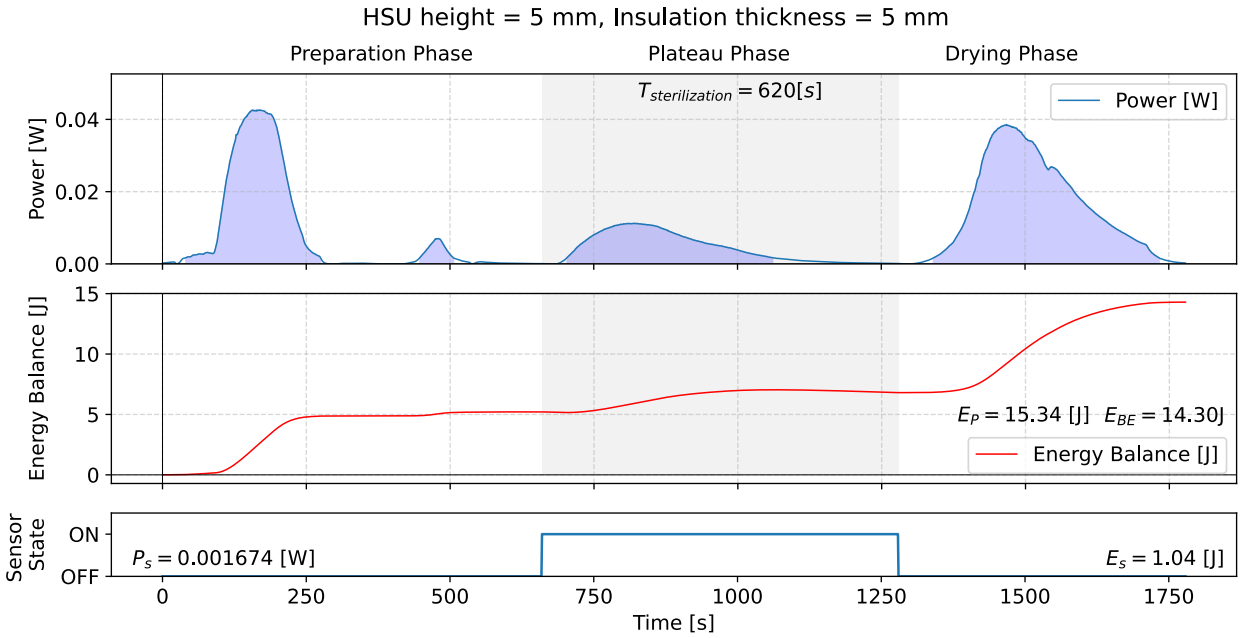

Figure 12.7. Generated power and energy balance during the preparation phase, plateau phase and drying phase of the steam sterilization procedure for a HSU of height 5 mm and insulation thickness of 5 mm. The sensor is turned on for the surveillance of sterilization phase, while remaining inactive in the preparation and drying phase.

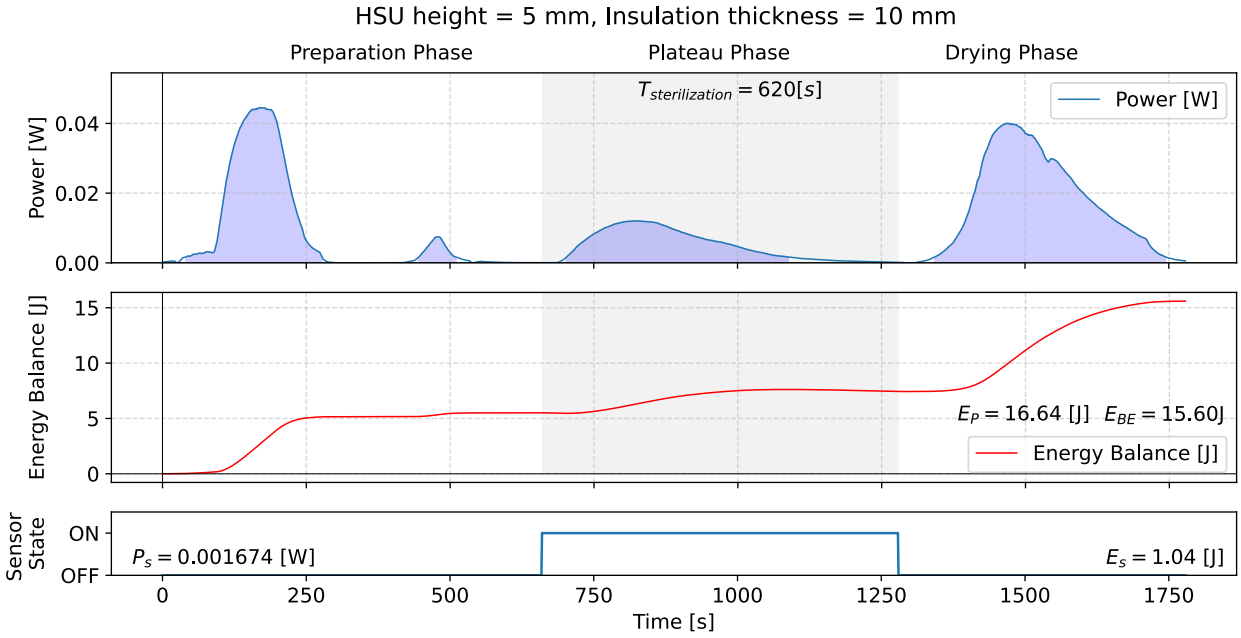

Figure 12.8. Generated power and energy balance during the preparation phase, plateau phase and drying phase of the steam sterilization procedure for a HSU of height 5 mm and insulation thickness of 10 mm. The sensor is turned on for the surveillance of sterilization phase, while remaining inactive in the preparation and drying phase.

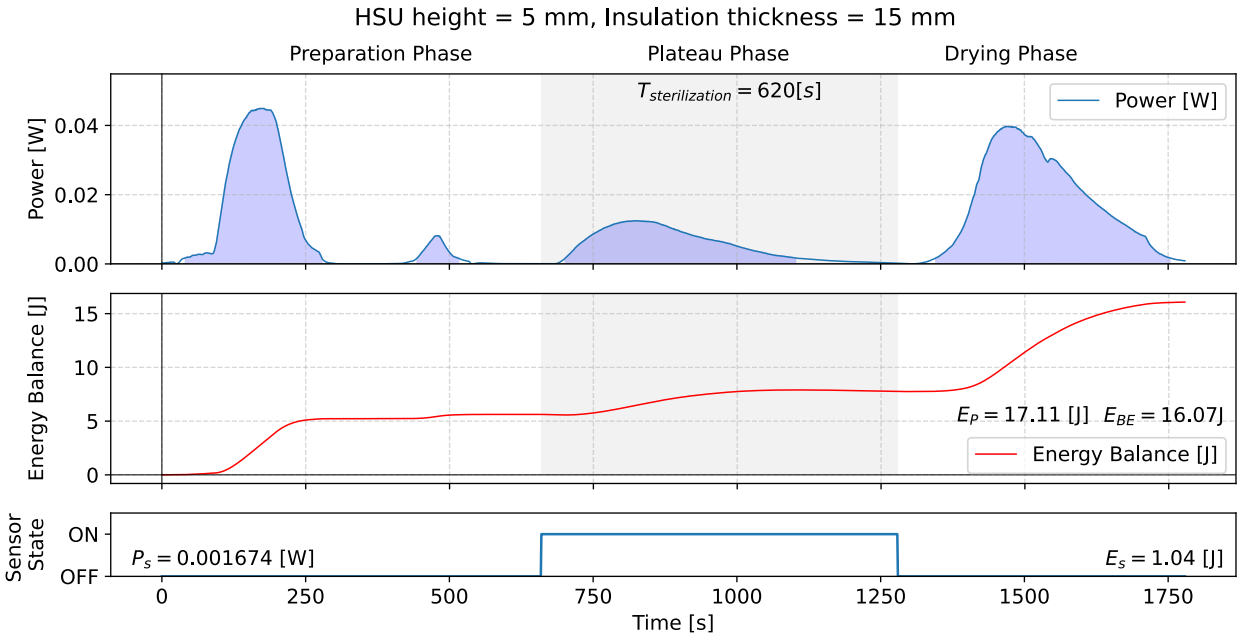

Figure 12.9. Generated power and energy balance during the preparation phase, plateau phase and drying phase of the steam sterilization procedure for a HSU of height 5 mm and insulation thickness of 15 mm. The sensor is turned on for the surveillance of sterilization phase, while remaining inactive in the preparation and drying phase.

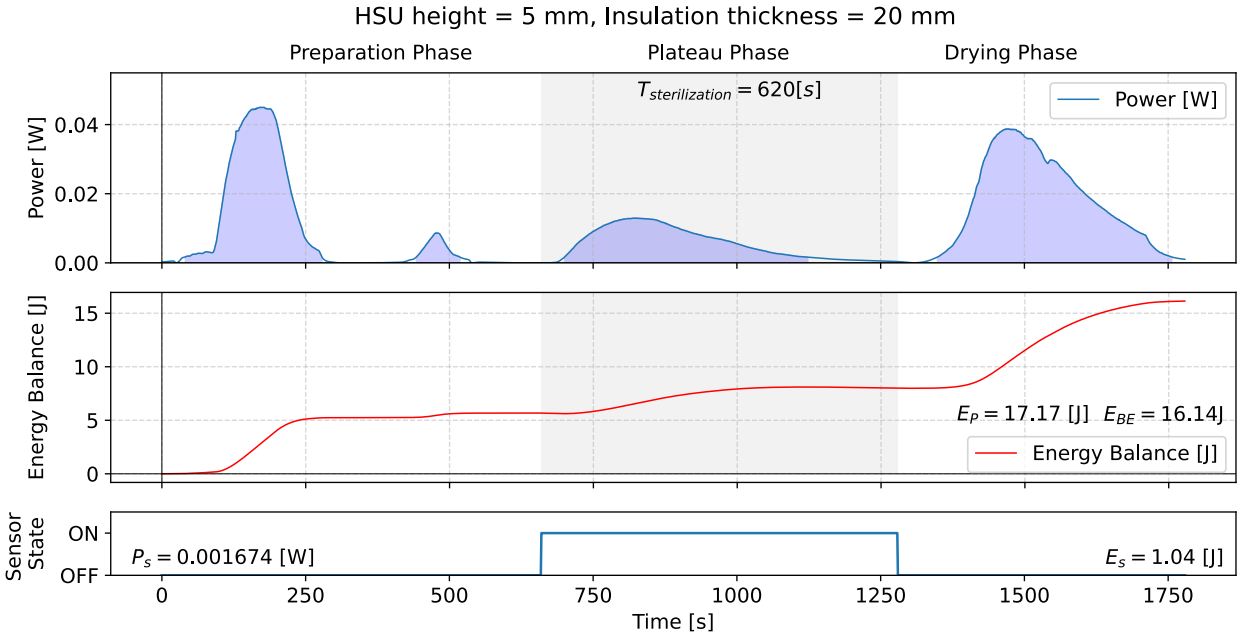

Figure 12.10. Generated power and energy balance during the preparation phase, plateau phase and drying phase of the steam sterilization procedure for a HSU of height 5 mm and insulation thickness of 20 mm. The sensor is turned on for the surveillance of sterilization phase, while remaining inactive in the preparation and drying phase.

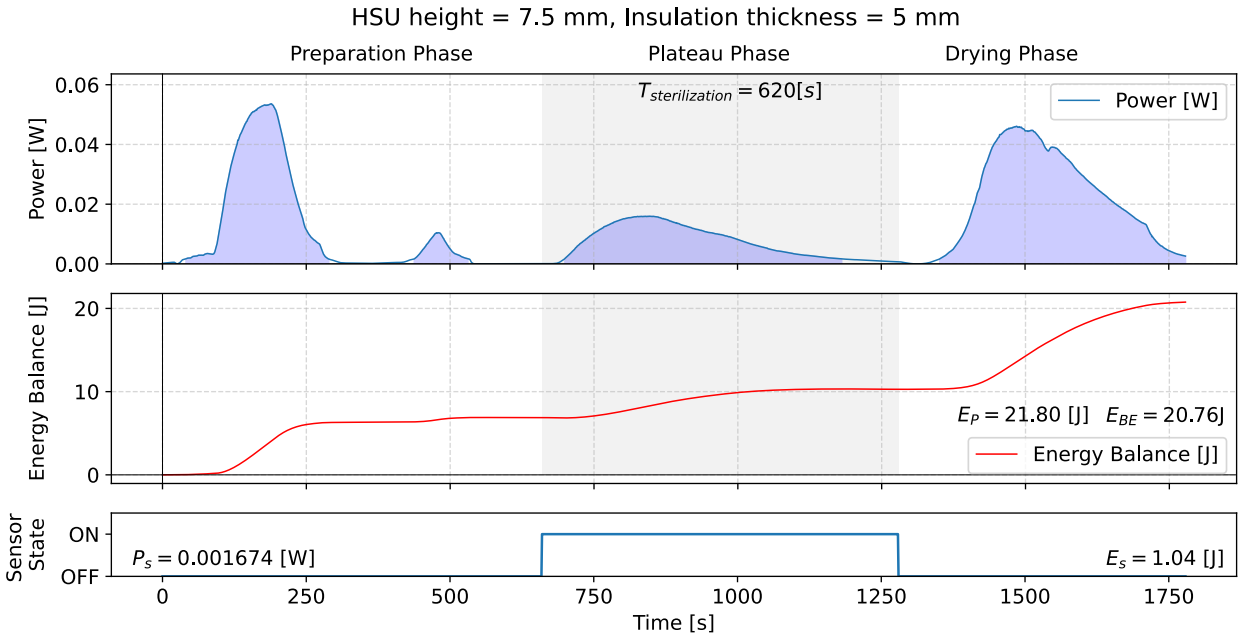

Figure 12.11. Generated power and energy balance during the preparation phase, plateau phase and drying phase of the steam sterilization procedure for a HSU of height 7.5 mm and insulation thickness of 5 mm. The sensor is turned on for the surveillance of sterilization phase, while remaining inactive in the preparation and drying phase.

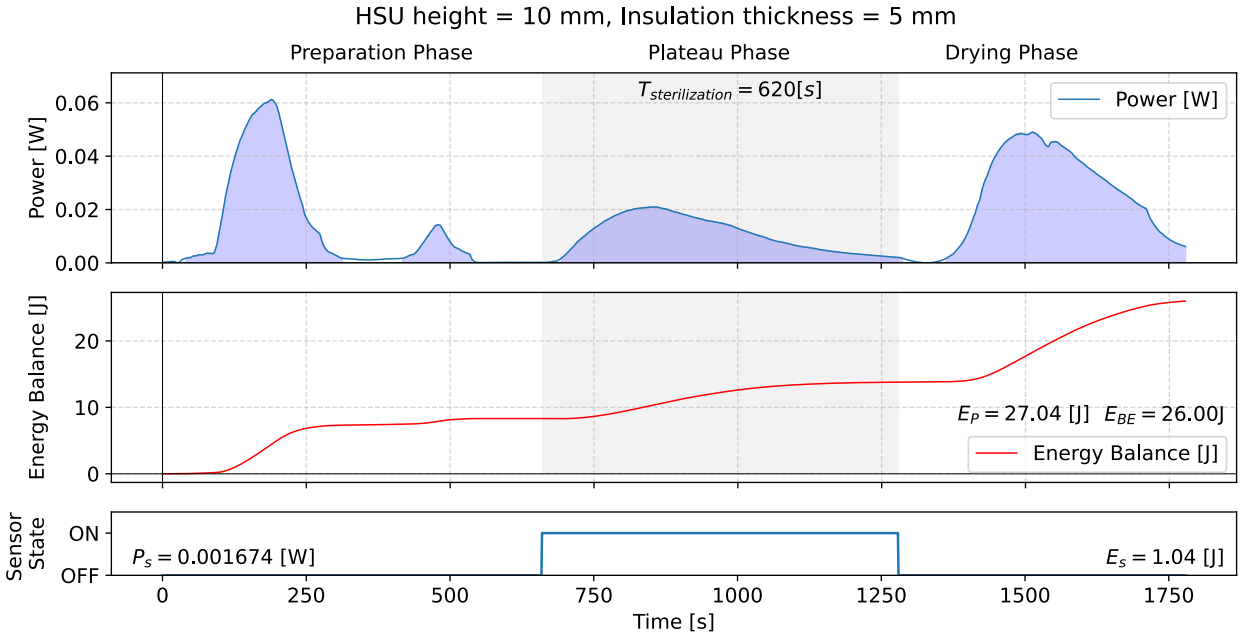

Figure 12.12. Generated power and energy balance during the preparation phase, plateau phase and drying phase of the steam sterilization procedure for a HSU of height 10 mm and insulation thickness of 5 mm. The sensor is turned on for the surveillance of sterilization phase, while remaining inactive in the preparation and drying phase.

Table 12.1. Summary of energy generated during the whole steam sterilization procedure with different design sizes and with sensor module in Active mode with average power consumption o 1.674 mW.

HSU height [mm]	Insulation thickness [mm]	Energy generated [J]	Energy consumed [J]	Energy balance [J]
2.5	5.0	7.63	1.04	6.59
2.5	10.0	8.37	1.04	7.33
2.5	15.0	8.58	1.04	7.54
2.5	20.0	8.85	1.04	7.81
5.0	5.0	15.34	1.04	14.30
5.0	10.0	16.64	1.04	15.60
5.0	15.0	17.11	1.04	16.07
5.0	20.0	17.17	1.04	16.14
7.5	5.0	21.80	1.04	20.76
7.5	10.0	23.57	1.04	22.53
7.5	15.0	24.18	1.04	23.15
7.5	20.0	24.26	1.04	23.22
10.0	5.0	27.04	1.04	26.00
10.0	10.0	29.07	1.04	28.04
10.0	15.0	29.82	1.04	28.78
10.0	20.0	30.03	1.04	28.99
12.5	5.0	31.25	1.04	30.21
12.5	10.0	33.46	1.04	32.43
12.5	15.0	34.46	1.04	33.42
12.5	20.0	34.74	1.04	33.70
15.0	5.0	34.70	1.04	33.66
15.0	10.0	37.26	1.04	36.22
15.0	15.0	38.30	1.04	37.26
15.0	20.0	38.59	1.04	37.55
17.5	5.0	37.60	1.04	36.56
17.5	10.0	40.15	1.04	39.11
17.5	15.0	41.43	1.04	40.39
17.5	20.0	41.88	1.04	40.84
20.0	5.0	39.96	1.04	38.92
20.0	10.0	42.96	1.04	41.92
20.0	15.0	44.25	1.04	43.21
20.0	20.0	44.77	1.04	43.73

Passive Mode

In the scenario considered, the energy from the TEG was stored in the energy storage system as in the previous section, but the sensor was operated in LPM3 (passive) mode. The same number of design configurations were analysed, i.e. HSU heights from 2.5 mm to 20 mm and thermal insulation thicknesses from 5 mm to 20 mm. The results are summarised in the following Table 12.2 Due to the slight differences from the previous scenario, only one figure (Figure 12.13) of the simulation run for the variant with HSU height of 2.5 mm and the insulation thickness of 5 mm was restricted.

As shown in the Table 12.2, the amount of energy produced in this mode varies from 7.63 J to 44.77 J, which after subtracting the energy used to power the sensor gives 7.41 J to 44.55 J of energy.

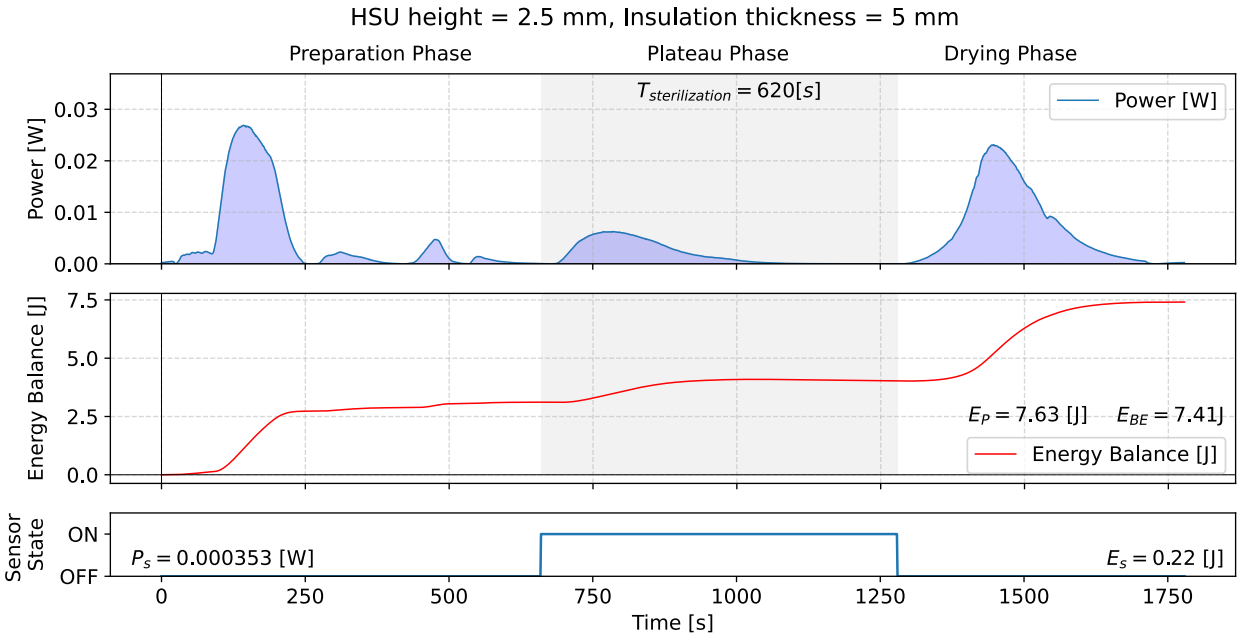

Figure 12.13. Generated power and energy balance during the preparation phase, plateau phase and drying phase of the steam sterilization procedure for a HSU of height 2.5 mm and insulation thickness of 5 mm. The sensor is turned on (LPM3 mode) for the surveillance of sterilization phase, while remaining inactive in the preparation and drying phase.

Table 12.2. Summary of energy generated during the whole steam sterilization procedure with different design sizes and with sensor module in Active mode with average power consumption o 0.353 mW.

HSU height [mm	Insulation thickness	Energy generated	Energy consumed	Energy balance
2.5	5.0	7.63	0.22	7.41
2.5	10.0	8.37	0.22	8.15
2.5	15.0	8.58	0.22	8.36
2.5	20.0	8.85	0.22	8.63
5.0	5.0	15.34	0.22	15.12
5.0	10.0	16.64	0.22	16.42
5.0	15.0	17.11	0.22	16.89
5.0	20.0	17.17	0.22	16.95
7.5	5.0	21.80	0.22	21.58
7.5	10.0	23.57	0.22	23.35
7.5	15.0	24.18	0.22	23.96
7.5	20.0	24.26	0.22	24.04
10.0	5.0	27.04	0.22	26.82
10.0	10.0	29.07	0.22	28.86
10.0	15.0	29.82	0.22	29.60
10.0	20.0	30.03	0.22	29.81
12.5	5.0	31.25	0.22	31.03
12.5	10.0	33.46	0.22	33.25
12.5	15.0	34.46	0.22	34.24
12.5	20.0	34.74	0.22	34.52
15.0	5.0	34.70	0.22	34.48
15.0	10.0	37.26	0.22	37.04
15.0	15.0	38.30	0.22	38.08
15.0	20.0	38.59	0.22	38.37
17.5	5.0	37.60	0.22	37.38
17.5	10.0	40.15	0.22	39.93
17.5	15.0	41.43	0.22	41.21
17.5	20.0	41.88	0.22	41.66
20.0	5.0	39.96	0.22	39.74
20.0	10.0	42.96	0.22	42.74
20.0	15.0	44.25	0.22	44.03
20.0	20.0	44.77	0.22	44.55

12.2.2. Scenario 2 – No ESS

From a functional point of view, the most important part of the whole steam sterilisation process is the moment when the temperature reaches 130 °C and remains at this level for at least 10 min. That's why special attention was paid to this part of the sterilisation process.

The simulation results were divided into two groups. In the first group, a **active mode** scenario was analysed. In this scenario, the sensor node operates in active mode with the ADC always on. In the second group, called **passive mode**, the sensor operated in LPM4 power saving mode with ADC turned on periodically.

Each figure consists of four subfigures. The first three subfigures show in turn the current, voltage and power during the entire sterilisation process. The grey colour indicates the period when the sterilisation cycle is in the plateau phase - the key phase during which the actual sterilisation takes place. The fourth subfigure shows the power generated by the TEG during the plateau phase. The blue colour in the figures indicates the period during which the power generated by the TEG is equal to or greater than the power required to power the sensor according to the minimum requirements in the scenario. For the active scenario, the minimum power to power the sensor is 1.674 mW. For the passive scenario it is only 0.353 mW. Each figure for the power generated during the plateau phase shows the length of the entire phase (620 s), the total amount of energy generated during the plateau phase (E_{total}) and the number of seconds during which the power generated by the TEG was sufficient to power the sensor (T_p), this value is also expressed as a percentage. Ideally, this value should be 100 %, while keeping the dimensions of the entire energy harvesting module as small as possible, according to the functional and business requirements of the industrial partner.

Active Mode Scenario

The active scenario considered sensor operation in LPM0 mode. The most interesting simulation results are shown in Figures 12.14 - 12.35 and all simulation results are summarised in Table 12.3.
Figures 12.14 - 12.35 show the simulation results for the variant in which the RF43FRL152H chip, acting as a sensor module, is active and monitors the plateau phase of the sterilisation process. The desired effect was to generate enough power and energy to supply the sensor module for 100 % of the plateau phase, as this is the critical phase of the entire sterilisation process. The simulations carried out show that it is possible to supply the measurement module directly from the TEG without using a buffer in the form of an energy storage system, provided that the overall dimensions of the device are appropriate. As Table 12.3 shows, the ability to power the measurement electronics during the plateau phase of the sterilisation process, i.e. the phase aimed at eliminating bacteria, viruses, and microorganisms, depends more on the size of the HSU than on the thickness of the insulation. Comparing the energy gain, it can be seen that increasing the height of the HSU by 2.5 mm gives an average gain of more than 134 % (for an increase in HSU height from 2.5 mm to 5 mm) to 15% (for an increase in HSU height from 17.5 mm to 20 mm). For the same HSU values, i.e. 2.5 mm and 17.5 mm, increasing the insulation by 5 mm results in an increase in the energy produced of up to 13.39 % and 14.38 % respectively. With the aim of minimising the size of the prototype, it can be seen that in order to achieve the maximum possible energy yield, the HSU size should be increased first, and then the insulation size, as it is the less critical parameter in terms of the energy generation capability of the prototype. As shown in Table 12.3, the ability to provide sufficient energy to power the sensor module during the sterilisation plateau phase already occurs with an HSU of 12.5 mm in height and insulation of 5 mm in height. This allows the overall device to remain relatively small at no more than 3 cm in height, which meets the assumed business requirements of the industrial partner.

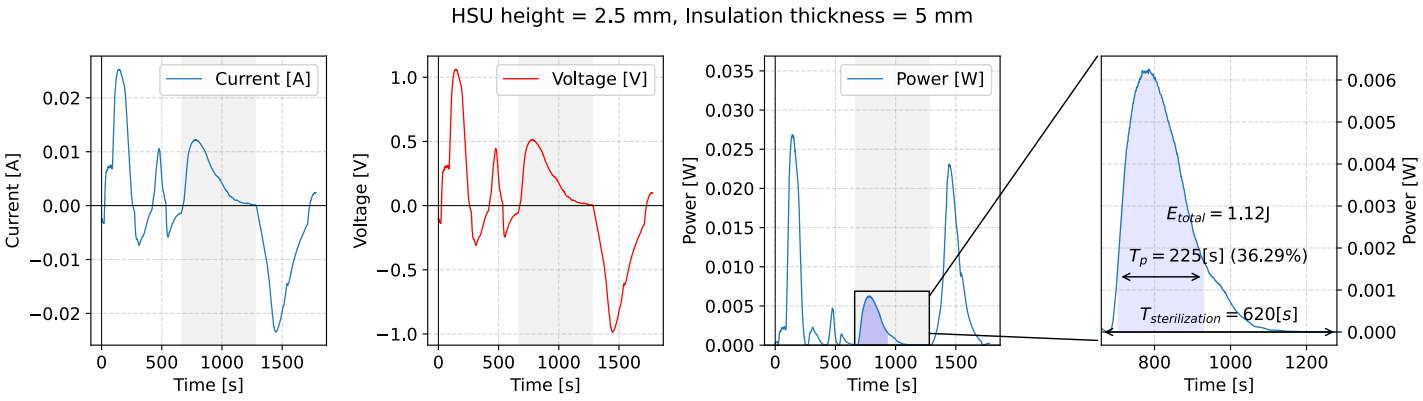

Figure 12.14. Model with HSU heigh of 2.5 mm and insulation thickness of 5 mm. Current, voltage, and power output during the steam sterilization procedure with special emphasis on plateau phase. Power sufficient for sensor supply is provided during 36.29 % of the plateau phase.

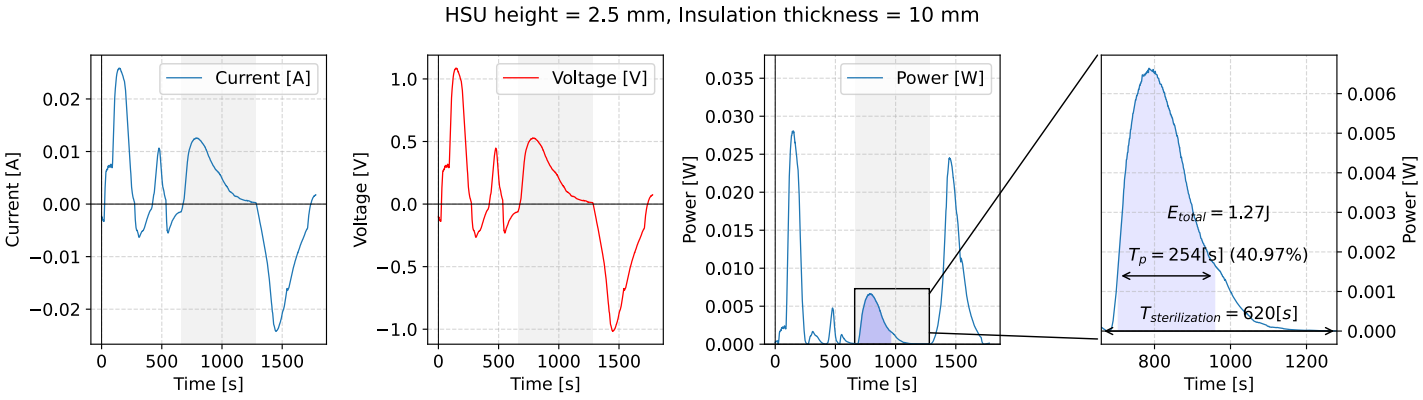

Figure 12.15. Model with HSU heigh of 2.5 mm and insulation thickness of 10 mm. Current, voltage, and power output during the steam sterilization procedure with special emphasis on plateau phase. Power sufficient for sensor supply is provided during 40.97 % of the plateau phase.

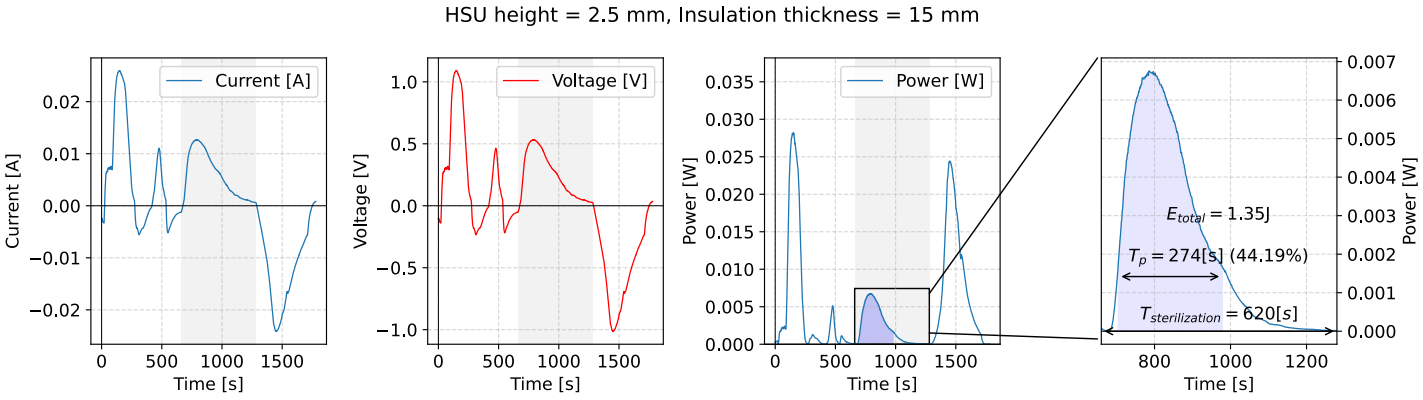

Figure 12.16. Model with HSU heigh of 2.5 mm and insulation thickness of 15 mm. Current, voltage, and power output during the steam sterilization procedure with special emphasis on plateau phase. Power sufficient for sensor supply is provided during 44.19 % of the plateau phase.

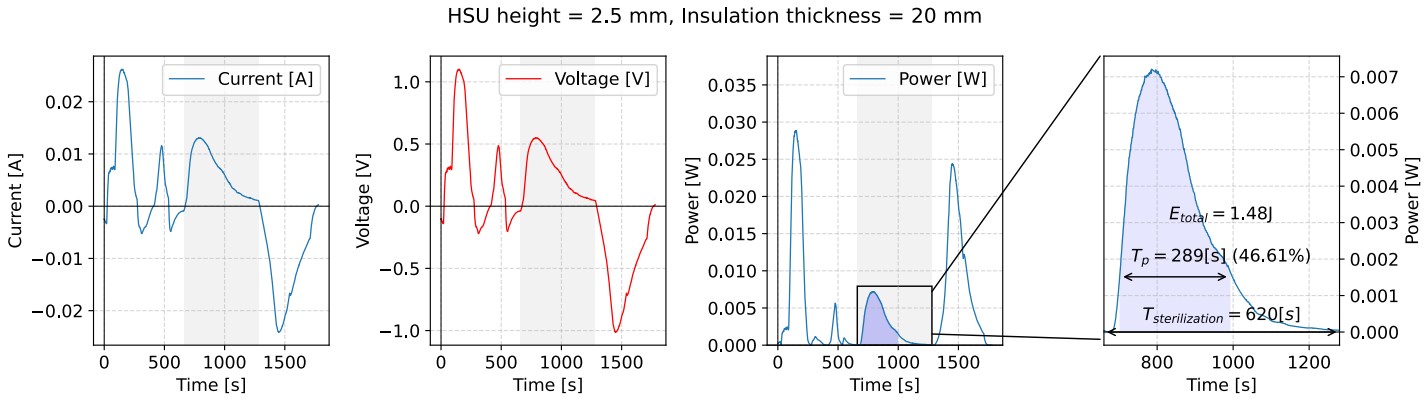

Figure 12.17. Model with HSU heigh of 2.5 mm and insulation thickness of 20 mm. Current, voltage, and power output during the steam sterilization procedure with special emphasis on plateau phase. Power sufficient for sensor supply is provided during 46.61 % of the plateau phase.

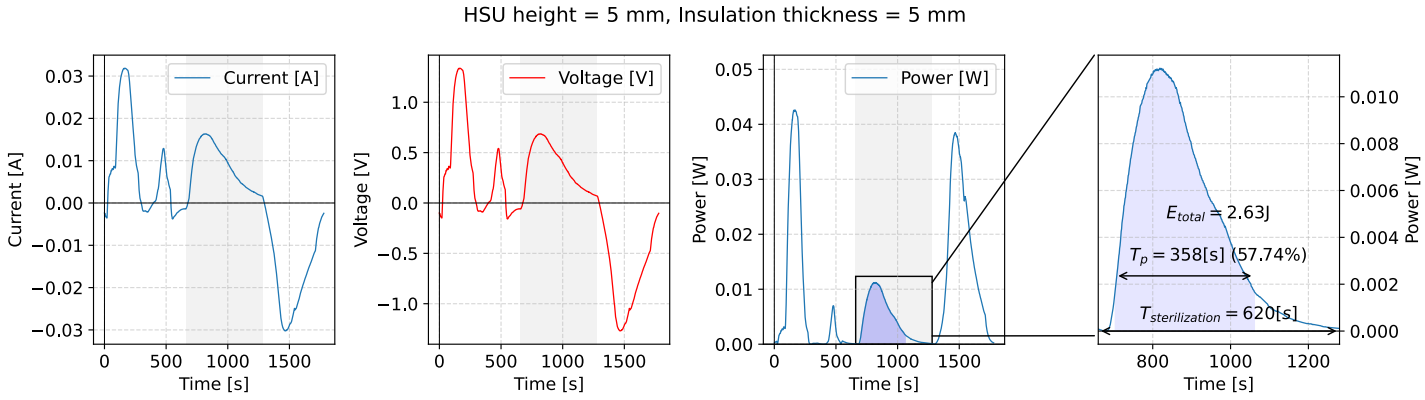

Figure 12.18. Model with HSU heigh of 5 mm and insulation thickness of 5 mm. Current, voltage, and power output during the steam sterilization procedure with special emphasis on plateau phase. Power sufficient for sensor supply is provided during 57.74 % of the plateau phase.

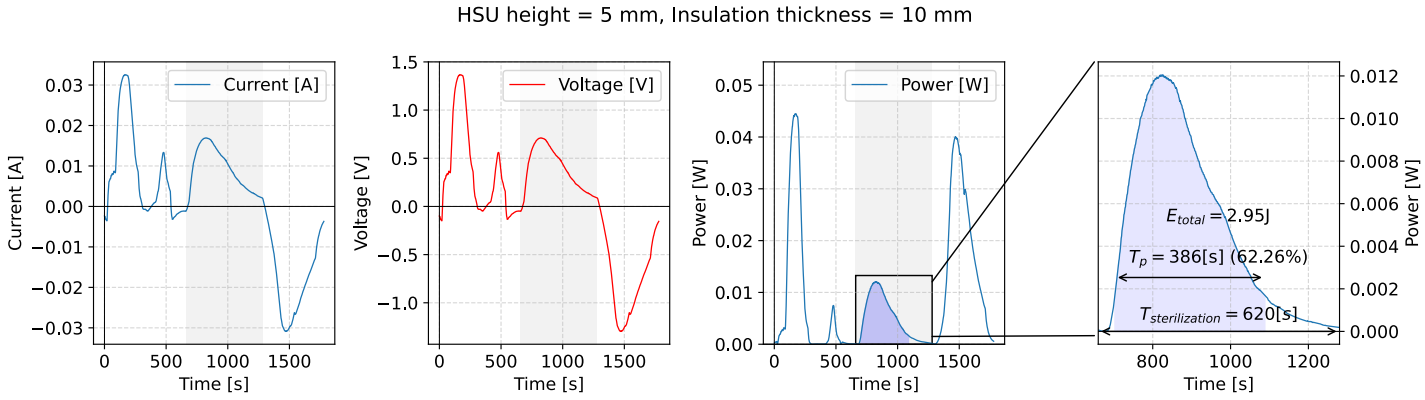

Figure 12.19. Model with HSU heigh of 5 mm and insulation thickness of 10 mm. Current, voltage, and power output during the steam sterilization procedure with special emphasis on plateau phase. Power sufficient for sensor supply is provided during 62.26 % of the plateau phase.

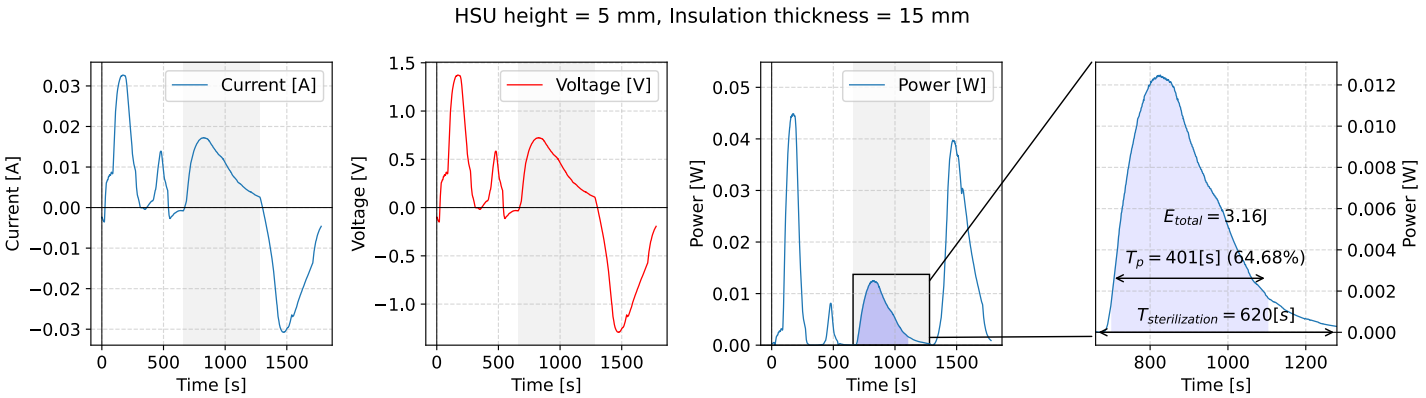

Figure 12.20. Model with HSU heigh of 5 mm and insulation thickness of 15 mm. Current, voltage, and power output during the steam sterilization procedure with special emphasis on plateau phase. Power sufficient for sensor supply is provided during 64.68 % of the plateau phase.

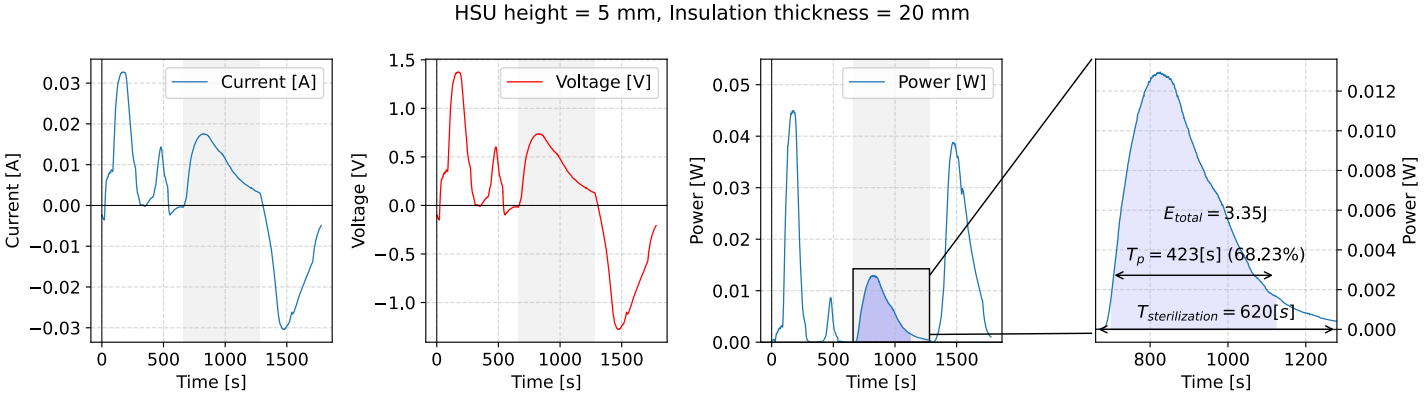

Figure 12.21. Model with HSU heigh of 5 mm and insulation thickness of 20 mm. Current, voltage, and power output during the steam sterilization procedure with special emphasis on plateau phase. Power sufficient for sensor supply is provided during 68.23 % of the plateau phase.

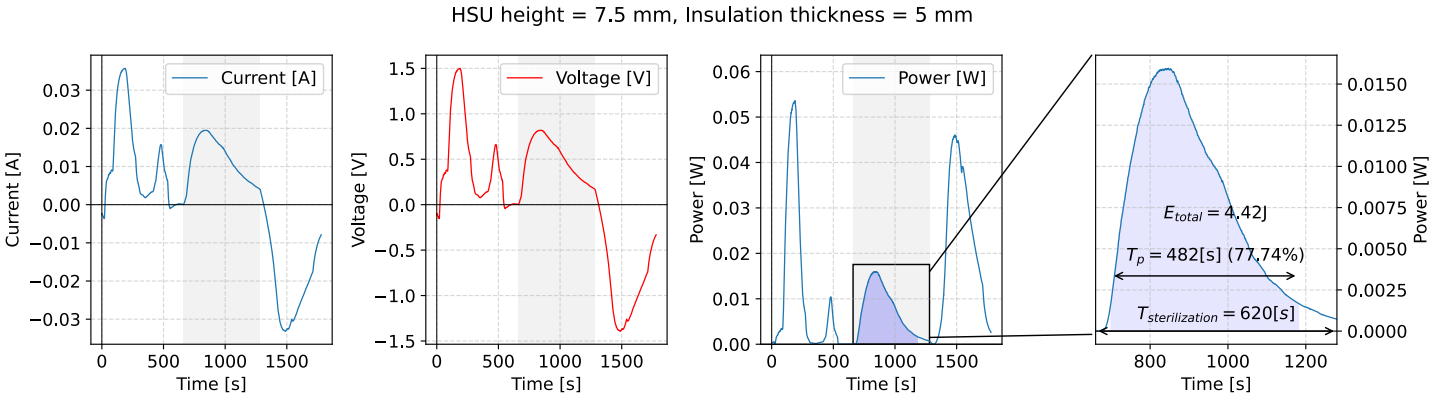

Figure 12.22. Model with HSU heigh of 7.5 mm and insulation thickness of 5 mm. Current, voltage, and power output during the steam sterilization procedure with special emphasis on plateau phase. Power sufficient for sensor supply is provided during 77.74 % of the plateau phase.

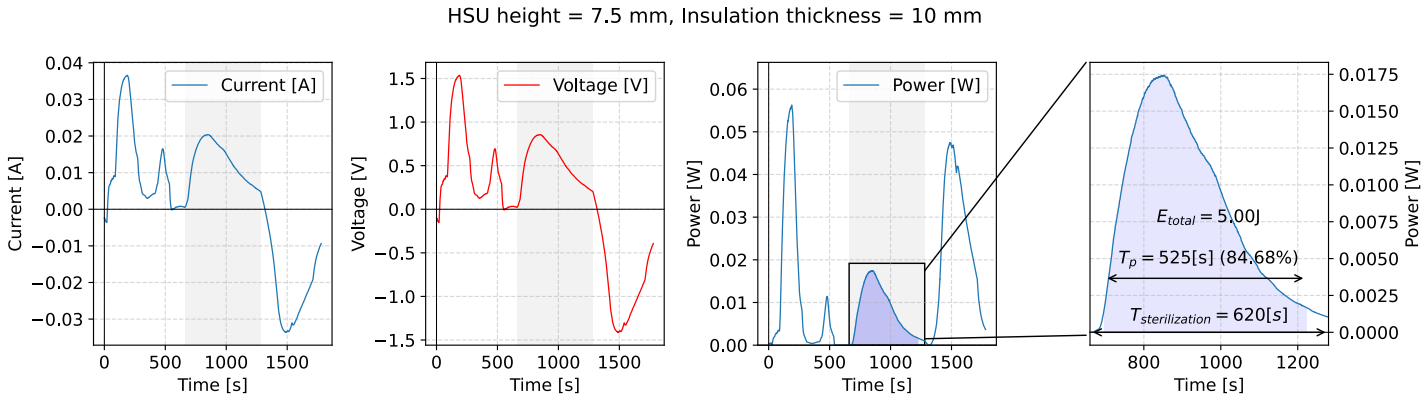

Figure 12.23. Model with HSU heigh of 7.5 mm and insulation thickness of 10 mm. Current, voltage, and power output during the steam sterilization procedure with special emphasis on plateau phase. Power sufficient for sensor supply is provided during 84.68 % of the plateau phase.

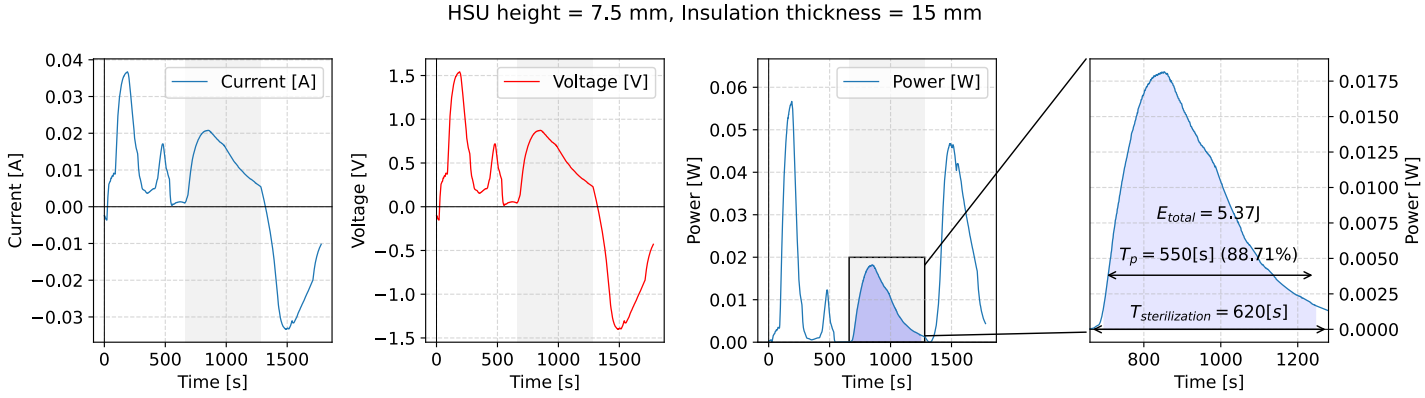

Figure 12.24. Model with HSU heigh of 7.5 mm and insulation thickness of 15 mm. Current, voltage, and power output during the steam sterilization procedure with special emphasis on plateau phase. Power sufficient for sensor supply is provided during 88.71 % of the plateau phase.

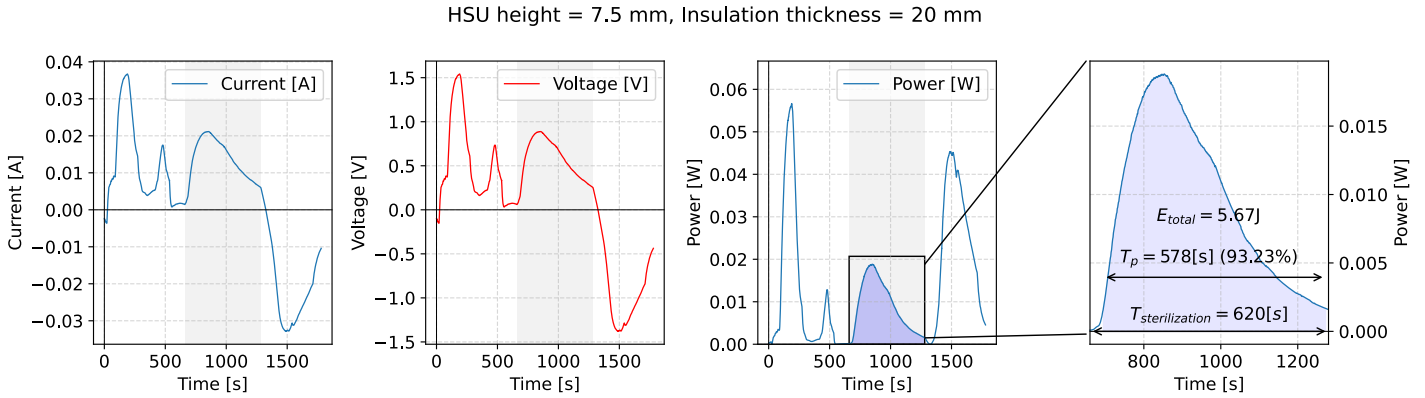

Figure 12.25. Model with HSU heigh of 7.5 mm and insulation thickness of 20 mm. Current, voltage, and power output during the steam sterilization procedure with special emphasis on plateau phase. Power sufficient for sensor supply is provided during 93.23 % of the plateau phase.

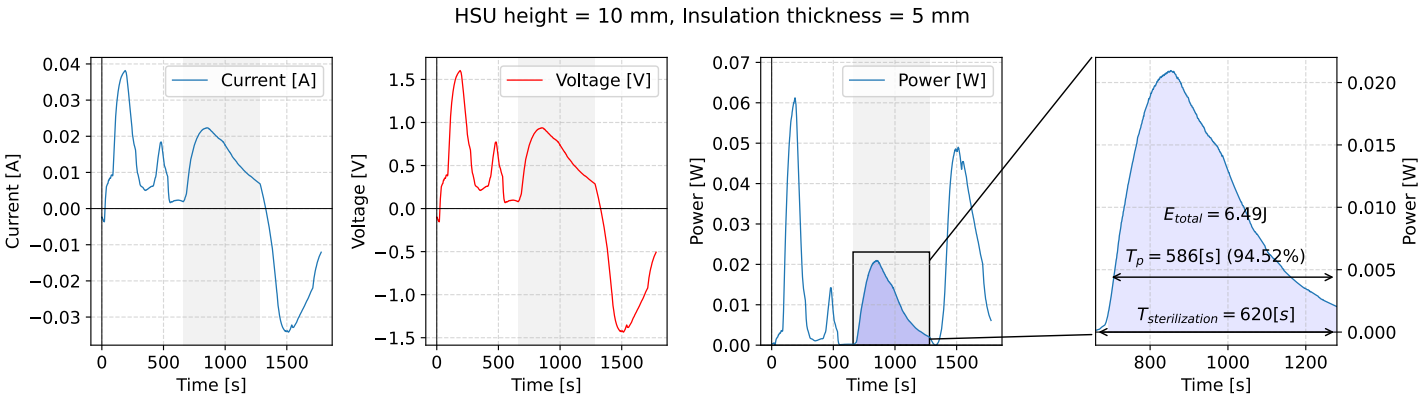

Figure 12.26. Model with HSU heigh of 10 mm and insulation thickness of 5 mm. Current, voltage, and power output during the steam sterilization procedure with special emphasis on plateau phase. Power sufficient for sensor supply is provided during 94.52 % of the plateau phase.

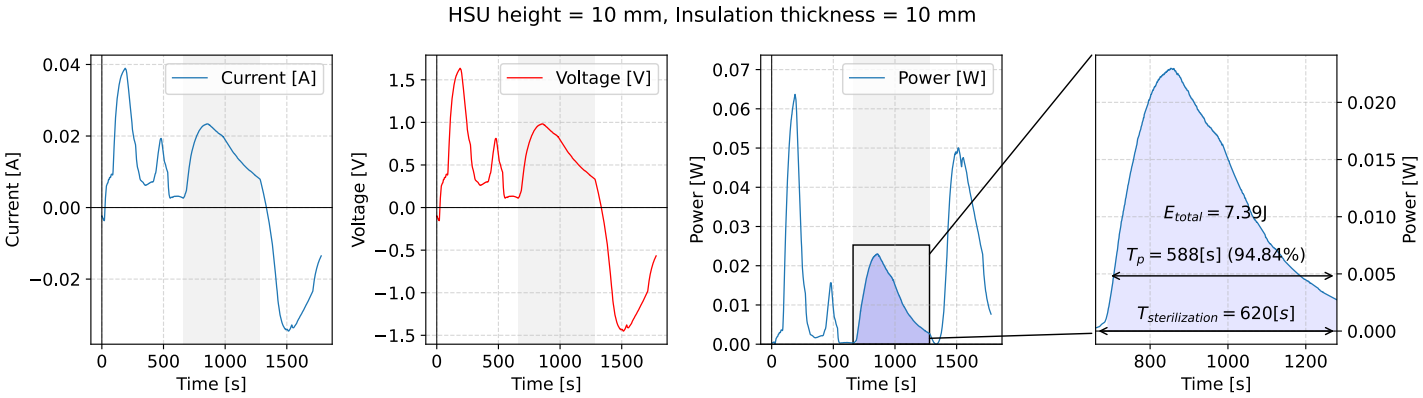

Figure 12.27. Model with HSU heigh of 10 mm and insulation thickness of 10 mm. Current, voltage, and power output during the steam sterilization procedure with special emphasis on plateau phase. Power sufficient for sensor supply is provided during 94.84 % of the plateau phase.

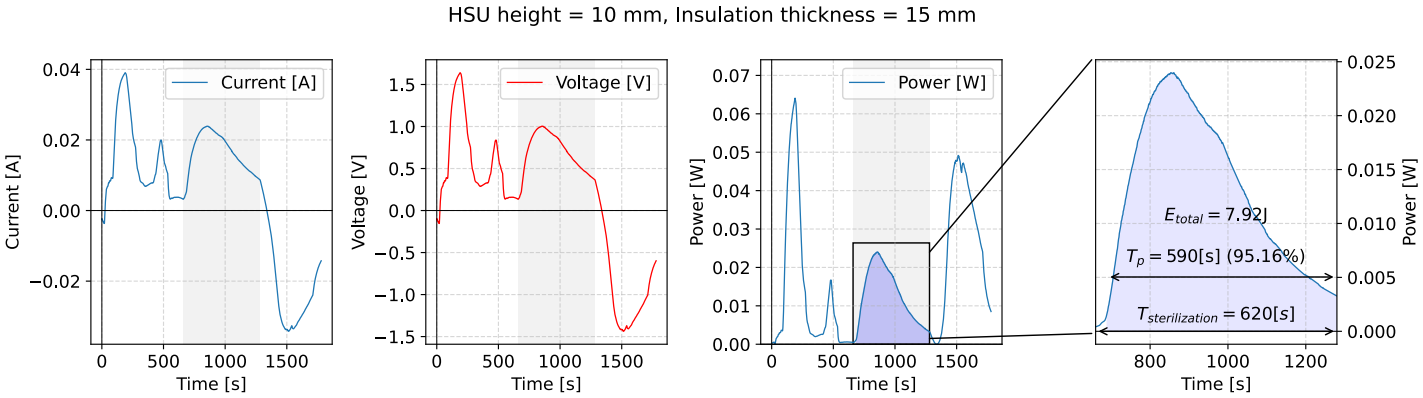

Figure 12.28. Model with HSU heigh of 10 mm and insulation thickness of 15 mm. Current, voltage, and power output during the steam sterilization procedure with special emphasis on plateau phase. Power sufficient for sensor supply is provided during 95.16 % of the plateau phase.

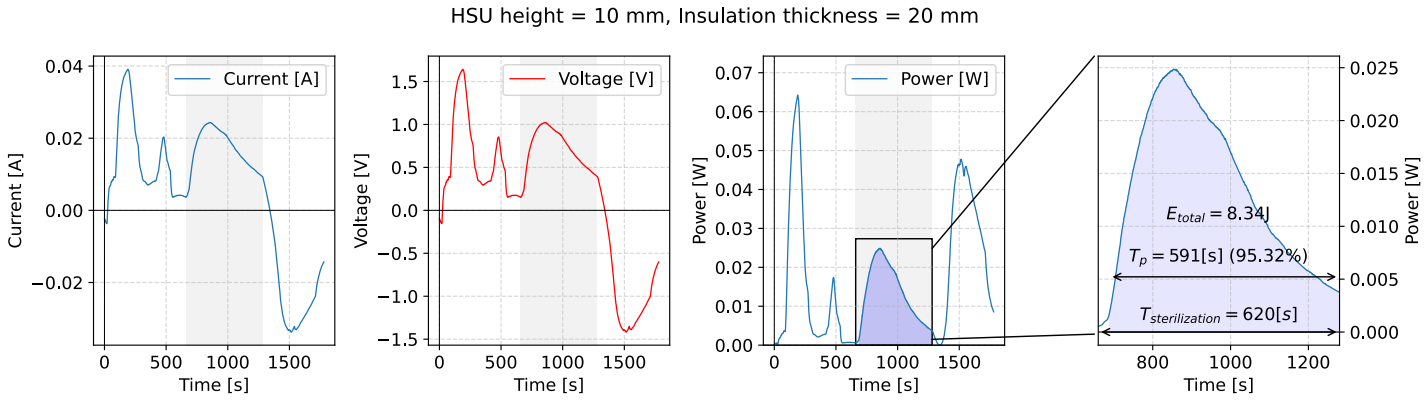

Figure 12.29. Model with HSU heigh of 10 mm and insulation thickness of 20 mm. Current, voltage, and power output during the steam sterilization procedure with special emphasis on plateau phase. Power sufficient for sensor supply is provided during 95.32 % of the plateau phase.

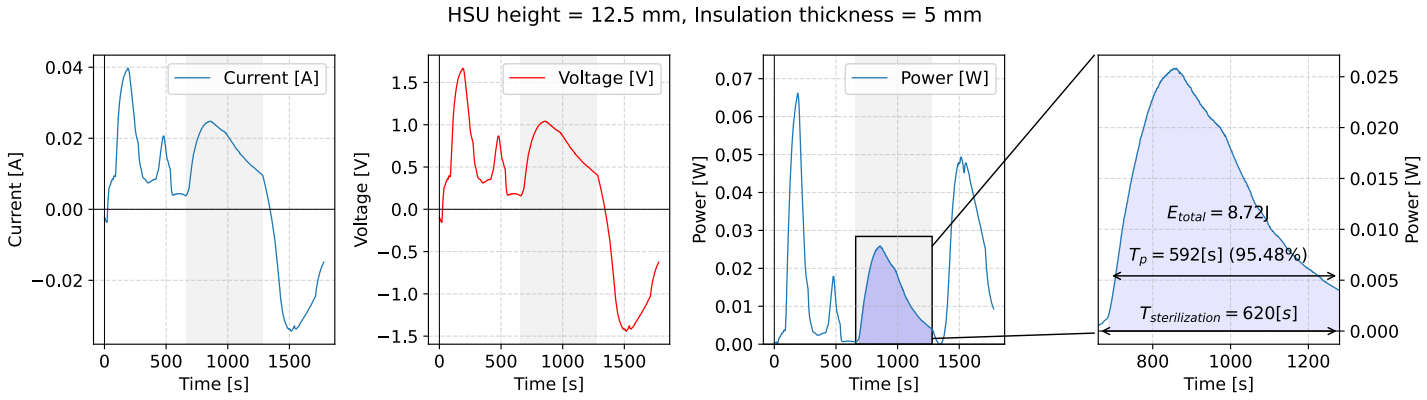

Figure 12.30. Model with HSU heigh of 12.5 mm and insulation thickness of 5 mm. Current, voltage, and power output during the steam sterilization procedure with special emphasis on plateau phase. Power sufficient for sensor supply is provided during 95.48 % of the plateau phase.

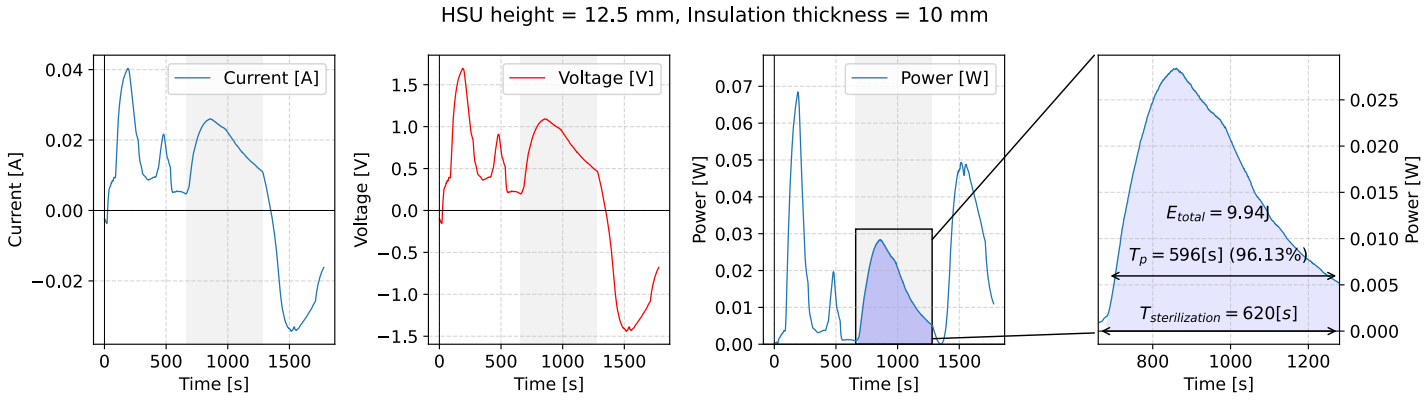

Figure 12.31. Model with HSU heigh of 12.5 mm and insulation thickness of 10 mm. Current, voltage, and power output during the steam sterilization procedure with special emphasis on plateau phase. Power sufficient for sensor supply is provided during 96.13 % of the plateau phase.

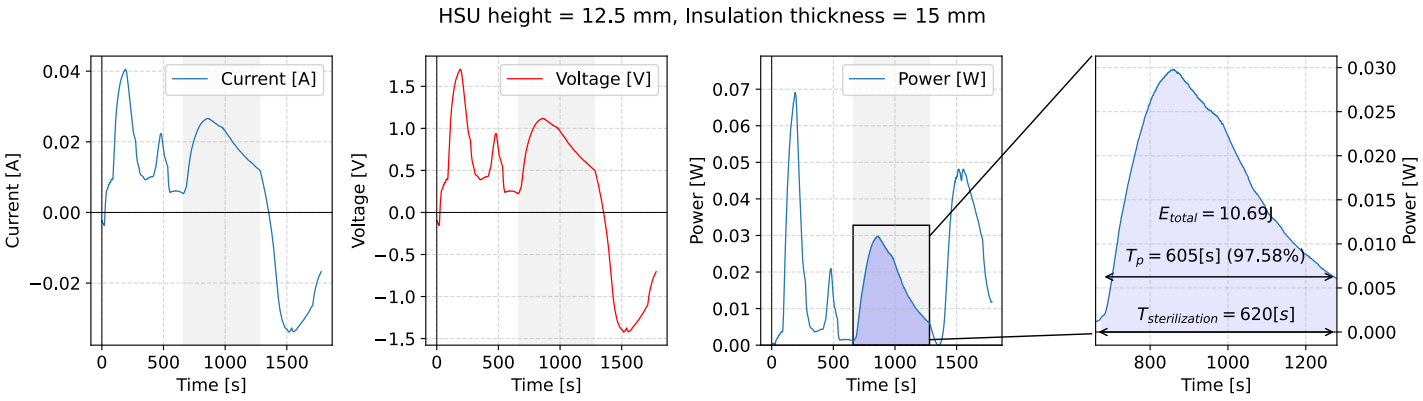

Figure 12.32. Model with HSU heigh of 12.5 mm and insulation thickness of 15 mm. Current, voltage, and power output during the steam sterilization procedure with special emphasis on plateau phase. Power sufficient for sensor supply is provided during 97.58 % of the plateau phase.

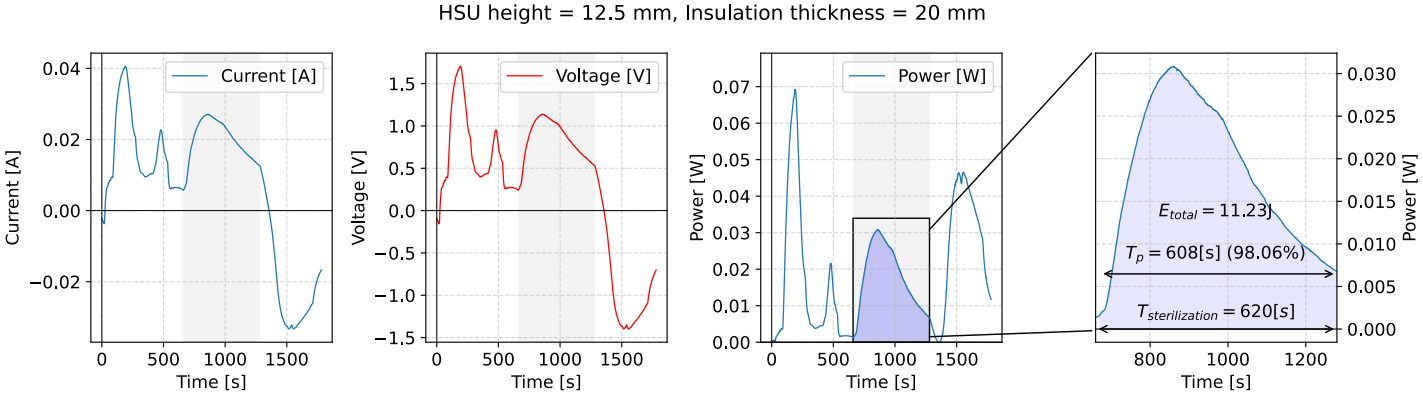

Figure 12.33. Model with HSU heigh of 12.5 mm and insulation thickness of 20 mm. Current, voltage, and power output during the steam sterilization procedure with special emphasis on plateau phase. Power sufficient for sensor supply is provided during 98.06 % of the plateau phase.

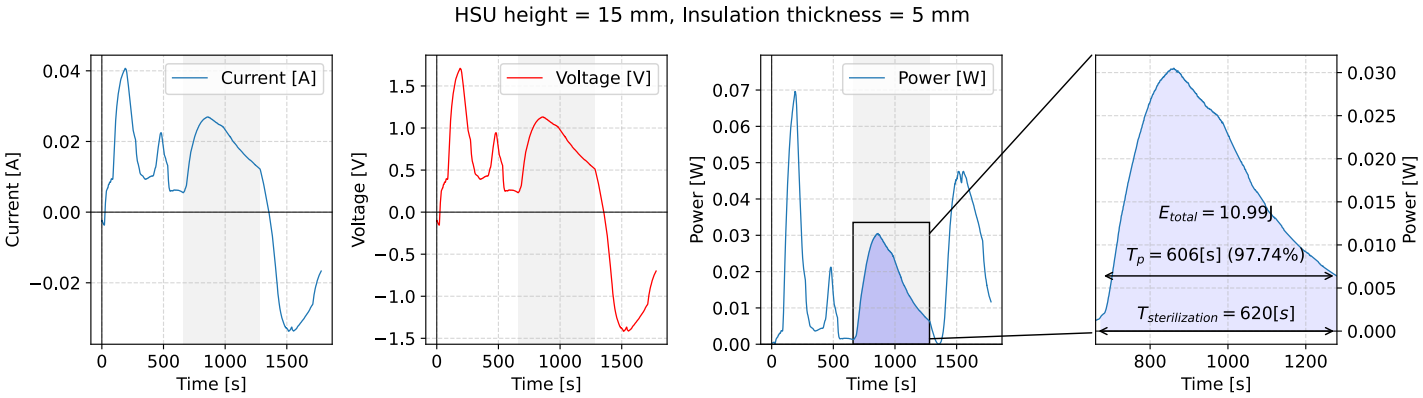

Figure 12.34. Model with HSU heigh of 15 mm and insulation thickness of 5 mm. Current, voltage, and power output during the steam sterilization procedure with special emphasis on plateau phase. Power sufficient for sensor supply is provided during 97.74 % of the plateau phase.

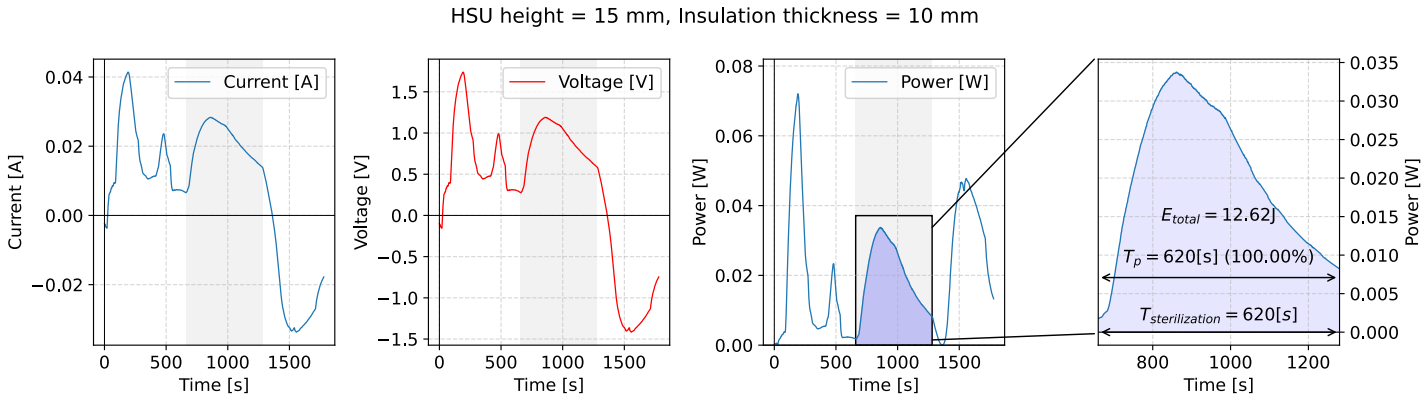

Figure 12.35. Model with HSU heigh of 15 mm and insulation thickness of 10 mm. Current, voltage, and power output during the steam sterilization procedure with special emphasis on plateau phase. Power sufficient for sensor supply is provided during 100 % of the plateau phase.

Table 12.3. Results summary of energy generated, average power and sensor activity in active mode scenario.

HSU height [mm]	Insulation thickness [mm]	Energy generated (plateau) [J]	Average power [W]	Plateau phase duration [s]	Sensor activity duration [s]	Sensor activity in plateau duration [%]
2.5	5.0	1.12	0.0006	620	225	36.29
2.5	10.0	1.27	0.0007	620	254	40.97
2.5	15.0	1.35	0.0076	620	274	44.19
2.5	20.0	1.48	0.0008	620	289	46.61
5.0	5.0	2.63	0.0015	620	358	57.74
5.0	10.0	2.95	0.0017	620	386	62.26
5.0	15.0	3.16	0.0018	620	401	64.68
5.0	20.0	3.35	0.0019	620	423	68.23
7.5	5.0	4.42	0.0025	620	482	77.74
7.5	10.0	5.00	0.0028	620	525	84.68
7.5	15.0	5.37	0.0030	620	550	88.71
7.5	20.0	5.67	0.0032	620	578	93.23
10.0	5.0	6.49	0.0036	620	586	94.52
10.0	10.0	7.39	0.0042	620	588	94.84
10.0	15.0	7.92	0.0045	620	590	95.16
10.0	20.0	8.34	0.0047	620	591	95.32
12.5	5.0	8.72	0.0049	620	592	95.48
12.5	10.0	9.94	0.0056	620	596	96.13
12.5	15.0	10.69	0.0060	620	605	97.58
15.0	5.0	10.99	0.0062	620	606	97.74
12.5	20.0	11.23	0.0063	620	608	98.06
17.5	5.0	13.21	0.0074	620	620	100.00
20.0	5.0	15.29	0.0086	620	620	100.00
15.0	10.0	12.62	0.0071	620	620	100.00
17.5	10.0	15.11	0.0085	620	620	100.00
20.0	10.0	17.59	0.0099	620	620	100.00
15.0	15.0	13.50	0.0759	620	620	100.00
17.5	15.0	16.21	0.0091	620	620	100.00
20.0	15.0	18.83	0.0106	620	620	100.00
15.0	20.0	14.12	0.0079	620	620	100.00
17.5	20.0	16.94	0.0095	620	620	100.00
20.0	20.0	19.65	0.0110	620	620	100.00

Passive Mode Scenario

In the passive scenario, the power supply of the sensor module operating in LPM3 energy-saving mode without using the energy storage system as a buffer was considered. In each scenario, the percentage of the plateau phase time that generates sufficient power to supply the sensor was considered.

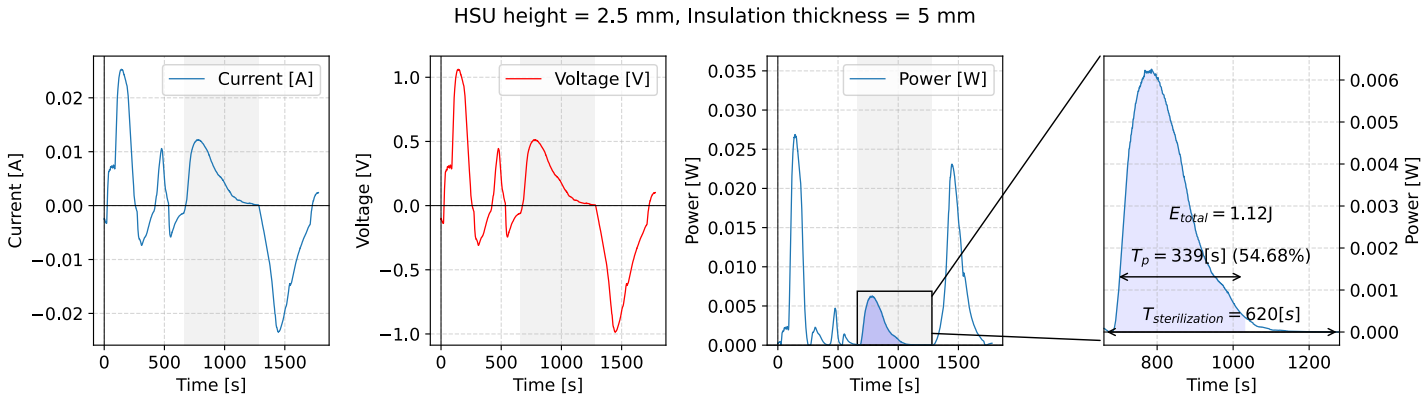

Figure 12.36. Current, voltage, and power generated through the steam sterilization procedure assuming no energy storage system connected. The power generated through the plateau phase which exceeds the minimum level for sensor operation is marked in blue.

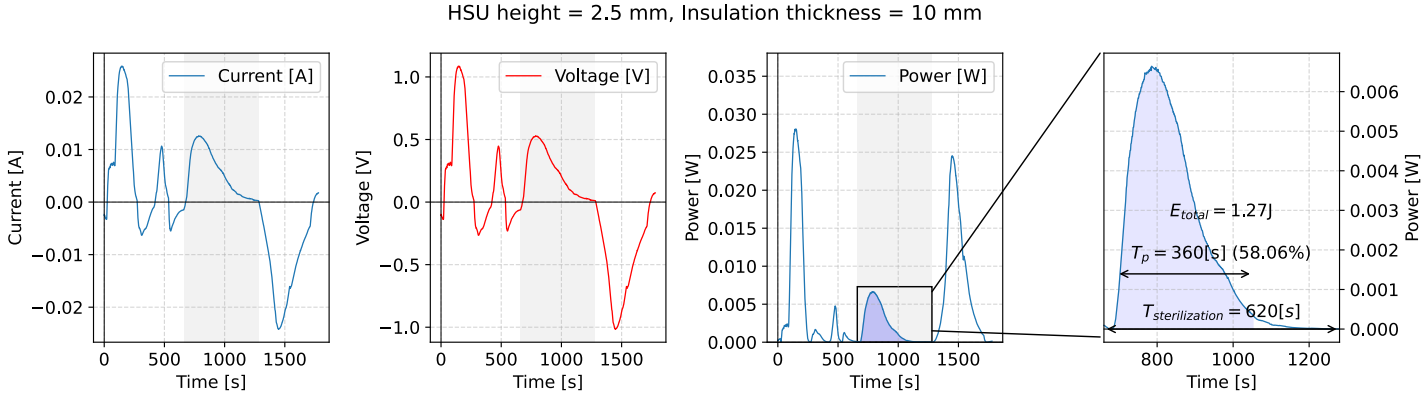

Figure 12.37. Current, voltage, and power generated through the steam sterilization procedure assuming no energy storage system connected. The power generated through the plateau phase which exceeds the minimum level for sensor operation is marked in blue.

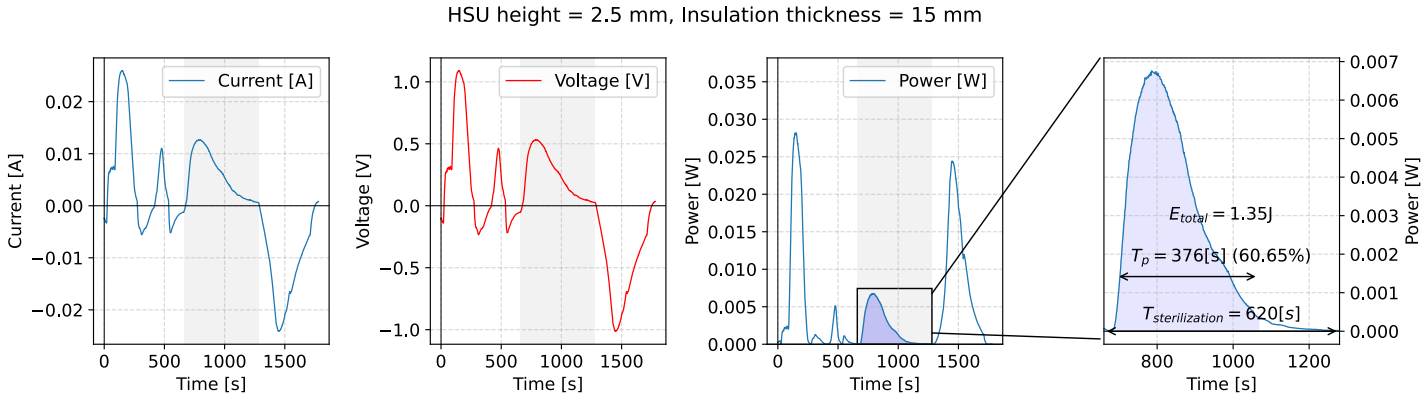

Figure 12.38. Current, voltage, and power generated through the steam sterilization procedure assuming no energy storage system connected. The power generated through the plateau phase which exceeds the minimum level for sensor operation is marked in blue.

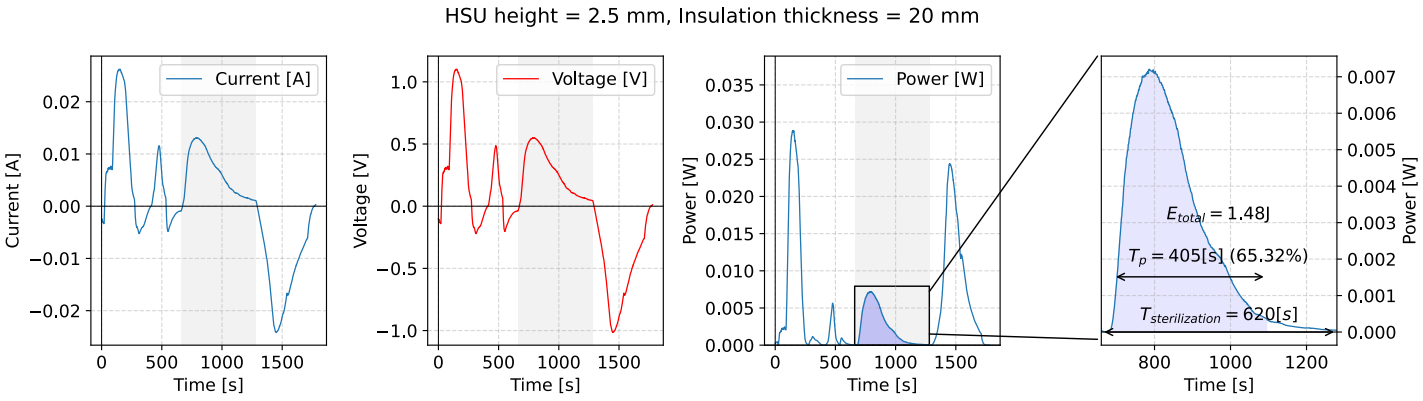

Figure 12.39. Current, voltage, and power generated through the steam sterilization procedure assuming no energy storage system connected. The power generated through the plateau phase which exceeds the minimum level for sensor operation is marked in blue.

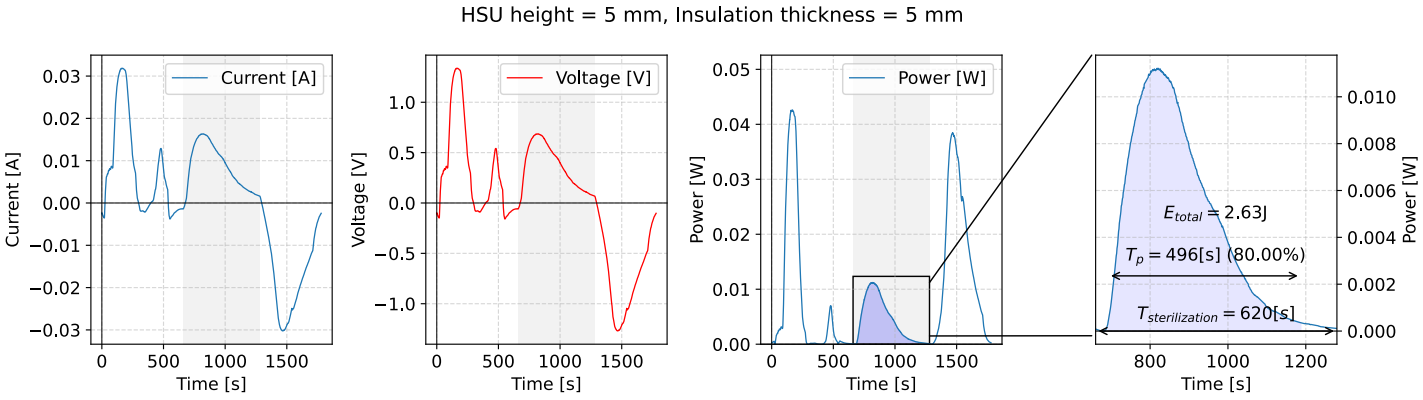

Figure 12.40. Current, voltage, and power generated through the steam sterilization procedure assuming no energy storage system connected. The power generated through the plateau phase which exceeds the minimum level for sensor operation is marked in blue.

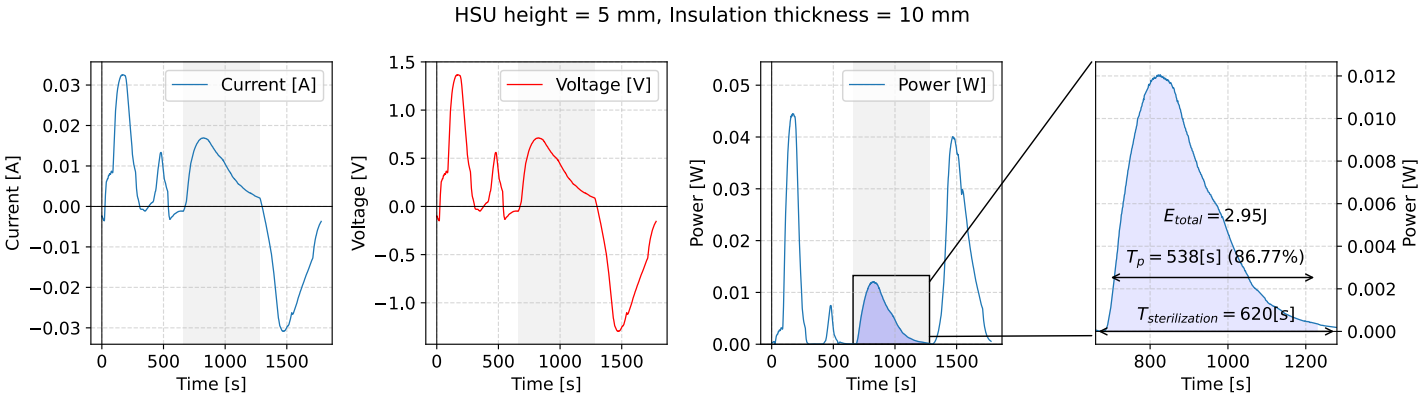

Figure 12.41. Current, voltage, and power generated through the steam sterilization procedure assuming no energy storage system connected. The power generated through the plateau phase which exceeds the minimum level for sensor operation is marked in blue.

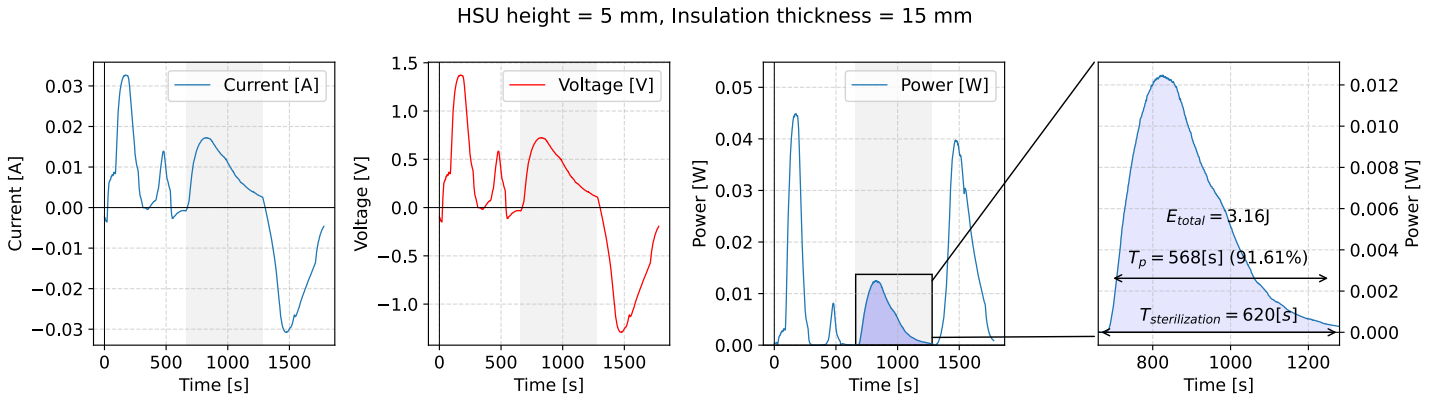

Figure 12.42. Current, voltage, and power generated through the steam sterilization procedure assuming no energy storage system connected. The power generated through the plateau phase which exceeds the minimum level for sensor operation is marked in blue.

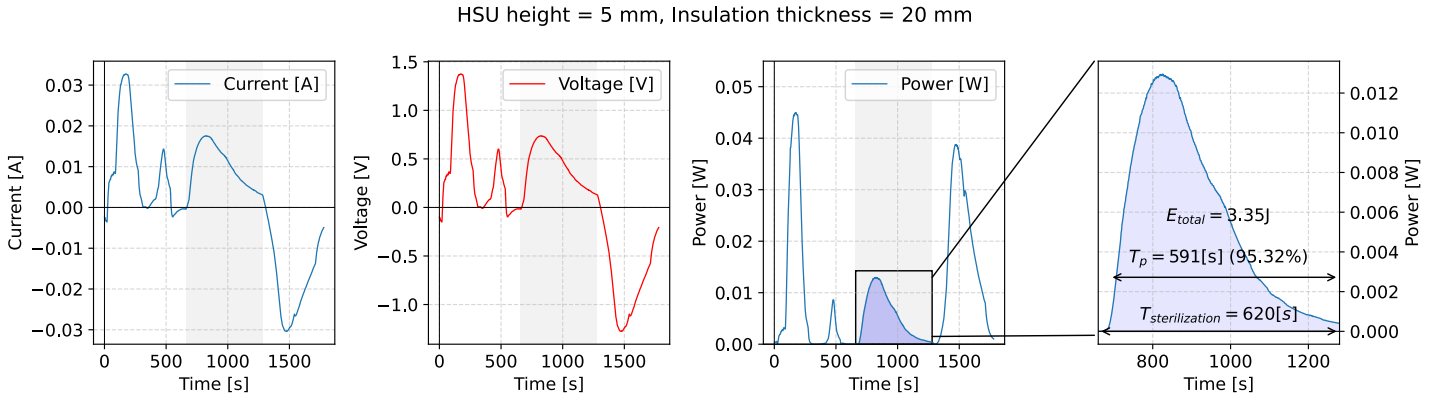

Figure 12.43. Current, voltage, and power generated through the steam sterilization procedure assuming no energy storage system connected. The power generated through the plateau phase which exceeds the minimum level for sensor operation is marked in blue.

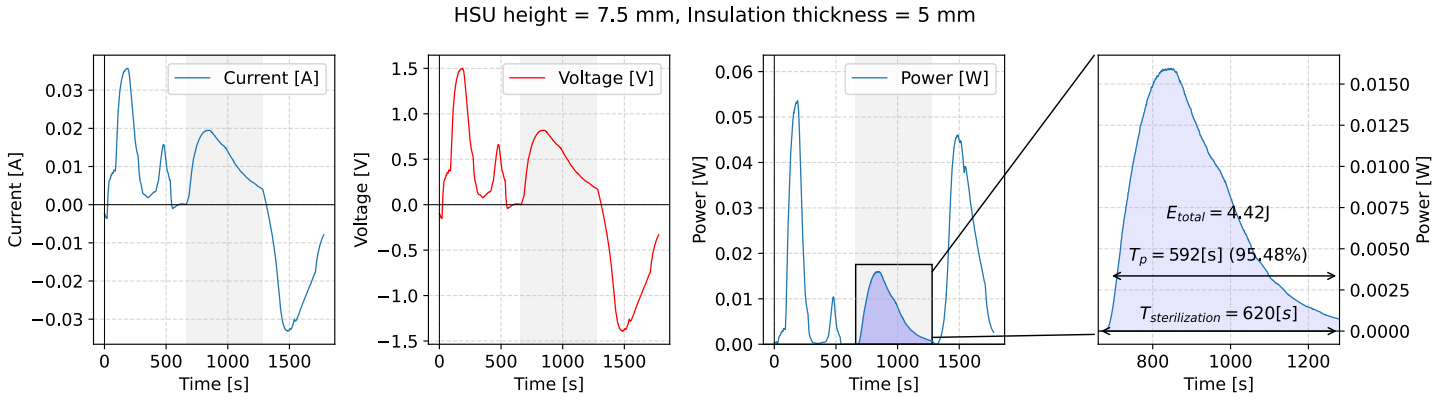

Figure 12.44. Current, voltage, and power generated through the steam sterilization procedure assuming no energy storage system connected. The power generated through the plateau phase which exceeds the minimum level for sensor operation is marked in blue.

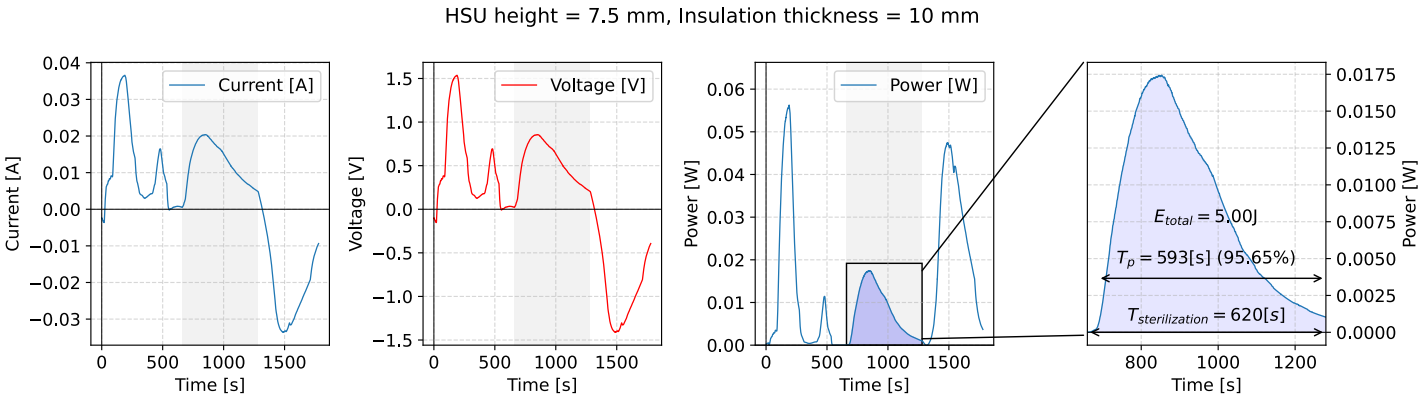

Figure 12.45. Current, voltage, and power generated through the steam sterilization procedure assuming no energy storage system connected. The power generated through the plateau phase which exceeds the minimum level for sensor operation is marked in blue.

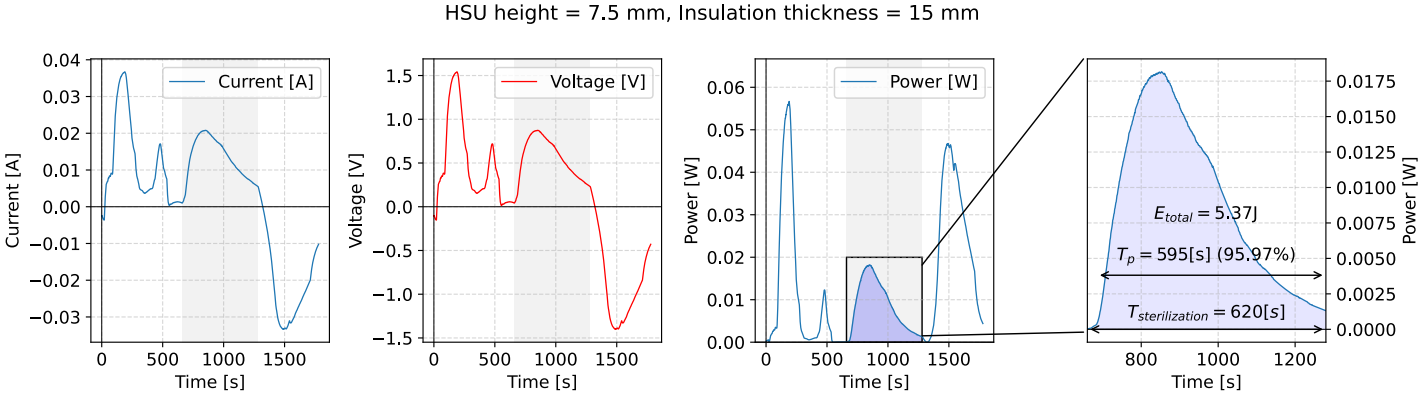

Figure 12.46. Current, voltage, and power generated through the steam sterilization procedure assuming no energy storage system connected. The power generated through the plateau phase which exceeds the minimum level for sensor operation is marked in blue.

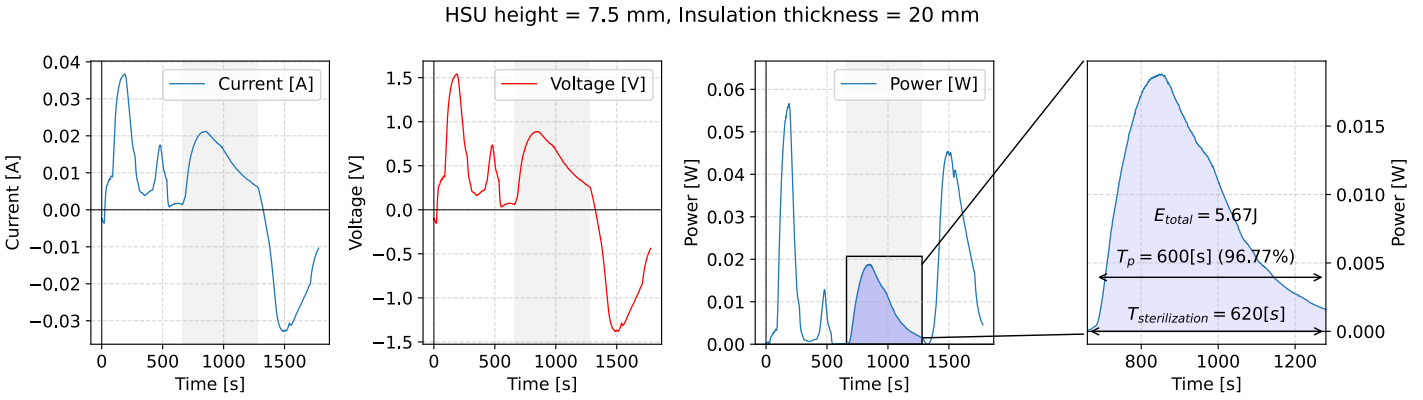

Figure 12.47. Current, voltage, and power generated through the steam sterilization procedure assuming no energy storage system connected. The power generated through the plateau phase which exceeds the minimum level for sensor operation is marked in blue.

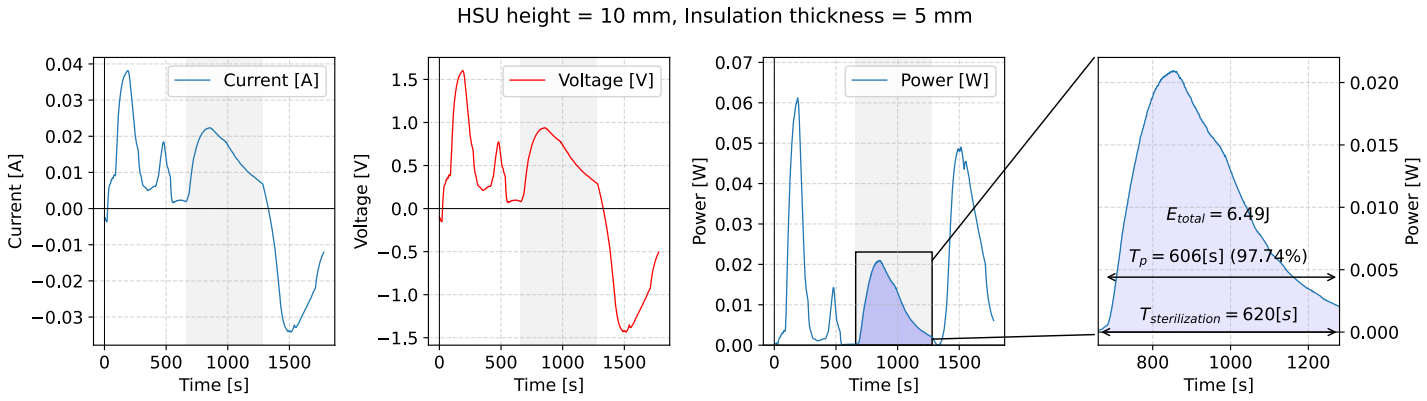

Figure 12.48. Current, voltage, and power generated through the steam sterilization procedure assuming no energy storage system connected. The power generated through the plateau phase which exceeds the minimum level for sensor operation is marked in blue.

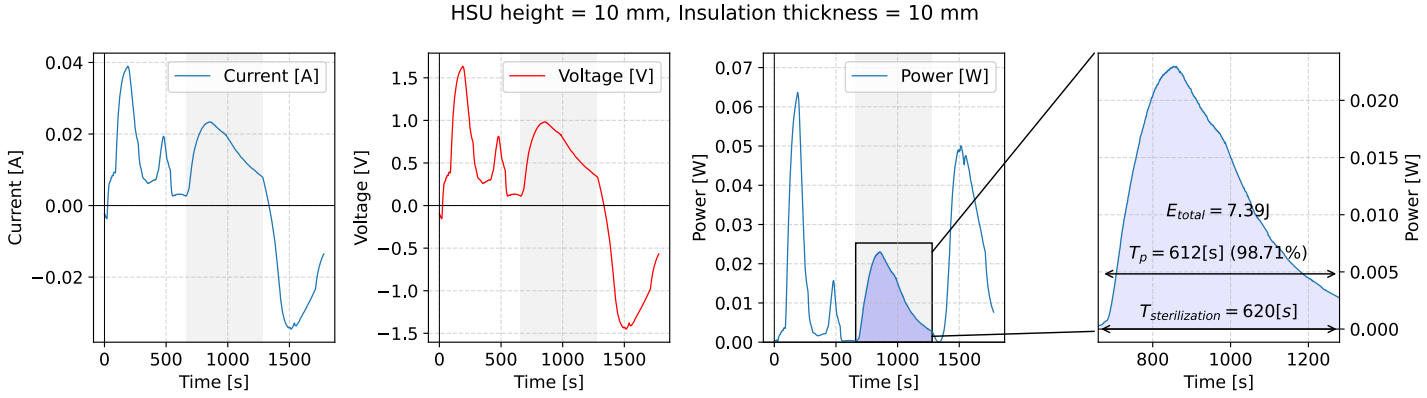

Figure 12.49. Current, voltage, and power generated through the steam sterilization procedure assuming no energy storage system connected. The power generated through the plateau phase which exceeds the minimum level for sensor operation is marked in blue.

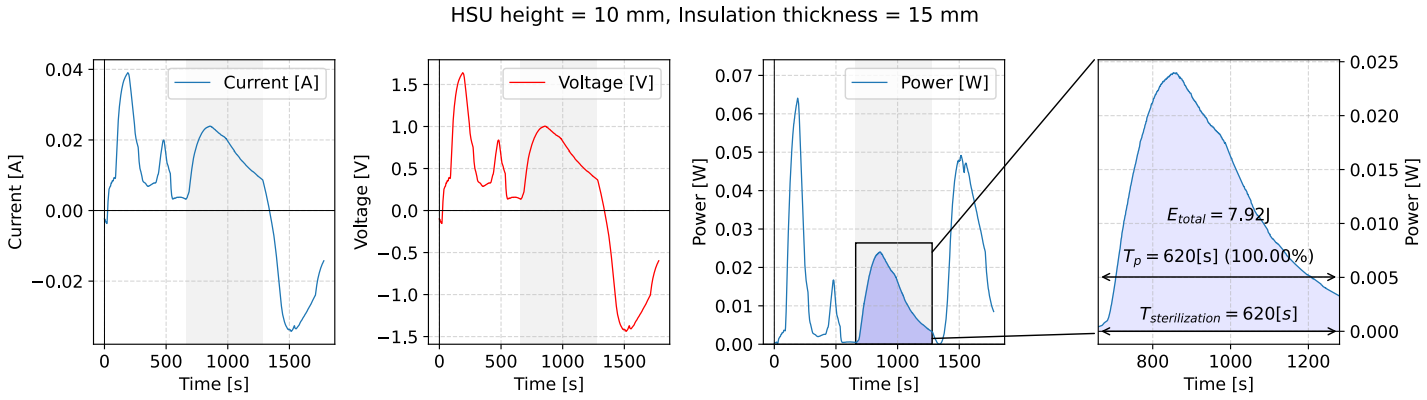

Figure 12.50. Current, voltage, and power generated through the steam sterilization procedure assuming no energy storage system connected. The power generated through the plateau phase which exceeds the minimum level for sensor operation is marked in blue.

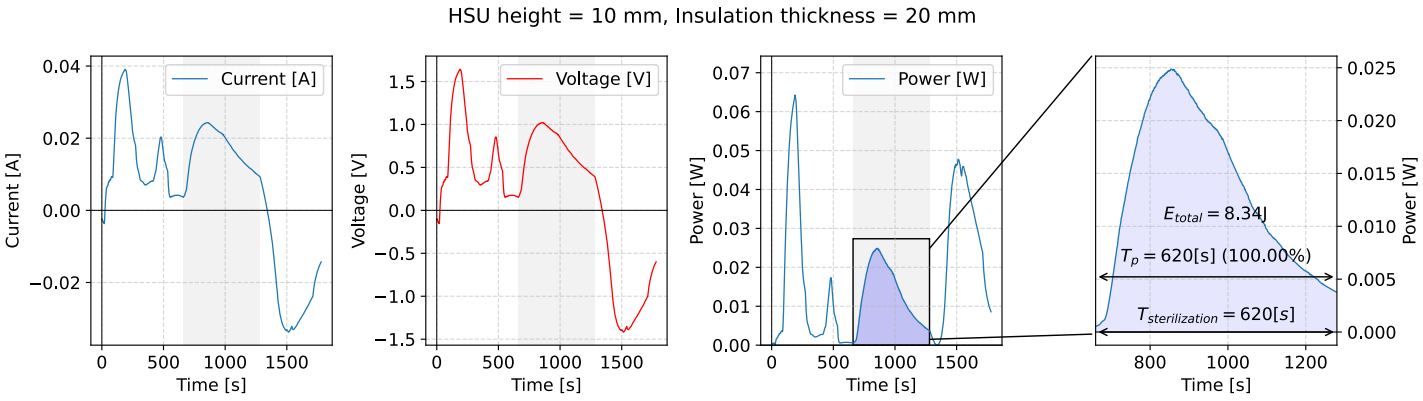

Figure 12.51. Current, voltage, and power generated through the steam sterilization procedure assuming no energy storage system connected. The power generated through the plateau phase which exceeds the minimum level for sensor operation is marked in blue.

Assuming that the sensor operates in passive mode, the simulation results are very optimistic. As shown in Figure 12.44, already an HSU of 7.5 mm in height with only 5 mm of thermal insulation ensures sensor operation during the 95.32 % plateau phase of steam sterilisation. Similar results brings the HSU with height of 5 mm as it is presented in the Figure 12.43, however it needs to be surrounded by as much as 20 mm of thermal insulation, which is not optimal from the miniatiurisation point of view. Increasing the thickness of the insulation, even to 20 mm, does not yield significant gains in terms of the time during which the specified minimum power generation is provided. Adequate power generation through 100 % of the plateau phase is only achieved with an HSU height of 10 mm and an insulation thickness of 15 mm, as it is presented in the Figure 12.50.

Table 12.4. Results summary of energy generated, average power and sensor activity in passive mode scenario.

HSU height [mm]	Insulation thickness [mm]	Energy generated (plateau) [J]	Average power [W]	Plateau phase duration [s]	Sensor activity duration [s]	Sensor activity in plateau duration [%]
2.5	5.0	1.12	0.0006	620	339	54.68
2.5	10.0	1.27	0.0007	620	360	58.06
2.5	15.0	1.35	0.0076	620	376	60.65
2.5	20.0	1.48	0.0008	620	405	65.32
5.0	5.0	2.63	0.0015	620	496	80.00
5.0	10.0	2.95	0.0017	620	538	86.77
5.0	15.0	3.16	0.0018	620	568	91.61
5.0	20.0	3.35	0.0019	620	591	95.32
7.5	5.0	4.42	0.0025	620	592	95.48
7.5	10.0	5.00	0.0028	620	593	95.65
7.5	15.0	5.37	0.0030	620	595	95.97
7.5	20.0	5.67	0.0032	620	600	96.77
10.0	5.0	6.49	0.0036	620	606	97.74
10.0	10.0	7.39	0.0042	620	612	98.71
12.5	5.0	8.72	0.0049	620	620	100.00
15.0	5.0	10.99	0.0062	620	620	100.00
17.5	5.0	13.21	0.0074	620	620	100.00
20.0	5.0	15.29	0.0086	620	620	100.00
12.5	10.0	9.94	0.0056	620	620	100.00
15.0	10.0	12.62	0.0071	620	620	100.00
17.5	10.0	15.11	0.0085	620	620	100.00
20.0	10.0	17.59	0.0099	620	620	100.00
10.0	15.0	7.92	0.0045	620	620	100.00
12.5	15.0	10.69	0.0060	620	620	100.00
15.0	15.0	13.50	0.0759	620	620	100.00
17.5	15.0	16.21	0.0091	620	620	100.00
20.0	15.0	18.83	0.0106	620	620	100.00
10.0	20.0	8.34	0.0047	620	620	100.00
12.5	20.0	11.23	0.0063	620	620	100.00
15.0	20.0	14.12	0.0079	620	620	100.00
17.5	20.0	16.94	0.0095	620	620	100.00
20.0	20.0	19.65	0.0110	620	620	100.00

13. Summary

Abstract

In this chapter a summary and outcomes of this PhD thesis are presented. At first all the research questions from chapter 1 are summarized, answered and discussed. Secondly, the summary of the whole PhD thesis is presented and resulting publications and patents are listed.

13.1. Research Questions Answers

As a result of this PhD thesis, following research questions (**RQ**) stated in the chapter 1 have been addressed and answered (**RA**):

1. **RQ1:** What are the possibilities of powering the low power electronics in the steam sterilization chamber using energy storage devices?
   RA1: The options for powering medical IoT devices that are subject to steam sterilisation are limited. Three groups of solutions can be distinguished. The first is based on primary high-temperature cells. However, it is characterised by a relatively high cell unit price and the need for regular battery replacement, which is unacceptable for maintenance-free IoMT devices. The second solution can be the use of secondary electrochemical energy storage - lithium-ion batteries, supercapacitors and hybrid capacitors. In this case, however, the need for regular recharging of the ESS must be taken into account. In addition, there are serious limitations to the use of ESS devices due to their thermal behaviour at elevated temperatures. These include accelerated ageing, increased internal resistance, increased degradation of the separator layer in secondary batteries and electrolyte degradation. In particular cases, this can lead to the exothermic chain reaction known as thermal runaway, which in the case of lithium-ion secondary cells can cause massive heat generation and explosion. Another factor that negatively affects the use of this solution is the very low availability of high temperature ESS solutions, which comes at a high price. There are individual technologies on the market that are designed for elevated temperatures, but the cost of such devices is significantly high, the certification process can be challenging, and the design process is highly dependent on the particular manufacturer, which can lead to supply chain issues.

2. **RQ2** Is it possible to design a maintenance-free power solution for sterilizable medical tools using energy harvesting solutions, what are the constraints of the design?
   RA2: The use of energy harvesting and the recovery of electricity from the heat of the steam sterilisation process seems particularly desirable for low-power electronic devices. The energy harvesting system can thus directly power the device during sterilisation or charge a high temperature ESS. The disadvantage is certainly the relatively high initial cost of such solutions, but in the long run this solution

can be economical due to its simplicity, reliability and maintenance-free operation. However, there are limitations to the design of such a solution. Firstly, it is necessary to create a thermal gradient across the TEG using a thermally insulated heat storage device. The dimensions and thermal capacity of this device must be matched to the desired working environment. Secondly, the selection of the TEG itself can be challenging as it needs to combine high energy efficiency with appropriate thermal conductivity and low hysteresis.

3. **RQ3** What is the energy balance of the proposed design, what are the main constraints and possibilities for size optimization?
   RA3: The proposed design is composed of the TMG-128-1.6-0.4 thermoelectric generator, which is capable of producing up to 11 mW of power on average in the design with 20 mm high HSU and 20 mm insulation. The power consumption of the RF430FRL152H chip varies from 0.353 mW to 1.674 mW including safety margins and taking into account the low power efficiency of the boost converter circuit. As can be seen, the power produced by the energy harvesting module exceeds the chip's requirements by many times. However, it is worth considering the use of other technologies such as Bluetooth low energy, which has much higher power requirements. However, there are some limitations in the design. The main constraint is the steam sterilisation process itself and the temperature variability inside the autoclave. The whole design has to be adapted to the need to create a thermal gradient across the TEG. Using the TMG-128-1.6-0.4 TEG and the RF430 chip, it was possible to limit the size of the HSU to 7.5 mm in height and the thickness of the aerogel insulation to 5 mm and to provide sufficient power to the chip for over 95 % of the steam sterilisation plateau phase time.

4. **RQ4** What are the limitations in terms of sensor design related to power consumption?
   RA4: In the case of sensor design constraints, the lowest possible power consumption and a flexible supply voltage range are of primary importance. In the case of the steam sterilisation process, the sensor should be able to operate continuously without the use of additional energy storage. This means that its power requirement should not exceed 0.353 mW. These types of sensors are systems with passive data transmission via the NFC protocol, where the energy required to read the information is taken from the reader. In the case of sensors with active data transmission - for example, devices based on the Bluetooth Low Energy protocol - despite the very low energy consumption for the transmission of data packets, a relatively rapid consumption of the energy generated during sterilisation should be expected.

Besides the research questions listed above, this PhD thesis had to deal with the requirements from industrial partner Aesculap AG. The main constraints from an industrial background were:

1. **IC1** Applicability in mass production,
2. **IC2** Robustness of the design,
3. **IC3** Maintenance-free nature of the target solution,
4. **IC4** Compatibility with the concept of the Medical Internet of Things system.

All the industrial requirements have been met.

13.2. Thesis Summary

This thesis attempts to analyse the problem of powering medical electronic sensor devices during steam sterilisation and to propose an alternative solution. This sterilisation is a particularly difficult environment

for all types of electronics, especially for portable power supplies. This thesis analyses the life cycle of surgical devices in the hospital and their logistics. The available types of sterilisation to which electronic sensors embedded in medical devices may be subjected are briefly described and characterised. Steam sterilisation – one of the methods analysed – is the cheapest and most commonly used method in medical institutions. At the same time, the problem of powering electronic devices that could monitor the life cycle of such surgical instruments remains unsolved. The study analysed solutions available on the market in the field of electrochemical energy storage methods. These include primary cells, secondary cells, electrochemical capacitors and lithium-ion capacitors. The analysis showed that there is currently only one battery model on the market that can store energy during the sterilisation process. Furthermore, the identified technological problems of lithium-ion batteries are related to the ageing mechanisms of these batteries and are caused by the material parameters of the substances and components used in the cell construction. It is therefore concluded that it is unlikely that batteries that can withstand such thermal conditions and are economically justified will be commercially available in the near future. Another issue is safety and the so-called "thermal runaway" – a mechanism of thermal chain reaction usually caused by the destruction of the separator structure, which leads to a rapid increase in temperature and pressure inside the cell, resulting in an explosion with the emission of flammable gases. These two factors led to the decision to look for alternative electrochemical methods of storing electricity. The second area of attention was electrolytic capacitors and lithium-ion hybrid capacitors. This solution, despite technologies that allowed operation at high temperatures, had disadvantages in the form of the need for frequent recharging of the capacitors and their relatively low capacity. Due to business requirements – i.e. low overheads associated with the operation of the device – it was decided not to continue development in this direction. However, based on technological and scientific analysis, a method for using hybrid lithium-ion capacitors to power surgical electromechanical devices was developed and national patent application **DE102020109931A1** has been filled. After analysing the available electrochemical energy storage technologies, attention was focused on energy harvesting technologies. Energy harvesting methods available on the market and in the literature were analysed and the possibilities of their use in the context of the surgical instrument logistics process were examined. As a result of the analysis, thermal energy harvesting was selected as the technology of choice. A preliminary concept of using this technology to power a sensor was also developed. In this concept, the sensor monitoring the steam sterilisation process is activated by the process itself and the heat contained in the autoclave. This was achieved by using a Peltier thermogenerator connected to an aluminium enclosure and an insulated Heat Storage Unit, which is subjected to a temperature gradient during the sterilisation process. This prototype design ensures that heat flows from the outside of the prototype to the inside during the autoclave sterilisation process. The HSU is surrounded by aerogel insulation, as mentioned above. As a result, the heat flow is mainly through a thermogenerator where a temperature gradient is created to generate electricity to power the sensors. Once the first version of the prototype had been developed, initial requirements were defined for the prototype to be useful from a business perspective. These requirements ranged from the size of the prototype, its design and the materials from which it was made, to the definition of the minimum power it had to generate. To this end, electronic circuits that could be used as intelligent temperature sensors in steam sterilisation environments were examined. Particular attention was paid to low power consumption, data security (passive data storage) and a communication interface that allows data to be read without contact. The Texas Instruments RF430FRL152H chip was selected. Its power consumption was then measured in various operating modes and using a sample measurement program. This data was used to determine the minimum level of power generated, which was 1.674 mW for active mode and 0.353 mW for passive mode.

Having defined the minimum requirements for the device, a methodology for further work was proposed. This methodology included the following steps:

1. Construction of the physical model of the device,
2. Construction of a virtual model and identification of its parameters using a given thermal step response validation method,
3. Constructing a model of the thermogenerator and identifying its parameters, determining the minimum temperature gradient required to generate the assumed power to supply the sensors,
4. Simulation of the steam sterilisation process on the basis of virtual models of the prototype device and the thermo-generator, in order to determine the power generated by the thermo-generator during this process,
5. Optimisation of the size and design of the entire prototype in order to miniaturise it.

The physical model of the device was built using a Ferrotec Nord TMG-127-0.4-1.6 thermogenerator, with a 25 mm x 25 mm x 15 mm stainless steel block as the heat storage unit. Aerogel foam with a thermal conductivity coefficient of $0.027\,\mathrm{W}\cdot\mathrm{m}^{-1}\cdot\mathrm{K}^{-1}$ were used as the insulation material and Hammond Manufacturing enclosures were used as the enclosure. The model was then parameterised using the thermal step response method. The data collected from this step have been identified, the time constants have been calculated and was used to create the virtual model. The virtual model was developed in CAD software and the simulations themselves were carried out in the SimScale environment and are described in detail in Chapter 10. The virtual model of the prototype thus created was used to determine the heat flow within the prototype during the simulated steam sterilisation process. The next step was to create a virtual model of the thermogenerator. For this purpose, the available modelling techniques were reviewed. Among the models available in the literature, the Kubov SPICE model was chosen. This model have been found as relative simple in implementation and sufficient in accuracy in terms of the temperature gradients expected during the steam sterilisation procedure. Once the thermogenerator model had been constructed using the parameters taken from its data sheet, the real thermogenerator TMG-127-0.4-1.6 have been validated under a load of 32 Ω and the results compared with the simulation results. The simulation and real data fit has been not satisfactory, so the real parameters of the TEG as internal resistance and Seebeck coefficient have been measured. Simulation was then adjusted with the measured parameters, and it fit with real data with the acceptable inaccuracy. Finally, the thermal simulation of the steam sterilisation process was carried out. The simulation results showed that the prototype built was able to generate the minimum gradient required to power the sensors throughout the sterilisation process. In addition, the power generated exceeded the minimum safe requirement. Therefore, it was decided to perform virtual size optimisation procedure to miniaturise the prototype. Ultimately, assuming the low power mode of the RF430FRL152H chip, it was possible to reduce the size of the prototype insulation and the height of the HSU itself to 7.5 mm in height and 5 mm in insulation thickness with no additional energy storage systems to buffer the energy generated. Assuming that the chip is working in it's active mode, consuming 1.674 mW of power, the minimal HSU height is 12.5 mm with insulation thickness of 5 mm. Assuming using the efficient energy storage system even the HSU of size 2.5 mm and insulation of 5 mm provides enough energy to power the sensor node for the whole steam sterilisation procedure in the active mode of the RF430FRL152H chip. These results suggest that it is possible to develop a fully autonomous and unmanned sensor system for measuring steam sterilisation parameters. This could have a very positive impact on the development of the Medical Internet of Things for surgical instruments. The results of this thesis have been used to complete the international patent applications: **WO2021148450A1**, **DE102020101654A1**, **CN115003338A**, **EP4093444A1**, **US20220354617A1**, **DE102020109931A1**, **DE102020129082A1**.

13.2.1. Original Input

The following objectives were achieved within the scope of the work which are original achievements of the author:

1. The feasibility of powering medical internet of things sensors in a steam sterilisation environment was analysed,
2. Defined the requirements for sensors operating in a steam sterilisation environment and performed a market review of available solutions, then selected the optimal sensor model and optimised its power consumption for energy harvesting from the temperature prevailing in the autoclave during sterilisation,
3. The concept of an energy harvesting module using aerogel insulation to power the sensor was developed and then its physical model was constructed,
4. The physical model of the energy harvesting module was parameterised and its digital twin was built for simulation purposes,
5. A simulation methodology was proposed using FEM and the SPICE environment,
6. The selected thermo-generator module was parameterised and simulated in a steam sterilisation environment,
7. Potential scenarios for powering the IoMT sensor in a steam sterilisation environment are defined,
8. Optimisation of the size of the energy harvesting module in terms of size, while maintaining the minimum required power generation was carried out,
9. Filing of a number of patent applications related to the subject matter addressed, in particular application WO2021148450A1 relating directly to the thesis matter addressed.

13.2.2. Further Research

This PhD only outlines the topic of powering smart sensors in a steam sterilisation environment. The results of the research carried out allow the identification of topics for future research. One of the first topics that should, in the author's opinion, be addressed is to carry out measurements using a physically built optimised module. These tests should give an answer to how the power generated by the thermogenerator in the physical model during steam sterilisation compares to the simulation results. The next step will certainly be to carry out a series of fatigue tests that will give an answer to the question of what the estimated lifespan of the device might be under real operating conditions. Finally, a major research area is the optimisation of the conversion and utilisation of the generated electrical power. This research should include an analysis of the use of different DC-DC converter architectures, energy management and storage methods. On the functional side, future research should include further optimisation of the sensor module in terms of reliability and minimisation of energy consumption.

13.3. Published Patent Applications

1. Patent Family: WO2021148450A1, DE102020101654A1, CN115003338A, EP4093444A1, US20220354617A1 – "Sterile Container with an NFC Module", Lukas Böhler, Matthias Henke, Mateusz Daniol,
2. Patent Family: WO2021148425A1, EP4093445A1, US20230033001A1, CN113613686A, DE102020101655A1 – "Method for Automatic and Sterile-container-specific Detection of Sterilisation Cycles Carried out by a Sterile Container", Lukas Böhler, Matthias Henke, Mateusz Daniol,
3. Patent Family: WO2021148642A1, EP4094212A1, US20230046713A1, CN115176259A, DE102020101651A1 – " Storage System and Method for Storing Medical Products", Mateusz Daniol, Matthias Henke, Lukas Böhler,
4. Patent Family: WO2021148425A1, EP4093445A1, US20230033001A1, CN113613686A, DE102020101655A1 – "Process for the Automatic and Sterile Container-specific Recording of Sterilization Cycles Carried out by Means of a Sterile Container", Lukas Böhler, Matthias Henke, Mateusz Daniol,
5. Patent Family: WO2022063718A1, EP4076264A1, DE102020125114A1 – "Modular Detection System for Sterile Circuit Monitoring and Method for Monitoring a Sterile Material Circuit"
6. Patent Family: WO2020221710A1, EP3962386A1, US20220047336A1, JP2022530399A, DE102019111177A1 – "Medical Bending System", Frederick Lenzenhuber, Lukas Böhler, Mateusz Daniol, Roland-Alois Högerle, Stephanie Auber, Ralf Pfister
7. Patent: DE102020109931A1 – "Wireless Medical Device", Mateusz Daniol, Lukas Böhler,
8. Patent: DE102020129082A1 – "Sterile Container with Transmitter Module and Sterile Container Monitoring System", Mateusz Daniol, Lukas Böhler.

13.4. Published Articles Related to the Thesis

1. M. Daniol, L. Boehler, R. Sroka, and A. Keller, “Modeling and Implementation of TEG-Based Energy Harvesting System for Steam Sterilization Surveillance Sensor Node,” Sensors, vol. 20, no. 21, p. 6338, Nov. 2020, doi: 10.3390/s20216338.
2. L. Boehler, M. Daniol, R. Sroka, D. Osinski, and A. Keller, “Sensors in the Autoclave-Modelling and Implementation of the IoT Steam Sterilization Procedure Counter,” Sensors, vol. 21, no. 2, p. 510, Jan. 2021, doi: 10.3390/s21020510.

Appendix A: Block Diagram of the TEG validation software

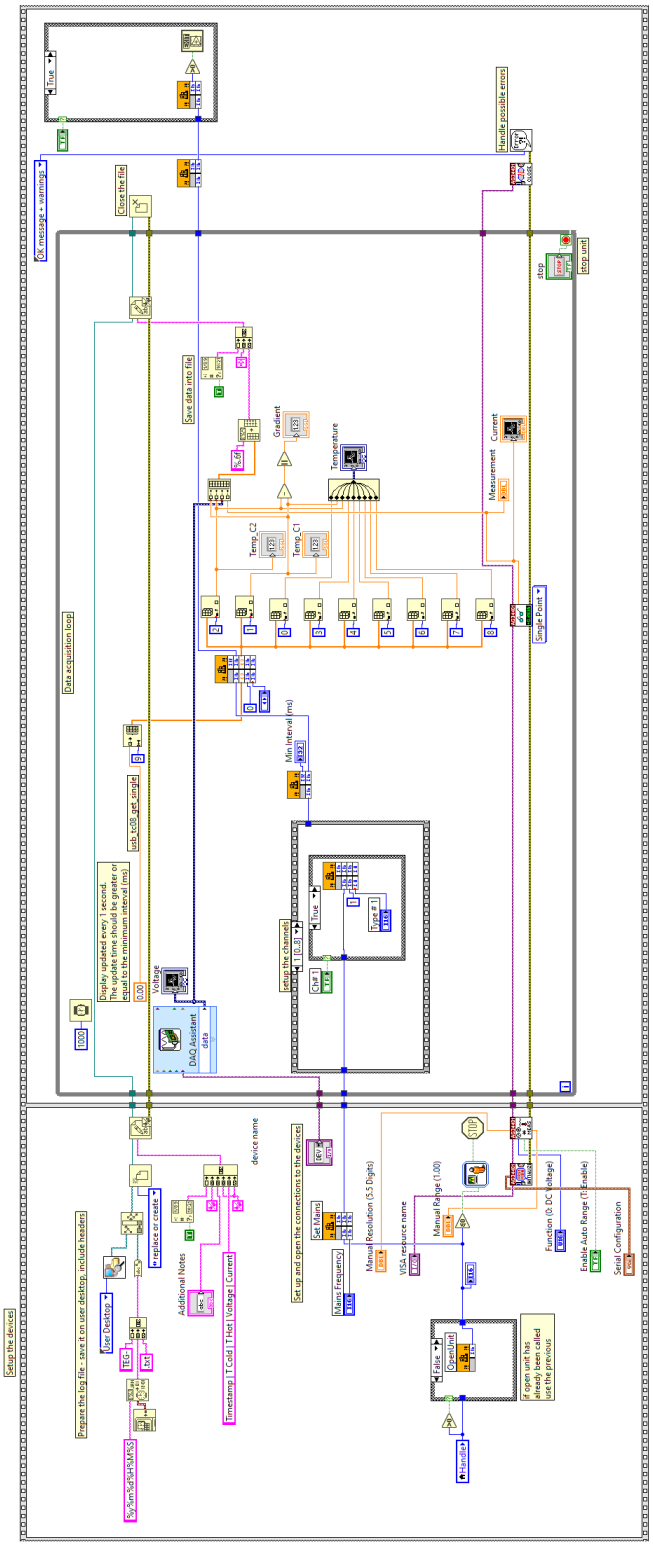

Figure 13.1. Schematics of Labview Program used for Logging the data

Appendix B: Theta Parameter

To understand the meaning of the θ parameter a short introduction into Crank-Nicolson Scheme needs to be made. This scheme is widely used in the heat conduction problems. Heat conduction can be described by heat conduction equation:

$$k\frac{\partial^2 T}{\partial x} = \frac{\partial T}{\partial t} \tag{13.1}$$

The Crank-Nicolson scheme (or method) is an semi-implicit scheme that is second order accurate in both time and space [166]. In Crank-Nicolson method difference approximations are obtained at the middle of time incrementation step by approximation of temporal first derivative at $t^{l+1/2}$ by:

$$\frac{\partial T}{\partial t} \cong \frac{T_i^{l+1} - T_i^l}{\Delta t} \tag{13.2}$$

The second derivative in both time and space can be described as follows:

$$\frac{\partial^2 T}{\partial^2 t} \cong \frac{1}{2}\left[\frac{T_{i+1}^{l+1} - 2T_i^{l+1} + T_{i-1}^{l+1}}{\Delta x^2} + \frac{T_{i+1}^{l} - 2T_i^{l} + T_{i-1}^{l}}{\Delta x^2}\right] \tag{13.3}$$

The difference equation can be stated now as follows:

$$T_{i-1}^{l+1} - 2(1 + \frac{1}{\lambda})T_i^{l+1} + T_{i+1}^{l+1} = -T_{i-1}^{l} + 2(1 - \frac{1}{\lambda})T^l i - T^l i + 1 \tag{13.4}$$

where $\lambda = k\frac{\Delta t}{(\Delta x)^2}$

The Crank-Nicolson method, as well as forward and backward Euler's method can be re-written in more general form, by introducing parameter θ, introducing so called unifying θ-Rule (giving us Theta-scheme) [167]:

$$T_i^{l+1} = T_i^l + \lambda\left[\theta(T_{i+1}^{l+1} - 2T_i^{l+1} + T_{i-1}^{l+1}) + (1-\theta)(T_{i+1}^{l} - 2T_i^{l} + T_{i-1}^{l})\right] \tag{13.5}$$

Finally, the θ parameter can vary from 0 to 1 changing the character of the Theta-scheme. $\theta = 0$ gives the forward Euler's scheme in time; $\theta = 1$ gives the backward Euler's scheme in time; $\theta = 0.5$ gives the Crank-Nicolson scheme in time.

Appendix C: SPICE listing of the Kubov's TEG model

```
* block symbol definitions
.subckt peltier p n Tc Th
* -------- Electrical Domain ----------
B01 n0 p V=Pe(V(Tc)+T0)
B02 p0 n V=Pe(V(Th)+T0)
Re n0 p0 {R_TEG}
* --------- Thermal Domain --------------
B1 0 Tc I=V(p,n0)*I(B02)
B2 0 Th I=V(p0,n)*I(B02)
B12 0 N001 I=V(n0,p0)*I(B02)
Rq1 N001 Tc {Rq/2}
Rq2 Th N001 {Rq/2}
Cq1 Tc 0 {Cq/2}
Cq2 Th 0 {Cq/2}
* --- params and functions --
.param Se=53m R_TEG=41
```

```
.param Cq=15 Rq=3
.func Pe(T) {Se*T}
.param T0=273
.ends peltier

.dc V1 -12 16 0.1
.backanno
.end
```

Listing 13.1. Spice netlist for Kubov's TEG model

Appendix D: SPICE listing of simulation setup

```
Vth Thot 0 PWL file= <filepath_hot_side>
Vtc Tcold 0 PWL file= <filepath_cold_side>
XPeltier Tcold Thot 0 TEG_OUT peltier_module params: Se=53m R_TEG=41 Cq=1.74 Rq=1408

* block symbol definitions
.subckt peltier_module Tc Th n p
Re p0 n0 {R_TEG}
Cq1 Tc 0 {Cq/2}
Cq2 Th 0 {Cq/2}
Rq1 N001 Tc {Rq/2}
Rq2 Th N001 {Rq/2}
B1 0 Tc I=V(p,n0)*I(B02)
B12 0 N001 I=V(n0,p0)*I(B02)
B2 0 Th I=V(p0,n)*I(B02)
B01 n0 p V=Pe(V(Tc)+T0)
B02 p0 n V=Pe(V(Th)+T0)
.param Se=53m R_TEG=41
.func Pe(T){Se*T}
.param T0=273
.param Cq=15 Rq=3
.ends peltier_module

.backanno
.end
```

Listing 13.2. LTSpice netlist used for power generation simulation. Filepaths to the CSV data with temperature of the TEG hot and cold side are denoted in angle brackets **<>**

Appendix E: Preparation of the RF430FRL152HEVM board to mimic the real sensor node behaviour

Measuring the power consumed by a benchmark program involves proper hardware preparation and compensation for parasitic power consumption by components of the measurement board not directly related to the chip. This is related to the design of the board power supply circuit itself. As shown in the Figure 13.2 the part related to the power supply can be divided into specialized areas numbered from 1 to 4. The first possibility to power the board is using the energy harvesting technique from the radio field emitted by the reader (numbered 1 in the figure). The next two methods are related to powering the board via USB and

from MSP-FET programmer (circuits 2 and 3 respectively in the figure 13.2. Circuit 3 is used to measure current and voltage using EnergyTrace technology. Note that it powers, among other things, the TPS72215 voltage regulator and the VDDSW line through jumper SV7. This line also powers the voltage translators (from the 3V logic used by the MSP-FET to the 1.5V logic on which the RF430FRL152H runs). This causes redundant power consumption, unrelated to the operation of the chip itself and the program running on it. We can define this as a so-called hardware bias in power consumption. The last way to power the chip on the board is directly from the battery. This is marked in blue in the figure 13.2. By default, the chip is powered from the VDDB input, which is connected to the VDDSW bus via jumper SV7. To measure the power consumed directly by the RF430FRL152H chip, connect the power supply to jumper JP3. A digital multimeter Agilent 34410A with logging function was inserted between the laboratory power supply and jumper JP3. Measurements were made using 500 sample current measurement. The measuring range of the multimeter has been set to 20 µA assuring that the most of it's range will be in use.

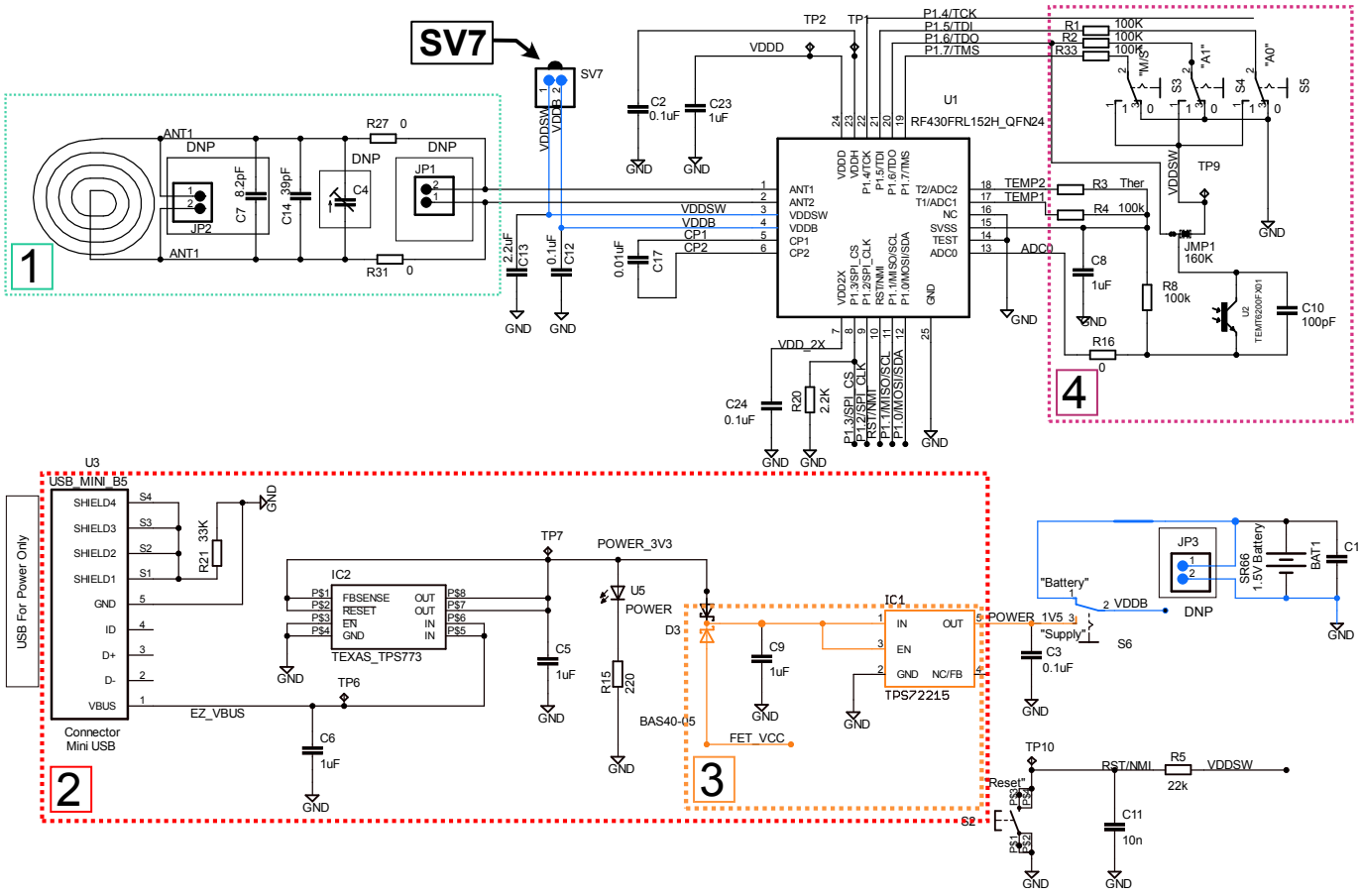

Figure 13.2. Schematic of power-related sections of RF430FRL152HEVM board.

.

Bibliography

[1] J. Al-Jaroodi, N. Mohamed, and E. Abukhousa, "Health 4.0: On the way to realizing the healthcare of the future", *IEEE Access*, vol. 8, pp. 211 189–211 210, 2020. DOI: 10.1109/ACCESS.2020.3038858.

[2] H. Feussner, D. Ostler, M. Kranzfelder, *et al.*, "Surgery 4.0", in *Health 4.0: How Virtualization and Big Data are Revolutionizing Healthcare*, C. Thuemmler and C. Bai, Eds. Cham: Springer International Publishing, 2017, pp. 91–107, ISBN: 978-3-319-47617-9. DOI: 10.1007/978-3-319-47617-9_5. [Online]. Available: https://doi.org/10.1007/978-3-319-47617-9_5.

[3] R. Kanan and O. Elhassan, "Batteryless radio system for hospital application", in *Proceedings of 2016 SAI Computing Conference, SAI 2016*, 2016, pp. 939–945, ISBN: 9781467384605. DOI: 10.1109/SAI.2016.7556093.

[4] A. Huang, G. Joerger, V. Fikfak, *et al.*, "The SmartOR: a distributed sensor network to improve operating room efficiency", *Surgical Endoscopy and Other Interventional Techniques*, 2017. DOI: 10.1007/s00464-016-5390-z.

[5] M. Mahfouz, G. To, and M. Kuhn, "Smart instruments: Wireless technology invades the operating room", in *RWW 2012 - Proceedings: 2012 IEEE Topical Conference on Biomedical Wireless Technologies, Networks, and Sensing Systems, BioWireleSS 2012*, 2012, ISBN: 9781457711541. DOI: 10.1109/BioWireless.2012.6172743.

[6] H. Zhang, J. Li, B. Wen, Y. Xun, and J. Liu, "Connecting Intelligent Things in Smart Hospitals using NB-IoT", *IEEE Internet of Things Journal*, vol. 4662, no. c, pp. 1–11, 2018, ISSN: 23274662. DOI: 10.1109/JIOT.2018.2792423.

[7] J. G. Solon and S. Killeen, "Decontamination and sterilization", *Surgery (United Kingdom)*, vol. 33, no. 11, pp. 572–578, 2015, ISSN: 18781764. DOI: 10.1016/j.mpsur.2015.08.006.

[8] R. Seavey, "High-level disinfection, sterilization, and antisepsis: Current issues in reprocessing medical and surgical instruments", *American Journal of Infection Control*, vol. 41, no. 5 SUPPL. Pp. 111–117, 2013, ISSN: 01966553. DOI: 10.1016/j.ajic.2012.09.030. [Online]. Available: http://dx.doi.org/10.1016/j.ajic.2012.09.030.

[9] *Aesculap aicon®*, 2021. [Online]. Available: https://ifdesign.com/en/winner-ranking/project/aesculap-aicon/312633.

[10] E. Ahmadi, D. T. Masel, A. Y. Metcalf, and K. Schuller, "Inventory management of surgical supplies and sterile instruments in hospitals: a literature review", *Health Systems*, vol. 8, no. 2, pp. 134–151, 2019, ISSN: 2047-6965. DOI: 10.1080/20476965.2018.1496875. [Online]. Available: https://doi.org/10.1080/20476965.2018.1496875.

[11] J. G. Solon and S. Killeen, "Decontamination and sterilization", *Surgery (United Kingdom)*, vol. 33, no. 11, pp. 572–578, 2015, ISSN: 18781764. DOI: 10.1016/j.mpsur.2015.08.006.

[12] J. V. Brooks, J. A. Williams, and K. Gorbenko, "The work of sterile processing departments: An exploratory study using qualitative interviews and a quantitative process database", *American Journal of Infection Control*, vol. 47, no. 7, pp. 816–821, 2019, ISSN: 15273296. DOI: 10.1016/j.ajic.2018.12.010.

[13] Centers for Disease Control and Prevention, "Guideline for Disinfection and Sterilization in Healthcare Facilities, 2008", *CDC website*, no. May, pp. 9–13, 2013. DOI: 1. arXiv: 1. [Online]. Available: http://www.cdc.gov/hicpac/Disinfection%7B%5C_%7DSterilization/10%7B%5C_%7D0MiscAgents.html.

[14] M. T. Mubarak, I. Ozsahin, and D. U. Ozsahin, "Evaluation of Sterilization Methods for Medical Devices", *2019 Advances in Science and Engineering Technology International Conferences, ASET 2019*, pp. 1–4, 2019. DOI: 10.1109/ICASET.2019.8714223.

[15] W. A. Rutala and D. J. Weber, "Disinfection, sterilization, and antisepsis: An overview", *American Journal of Infection Control*, vol. 47, A3–A9, 2019, ISSN: 15273296. DOI: 10.1016/j.ajic.2019.01.018. [Online]. Available: https://doi.org/10.1016/j.ajic.2019.01.018.

[16] Gamma Irradiation Processing Alliance and International Irradiation Assoc., "A Comparison of Gamma, E-beam, X-ray and Ethylene Oxide Technologies for the Industrial Sterilization of Medical Devices and Healthcare Products", pp. 1–49, 2017. [Online]. Available: www.gipalliance.net.

[17] E. M. Darmady, K. E. Hughes, J. D. Jones, D. Prince, and W. Tuke, "Sterilization by dry heat.", *Journal of clinical pathology*, vol. 14, pp. 38–44, 1961, ISSN: 00219746. DOI: 10.1136/jcp.14.1.38.

[18] W. J. Rogers, *The effects of sterilization on medical materials and welded devices*. Woodhead Publishing Limited, 2013, pp. 79–130, ISBN: 9781845695774. DOI: 10.1533/9780857096425.1.79. [Online]. Available: http://dx.doi.org/10.1533/9780857096425.1.79.

[19] H. Isomoto, M. Urata, K. Kawazoe, *et al.*, "Endoscope disinfection using chlorine dioxide in an automated washer-disinfector", en, *J. Hosp. Infect.*, vol. 63, no. 3, pp. 298–305, Jul. 2006.

[20] S. Lerouge, "5 - non-traditional sterilization techniques for biomaterials and medical devices", in *Sterilisation of Biomaterials and Medical Devices*, ser. Woodhead Publishing Series in Biomaterials, S. Lerouge and A. Simmons, Eds., Woodhead Publishing, 2012, pp. 97–116, ISBN: 978-1-84569-932-1. DOI: https://doi.org/10.1533/9780857096265.97. [Online]. Available: https://www.sciencedirect.com/science/article/pii/B9781845699321500052.

[21] W. A. Rutala and D. J. Weber, "301 - disinfection, sterilization, and control of hospital waste", in *Mandell, Douglas, and Bennett's Principles and Practice of Infectious Diseases (Eighth Edition)*, J. E. Bennett, R. Dolin, and M. J. Blaser, Eds., Eighth Edition, Philadelphia: W.B. Saunders, 2015, pp. 3294–3309, ISBN: 978-1-4557-4801-3. DOI: https://doi.org/10.1016/B978-1-4557-4801-3.00301-5. [Online]. Available: https://www.sciencedirect.com/science/article/pii/B9781455748013003015.

[22] H. Shintani, A. Sakudo, P. Burke, and G. McDonnell, "Gas plasma sterilization of microorganisms and mechanisms of action", *Experimental and Therapeutic Medicine*, vol. 1, no. 5, pp. 731–738, 2010, ISSN: 17920981. DOI: 10.3892/etm.2010.136.

[23] *Sterilization methods and their impact on medical devices containing electronics*, AN5068, Maxim Integrated Inc., 2014. [Online]. Available: https://pdfserv.maximintegrated.com/en/an/AN5068.pdf.

[24] A. Simmons, "11 - future trends for the sterilisation of biomaterials and medical devices", in *Sterilisation of Biomaterials and Medical Devices*, ser. Woodhead Publishing Series in Biomaterials, S. Lerouge and A. Simmons, Eds., Woodhead Publishing, 2012, pp. 310–320, ISBN: 978-1-84569-932-1. DOI: https://doi.org/10.1533/9780857096265.310. [Online]. Available: https://www.sciencedirect.com/science/article/pii/B9781845699321500118.

[25] H. Nguyen, D. A. F. Morgan, and M. R. Forwood, "Sterilization of allograft bone: Is 25 kgy the gold standard for gamma irradiation?", en, *Cell Tissue Bank.*, vol. 8, no. 2, pp. 81–91, 2007.

[26] M. Silindir and A. Y. Özer, "Sterilization methods and the comparison of e-beam sterilization with gamma radiation sterilization", *Fabad Journal of Pharmaceutical Sciences*, vol. 34, no. 1, p. 43, 2009.

[27] A. Abdel-Fattah, A. Berejka, A. Chmielewski, *et al.*, *Trends in Radiation Sterilization of Health Care Products*. Vienna: International Atomic Energy Agency, Jul. 2008, ISBN: 978-92-0-111007-7.

[28] F. R. McLarnon and E. J. Cairns, "Energy storage", *Annual review of energy*, vol. 14, no. 1, pp. 241–271, 1989.

[29] I. Buchmann and C. E. Inc, *Batteries in a Portable World: A Handbook on Rechargeable Batteries for Non-engineers*. Cadex Electronics, 2001, ISBN: 9780968211823. [Online]. Available: https://books.google.de/books?id=YIBhAAAACAAJ.

[30] A. Jagadale, X. Zhou, R. Xiong, D. P. Dubal, J. Xu, and S. Yang, "Lithium ion capacitors (LICs): Development of the materials", *Energy Storage Materials*, vol. 19, no. December 2018, pp. 314–329, 2019, ISSN: 24058297. DOI: 10.1016/j.ensm.2019.02.031. [Online]. Available: https://doi.org/10.1016/j.ensm.2019.02.031.

[31] Y. Kato, S. Hori, T. Saito, *et al.*, "High-power all-solid-state batteries using sulfide superionic conductors", *Nature Energy*, vol. 1, no. 4, pp. 1–7, 2016, ISSN: 20587546. DOI: 10.1038/nenergy.2016.30.

[32] S. Koohi-Fayegh and M. A. Rosen, "A review of energy storage types, applications and recent developments", *Journal of Energy Storage*, vol. 27, no. July, 2020, ISSN: 2352152X. DOI: 10.1016/j.est.2019.101047.

[33] X. Lin, M. Salari, L. M. R. Arava, P. M. Ajayan, and M. W. Grinstaff, "High temperature electrical energy storage: advances, challenges, and frontiers", *Chem. Soc. Rev.*, vol. 45, no. 21, pp. 5848–5887, 2016, ISSN: 0306-0012. DOI: 10.1039/C6CS00012F. [Online]. Available: http://xlink.rsc.org/?DOI=C6CS00012F.

[34] G. Zubi, R. Dufo-López, M. Carvalho, and G. Pasaoglu, "The lithium-ion battery: State of the art and future perspectives", *Renewable and Sustainable Energy Reviews*, vol. 89, no. April 2017, pp. 292–308, 2018, ISSN: 18790690. DOI: 10.1016/j.rser.2018.03.002.

[35] Q. Wang, P. Ping, X. Zhao, G. Chu, J. Sun, and C. Chen, "Thermal runaway caused fire and explosion of lithium ion battery", *Journal of Power Sources*, vol. 208, 2012. DOI: 10.1016/j.jpowsour.2012.02.038.

[36] J. T. Warner, "Chapter 3 - Lithium-ion battery operation", in J. T. B. T. .-. L.-I. B. C. Warner, Ed., Elsevier, 2019, pp. 43–77, ISBN: 978-0-12-814778-8. DOI: https://doi.org/10.1016/B978-0-12-814778-8.00003-X. [Online]. Available: http://www.sciencedirect.com/science/article/pii/B978012814778800003X.

[37] K. W. Beard, *Linden's Handbook of Batteries*. McGraw-Hill Education, 2019.

[38] P. H. Smith, T. N. Tran, T. L. Jiang, and J. Chung, "Lithium-ion capacitors: Electrochemical performance and thermal behavior", *Journal of Power Sources*, vol. 243, pp. 982–992, 2013, ISSN: 03787753. DOI: 10.1016/j.jpowsour.2013.06.012. [Online]. Available: http://dx.doi.org/10.1016/j.jpowsour.2013.06.012.

[39] T. M. Bandhauer, S. Garimella, and T. F. Fuller, "A Critical Review of Thermal Issues in Lithium-Ion Batteries", *Journal of The Electrochemical Society*, vol. 158, no. 3, R1, 2011, ISSN: 00134651. DOI: 10.1149/1.3515880. [Online]. Available: http://jes.ecsdl.org/cgi/doi/10.1149/1.3515880.

[40] S. Ma, M. Jiang, P. Tao, *et al.*, "Temperature effect and thermal impact in lithium-ion batteries: A review", in *Progress in Natural Science: Materials International*, 6, vol. 28, 2018, pp. 653–666. DOI: 10.1016/j.pnsc.2018.11.002.

[41] J. Vetter, P. Novák, M. R. Wagner, *et al.*, "Ageing mechanisms in lithium-ion batteries", *Journal of Power Sources*, vol. 147, no. 1-2, pp. 269–281, 2005, ISSN: 03787753. DOI: 10.1016/j.jpowsour.2005.01.006.

[42] Q. Wang, P. Ping, X. Zhao, G. Chu, J. Sun, and C. Chen, "Thermal runaway caused fire and explosion of lithium ion battery", *Journal of Power Sources*, vol. 208, pp. 210–224, Jun. 2012, ISSN: 03787753. DOI: 10.1016/j.jpowsour.2012.02.038. [Online]. Available: https://linkinghub.elsevier.com/retrieve/pii/S0378775312003989 (visited on 07/21/2020).

[43] S. Hess, M. Wohlfahrt-Mehrens, and M. Wachtler, "Flammability of li-ion battery electrolytes: Flash point and self-extinguishing time measurements", *Journal of The Electrochemical Society*, vol. 162, no. 2, A3084, Jan. 7, 2015, Publisher: IOP Publishing, ISSN: 1945-7111. DOI: 10.1149/2.0121502jes. [Online]. Available: https://iopscience.iop.org/article/10.1149/2.0121502jes/meta (visited on 05/17/2021).

[44] Q. Wang, B. Mao, S. I. Stoliarov, and J. Sun, "A review of lithium ion battery failure mechanisms and fire prevention strategies", *Progress in Energy and Combustion Science*, vol. 73, pp. 95–131, Jul. 2019, ISSN: 03601285. DOI: 10.1016/j.pecs.2019.03.002. [Online]. Available: https://linkinghub.elsevier.com/retrieve/pii/S0360128518301801 (visited on 04/26/2021).

[45] F. Richter, P. J. Vie, S. Kjelstrup, and O. S. Burheim, "Measurements of ageing and thermal conductivity in a secondary NMC-hard carbon li-ion battery and the impact on internal temperature profiles", *Electrochimica Acta*, vol. 250, pp. 228–237, Oct. 2017, ISSN: 00134686. DOI: 10.1016/j.electacta.2017.07.173. [Online]. Available: https://linkinghub.elsevier.com/retrieve/pii/S0013468617316146 (visited on 12/09/2020).

[46] S. Liu, "Review on reliability of supercapacitors in energy storage applications", *Applied Energy*, p. 13, 2020.

[47] V. Kumaravel, J. Bartlett, and S. C. Pillai, "Solid electrolytes for high-temperature stable batteries and supercapacitors", *Advanced Energy Materials*, vol. 11, no. 3, p. 2 002 869, Jan. 2021, ISSN: 1614-6832, 1614-6840. DOI: 10.1002/aenm.202002869. [Online]. Available: https://onlinelibrary.wiley.com/doi/10.1002/aenm.202002869 (visited on 05/10/2021).

[48] S. Ma, M. Jiang, P. Tao, *et al.*, "Temperature effect and thermal impact in lithium-ion batteries: A review", *Progress in Natural Science: Materials International*, vol. 28, no. 6, pp. 653–666, Dec. 2018, ISSN: 10020071. DOI: 10.1016/j.pnsc.2018.11.002. [Online]. Available: https://linkinghub.elsevier.com/retrieve/pii/S1002007118307536 (visited on 07/21/2020).

[49] J. Vetter, P. Novák, M. Wagner, *et al.*, "Ageing mechanisms in lithium-ion batteries", *Journal of Power Sources*, vol. 147, no. 1, pp. 269–281, Sep. 2005, ISSN: 03787753. DOI: 10.1016/j.jpowsour.2005.01.006. [Online]. Available: https://linkinghub.elsevier.com/retrieve/pii/S0378775305000832 (visited on 07/21/2020).

[50] T. M. Bandhauer, S. Garimella, and T. F. Fuller, "A critical review of thermal issues in lithium-ion batteries", *Journal of The Electrochemical Society*, vol. 158, no. 3, R1, 2011, ISSN: 00134651. DOI: 10.1149/1.3515880. [Online]. Available: https://iopscience.iop.org/article/10.1149/1.3515880 (visited on 07/19/2020).

[51] R. S. Tichy, "Design of medical devices: Batteries designed to accommodate sterilization", English, *ECN Electronic Component News*, vol. 51, no. 6, pp. 28–30, 2007. [Online]. Available: www.scopus.com.

[52] I. Serdiuk, *Li-ion battery diagram*, Royalty Free License acquired, 2022. [Online]. Available: https://www.dreamstime.com/stock-illustration-li-ion-battery-diagram-vector-illustration-rechargeable-which-lithium-ions-move-negative-electrode-to-image97122319 (visited on 05/22/2023).

[53] V. S. Bagotskiĭ, A. M. Skundin, and Y. V. Volfkovich, *Electrochemical power sources: batteries, fuel cells, and supercapacitors*. Hoboken, New Jersey: Wiley, 2014, 1 p., ISBN: 978-1-118-94253-6 978-1-118-94251-2.

[54] C. Breitkopf and K. Swider-Lyons, Eds., *Springer Handbook of Electrochemical Energy*. Springer Berlin Heidelberg, 2017. DOI: 10.1007/978-3-662-46657-5. [Online]. Available: https://doi.org/10.1007%2F978-3-662-46657-5.

[55] W. H. Mark A. Schubert Matthew T. Wendling, "Lithium iron disulfide battery", European pat. 2766942A1, 2012.

[56] F. Leng, C. M. Tan, and M. Pecht, "Effect of temperature on the aging rate of li ion battery operating above room temperature", *Scientific Reports*, vol. 5, no. 1, p. 12967, Oct. 2015, ISSN: 2045-2322. DOI: 10.1038/srep12967. [Online]. Available: http://www.nature.com/articles/srep12967 (visited on 05/18/2021).

[57] F. Leng, C. M. Tan, and M. Pecht, "Effect of temperature on the aging rate of li ion battery operating above room temperature", *Scientific Reports*, vol. 5, no. 1, Aug. 2015. DOI: 10.1038/srep12967. [Online]. Available: https://doi.org/10.1038/srep12967.

[58] H. Liu, Z. Wei, W. He, and J. Zhao, "Thermal issues about li-ion batteries and recent progress in battery thermal management systems: A review", *Energy Conversion and Management*, vol. 150, pp. 304–330, Oct. 2017, ISSN: 01968904. DOI: 10.1016/j.enconman.2017.08.016. [Online]. Available: https://linkinghub.elsevier.com/retrieve/pii/S0196890417307288 (visited on 07/21/2020).

[59] N. E. Galushkin, N. N. Yazvinskaya, and D. N. Galushkin, "Mechanism of thermal runaway in lithium-ion cells", *Journal of The Electrochemical Society*, vol. 165, no. 7, A1303, May 2, 2018, Publisher: IOP Publishing, ISSN: 1945-7111. DOI: 10.1149/2.0611807jes. [Online]. Available: https://iopscience.iop.org/article/10.1149/2.0611807jes/meta (visited on 05/18/2021).

[60] A. W. Golubkov, D. Fuchs, J. Wagner, *et al.*, "Thermal-runaway experiments on consumer li-ion batteries with metal-oxide and olivin-type cathodes", *RSC Advances*, vol. 4, no. 7, pp. 3633–3642, Dec. 12, 2013, Publisher: The Royal Society of Chemistry, ISSN: 2046-2069. DOI: 10.1039/C3RA45748F. [Online]. Available: https://pubs.rsc.org/en/content/articlelanding/2014/ra/c3ra45748f (visited on 05/18/2021).

[61] C. Schlasza, P. Ostertag, D. Chrenko, R. Kriesten, and D. Bouquain, "Review on the aging mechanisms in li-ion batteries for electric vehicles based on the fmea method", *2014 IEEE Transportation Electrification Conference and Expo (ITEC)*, pp. 1–6, 2014.

[62] S. Karthikeyan, B. Narenthiran, A. Sivanantham, L. D. Bhatlu, and T. Maridurai, "Supercapacitor: Evolution and review", *Materials Today: Proceedings*, S2214785321016679, Mar. 2021, ISSN: 22147853. DOI: 10.1016/j.matpr.2021.02.526. [Online]. Available: https://linkinghub.elsevier.com/retrieve/pii/S2214785321016679 (visited on 04/26/2021).

[63] X. Hua, "Power management techniques for supercapacitor based IoT applications", Advisor: Ramesh Harjani, Ph.D. dissertation, University of Minnesota, Minnesota, Jan. 2018, 89 pp. [Online]. Available: https://hdl.handle.net/11299/195396 (visited on 05/20/2022).

[64] K. W. Beard, *Linden's handbook of batteries*. McGraw-Hill Education, 2019.

[65] S. Satpathy, S. Das, and B. K. Bhattacharyya, "How and where to use super-capacitors effectively, an integration of review of past and new characterization works on super-capacitors", *Journal of Energy Storage*, vol. 27, p. 101 044, Feb. 2020, ISSN: 2352152X. DOI: 10.1016/j.est.2019.101044. [Online]. Available: https://linkinghub.elsevier.com/retrieve/pii/S2352152X19309843 (visited on 07/21/2020).

[66] A. H. Mohd Aman, N. Shaari, and R. Ibrahim, "Internet of things energy system: Smart applications, technology advancement, and open issues", *International Journal of Energy Research*, vol. 45, no. 6, pp. 8389–8419, May 2021, ISSN: 0363-907X, 1099-114X. DOI: 10.1002/er.6451. [Online]. Available: https://onlinelibrary.wiley.com/doi/10.1002/er.6451 (visited on 05/28/2021).

[67] S. Priya and D. J. Inman, Eds., *Energy Harvesting Technologies*, Boston, MA: Springer US, 2009, ISBN: 978-0-387-76463-4 978-0-387-76464-1. DOI: 10.1007/978-0-387-76464-1. [Online]. Available: http://link.springer.com/10.1007/978-0-387-76464-1 (visited on 07/19/2020).

[68] Y. Wang, H. Wang, J. Xuan, and D. Y. C. Leung, "Powering future body sensor network systems: A review of power sources", *Biosensors and Bioelectronics*, vol. 166, p. 112 410, Oct. 15, 2020, ISSN: 0956-5663. DOI: 10.1016/j.bios.2020.112410. [Online]. Available: https://www.sciencedirect.com/science/article/pii/S0956566320304048 (visited on 05/28/2021).

[69] Pozo, Garate, Araujo, and Ferreiro, "Energy harvesting technologies and equivalent electronic structural models - review", *Electronics*, vol. 8, no. 5, p. 486, Apr. 30, 2019, ISSN: 2079-9292. DOI: 10.3390/electronics8050486. [Online]. Available: https://www.mdpi.com/2079-9292/8/5/486 (visited on 05/28/2021).

[70] F. K. Shaikh and S. Zeadally, "Energy harvesting in wireless sensor networks: A comprehensive review", *Renewable and Sustainable Energy Reviews*, vol. 55, pp. 1041–1054, Mar. 1, 2016, ISSN: 1364-0321. DOI: 10.1016/j.rser.2015.11.010. [Online]. Available: https://www.sciencedirect.com/science/article/pii/S1364032115012629 (visited on 05/28/2021).

[71] H. J. Goldsmid *et al.*, *Introduction to thermoelectricity*. Springer, 2010, vol. 121.

[72] H. Lee, *Thermoelectrics: design and materials*. John Wiley & Sons, 2016.

[73] T. L. Bergman, F. P. Incropera, D. P. DeWitt, and A. S. Lavine, *Fundamentals of heat and mass transfer*. John Wiley & Sons, 2011.

[74] S. Lineykin and S. Ben-Yaakov, "Modeling and analysis of thermoelectric modules", *IEEE Transactions on Industry Applications*, vol. 43, no. 2, pp. 505–512, 2007, ISSN: 0093-9994. DOI: 10.1109/TIA.2006.889813. [Online]. Available: http://ieeexplore.ieee.org/document/4132878/ (visited on 07/21/2020).

[75] E. Maciá, *Thermoelectric Materials: Advances and Applications*. New York: Jenny Stanford Publishing, 2015, 364 pp., ISBN: 978-0-429-17179-6. DOI: 10.1201/b18439.

[76] D. M. Rowe, Ed., *CRC handbook of thermoelectrics*. Boca Raton, FL: CRC Press, 1995, 701 pp., ISBN: 978-0-8493-0146-9.

[77] E. Bilotti, O. Fenwick, B. C. Schroeder, *et al.*, "6.14 organic thermoelectric composites materials", in *Comprehensive Composite Materials II*, P. W. Beaumont and C. H. Zweben, Eds., Oxford: Elsevier, 2018, pp. 408–430, ISBN: 978-0-08-100534-7. DOI: https://doi.org/10.1016/B978-0-12-803581-8.10024-4. [Online]. Available: https://www.sciencedirect.com/science/article/pii/B9780128035818100244.

[78] *Thomson effect*, Jul. 1998. [Online]. Available: https://www.britannica.com/science/Thomson-effect.

[79] H. Jouhara, A. Żabnieńska-Góra, N. Khordehgah, *et al.*, "Thermoelectric generator (TEG) technologies and applications", *International Journal of Thermofluids*, vol. 9, p. 100 063, Feb. 1, 2021, ISSN: 2666-2027. DOI: 10.1016/j.ijft.2021.100063. [Online]. Available: https://www.sciencedirect.com/science/article/pii/S266620272100001X (visited on 07/14/2021).

[80] M. T. Dunham, T. J. Hendricks, and K. E. Goodson, "Thermoelectric generators: A case study in multi-scale thermal engineering design", in *Advances in Heat Transfer*, vol. 51, Elsevier, 2019, pp. 299–350, ISBN: 978-0-12-817700-6. DOI: 10.1016/bs.aiht.2019.08.001. [Online]. Available: https://linkinghub.elsevier.com/retrieve/pii/S0065271719300048 (visited on 07/09/2021).

[81] H. Lee, "The thomson effect and the ideal equation on thermoelectric coolers", *Energy*, vol. 56, pp. 61–69, 2013, ISSN: 0360-5442. DOI: https://doi.org/10.1016/j.energy.2013.04.049. [Online]. Available: https://www.sciencedirect.com/science/article/pii/S0360544213003629.

[82] C. Lee, U. Kim, D.-H. Lee, *et al.*, "Development of a smart handheld surgical tool with tactile feedback", *Intelligent Service Robotics*, vol. 10, no. 2, 2017. DOI: 10.1007/s11370-016-0214-5.

[83] H. Lee, *Thermal design: heat sinks, thermoelectrics, heat pipes, compact heat exchangers, and solar cells*. John Wiley & Sons, 2022.

[84] A. Montecucco and A. R. Knox, "Accurate simulation of thermoelectric power generating systems", *Applied Energy*, vol. 118, pp. 166–172, 2014.

[85] V. Zlatić and A. C. Hewson, Eds., *Properties and Applications of Thermoelectric Materials* (NATO Science for Peace and Security Series B: Physics and Biophysics). Dordrecht: Springer Netherlands, 2009, ISBN: 978-90-481-2891-4 978-90-481-2892-1. DOI: 10.1007/978-90-481-2892-1. [Online]. Available: http://link.springer.com/10.1007/978-90-481-2892-1 (visited on 07/19/2021).

[86] D. M. Rowe, *Materials, Preparation, and Characterization in Thermoelectrics: Thermoelectrics and Its Energy Harvesting*, 1st ed., D. M. Rowe, Ed. CRC Press, Dec. 19, 2017, ISBN: 978-1-315-21690-4. DOI: 10.1201/b11891. [Online]. Available: https://www.taylorfrancis.com/books/9781439874714 (visited on 07/19/2021).

[87] D. Beretta, N. Neophytou, J. M. Hodges, *et al.*, "Thermoelectrics: From history, a window to the future", *Materials Science and Engineering: R: Reports*, vol. 138, p. 100 501, Oct. 1, 2019, ISSN: 0927-796X. DOI: 10.1016/j.mser.2018.09.001. [Online]. Available: https://www.sciencedirect.com/science/article/pii/S0927796X18301566 (visited on 06/23/2021).

[88] D. Dávila Pineda and A. Rezania, Eds., *Thermoelectric Energy Conversion: Basic Concepts and Device Applications* (Advanced Micro and Nanosystems), 1st ed. Wiley, Sep. 25, 2017, ISBN: 978-3-527-34071-2 978-3-527-69811-0. DOI: 10.1002/9783527698110. [Online]. Available: https://onlinelibrary.wiley.com/doi/book/10.1002/9783527698110 (visited on 07/19/2021).

[89] A. Montecucco and A. R. Knox, "Accurate simulation of thermoelectric power generating systems", *Applied Energy*, vol. 118, pp. 166–172, Apr. 1, 2014, ISSN: 0306-2619. DOI: 10.1016/j.apenergy.2013.12.028. [Online]. Available: https://www.sciencedirect.com/science/article/pii/S0306261913010271 (visited on 06/24/2021).

[90] R. He, G. Schierning, and K. Nielsch, "Thermoelectric devices: A review of devices, architectures, and contact optimization", *Advanced Materials Technologies*, vol. 3, no. 4, p. 1 700 256, 2018, _eprint: https://onlinelibrary.wiley.com/doi/pdf/10.1002/admt.201700256, ISSN: 2365-709X. DOI: 10.1002/admt.201700256. [Online]. Available: https://onlinelibrary.wiley.com/doi/abs/10.1002/admt.201700256 (visited on 07/14/2021).

[91] *Modeling and application of a thermoelectric generator*, in collab. with D. Yan, Toronto, ON, Canada, 2011.

[92] S. Vostrikov, A. Somov, and P. Gotovtsev, "Low temperature gradient thermoelectric generator: Modelling and experimental verification", *Applied Energy*, vol. 255, p. 113 786, Dec. 2019, ISSN: 03062619. DOI: 10.1016/j.apenergy.2019.113786. [Online]. Available: https://linkinghub.elsevier.com/retrieve/pii/S0306261919314734 (visited on 12/28/2021).

[93] M. Hodes, "Optimal pellet geometries for thermoelectric power generation", *IEEE Transactions on Components and Packaging Technologies*, vol. 33, no. 2, pp. 307–318, Jun. 2010. DOI: 10.1109/tcapt.2009.2039934. [Online]. Available: https://doi.org/10.1109/tcapt.2009.2039934.

[94] "Efficiently maximising power generation from thermoelectric generators", Ph.D. dissertation, University of Glasgow, Glasgow, Scotland, 2014, 161 pp. [Online]. Available: https://theses.gla.ac.uk/5213/1/2014montecuccophd.pdf (visited on 02/25/2023).

[95] A. A. Sherchenkov, Y. I. Shtern, R. E. Mironov, M. Y. Shtern, and M. S. Rogachev, "Current state of thermoelectric material science and the search for new effective materials", *Nanotechnologies in Russia*, vol. 10, no. 11-12, pp. 827–840, Nov. 2015. DOI: 10.1134/s1995078015060117. [Online]. Available: https://doi.org/10.1134/s1995078015060117.

[96] J. He, M. G. Kanatzidis, and V. P. Dravid, "High performance bulk thermoelectrics via a panoscopic approach", *Materials Today*, vol. 16, no. 5, pp. 166–176, May 2013. DOI: 10.1016/j.mattod.2013.05.004. [Online]. Available: https://doi.org/10.1016/j.mattod.2013.05.004.

[97] D. Zabek and F. Morini, "Solid state generators and energy harvesters for waste heat recovery and thermal energy harvesting", *Thermal Science and Engineering Progress*, vol. 9, pp. 235–247, Mar. 1, 2019, ISSN: 2451-9049. DOI: 10.1016/j.tsep.2018.11.011. [Online]. Available: https://www.sciencedirect.com/science/article/pii/S2451904918305298 (visited on 07/20/2021).

[98] S. Twaha, J. Zhu, Y. Yan, and B. Li, "A comprehensive review of thermoelectric technology: Materials, applications, modelling and performance improvement", *Renewable and Sustainable Energy Reviews*, vol. 65, pp. 698–726, Nov. 2016, ISSN: 13640321. DOI: 10.1016/j.rser.2016.07.034. [Online]. Available: https://linkinghub.elsevier.com/retrieve/pii/S1364032116303653 (visited on 12/26/2021).

[99] H. Böttner, D. Jänsch, M. Klein Altstedde, *et al.*, "Thermoelektrik: Strom aus Abwärme", p. 25, 2016, BINE Informationsdienst.

[100] G. Smith and R. Wolfe, "Thermoelectric properties of bismuth-antimony alloys", *Journal of Applied Physics*, vol. 33, no. 3, pp. 841–846, 1962.

[101] T. Tritt, *Advances in Thermoelectric Materials I* (ISSN). Elsevier Science, 2000, ISBN: 978-0-08-054097-9. [Online]. Available: https://books.google.pl/books?id=jO3nzAbzAWYC.

[102] C. B. Vining, "Zt 3.5: Fifteen years of progress and things to come", in *European Conference on Thermoelectrics, ECT2007, available at http://ect2007.its.org/system/files/u1/pdf/02.pdf*, V. Semenyuk, Ed., Odessa, Ukraine, 2007. [Online]. Available: http://ect2007.its.org/system/files/u1/pdf/02.pdf.

[103] S. Lin, W. Li, Z. Chen, J. Shen, B. Ge, and Y. Pei, "Tellurium as a high-performance elemental thermoelectric", *Nature Communications*, vol. 7, no. 1, p. 10 287, Jan. 11, 2016, Bandiera_abtest: a Cc_license_type: cc_by Cg_type: Nature Research Journals Number: 1 Primary_atype: Research Publisher: Nature Publishing Group Subject_term: Applied physics;Semiconductors;Thermoelectrics Subject_term_id: applied-physics;semiconductors;thermoelectrics, ISSN: 2041-1723. DOI: 10.1038/ncomms10287. [Online]. Available: https://www.nature.com/articles/ncomms10287 (visited on 07/20/2021).

[104] P. K. Sharma, T. D. Senguttuvan, V. K. Sharma, and S. Chaudhary, "Revisiting the thermoelectric properties of lead telluride", *Materials Today Energy*, vol. 21, p. 100 713, Sep. 1, 2021, ISSN: 2468-6069. DOI: 10.1016/j.mtener.2021.100713. [Online]. Available: https://www.sciencedirect.com/science/article/pii/S2468606921000782 (visited on 07/19/2021).

[105] Z. Ren, Y. Lan, and Q. Zhang, Eds., *Advanced Thermoelectrics: Materials, Contacts, Devices, and Systems*, 1st ed. Boca Raton, FL : CRC Press, Taylor & Francis Group, [2017] | Series: Series in materials science and engineering: CRC Press, Nov. 6, 2017, ISBN: 978-1-315-15376-6. DOI: 10.1201/9781315153766. [Online]. Available: https://www.taylorfrancis.com/books/9781498765732 (visited on 07/19/2021).

[106] D. Champier, "Thermoelectric generators: A review of applications", *Energy Conversion and Management*, vol. 140, pp. 167–181, May 2017, ISSN: 01968904. DOI: 10.1016/j.enconman.2017.02.070. [Online]. Available: https://linkinghub.elsevier.com/retrieve/pii/S0196890417301851 (visited on 07/19/2020).

[107] Z. Soleimani, S. Zoras, B. Ceranic, S. Shahzad, and Y. Cui, "A review on recent developments of thermoelectric materials for room-temperature applications", *Sustainable Energy Technologies and Assessments*, vol. 37, p. 100 604, Feb. 1, 2020, ISSN: 2213-1388. DOI: 10.1016/j.seta.2019.100604. [Online]. Available: https://www.sciencedirect.com/science/article/pii/S2213138819305831 (visited on 07/20/2021).

[108] M. A. Zoui, S. Bentouba, J. G. Stocholm, and M. Bourouis, "A review on thermoelectric generators: Progress and applications", *Energies*, vol. 13, no. 14, p. 3606, Jul. 13, 2020, ISSN: 1996-1073. DOI: 10.3390/en13143606. [Online]. Available: https://www.mdpi.com/1996-1073/13/14/3606 (visited on 07/19/2021).

[109] N. Jaziri, A. Boughamoura, J. Müller, B. Mezghani, F. Tounsi, and M. Ismail, "A comprehensive review of thermoelectric generators: Technologies and common applications", *Energy Reports*, SI:Energy Storage - driving towards a clean energy future, vol. 6, pp. 264–287, Dec. 1, 2020, ISSN: 2352-4847. DOI: 10.1016/j.egyr.2019.12.011. [Online]. Available: https://www.sciencedirect.com/science/article/pii/S2352484719306997 (visited on 07/14/2021).

[110] C.-C. Wu, W.-C. Kuo, H.-J. Wang, *et al.*, "A pliable and batteryless real-time ECG monitoring system-in-a-patch", in *2015 International Symposium on VLSI Design, Automation and Test, VLSI-DAT 2015*, 2015. DOI: 10.1109/VLSI-DAT.2015.7114521. [Online]. Available: https://www.scopus.com/inward/record.uri?eid=2-s2.0-84936976575&doi=10.1109%2fVLSI-DAT.2015.7114521&partnerID=40&md5=4566e31351a3e561d269d075713046a5.

[111] S. Bose, B. Shen, and M. Johnston, "A batteryless motion-adaptive heartbeat detection system-on-chip powered by human body heat", *IEEE Journal of Solid-State Circuits*, vol. 55, no. 11, pp. 2902–2913, 2020. DOI: 10.1109/JSSC.2020.3013789. [Online]. Available: https://www.scopus.com/inward/record.uri?eid=2-s2.0-85094922636&doi=10.1109%2fJSSC.2020.3013789&partnerID=40&md5=2bb5e504d01ad31fc34861f62df90e0e.

[112] M. Van Bavel, V. Leonov, R. F. Yazicioglu, *et al.*, "Wearable battery-free wireless 2-channel eeg systems powerd by energy scavengers", *Sensors & Transducers Journal*, vol. 94, no. 7, pp. 103–115, 2008.

[113] J. Yuan and R. Zhu, "A fully self-powered wearable monitoring system with systematically optimized flexible thermoelectric generator", *Applied Energy*, vol. 271, p. 115 250, Aug. 1, 2020, ISSN: 0306-2619. DOI: 10.1016/j.apenergy.2020.115250. [Online]. Available: https://www.sciencedirect.com/science/article/pii/S0306261920307625 (visited on 07/28/2021).

[114] A. Nozariasbmarz, H. Collins, K. Dsouza, *et al.*, "Review of wearable thermoelectric energy harvesting: From body temperature to electronic systems", *Applied Energy*, vol. 258, p. 114 069, Jan. 15, 2020, ISSN: 0306-2619. DOI: 10.1016/j.apenergy.2019.114069. [Online]. Available: https://www.sciencedirect.com/science/article/pii/S0306261919317568 (visited on 06/23/2021).

[115] T. Torfs, V. Leonov, C. Van Hoof, and B. Gyselinckx, "Body-heat powered autonomous pulse oximeter", in *SENSORS, 2006 IEEE*, IEEE, 2006, pp. 427–430.

[116] B. Farahani, F. Firouzi, V. Chang, M. Badaroglu, N. Constant, and K. Mankodiya, "Towards fog-driven IoT eHealth: Promises and challenges of IoT in medicine and healthcare", *Future Generation Computer Systems*, vol. 78, pp. 659–676, Jan. 1, 2018, ISSN: 0167-739X. DOI: 10.1016/j.future.2017.04.036. [Online]. Available: https://www.sciencedirect.com/science/article/pii/S0167739X17307677 (visited on 07/28/2021).

[117] M. Haras and T. Skotnicki, "Thermoelectricity for IoT – a review", *Nano Energy*, vol. 54, pp. 461–476, Dec. 1, 2018, ISSN: 2211-2855. DOI: 10.1016/j.nanoen.2018.10.013. [Online]. Available: https://www.sciencedirect.com/science/article/pii/S2211285518307286 (visited on 07/28/2021).

[118] M. Markiewicz, P. Dziurdzia, T. Konieczny, *et al.*, "Software controlled low cost thermoelectric energy harvester for ultra-low power wireless sensor nodes", *IEEE Access*, vol. 8, pp. 38 920–38 930, 2020, Conference Name: IEEE Access, ISSN: 2169-3536. DOI: 10.1109/ACCESS.2020.2975424.

[119] M. Daniol, L. Böhler, A. Keller, and R. Sroka, "Autoclave sterilization powered medical IoT sensor systems", in *Methods and Techniques of Signal Processing in Physical Measurements*, R. Hanus, D. Mazur, and C. Kreischer, Eds., ser. Lecture Notes in Electrical Engineering, Cham: Springer International Publishing, 2019, pp. 31–43, ISBN: 978-3-030-11186-1. DOI: 10.1007/978-3-030-11187-8_3.

[120] M. Daniol, L. Boehler, R. Sroka, and A. Keller, "Modeling and implementation of TEG-based energy harvesting system for steam sterilization surveillance sensor node", *Sensors*, vol. 20, no. 21, 2020, ISSN: 1424-8220. DOI: 10.3390/s20216338. [Online]. Available: https://www.mdpi.com/1424-8220/20/21/6338.

[121] *Rf430frl15xh family - technical reference manual*, SLAU506, Texas Instruments Inc., Dec. 2014.

[122] *Rf430frl15xh device errata sheet*, SLAZ680A, Rev. A, Texas Instruments Inc., Dec. 2016.

[123] *Rf430frl15xh nfc iso 15693 sensor transponder*, SLAS834C, Rev. C, Texas Instruments Inc., Dec. 2014.

[124] F. Rusu, *Specs & architecture*, Sep. 2018. [Online]. Available: https://lowpowerlab.com/guide/currentranger/specs-architecture/.

[125] *Lowpowerlab current ranger - documentation - specs and architecture*, LowPowerLabs, 2018. [Online]. Available: https://lowpowerlab.com/guide/currentranger/?view=all#specs-architecture.

[126] J. George, T. Compagno, F. Waldron, and J. Barrett, "Reliability analysis of plastic encapsulated coin batteries under harsh environmental conditions", in *2012 4th Electronic System-Integration Technology Conference*, Amsterdam, Netherlands: IEEE, Sep. 2012, pp. 1–3, ISBN: 978-1-4673-4644-3 978-1-4673-4645-0 978-1-4673-4643-6. DOI: 10.1109/ESTC.2012.6542109.

[127] L. Boehler, M. Daniol, R. Sroka, D. Osinski, and A. Keller, "Sensors in the autoclave-modelling and implementation of the IoT steam sterilization procedure counter", *Sensors*, vol. 21, no. 2, p. 510, Jan. 2021. DOI: 10.3390/s21020510. [Online]. Available: https://doi.org/10.3390/s21020510.

[128] "1590Z110 Technical Datasheet", Hammond Electronics, Tech. Rep., 2022.

[129] B. Baker, "Chapter 3 - the right adc for the right application", in *A Baker's Dozen - Real Analog Solutions for Digital Designers*, B. Baker, Ed., Burlington: Newnes, 2005, pp. 65–89, ISBN: 978-0-7506-7819-3. DOI: https://doi.org/10.1016/B978-075067819-3/50005-1. [Online]. Available: https://www.sciencedirect.com/science/article/pii/B9780750678193500051.

[130] "Thermocouples. Part 1: Specifications and Tolerances EMF", PKN - Polish Committee for Standardization, Warsaw, PL, Standard, 2014.

[131] *Specification of temperature probe tt4-pt100b-t180-c312-200*, Rev. 00, TEWA Temperature Sensors, Sep. 2019.

[132] *34410a and 34411a multimeters datasheet*, Keysight Technologies, May 2015.

[133] "Industrial platinum resistance thermometers and platinum temperature sensors", International Electrotechnical Commission, Geneva, CH, Standard, Jan. 2022.

[134] *Tc-08 cloud-connected 8-channel thermocouple data logger - datasheet*, Rev. 11, Pico Technology Ltd., Sep. 2021.

[135] P. Dziurdzia and A. Mirocha, "From constant to temperature dependent parameters based electrothermal models of teg", in *2009 MIXDES-16th International Conference Mixed Design of Integrated Circuits & Systems*, 2009, pp. 555–559.

[136] A. Zatorski and R. Sroka, *Podstawy metrologii elektrycznej*, pol. Kraków: Wydawnictwa AGH, 2011, OCLC: 803873752, ISBN: 9788374644051.

[137] J. Carvill, *3 - Thermodynamics and heat transfer*, J. Carvill, Ed. Oxford: Butterworth-Heinemann, 1993, pp. 102–145, ISBN: 978-0-08-051135-1. DOI: https://doi.org/10.1016/B978-0-08-051135-1.50008-X. [Online]. Available: https://www.sciencedirect.com/science/article/pii/B978008051135150008X.

[138] *Active aerogels silfoam - datasheet*. [Online]. Available: https://www.activeaerogels.com/spray-on/.

[139] "Basic physical properties of chemical compounds", in *Knovel Critical Tables (2nd Edition)*, Knovel, 2008. [Online]. Available: https://app.knovel.com/hotlink/toc/id:kpKCTE000X/knovel-critical-tables/knovel-critical-tables.

[140] M.-K. Han, Y. Jin, D.-H. Lee, and S.-J. Kim, "Thermoelectric Properties of Bi2Te3: CuI and the Effect of Its Doping with Pb Atoms", en, *Materials*, vol. 10, no. 11, p. 1235, Oct. 2017, ISSN: 1996-1944. DOI: 10.3390/ma10111235. [Online]. Available: http://www.mdpi.com/1996-1944/10/11/1235 (visited on 12/12/2021).

[141] I. T. Witting, T. C. Chasapis, F. Ricci, *et al.*, "The Thermoelectric Properties of Bismuth Telluride", en, *Advanced Electronic Materials*, vol. 5, no. 6, p. 1 800 904, Jun. 2019, ISSN: 2199-160X, 2199-160X. DOI: 10.1002/aelm.201800904. [Online]. Available: https://onlinelibrary.wiley.com/doi/10.1002/aelm.201800904 (visited on 12/12/2021).

[142] T. Arisaka, M. Otsuka, and Y. Hasegawa, "Measurement of thermal conductivity and specific heat by impedance spectroscopy of Bi_2Te_3 thermoelectric element", en, *Review of Scientific Instruments*, vol. 90, no. 4, p. 046 104, Apr. 2019, ISSN: 0034-6748, 1089-7623. DOI: 10.1063/1.5079832. [Online]. Available: http://aip.scitation.org/doi/10.1063/1.5079832 (visited on 12/12/2021).

[143] W. Liu, K. C. Lukas, K. McEnaney, *et al.*, "Studies on the Bi_2Te_3–Bi_2Se_3–Bi_2S_3 system for mid-temperature thermoelectric energy conversion", en, *Energy Environ. Sci.*, vol. 6, no. 2, pp. 552–560, 2013, ISSN: 1754-5692, 1754-5706. DOI: 10.1039/C2EE23549H. [Online]. Available: http://xlink.rsc.org/?DOI=C2EE23549H (visited on 12/12/2021).

[144] D. O. Kipp, *MatWeb Ceramics Material Data Sheets (MDS)*. Knovel, 2021, ISBN: 978-1-5231-4947-6. [Online]. Available: https://app.knovel.com/hotlink/itble/id:kt012ULQRO/table-2-material-properties/table-2-material-properties.

[145] "CFD numerics: Non-orthogonal correctors". Simscale GmbH. (2022), [Online]. Available: https://www.simscale.com/docs/simulation-setup/numerics/non-orthogonal-correctors/ (visited on 05/21/2023).

[146] "How to check and improve mesh quality". Simscale GmbH. (2022), [Online]. Available: https://www.simscale.com/knowledge-base/how-to-check-and-improve-mesh-quality/ (visited on 05/22/2023).

[147] *Structural analysis numerics: Simulation setup*, Feb. 2023. [Online]. Available: https://www.simscale.com/docs/simulation-setup/numerics/structural-analysis/.

[148] D. Madier, *Practical Finite Element Analysis for Mechanical Engineers*. FEA academy., 2020, ISBN: 978-1-9990475-0-4. [Online]. Available: https://books.google.pl/books?id=7TxhzgEACAAJ.

[149] E. Agullo *et al.*, "Multifrontal massively parallel solver (mumps 5.3. 0) user's guide", Tech. rep., CERFACS, ENS Lyon, INPT (ENSEEIHT)-IRIT, Inria, Mumps ..., Tech. Rep., 2020.

[150] C. T. Kelley and D. E. Keyes, "Convergence analysis of pseudo-transient continuation", *SIAM Journal on Numerical Analysis*, vol. 35, no. 2, pp. 508–523, 1998.

[151] S. Twaha, J. Zhu, Y. Yan, and B. Li, *A comprehensive review of thermoelectric technology: Materials, applications, modelling and performance improvement*, 2016. DOI: 10.1016/j.rser.2016.07.034.

[152] V. Leonov, "Thermoelectric Energy Harvesting of Human Body Heat for Wearable Sensors", *IEEE Sensors Journal*, vol. 13, no. 6, pp. 2284–2291, Jun. 2013, ISSN: 1558-1748. DOI: 10.1109/JSEN.2013.2252526.

[153] L. Sigrist, N. Stricker, D. Bernath, J. Beutel, and L. Thiele, "Thermoelectric Energy Harvesting From Gradients in the Earth Surface", *IEEE Transactions on Industrial Electronics*, vol. 67, no. 11, pp. 9460–9470, Nov. 2020, ISSN: 1557-9948. DOI: 10.1109/TIE.2019.2952796.

[154] M. Thielen, L. Sigrist, M. Magno, C. Hierold, and L. Benini, "Human body heat for powering wearable devices: From thermal energy to application", *Energy Conversion and Management*, vol. 131, 2017. DOI: 10.1016/j.enconman.2016.11.005.

[155] Y. Apertet, H. Ouerdane, O. Glavatskaya, C. Goupil, and P. Lecoeur, "Optimal working conditions for thermoelectric generators with realistic thermal coupling", *EPL (Europhysics Letters)*, vol. 97, no. 2, p. 28 001, Jan. 2012, ISSN: 0295-5075, 1286-4854. DOI: 10.1209/0295-5075/97/28001.

[156] A. Massaguer and E. Massaguer, "Faster and more accurate simulations of thermoelectric generators through the prediction of the optimum load resistance for maximum power and efficiency points", *Energy*, vol. 226, p. 120 248, Jul. 2021, ISSN: 03605442. DOI: 10.1016/j.energy.2021.120248.

[157] K. Yazawa and A. Shakouri, "Cost-Efficiency Trade-off and the Design of Thermoelectric Power Generators", *Environmental Science & Technology*, vol. 45, no. 17, pp. 7548–7553, Sep. 2011, ISSN: 0013-936X, 1520-5851. DOI: 10.1021/es2005418.

[158] K. Zhu, B. Deng, P. Zhang, H. S. Kim, P. Jiang, and W. Liu, "System efficiency and power: The bridge between the device and system of a thermoelectric power generator", *Energy & Environmental Science*, vol. 13, no. 10, pp. 3514–3526, 2020, ISSN: 1754-5692, 1754-5706. DOI: 10.1039/D0EE01640C.

[159] J. Yuan, R. Zhu, and G. Li, "Self-Powered Electronic Skin with Multisensory Functions Based on Thermoelectric Conversion", *Advanced Materials Technologies*, vol. 5, no. 9, p. 2 000 419, 2020, ISSN: 2365-709X. DOI: 10.1002/admt.202000419.

[160] M. M. Barry, K. A. Agbim, P. Rao, C. E. Clifford, B. V. K. Reddy, and M. K. Chyu, "Geometric optimization of thermoelectric elements for maximum efficiency and power output", *Energy*, vol. 112, pp. 388–407, 2016, ISSN: 03605442. DOI: 10.1016/j.energy.2016.05.048. [Online]. Available: http://dx.doi.org/10.1016/j.energy.2016.05.048.

[161] Z. Liu, S. Zhu, Y. Ge, F. Shan, L. Zeng, and W. Liu, "Geometry optimization of two-stage thermoelectric generators using simplified conjugate-gradient method", *Applied Energy*, vol. 190, pp. 540–552, Mar. 2017, ISSN: 0306-2619. DOI: 10.1016/j.apenergy.2017.01.002.

[162] W.-H. Chen, P.-H. Wu, and Y.-L. Lin, "Performance optimization of thermoelectric generators designed by multi-objective genetic algorithm", *Applied Energy*, vol. 209, pp. 211–223, Jan. 2018, ISSN: 0306-2619. DOI: 10.1016/j.apenergy.2017.10.094.

[163] H. He, Y. Wu, W. Liu, M. Rong, Z. Fang, and X. Tang, "Comprehensive modeling for geometric optimization of a thermoelectric generator module", *Energy Conversion and Management*, vol. 183, pp. 645–659, Mar. 2019, ISSN: 0196-8904. DOI: 10.1016/j.enconman.2018.12.087.

[164] V. I. Kubov, Y. Y. Dymytrov, and R. M. Kubova, "Ltspice-model of thermoelectric peltier-seebeck element", in *2016 IEEE 36th International Conference on Electronics and Nanotechnology (ELNANO)*, 2016, pp. 47–51. DOI: 10.1109/ELNANO.2016.7493007.

[165] K. Posobkiewicz, "Modelowanie modułów termoelektrycznych w programie SPICE - przegląd", *Przegląd Elektrotechniczny*, vol. 1, no. 2, pp. 3–7, Feb. 1, 2021, ISSN: 0033-2097. DOI: 10.15199/48.2021.02.01. [Online]. Available: https://sigma-not.pl/publikacja-130165-2021-2.html (visited on 02/21/2022).

[166] S. C. Chapra and R. P. Canale, *Numerical methods for engineers / Steven C. Chapra, Berger Chair in Computing and Engineering, Tufts University, Raymond P. Canale Professor Emeritus of Civil Engineering, University of Michigan.* 8th ed. New York, NY: McGraw-Hill Education, 2021, ISBN: 978-1-260-23207-3.

[167] S. Linge and H. P. Langtangen, "Diffusion equations", in *Finite Difference Computing with PDEs: A Modern Software Approach*. Cham: Springer International Publishing, 2017, pp. 207–322, ISBN: 978-3-319-55456-3. DOI: 10.1007/978-3-319-55456-3_3. [Online]. Available: https://doi.org/10.1007/978-3-319-55456-3_3.